HOLOGRAPHIC INTERFEROMETRY OF PLASMAS

by

ATHAR SAEED NAQVI

A Thesis presented for the Degree

of Doctor of Philosophy at the

University of London

October 1969

Physics Department

Imperial College of Science and Technology

London, S.W.7

Abstract

The work presented in this thesis is directed at the developement of the new field of holographic interferometry as applied to plasma diagnostics. The first aspect of the work is the exposition of the basic principles of holography and the laying down of the criteria for the choice of an experimental setup. The use of the Scatter-plate system is shown to be very fruitful for holographic interferometry of the plasma due to its minimal demands on the quality of the laser and the associated optics.

The second aspect of the work is the demonstration of the technique to yield quantitative results of accuracy comparable to that of conventional interferometry, but with much greater ease. The technique is used for this purpose to determine the time resolved electron density distributions in the Z-pinch discharge whose construction is also described.

The measurements are performed with side-on configuration to reduce refraction of the probing beam due to large refractive index gradients in the pinched plasma column. This becomes acute in end-on configuration. The holographic interferometry is shown to have a smaller error in the fringe shifts due to refraction as compared to that with conventional interferometry. This and many other advantages of holographic interferometry are emphasized to estabilish its worth over other dignostic methods.

The results obtained with holographic interferometry are compared with those obtained by the complimentary technique of Michelson interferometry using He-Ne cw laser. These are found to agree very well with each other. The Michelson interferometry is also shown to be very valuable in its own right for performing measurements on a very fast discharge as used in the present work.

The behaviour of the discharge under various experimental conditions is qualitatively explained on the basis of simple plasma theory. The prospects of using holography for determining plasma temperatures by plasma absorption of the laser radiation are also discussed. Some calculations of the resonance absorption of ruby laser radiation in nitrogen plasma with N_{II} line at 6942.9 Å are presented for enabling the measurements of temperature by this method.

Finally suggestions are made for future work on plasma diagnostics by both holography and holographic interferometry.

CONTENTS

Chapter 1

1.1 Introduction

For any meaningful study of the plasma, it is essential to have reliable and accurate diagnostic methods at one's disposal. Although various techniques were previously available for the measurement of plasma parameters, such as electric and magnetic probes, high speed photography and plasma spectroscopy, these, however, provided approximate results and required various assumptions about the plasma state for the interpretation of these results. It is only after the advent of lasers that plasma diagnostics has acquired a sound base.

The study of the interaction of the external probing electromagnetic radiation with the plasma, resulting in the attenuation, scattering or pure phase changes of the radiation, leads to a knowledge of the plasma state. It is due to the laser that the techniques namely the Thomson scattering, resonance and bremsstrahlung absorption, laser interferometry and holographic interferometry have become possible. Although these techniques have been successfully applied to measure various plasma parameters, these are still being developed and perfected. The most recent of these techniques are the holography and holographic interferometry of the plasmas. When the present work was started, these were still in their infancy. Although the basic principles were established, a convincing application to the quantitative study of any plasma was still lacking. In this thesis it is intended to provide exactly this.

The objectives are defined as

i) to examine the usefulness of holography and holographic interferometry to plasma diagnostics, i.e. to find out exactly what information about the plasma can be extracted by using these techniques,

ii) to examine the demands this technique places on the resources of apparatus etc.;to judge the relative ease of obtaining the same information by other techniques,

iii) to apply the technique to a particular plasma, sort out all the

practical details and to show its usefulness to obtain results of reasonable accuracy.

These objectives are partly discussed in the next section and the discussion is carried through in the succeeding chapters.

It is shown in this thesis that holographic interferometry can be very useful to study plasmas in the situations which fall beyond the range of most other diagnostic methods. This is partly done in Chapter 5 where a comparison is also made with its sister field, namely the optical interferometry, using for instance the Mach-Zehnder system.

The science of holography is a branch of applied optics. Due to its rapid expansion in the last few years, the time involved is rather short for its proper dissemination even among scientists. This is because until very recently no text was available explaining the physical principles and the practical details of holography. As a by-product of the work on plasma diagnostics, the thesis also tries to fill this gap by giving a thorough exposition of the basic principles and the experimental details of holography and holographic interferometry. This is done in chapters 3 and 4.

Since holographic interferometry is only one of the numerous diagnostic techniques employing lasers that measure electron densities, its usefulness can not be properly assessed unless a comparative evaluation is made of these techniques as regards their relative ease of operation and the range of measurements each affords. This is done in the next section.

1.2 Comparative evaluation of various diagnostic techniques using lasers

The parameters of interest in a plasma are the electron and ion density distributions, their temperature distributions and the magnetic field in the plasma. Before the advent of laser, only the plasma spectroscopy provided means of studying the plasma with non-interfering probes.

This was done using the plasma light itself. It was almost impossible

Table 1.1

CW Gas Lasers

laser	wavelength	Electron Density	Electron Temperature	Magnetic Field
He - Ne laser	0.63 μ	Interferometry	-	Faraday rotation
	3.39 μ	"	Free-Free Absorption	"
Argon laser	4880 Å	Interferometry (non-resonant transmission)	Resonance Absorption in Argon plasma (also measured using holography)	Faraday Effect using resonant laser radiation in Argon
	5145 Å	"	"	-
CO_2 laser	10.6 μ	Interferometry	Free-Free Absorption	Faraday rotation
HCN laser	337 μ	Interferometry	Free-Free Absorption	Faraday rotation

Ruby Laser (6943 Å)

Technique	N_e	T_e	N_i	T_i
Thomson Scattering ($\alpha<<1$)	Yes	Yes	--	--
Collective Scattering ($\alpha>>1$)	Yes	Yes	--	Yes
Mach-Zehnder Interferometry	Yes	--	--	--
Holography (interferometry)	Yes	--	--	--
Holography	--	Resonance absorption in N_{II} line (6942.9 Å)	--	--

to use external electromagnetic waves in the visible region of the spectrum to act as the non-interfering probe. This was because the intense plasma radiation in the visible range of the spectrum nearly always masked the probing radiation. The laser with its unique characteristics (section 1.2.1) made it possible to overcome this limitation. This opened a whole new field of diagnostic methods which are listed in Table (1.1).

The purpose here is to make a comparison of these techniques with holographic interferometry as regards their relative ease of operation and the amount of information each yields. This is best done by examining each method separately as in the following.

1.2.1 Plasma diagnostics by light scattering

The measurement of light scattered by the plasma electrons was not possible before the advent of laser because of the extremely small value of the Thomson scattering cross-section. The laser overcame the limitation of large plasma background radiation because of

i) the very large intensity of the laser beam

ii) its monochromaticity allowing the use of narrow-band optical filters to suppress the plasma radiation

iii) its directionality; allowing the use of narrow apertures for stopping undesired plasma light reaching the detectors

iv) its polarization; since the plasma radiation is essentially unpolarized and hence can be eliminated by using appropriate optics.

As can be seen in Table (1.1), the scattering experiment allows the measurements of the electron density and electron and ion temperatures. These are both spatially and temporally resolved. The theory of light scattering by plasmas has been extensively developed and an excellent review is given in Reference (2). To get an understanding of how the above mentioned parameters can be measured, the results of the theory are briefly outlined in the following.

The density fluctuations in a plasma are considered in two parts: one containing the fluctuations of freely moving electrons and the other containing the electron fluctuations correlated with the motion of the ions. Salpeter[1] has shown that the form of these components is determined by a parameter α defined by

$$\alpha = \frac{\lambda_o}{4\pi\lambda_D \sin \theta/2}$$

where λ_D is the Debye length, λ_o is the wavelength of the incident radiation and θ is the angle between the direction of the incident and scattered radiation.

When $\alpha << 1$, the correlations between electrons and ions are negligible. The width of the spectral distribution of the scattered signal gives the electron temperatures and the peak intensity of the scattered light is a measure of electron density.

When $\alpha >> 1$, the spectra are determined completely by collective effects between the particles. They consist of three lines; a central line which has a half width determined by the thermal velocity of the ions and two small symmetrically located so-called plasma lines. The separation of these satellite lines from the central line determines the electron density while their half width determines the electron temperature. The Fig. (1.1) explains the various regions of operation and the associated parameters that can be measured.

Although in principle this technique appears to be the best as it can yield information about various plasma parameters, in practice it is very difficult to carry out these measurements. This is because in the case $\alpha >> 1$, the plasma line is very faint and extremely difficult to detect and to measure its width. The extremely small scattered light causes the signal/noise ratio to be small where noise is the shot noise in the photodetector. Also the large plasma background radiation makes the detection of the scattered signal difficult. To overcome these limitations more powerful lasers are required which made the whole

Fig (1.1) The diagram showing the range of parameters measurable under various operating conditions.

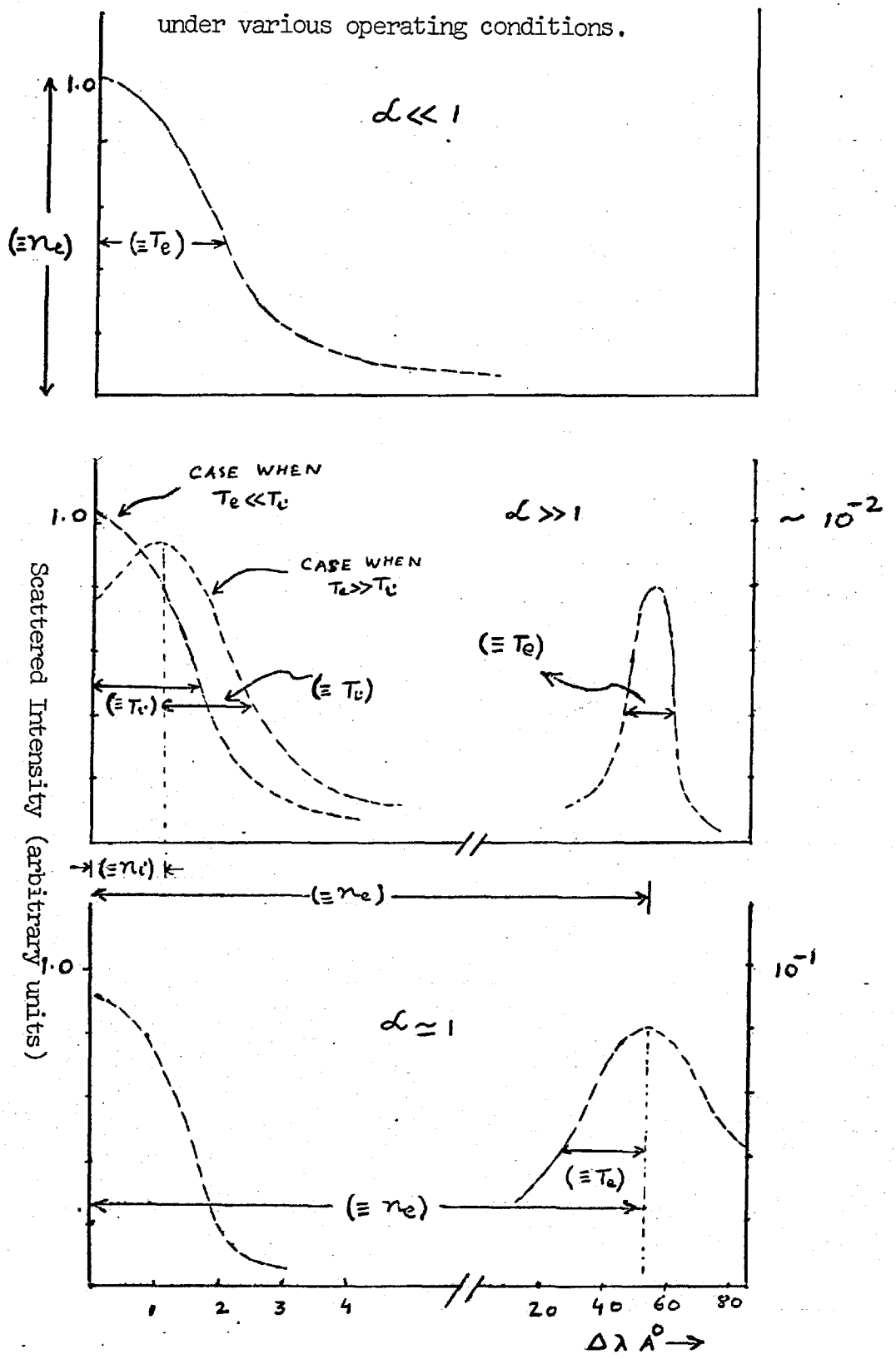

operation very expensive. Also the sophicticated detection systems add their share to the expenses.

One other limitation of the method is the fact that it is difficult to measure particle density and temperature distributions due to the practical difficulty of scanning through the plasma.

If one considers the ease with which the electron density distributions can be measured by gas laser interferometry (1.2.2) and holographic interferometry (1.2.3), then this certainly seems to outweigh the advantages offered by the scattering experiment.

1.2.2 Electron density measurements with cw laser interferometry

This technique is in many ways complimentary to holographic interferometry using a ruby laser. The latter yields time resolved spatial distributions of plasma refractive index while the former measures its time variation at a particular point in space. One therefore has to scan the plasma to build a picture of the spatial distributions of the refractive index. The disadvantage of cw laser interferometry thus is the fact that for obtaining electron density distributions one has to depend on the reproducibility of the plasma.

In the present work this technique was used to check the measurements of holographic interferometry. This work is presented in Chapter 7. There is a whole range of adaptations of the method for obtaining various time and space resolutions and sensitivities in different plasma conditions. These are shown in tabular form in Table (7.1). In some of these interferometers the laser is used simply as a source of light while in others it is coupled to the reference cavity containing the plasma. The frequency response in the latter case where the laser and reference cavities are coupled is much smaller than in the former. This is further discussed in Chapter 7.

To perform measurements on fast pinches, such as the one used in the present work (Chapter 5), the frequency response of the interfero-

meter must be large. The Michelson and Mach-Zehnder interferometers (section 7.2) are ideal for such measurements because of small number of transits of the beam in the system. These also allow the use of very narrow pinhole apertures to provide good spatial resolution of the measurements. This is explained and discussed in Section (7.4), where it is also shown that the use of narrow apertures is not possible in Fabry-Perot interferometers due to large diffraction of the light by the pinhole. Such a problem does not arise in Michelson system because the pinhole is outside the interferometer.

As a consequence of using a beam of very small effective diameter in the Michelson system, it was possible to identify sharp shock front, generated by the current sheet (8.2.2), moving across the beam. The observation of this interesting effect made it possible to estimate the shock speed in the collapsing phase of the discharge. This result was used to obtain a rough estimation of the total energy stored as the kinetic energy during the implosion (section 8.3).

The results obtained by the Michelson interferometer using He-Ne laser agreed very well with those of holographic interferometry. Fortunately, the discharge was reproducible and hence the measurements with gas laser interferometry could be performed as accurately as with holographic interferometry.

1.2.3 Holography and Holographic Interferometry

Although holography has been applied to measure pure phase changes caused by the plasma, as also is the purpose of this thesis, it has been shown to be equally good for measuring the absorption of light by the plasma. This latter fact can be used to measure the plasma temperature using holography. In the conventional method for measuring the plasma resonance absorption by using a photodetector the main limitation arises due to the large resonance line emission acting as a noise. The holographic method has the distinct advantage over the conventional method that the reconstructed image of the hologram is completely insensitive

to the incoherent plasma light.

In the usual laboratory plasmas such as pinch discharges, there is detectable free-free absorption only at infra-red frequencies where it is not possible to make a hologram. One can, however, use lasers in the visible range of the spectrum to measure resonance absorption by holographic method and hence obtain plasma temperature. This is possible using argon laser at 4880 Å with the A_{II} plasma line at the same wavelength. This is discussed in Appendix I, which also describes some calculations performed to examine the feasibility of resonance absorption using ruby laser (6943 Å) in nitrogen plasma with N_{II} line at 6942.9 Å.

Holographic interferometry is used in our work to measure the refractive index distribution in the plasma. The refractive index of the plasma is mainly due to electronic contribution as shown in Chapter 5. The non-electronic contribution, if any, can be eliminated by interferometry at two different wavelengths. The need for this, however, did not arise in the present work.

Most of the systems, reported in the literature, for holographic interferometry require a mode-controlled ruby laser and expensive optics. Single mode operation of the laser is achieved at the expense of power and energy of the output pulse as shown in Chapter 2. In our present work the problem is solved by the use of scatter-plate interferometer which relaxes the demands both on the laser as well as the optics as discussed in Chapter 4.

Holographic interferograms of the plasma can be obtained by using ordinary optical elements without distorting the interference fringe pattern. This contrasts distinctly with conventional interferometry which requires expensive good quality optics if one is to obtain undistorted interferograms of the plasma.

1.3 Layout of the Thesis

This Chapter (1) describes various diagnostic techniques that can

be performed using lasers. These techniques are compared with holographic interferometry and their usefulness evaluated.

Chapter 2 describes the ruby laser to be employed for holographic interferometry of the plasma. It discusses the pumping characteristics from the basic rate equations derived from the energy level diagram of the ruby. A Q-switching method giving well timed short-duration pulses utilizing a simple combination of active and passive Q-switches is described. Relevant mode structure of the laser is discussed because it has a direct bearing on the coherence of the output radiation - a parameter of significance in holography.

Chapter 3 contains an elaborate discussion of the basic principles of the science of holography. A simplified approach giving a physical insight into the working of a hologram is adopted. Magnification considerations of a holographic system are described in view of their usefulness in determining the object size from the reconstructed image. Coherence requirements of the laser illumination to form and reconstruct the holograms are discussed. Other practical considerations helpful in chosing an experimental system for holography of the plasma are outlined.

Chapter 4 describes the scatter plate system to be used for holographic interferometry of the plasma. The aberrations in the optical system are shown to place a demand on the degree of coherence of the radiation. Practical considerations of the photographic materials and processes are discussed as they are of much importance for obtaining good holograms.

Chapter 5 discusses the contribution of various components of the plasma to its refractive index. The sum of all non-electronic contributions is shown to be less than a few percent of the electronic contribution to the refractive index of the plasma. The construction of a Z-pinch device is described. It is shown that when electron density gradients are large, it is only in side-on configuration that the probing rays do not suffer appreciable deviation to distort the fringe pattern. The chapter closes with the description of preliminary measurements on the Z-pinch device.

Chapter 6 describes the experiment which combines the principles and techniques described in the last four chapters. The most suitable holographic system is assembled along with the simple laser source for performing holographic interferometric measurements on the Z-pinch plasma. The radial distributions of the electron densities are calculated by Abel inversion of the fringe distribution obtained in circularly symmetric case. Some results of electron density distributions under various experimental conditions are presented. The sensitivity of measurements and influence of various factors effecting the results are discussed. The chapter ends with the description of some miscellaneous techniques that could be usefully applied to study plasmas under various circumstances.

Chapter 7 describes the Michelson interferometry of the plasma with He-Ne laser performed to verify the results of Chapter 6. A comparison is made of the results obtained by the two methods for plasma under similar circumstances.

Chapter 8 contains a simplified theoretical discussion of the mechanisms involved in the Z-pinch collapse. It explains various experimental observations such as time to pinch, the presence of appreciable axial electron densities well before the pinch, peaking of the electron density at a certain filling pressure etc. on the basis of relevant plasma theories. Plasma temperature is estimated from the energy balance considerations with the knowledge of a few plasma parameters, namely, the electron density, the radius of the pinch and the current at the pinch.
Chapter 9 contains the concluding remarks about the work presented in this thesis and suggestions for the future work.

The Appendix (I) contains the calculation of the absorption of the ruby laser light in N_{II} line at 6942.9 Å in a nitrogen plasma. The measurement of absorption enables one to obtain directly the plasma electron temperature from the above calculations if the plasma electron densities are known. Difficulties involved in carrying out the measurements with the present Z-pinch plasma are described. A simple situation is suggested where these absorption measurements could be performed both with

conventional methods and also with holography of the plasma.

The Appendix (II) contains the simple computer program to calculate the radial distribution of electron densities by Abel inversion of the experimentally obtained fringe distributions.

References

1) Salpeter, E.E. J. Geophys. Res. 68, (1963) 1291.

2) Lochte-Holtgreven, W. 'Plasma Diagnostics' p. 598, (North-Holland Publishing Company - Amsterdam 1968).

Chapter 2

The Ruby Laser

2.1 Introduction

The application of holographic interferometry for plasma diagnostics necessitates the use of a giant pulse ruby laser as the source of the radiation. In this case the most important characteristic of the laser output is its coherence. The output from a normal Q-spoilt laser consists of many axial modes of the resonant cavity contained within the ruby fluorescent line and also of many transverse modes. As discussed in the following chapters, good quality holograms can be obtained only if the laser output has a reasonable degree of coherence which is determined by its mode structure.

In this chapter various factors contributing to the mode structure of the laser output are discussed. The exact nature of the mode structure depends, among other factors, on the method of Q-switching the ruby laser cavity. For this reason the Q-spoiling dynamics using both active and passive Q-switches are discussed. This moreover, helps to obtain short duration well timed pulses essential for time resolved study of the fast moving plasma.

2.2 Principle of operation of the laser

After the first successful operation of the laser by Maiman[1], its behaviour has been thoroughly investigated by various workers. Lasing has been achieved in materials in all the four states of matter, i.e. solid, liquid, gaseous and plasma states. The following discussion will be confined to ruby crystal lasers. Since many thorough accounts exist in the literature, only relevent aspects will be briefly described.

The reasons for the feasibility of laser action by stimulated emission in ruby can be understood with the help of the energy level diagram of

the pink ruby (0.05% chromium) shown in Fig. (2.1). When the ruby is irradiated by green wavelength 5600 Å causing the transition $^4A_2 \rightarrow {}^4F_2$, the output is almost all in red by the transition $2E \rightarrow {}^4A_2$. The quantum efficiency of this process is almost unity. This is because the transition $^4F_2 \rightarrow {}^2E$ is almost non-radiative and the transition $^2E \rightarrow {}^4A_2$ is almost entirely radiative. The presence of wide absorption band $^4F_2$ makes it possible to indirectly transfer larger numbers of ground state electrons to metastable level ^2E by optical pumping. This produces the condition of population inversion thus bringing the ruby in a state of negative absorption.

The laser action is produced in the ruby by placing the active medium, i.e. in the state of population inversion, in an optical resonant cavity. Any photons emitted by spontaneous emission in the direction of the cavity mirrors are reflected back to the active medium and are thus amplified as they pass through it.
The gain per unit path length α is a function of temperature, doping and population inversion. For a 0.05% doped ruby at room temperature the gain is given as[2]

$$\alpha = 0.4 \left(\frac{N_2 - N_1}{N_0}\right) \text{ cm}^{-1} \qquad - (2.1)$$

where N_0 is the total number of chromium ions.

Assuming the losses to be entirely due to transmission from the resonant mirrors, the threshold condition for relaxation oscillations is

$$R_1 R_2 e^{2\alpha L} = 1 \qquad - (2.2)$$

where L is the ruby length and R_1, R_2 are the reflectivities of the mirrors.

To estimate the amount of input light energy to bring the laser to the threshold of operation, the rate equations of ruby treated as three level system have to be solved. These equations can be written with the

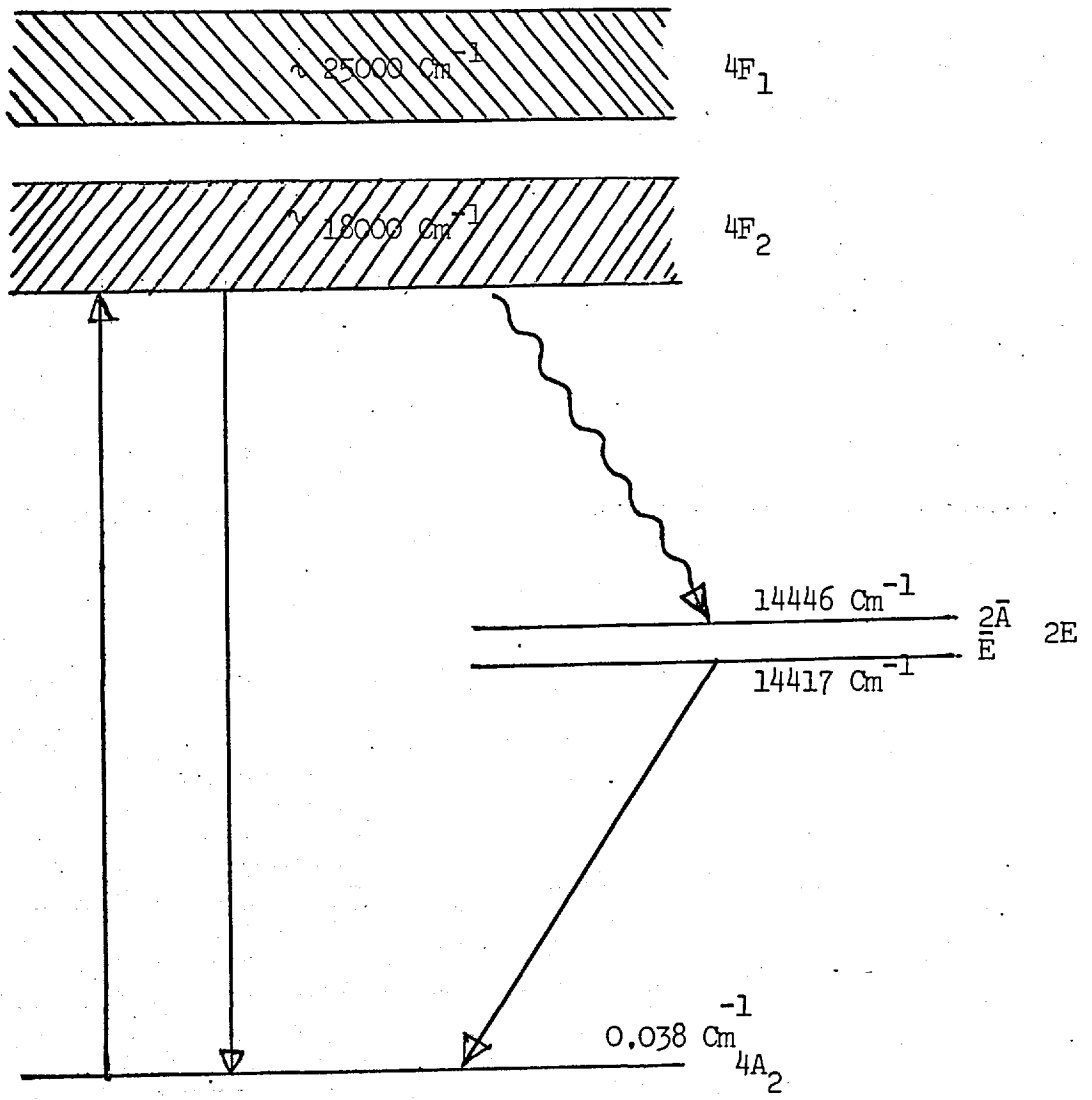

Fig (2.1) An approximate Energy - Level diagram of the ruby.

help of the Fig. (2.1). If we make the assumptions that $N_1 >> N_3$ and the transition probability A_{31} is negligible in comparison with W_{31}, the probability of stimulated emission, then the rate equations can be written as

$$\frac{dN_3}{dt} = W_{13} N_1 - N_3 S_{32}$$

$$\frac{dN_2}{dt} = N_3 S_{32} - N_2(A_{21} + W_{21}) + W_{12} N_1$$

$$N_0 = N_1 + N_2 + N_3 \qquad - (2.3)$$

Noting that $W_{21} = W_{12}$, the above equations can be solved for the relative population inversion, and since in a steady state the derivatives are 0, we obtain

$$\frac{N_2 - N_1}{N_0} = \frac{W_{13} - A_{21}}{W_{13} + A_{21} + 2W_{12}} \qquad - (2.4)$$

The quantity W_{13} is proportional to the incident exciting light and W_{12} is proportional to the laser action in progress. At the threshold of oscillations $W_{12} = 0$.

Knowing R_1, R_2 and L, $\left(\frac{N_2 - N_1}{N_0}\right)_{\text{threshold}}$ can be determined from Equations (2.1) and (2.2). The minimum value of W_{13} necessary to achieve the threshold of oscillation is then obtained from Eq. (2.4). The flash tubes pumping the ruby are black-body radiators. The knowledge of W_{13} enables one to estimate the minimum temperature of the black-body source which may produce population inversion in a three-level system.

2.3 Considerations of the pumping of the ruby

In the practical design of the laser, the parameter of interest is the efficiency of laser operation, i.e. the ratio of the output laser light energy to the electrical energy fed to the flash tube. The overall

efficiency of the optically pumped lasers is less than one per cent. This is because of poor conversion of electrical energy to light energy absorbed by the crystal and also poor utilization of this absorbed energy in contributing to the output of the laser. The latter is about 50% and hence the low efficiency is mainly due to the low pumping efficiency.

The output from the flash tube is mainly blackbody radiation[3]. The narrow absorption band of the laser crystal combined with this broad emission band of the tube gives an intrinsic low effeciency. Although the plasma has a blackbody spectral distribution it has a low emissivity. Moreover only a very small amount (~5%) of the radiation incident on the ruby is absorbed, some is reflected and the rest passes through.

The disadvantage of the above method of pumping apart from poor efficiency is the heating it produces on the ruby rod and the cavity. The practical limitations of the cooling rate of the cavity limits the frequency of operation of the laser. The above disadvantage can be easily overcome by the use of plasma theta-pinch for the pumping of the laser rod. Such a system has been investigated by Feldman et. al.[4,5] and also by Aisenberg et. al.[6]. The light output from the electrodeless flash tube is primarily line spectra in contrast to blackbody radiation from Xe-flash tubes normally used. This has the great advantage of not heating either the ruby or the flash tube and hence the laser can be operated with larger repetition rates. Moreover the line spectrum of the plasma can be adjusted to coincide with the absorption bands of the laser rod and a much higher efficiency of energy utilization can be attained. This can be done by the choice of the gas and the operating pressure and voltage and the rate of change of discharge current in the theta pinch coil.

The results reported by the authors referred to above were very encouraging. They attained lasing both in ruby at 6943 A^{o} and in Nd^{3+} glass rods. The output power with this method of pumping was larger by an order of magnitude compared to the Xe-flash tubes for the same input energy. The output pulse had also very different characteristics.

In ruby a pulse with a width of 10 μsec, was obtained in contrast to spiking for 100 μsec. when pumped with conventional flash tubes. The better matching existed between the blue U.V. (3200 - 4400 Å) ruby pump band (see Fig. 2.1) and argon at 10 torr filling pressure.

Due to the very desirable output characteristics of this method of pumping, a similar project was undertaken by the present author. This was with the intention of trying to operate such a laser with Q-switching for obtaining very short and powerful laser pulse to be used for plasma diagnostics. A small theta pinch device , built by Key[7], was available. A glass flash tube was made which would hold the ruby along the axis of the tube allowing it to be pumped both by plasma light and also by direct impact of the plasma on the crystal. It was following the idea of Fonda-Bonardi[8]. Since the theta pinch system was about six years old, unfortunately the insulation at the spark gap broke down at 30 KV. The project had thus to be abandoned, due to the pressure of other work on holography etc.

In conclusion it may be remarked that the theta pinch pumping can be a very useful method if a large repetition rate of the laser is required. This especially applies to bubble chamber holography and also stroboscopic applications. Haskell et. al.[9] have reported operation of Nd^{3+} glass laser with 60 pulses per second. The coherence properties of the output and its mode structure need yet to be investigated.

2.4 Q-switching techniques

It is necessary to obtain short duration large intensity pulse for obtaining time resolved interferograms of the plasma. Although the fast theta pinch pumping of the laser discussed in the last section produces a single pulse of the laser output, it is not narrow enough to give sufficient time resolution of fast plasmas. One can however employ various Q-switching techniques for this purpose. These are generally classified as active and passive switches. As the name implies, the former type can be employed to give a controlled well timed output pulse;

while in the latter, which includes saturable dyes no accurate control of the timing of the output pulse is possible.

The electro-optic modulators including the Kerr and Pockels cells are among the fast switches. In these modulators the change of cavity from low to high Q condition is achieved in a time short compared to the time taken for the laser pulse to form. The rotating prism type of mechanical modulator can also be called fast switch if the rate of rotation is large. Usually a mirror rotation rate of 20,000 r.p.m. with a meter long cavity with an average quality ruby produces pulses of 50 nsec. duration. With a rotating 'roof' prism and a stationary low reflectivity mirror the light of superior coherence is produced. This is because the cavity contains only the laser material and this causes the beam to emergy in a diffraction limited cone. This method has the disadvantage of a time jitter produced by slight movement of the stationary mirror. This together with the difficulty of making a mechanically stable rotating prism and timing apparatus barred it from the choice.

The Pockels cell employing a KDP crystal is often used as a fast Q-switch. It has the disadvantage of lower optical quality, inherent birefringence and its rapid deterioration in humid air. The Kerr cell uses nitrobenzene which is a loss free Kerr material. However, nitrobenzene often causes large deviations in both pulse shape and spectrum when the light energy flux in the cell becomes of the order of 10 MW/cm^2 or larger. This is mainly because of stimulated Raman scattering in nitrobenzene.

The effect of the Raman transition on the spectrum of a giant pulse produced with a nitrobenzene Kerr shutter was first shown by McClung et. al.[16]. At higher powers the spectrum is smeared out over several angstroms. This causes an effective shortening of the coherence length of the radiation, thus imposing stringent constraints on the holographic set-up. In our experiments, however, the power level of laser output was not too high to produce any serious smearing out of the spectrum.

The Kerr cell was used in $\lambda/4$ switching mode. This was because of

its simplicity and since no large power levels were required which would be attained by using $\lambda/2$ switching. In the first method, the average gain per pass is modulated by modulating the polarization of light inside the cavity. It utilizes the fact that the ruby R line pumped to inversion has a larger absorption cross-section $\sigma_{\perp}$ for light plane-polarized perpendicular to the plane of the c-axis than $\sigma_{\parallel}$ for light polarized parallel to the c-axis.

Under low Q condition with the Kerr cell being active, the coupling and gain on every other pass is reduced. Under high Q condition, the laser photons remain polarized perpendicular to the plane of the c-axis and experience full gain on every pass. This method works because in ruby $\sigma_{\perp}/\sigma_{\parallel} \sim 5$. However, if the degree of over-inversion exceeds 1.7 the threshold of low Q cavity is exceeded and a "spill over" occurs resulting in relaxation oscillations. This can be prevented by using a polarizon in series with the Kerr cell acting as a Kerr shutter.

The loss in low Q condition is not quite 100%, because small reflections at various dielectric interfaces cause some photons to be fed back through the ruby. However, the low Q-threshold is considerably increased. Since the introduction of additional surfaces in the cavity causes the losses to increase, the use of $\lambda/4$ switching was preferred.
The Kerr cell voltage was set at 11.6 KV for $\lambda/4$ switching. The simple check could be made using already polarized light of He-Ne laser. The arrangement is shown in Fig. (2.2). The rotation of the polarization vector is given by

$$\Delta = j \frac{\ell V^2 \lambda}{d^2} \qquad - (2.8)$$

where j is the Kerr constant which varies only very slowly with wavelength and is practically the same for the ruby and He-Ne laser wavelength. V is the potential difference across plates.
ℓ is the length the light traverses between the plates and d the separation of the plates.

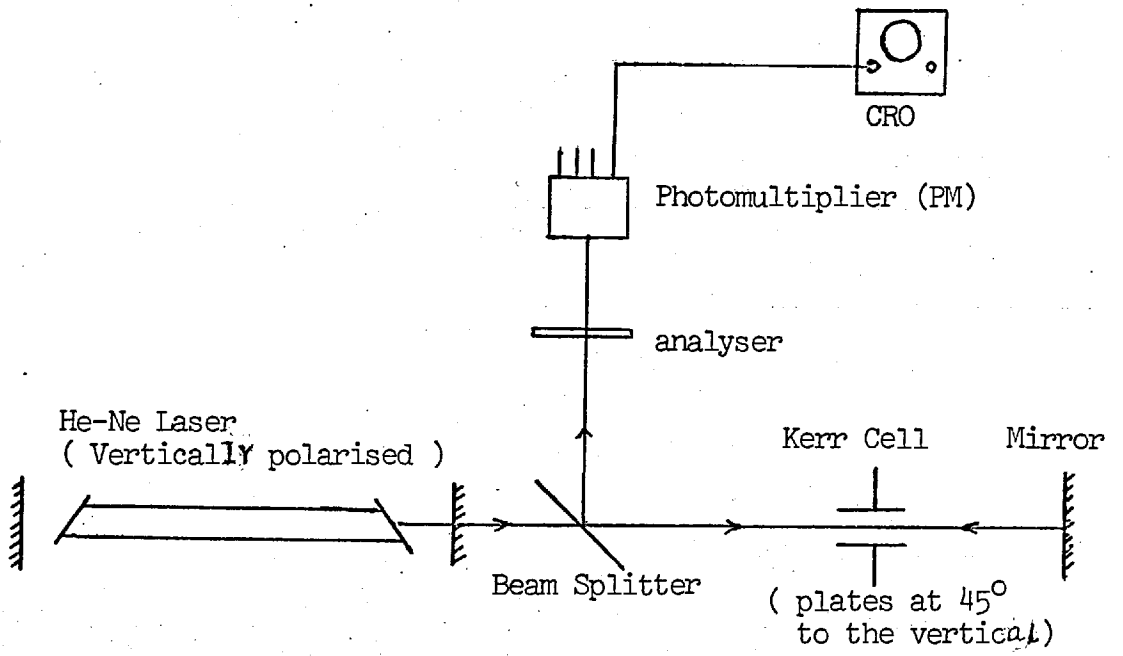

Fig (2.2) Setting the Kerr Cell voltage for $\lambda/4$ switching.

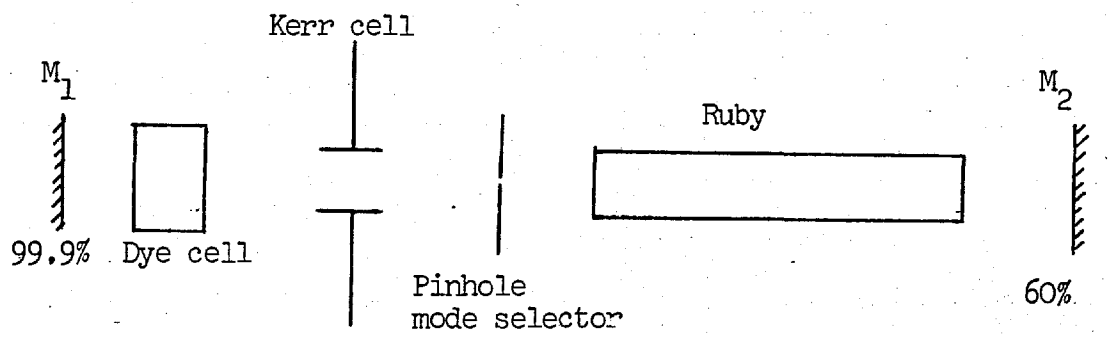

Fig (2.3) Schematic diagram of the Ruby Laser,

For the same rotation we have

$$V_1^2 \lambda_1 = V_2^2 \lambda_2$$

For $\lambda_1 = 6328$ Å and $\lambda_2 = 6943$ Å

$$V_1 = 1.048 V_2.$$

The analyser was set to give maximum signal in the photomultiplier. When V_2 was applied to the Kerr cell, it changed the polarization of E ray by $\pi/2$ in double transit through the cell. The signal dropped to about 5% of the initial value. This agrees with the expected value for 6328 Å since the voltage was set for 6943 Å.

As mentioned before the saturable dyes can be used to Q-switch the laser cavity. The giant pulse output in this case is determined by the unbleached absorption of the dye. The pulse will occur as soon as the ruby reaches the threshold level of bleaching of the dye. The population inversion will be depleted by the pulse but if the pumping is continued further pulses will occur.

Since the use of saturable dye alone does not yield a well timed pulse, it is used with a Kerr cell for this purpose. It produces a timed pulse of higher initial inversion/threshold inversion than is possible with the Kerr cell alone. It however requires a careful control of the amount of the input energy such that the threshold for the saturable material does not exceed much earlier than the electrical switching time. If this happens, then the level of over-inversion exceeds the value which the Kerr cell can hold. This results in an early pulse. On the other hand, no pulse may emerge if the level of over-inversion is less than the threshold for the saturable material even after opening the Kerr cell.

The use of saturable material either with or without the Kerr cell results in an improvement of coherence of the emerging beam. This

results from the mode selection properties of the saturable dyes as discussed in a later section.

2.5 Description and operation of the ruby laser system

The laser was basically that designed by Key[7] but with many alterations. It is shown in Fig. (2.3) and consisted of a mirror M_1 having dielectrically coated surface with a reflectivity of 99.9% at 6943 Å, a $\lambda/4$ Kerr cell, 3" x 3/8" ruby in an aluminium cavity and the mirror M_2 with 60% reflectivity. A 3" long and 9 mm. diameter flash tube was energized from a capacitor bank of 624 μf, consisting of capacitors of 2.4 KV maximum charging voltage. This stored a maximum of 1.79 kilojoules. Only about 66% of the energy was delivered to the flash tube, the rest being dissipated in the cables and the inductance. Thus the maximum energy utilized in the flash tube was 1186 joules.

The inductance consisted of 90 turns of 10 s.w.g. insulated copper wire, would on a tufnol tube former of approximately 8" diameter giving an inductance of 520 μH. To switch the Kerr cell for $\lambda/4$ operation a voltage of 11.6 KV was applied across its electrodes through a thyratron unit. The latter was triggered from a timing unit to obtain a controlled giant pulse output.

The laser cavity was aligned using a He-Ne laser, its beam passing through a pinhole to the ruby laser cavity. The various surfaces are adjusted such that they all reflect the laser beam on to the pinhole. If the gas laser is not far enough from the ruby laser cavity, the alignment is not perfect. The final alignment was made using an autocollimator.

Originally the flash tube used was XL 615/9/3 of English Electric. This had to be triggered by 16 KV pulse applied to a thin wire coiled over the quartz envelope of the tube. This was found to be a source of irritation because the spacing of windings of the wire and also the distance of the last turn from the live electrode were quite critical factors. If the latter was slightly less than the critical value, the

tube was found to breakdown by itself. The reason for this could be that any electrostatic fields between the live electrode and the trigger wire would help to accelerate stray electrons and thus could breakdown the tube. Moreover the relatively large value of the trigger pulse was a disadvantage as it was more apt to spark over to the cavity, thus damaging the flash tube. An insulation of the flash tube was provided by using 'pyrophyllite', a machinable asbestos which had high electrical resistance. Later T.W. Wingent flash tube type Xe/s/9/7.6/k with 450 mm. filling pressure of Xe was used. This was cheaper and much quicker to obtain and had reasonably long life. The tube was triggered by a 14 KV pulse directly applied to the live electrode through a low inductance high voltage capacitance. The latter prevented the triggering pulse amplifier being ruined by the flash electrical energy shorting through it. This proved to be a reliable triggering method.

The threshold of laser operation was a function of cavity losses. These depended on the reflectivity of the output mirror, the mirror separation, the surface conditions of the liners in the aluminium cavity and also the age of the flash tube etc. Under the optimum conditions the threshold for relaxation oscillation was 540 Joules and that for giant pulse was ~ 590 Joules for a 50 cms. long cavity.

At one time the giant pulse output from the laser was found to consist of wide single or double pulses of half-widths about 200 nsec. Since these were too wide to allow sufficient time resolution, a systematic search for the cause of the phenomenon was made and is discussed in Sec. (6.4.1). It was discovered that due to a fault in the electrical circuit of the preamplifier for the thyratron, the latter was switching the Kerr cell much more slowly than normal. As discussed in Sec. (2.7), it produced pulses corresponding to slow switching case where the rate of change of cavity Q is slower than the pulse build-up rate. A set of output pulses obtained under various operating conditions is shown in Fig. (2.4).

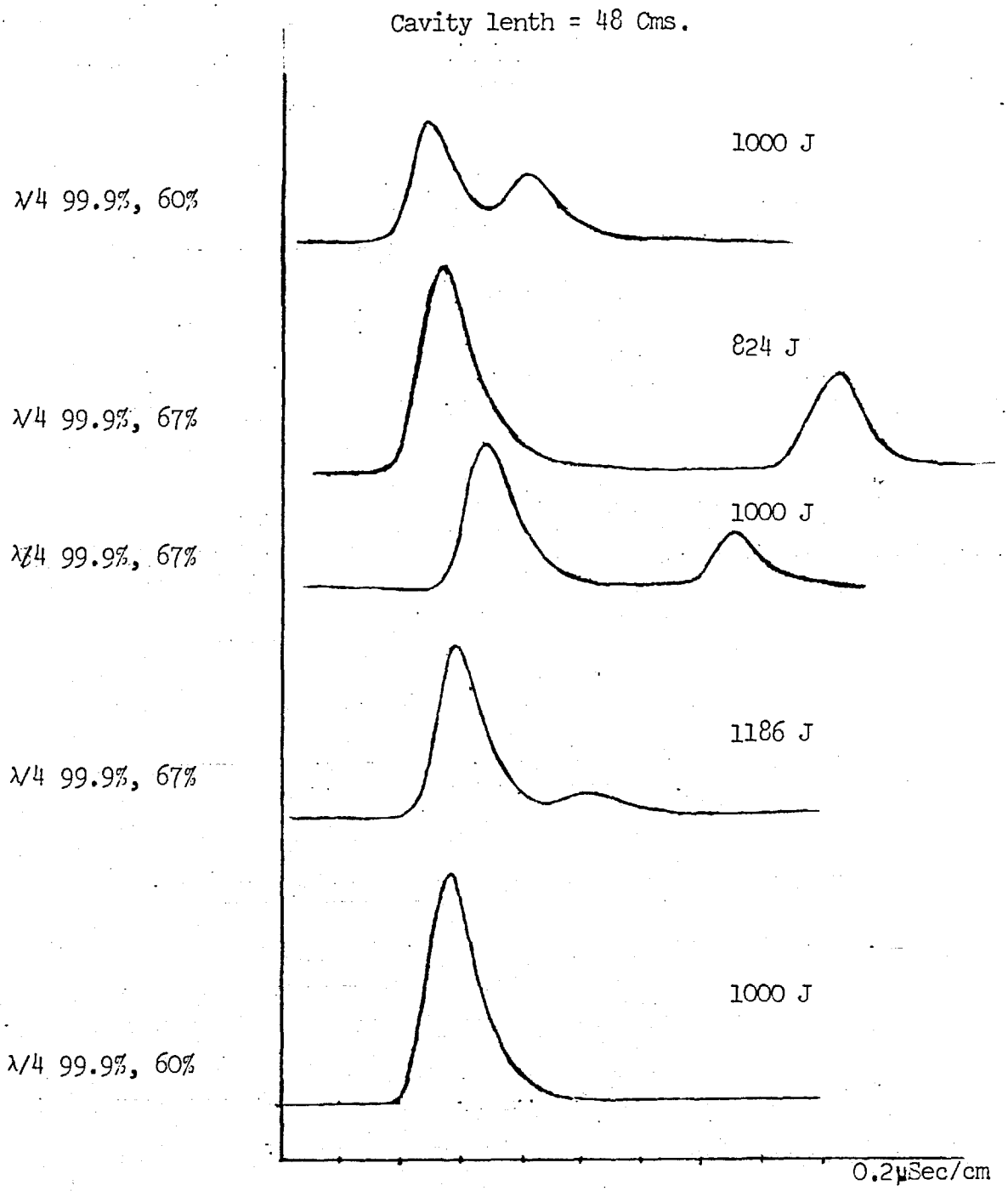

Fig (2.4) Ruby Laser output for Slow Switching case.

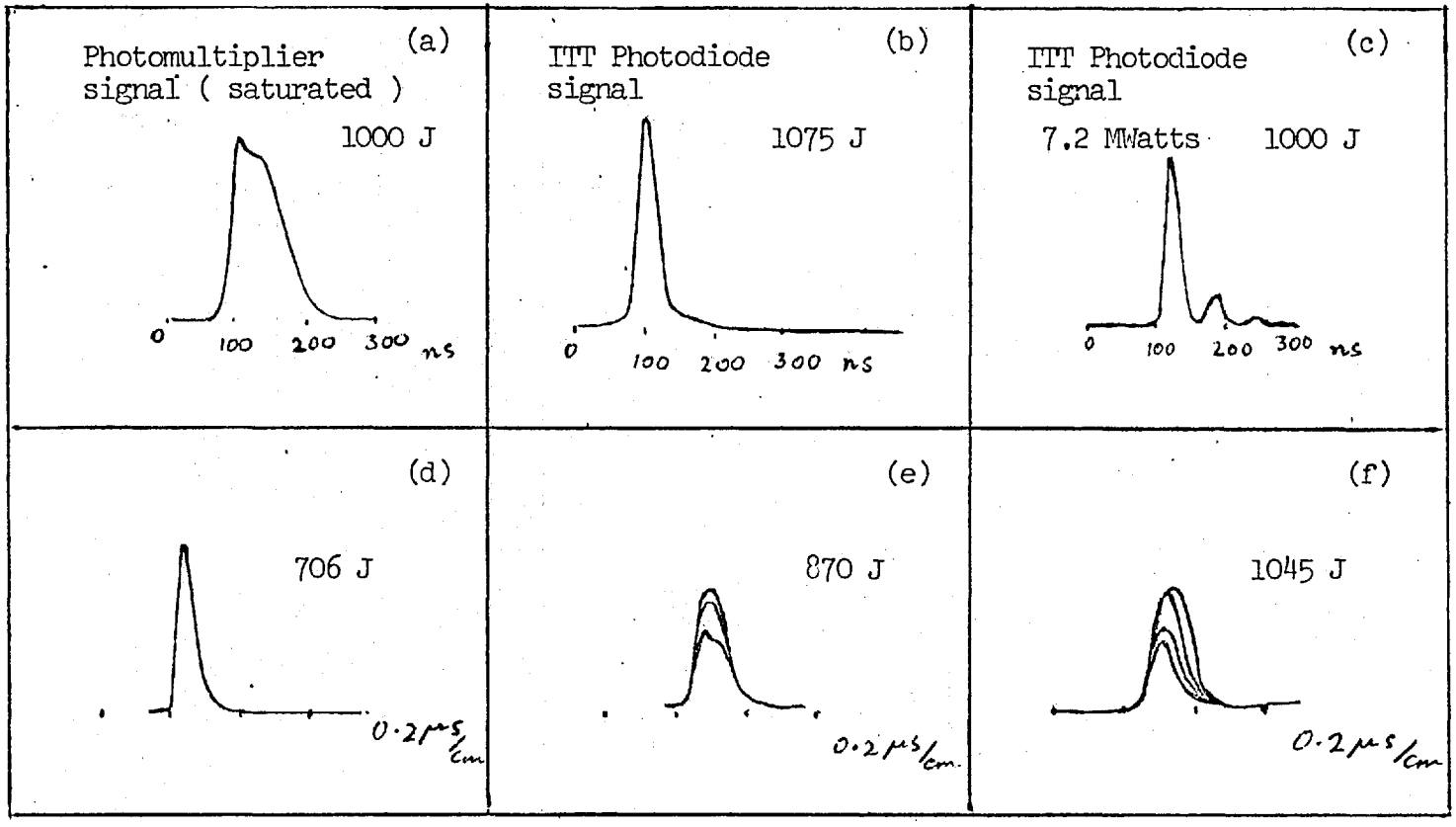

Fig (2,5) (a) to (c) Cavity lenth = 26.5 Cms. Cryptocyanine in methanol
(d) to (f) " " = 46.0 Cms. Vanadyl Phthalocyanine in nitrobenzene.

Before the electrical fault could be eliminated, it was attempted to obtain well timed narrow pulses with the saturable dye solutions in conjunction with the Kerr cell. As has been discussed in the last section (2.4), the attempts were crowned with success but only so under rather critical limits to the input energy to the flash tube. Some pulse shapes with saturable dyes alone are shown in Fig. (2.5). In addition to the normally used cryptocyanine dissolved in methanol, a new dye Vanadyl phthalocyanine in nitrobenzene was also used. The latter is much more stable and the cell needed no replenishing for a long time unlike the other dye solution.

The rather strange shape of the pulse in Fig. (2.5a) was also reported by Key[7]. However, the reason for this shape was not the mirror damage and subsequent additional loss in the cavity causing a slow fall off as postulated by Key. It was found to be due to the saturation of the photomultiplier. This was confirmed by the simultaneous measurement of the laser power using the ITT photodiode F4000 which produced a normal pulse shape. The further confirmation was provided by using the photomultiplier in its linear range by attenuating the input light signal as seen in Fig. (2.5b).

The pulses of smaller amplitude following the main pulse in Fig. (2.5c) are the reflections at the mismatched coaxial cable. Later the use of proper coaxial matching resistor of 50 Ω with a 50 Ω cable eliminated such reflections. Fig. (2.5f) shows multiple pulses due to heavy pumping producing much higher over-inversion than the threshold of low Q cavity. The pulses were of increasing power as also discussed by Key[7].

As discussed earlier, the final arrangement was the use of $\lambda/4$ Kerr switch with saturable dye to produce single pulse at 1155 Joule input energy.

2.6 Power and Energy measurement of the Ruby Laser output

To understand the behaviour of ruby laser operation it was essential

to know the power and energy in the output pulse. For this purpose three different methods were utilized. The first was the measurement of absorption of the ruby output in a saturated solution of Cu So_4 in water. The second was the use of a calibrated fast photodiode ITT F4000 and the last was a power meter using non linear polarization in quartz crystal. These methods are described in the following.

1) Absorption in Cu So_4 cell

The method is based on the fact that a saturated solution of Cu So_4 has a large absorption coefficient at 6943 Å equal to $-3.6\ cm^{-1}$. The cell was constructed in perspex with thin microscope coverslides as glass windows. For a path length of 0.6 cm. in the solution the absorption is 89%. The cell diameter was also 0.6 cm. It rested on rubber pads on perspex block to ensure minimum loss of heat by conduction.

Since the thermal capability of the cell was small a detectable temperature rise was produced by the absorption of laser energy. This was detected by a thermocouple junction cemented in the side of the cell. A Cu-constantan thermocouple was used with very short leads to give low resistance. The other junction was immersed in an identical solution in a small reservoir to keep the temperature constant. Using a very sensitive lamp and scale arrangement, very small temperature rise could be measured. The cell was calibrated by passing an electric current through short length of constantan wire placed in the cell. The current was passed for a very short time (3 secs), compared to the time of the system to respond. This was to avoid any errors being introduced in the measurement of input electric energy due to radiation loss analogous to the absorption of the laser energy.

The amount of deflection depended on the position of the heating coil in the cell. A difference of ~ 12% was observed between the central position and the coil at maximum distance from the thermocouple junction. Since the laser beam was focused to be absorbed at the centre, the calibration was performed by placing the coil centrally in the cell.

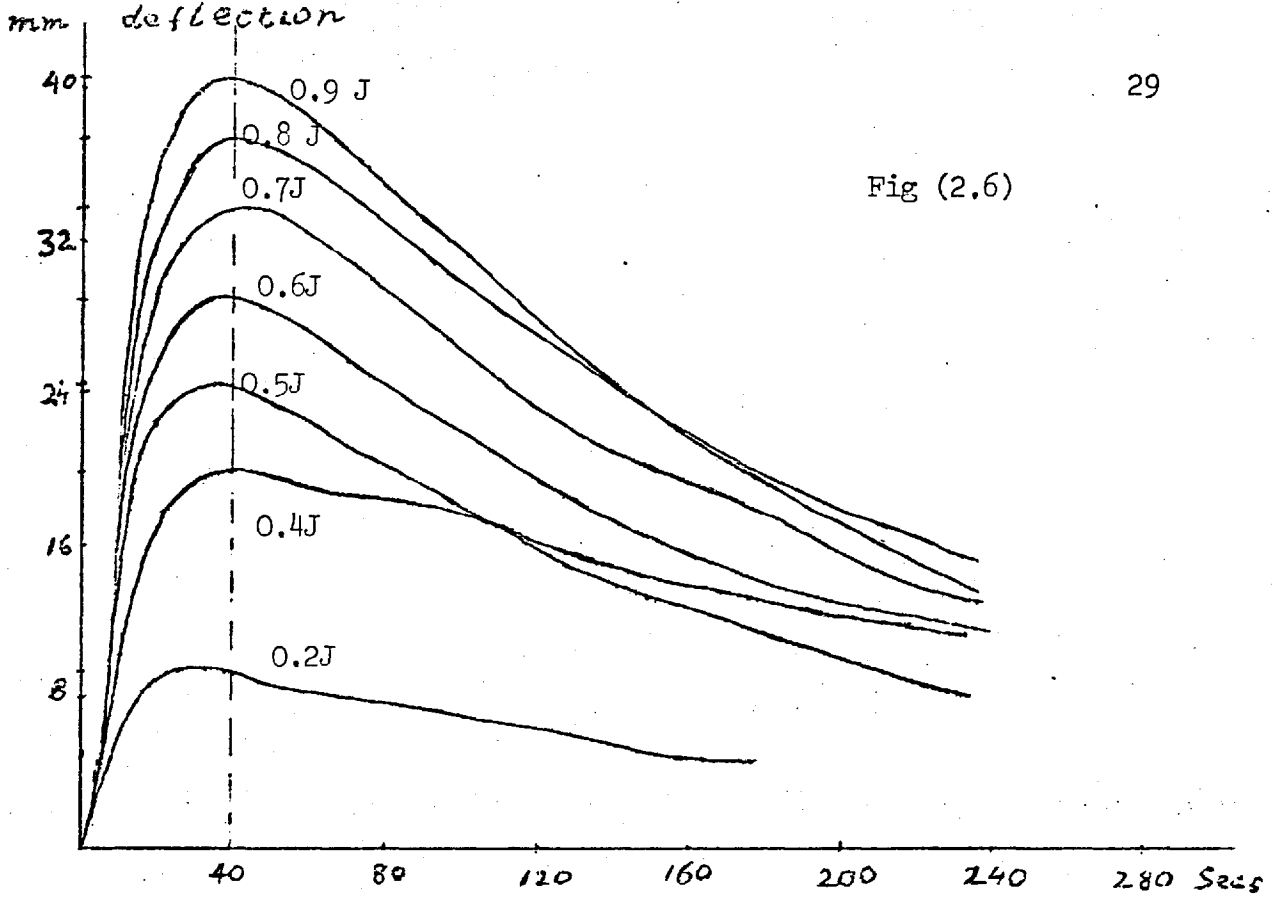

Fig (2.6)

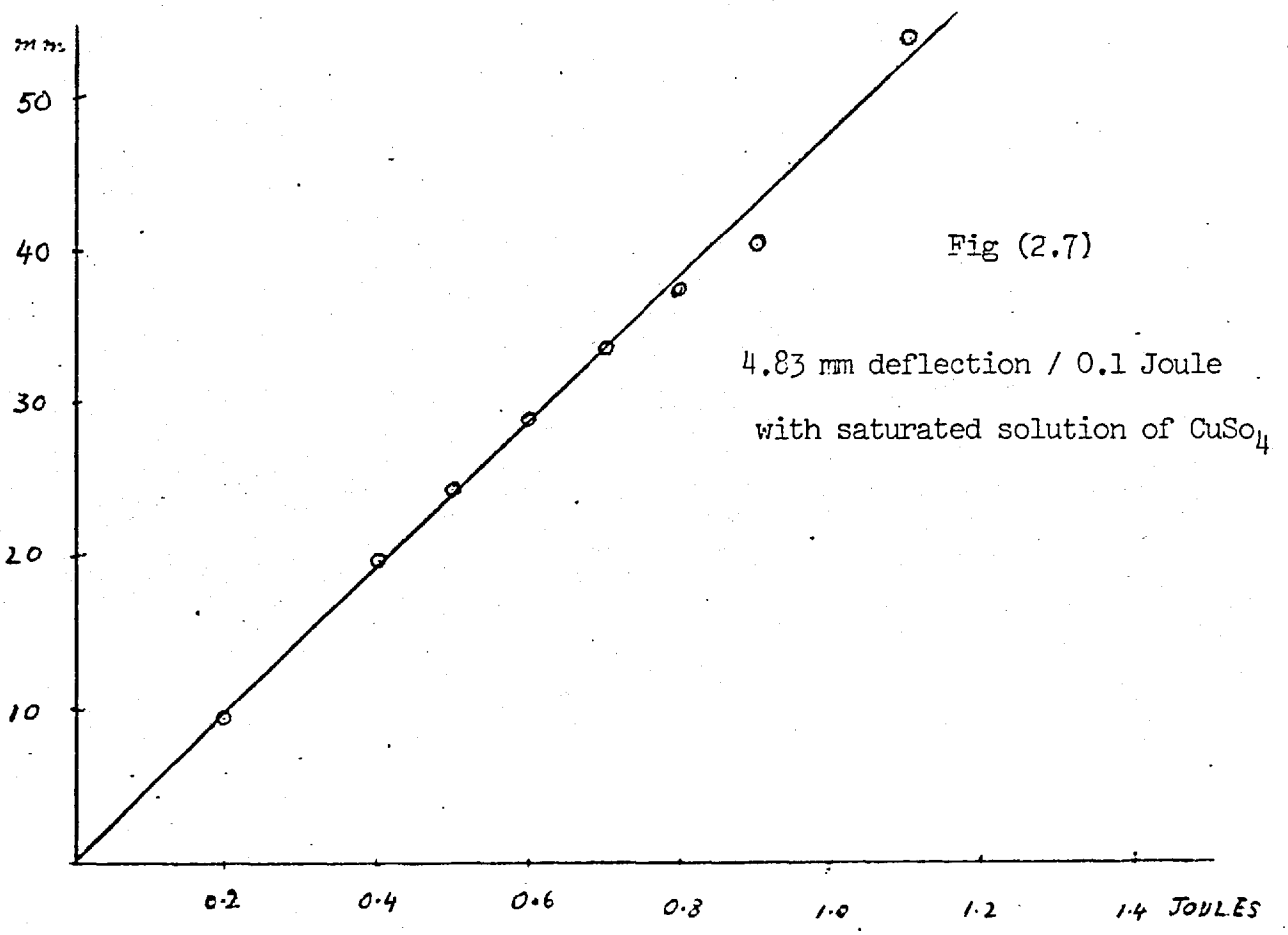

Fig (2.7)

4.83 mm deflection / 0.1 Joule

with saturated solution of $CuSo_4$

As seen in Fig. (2.6) the maximum deflection for each input energy occurs almost at the same time. The calibration curve showing the deflection of the galvanometer spot on the scale versus the input energy is shown in Fig. (2.7). The sensitivity of the cell used with the lamp and scale galvanometer arrangement was 5 mm./0.1 J.

At 600 Joules pump energy the energy output in the relaxation oscillations was measured to be 0.18 ± 0.02 Joules. This was for the cavity having 3" x 3/8" ruby and 98%, 60% reflectivity mirrors.

2) Calibrated photodiode

The ITT Biplanar Photodiode F4000(sL) was available for measurements of power and energy of the ruby laser output. This photodiode has plane parallel (biplanar) and coaxial electrode geometry and when used with a terminated coaxial cable has a rise time of less than 0.5 nsecs. The rise time of the output current is largely determined by the transit time of the photoelectrons as they move from cathode to anode and by applying larger voltages to the gap (usual spacing 0.25") can be made very small. The calibration charts could be available from the manufacturers, which enables one to determine the power and energy of the pulse at a particular wavelength. Since the photodiode could provide large output currents, no preamplifier was needed which would otherwise degrade the time response of the system.

The Fig. (2.8) shows the traces with relaxation oscillations of the ruby output. The upper trace gives the energy and is obtained by integrating the signal from the photodiode. With a 50 Ω terminated cable, the 1 volt output signal corresponds to an energy of 120 mJoule. The lower trace measures the power of each spike in the relaxation oscillation output. The sensitivity of measurement at 6943 Å is 1.08 KWatt/ampere. The ruby laser output consists of ~ 40 - 50 spikes, with rangom fluctuation of height. At input energy of 824 Joule to the flash tube, the peak power in a spike is only ~ 45 K.W.

The output energy is much smaller than expected at these input energy

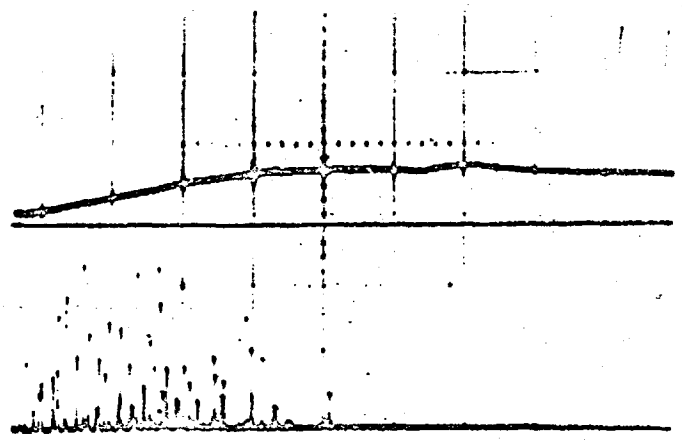

824 Joules input

5.4 mJoules output

Peak power = 45 KW

No: of spikes = 45

50 μsecs/Cm

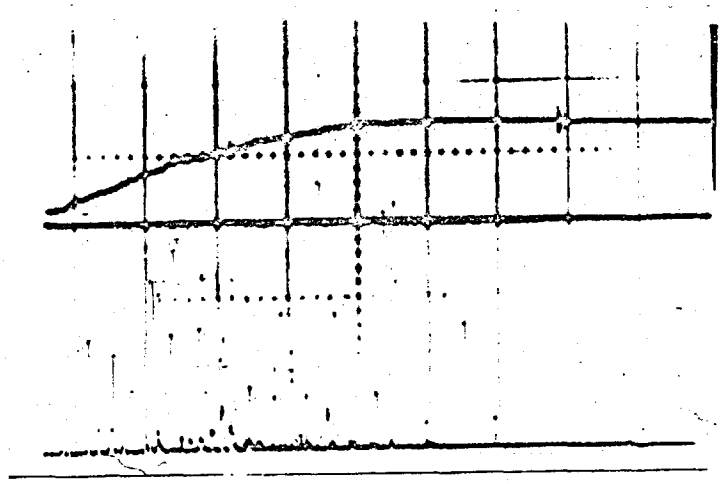

870 Joules input

8.4 mJoules output

Peak power in a spike

= 75 KW

50 μsecs/Cm

Fig (2.8) Upper Trace in each frame ≡ Energy (Integrated)

Lower " " " ≡ Power of the spikes.

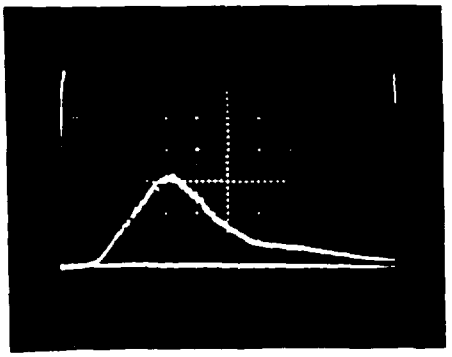

(a) 635 Joules
$\Delta t_{\frac{1}{2}}$ = 68 nsecs
2.9 MWatts

20 nsecs/Cm

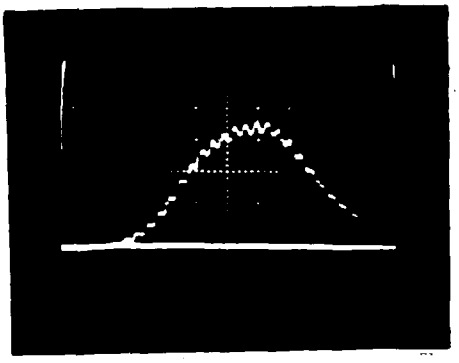

(b) 664 Joules
$\Delta t_{\frac{1}{2}}$ = 44 nsecs
4.0 MWatts

10 nsecs/Cm

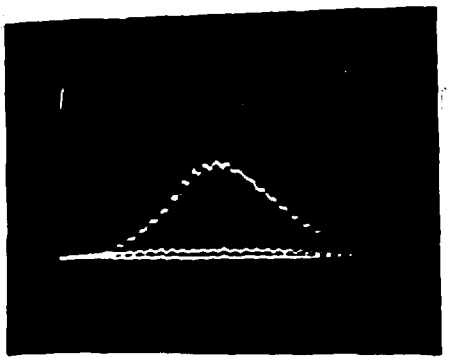

(c) 744 Joules
$\Delta t_{\frac{1}{2}}$ = 40 nsecs
6.0 MWatts

10 nsecs/CM

Fig (2.9) ITT Biplanar Photodiode F4000(S1) (Rise time =0.5 nsecs)
Tetronix type 454 Oscilloscope (Rise time = 2.4 nsecs)

FIG (2.10)

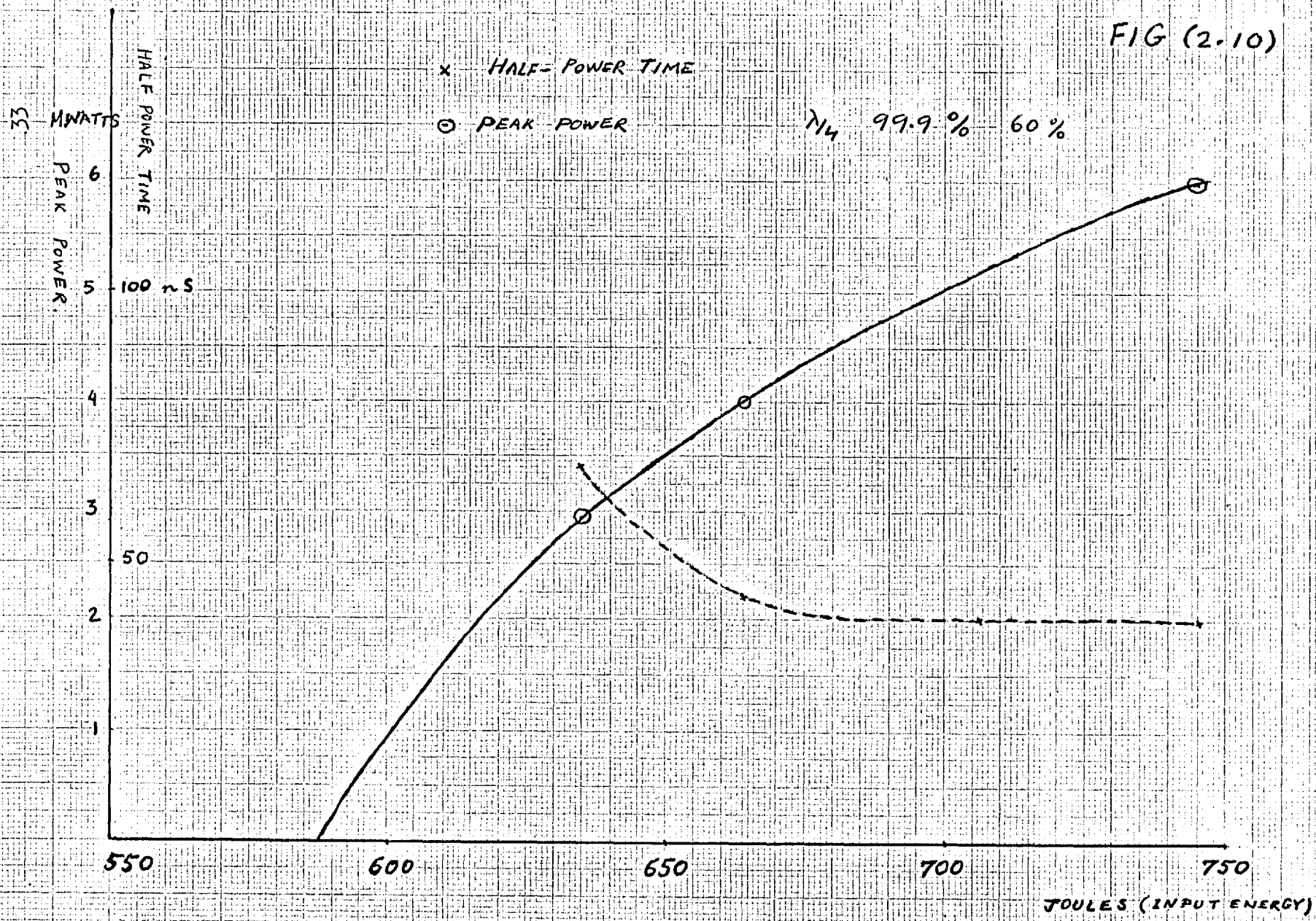
× HALF-POWER TIME
⊙ PEAK POWER
λ/4 99.9 % 60 %
HALF POWER TIME
100 nS
50
PEAK POWER
MWATTS
6
5
4
3
2
1
550
600
650
700
750
JOULES (INPUT ENERGY)

values. On an examination of the ruby cavity, it was discovered that the silver coating on the stainless steel liners of the cavity was completely destroyed by the heat from the flash tube. This caused the pumping of the ruby to be very inefficient. The liners were originally coated with silver because the stainless steel has a strong absorption coefficient near the ruby absorption band. It was found that the aluminium coating was much more durable although it had a slightly smaller reflection coefficient as compared to that of silver coating.

On replacing aluminized liners the power output of the ruby increased by an order of magnitude. The Fig. (2.9) shows the giant pulse output at various input energies. The output was measured with photodiode using Tetronix Type 454 oscilloscope which has a rise time of 2.4 nsecs. The Fig. (2.10) shows the plot of output power and half-power width of the giant pulse versus the input energy. The output power exponentially increases while the half-width of the pulse approaches the minimum value of ~ 40 nsec.

The otherwise normal pulses are seen to be modulated by a periodic structure. This is due to the interference of adjacent axial modes of the cavity as discussed in Sec. (2.8). The power output of the giant pulse from the ruby agrees closely with the measurements by Key[7]. However, these measurements are smaller than his computed results. The reason is that the computations are based on many simplifying assumptions.

3) Power meter using non-linear polarization in quartz crystal

A power meter utilizing the dc polarization produced by high intensity laser beam in a crystalline medium that lacks inversion symmetry was constructed. The principle of the device has been described by Kamal and Subramanian[11] and is briefly presented in the following.

When an electromagnetic wave travels through a non-linear medium, the scalar form of polarization produced in the uniform and isotropic

medium is given by

$$P = a_1E + a_2E^2 + a_3E^3 + \ldots \qquad - (2.9)$$

where a_1, a_2, a_3 . . . are the 1st, 2nd, 3rd . . . order polarization coefficients. Writing $E = E_o \cos \omega t$ in Eq. (2.9), one obtains

$$P = a_1 E_o \cos \omega t + \frac{a_2}{2} E_o^2 (1 + \cos 2\omega t) + \frac{a_3}{4} E_o^3 (3 \cos \omega t + \cos 3\omega t) + \ldots \qquad - (2.10)$$

Thus it can be seen that a dc-polarization of magnitude $\frac{a_2 E_o^2}{2}$ is developed in the medium in the same way as dc currents are produced in a square law detector. The contributions from higher harmonics are negligible because the higher order polarization coefficients are much smaller than a_2.
The dc-polarization is proportional to the power in the radiation field.

If one writes the more general equation for the polarization, the term which contributed to the dc polarization is given by[12]

$$P_i = \chi''_{ijk} E_j E_k \qquad - (2.11)$$

The coefficient χ''_{ijk} is a tensor possessing the same symmetry properties as the piezoelectric modulus and is present only in crystals that lack inversion symmetry. Quartz belongs to the class of such crystals.

For a linearly polarized plane wave propagating in the Z-direction of the crystal ($E_Z = 0$), the dc polarization is shown by Kamal et. al.[11] to be

$$|P| = \frac{\alpha}{2} (a_x^2 + a_y^2) \qquad - (2.12)$$

where α is a constant involved in the second-order polarization tensor for quartz. a_x and a_y are the components of the amplitude of the electromagnetic wave along x- and y- direction.

Thus for linearly polarized wave the dc polarization caused by the propagating wave is directly proportional to its power. A measurement of the former would give the latter.

To see how the power in a linearly polarized beam can be experimentally measured with the help of Eq. (2.12), consider a cylindrical quartz rod of radius b. The Fig. (2.11a) shows the cross-section of this rod with its Z-axis perpendicular to the plane of the paper. The incident plane-polarized unfocused laser beam of radius a propagates along the Z-direction. It causes a uniform dc polarization P_o given by Eq. (2.12) in the transverse direction making an angle ϕ with the x-axis of the crystal. Kamal et. al.[11] have solved the two-dimensional boundary-value problem for the case of the crystal of infinite length, and obtain the potential distribution outside the quartz crystal as

$$V = \frac{P_o a^2}{\varepsilon_o (1 + \varepsilon_r)} \frac{1}{r} \cos(\theta - \phi) \qquad - (2.13)$$

where ε_o = permittivity of free space surrounding the crystal

ε_r = relative dielectric constant of the quartz medium

and θ = the angle any vector makes with the x-axis (see Fig. (2.11b)).

The electric field intensity E of the laser beam of power P_L is given by (MKS units)

$$E^2 = \frac{2 P_L}{\pi} \eta \frac{1}{a^2} \qquad - (2.14)$$

where η is the intrinsic impedence of the electromagnetic wave.

By combining Eqs. (2.12) and (2.14), the Eq. (2.13) can be written as

$$V = \frac{2 \alpha \eta}{\pi \varepsilon_o (1 + \varepsilon_r)} P_L \frac{1}{r} \cos(\theta - \phi) \qquad - (2.15)$$

If the electric vector of the laser beam is in the direction of crystal X-axis, then $\phi = 0$. The equation (2.15) then describes equipotential lines shown in Fig. (2.11b). Also the curves $r = k \cos\theta$ describe

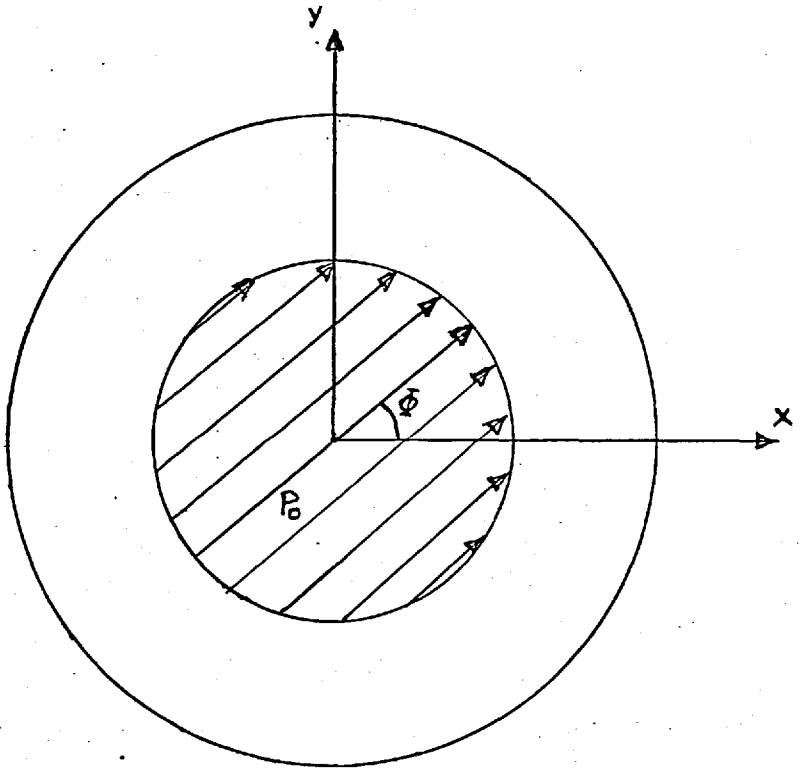

Fig (2.11a) Cross-section of Quartz Rod (radius b) with the concentric laser beam (radius a).

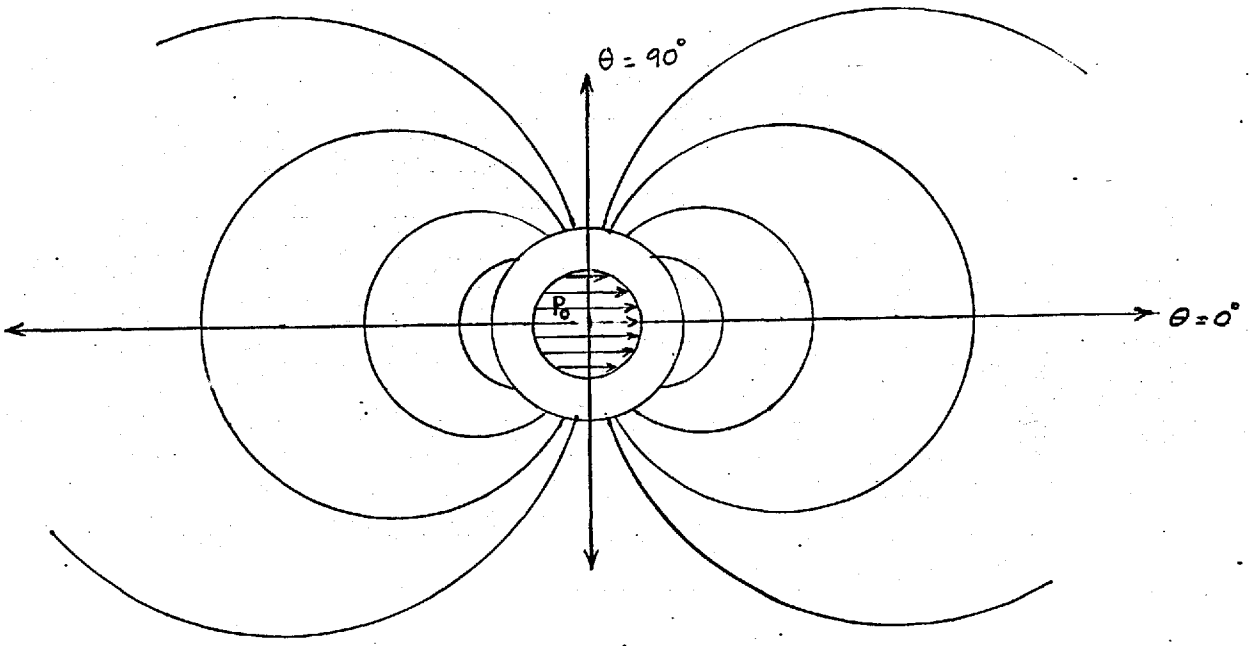

Fig (2.11b) Equipotential lines outside Quartz cylinder.

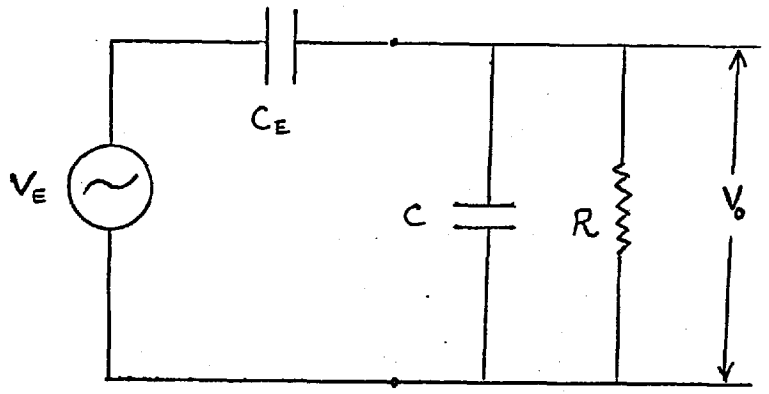

Fig (2.12) Equivalent Circuit of the detector.

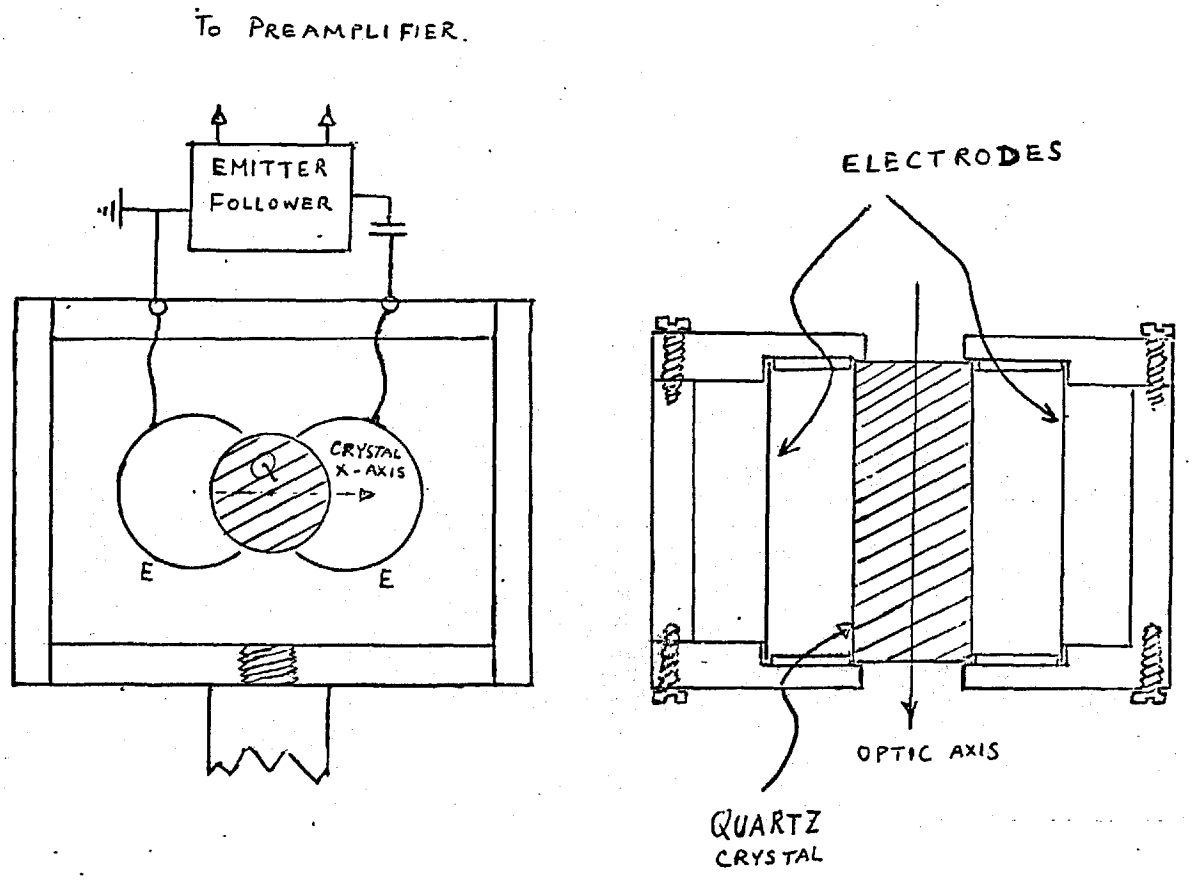

Fig (2.13) The Detector Assembly.

equipotential surfaces, where k is an arbitrary constant.

Substituting $r = k \cos \theta$ and $\phi = 0$ in Eq. (2.15), one obtains

$$V = K_1 P_L \qquad - (2.16)$$

where

$$K_1 = \frac{2 \alpha \eta}{k \pi \varepsilon_o (1 + \varepsilon_r)} \qquad - (2.17)$$

For various values of k, Eq. (2.16) describes equipotential surfaces outside the quartz cylinder which are pairs of circles with centres at $(\pm k K_1 \frac{P_L}{2}, 0)$ and of radius $k K_1 \frac{P_L}{2}$ as can be observed in Eq. (2.15).

If a pair of electrodes is placed along these equipotential lines $\pm V$ corresponding to $r = k \cos \theta$ and aligned perpendicular to the x-axis of the crystal, the plates form a capacitance with voltages +V and -V on the two plates. Thus from Eq. (2.16), the voltage across the plates can be written as

$$V = K_2 P_2 \qquad - (2.18)$$

where

$$K_2 = \frac{4 \alpha \eta}{k_1 \pi \varepsilon_o (1 + \varepsilon_r)} \qquad - (2.19)$$

The equation (2.18) shows that the output voltage is directly proportional to the power of the laser beam. The equivalent circuit for the system is shown in Fig. (2.12). C_E is the capacitance formed by the two electrodes, C the input capacitance and R the input resistance of the measuring device. Thus one would measure the peak output voltage V_o given as

$$V_o = \frac{K_2 P_L C_E}{C + C_E} \qquad - (2.20)$$

The greatest output voltage will be measured with the input capacitance as small as possible. To obtain the output voltage resembling the laser pulse shape without distortion, the time constant RC of the

circuit must be large compared with the duration of the pulse.

Construction of the device

Although the assumption of infinite length of the crystal was made in deriving the Eq. (2.13), the results are generally valid if the length of the cylinder is larger than its diameter. A Z-cut crystal of appropriate size could be commercially obtained by getting it made to the specifications but was of prohibitive cost. A simpler and cheaper method was adopted. Very cheap and almost perfect natural crystal of quartz was obtained from a mineralogist and turned to a cylinder of a length of 4 cms and 1.5 cm. diameter in the optical workshop of the Applied Optics Section at Imperial College Physics Department. The optic axis of the crystal was along the crystal axis. The ends were parallel to 1' of arc and flat to one fringe of mercury green light. Unfortunately the x and y axes of the crystal could not be initially marked before cutting the crystal and so had to be determined using x-ray diffraction method.

The crystal and the electrodes were mounted in a perspex holder. The latter was machined to hold these firmly but still allowing adjustment by merely screwing off the lid. The Fig. (2.13) shows two views drawn to the scale. A photograph of the actual assembly and the associated electronics is shown in Fig. (2.14).

The choice of the parameter k_1 om Eq. (2.19) was dictated from the consideration of maximizing the output voltage, k_1 being the diameter of the electrodes. A smaller k_1 will result in a larger output voltage as seen in Eq. (2.19). But the capacitance of this assembly has to be maximized so that a larger fraction of the voltage appears across the measuring device. A very rough guess for the capacitance from the parallel plate condensor formula requires a larger surface area of the electrodes. As a compromise between the two contradictory criteria, the value of k_1 = 2 cm. was chosen. An estimation of the expected value of the output voltage for a certain power input in the ruby laser pulse is made in the following.

Using MKS units, the various factors in Eqs. (2.19) and (2.20) are given below.

η = intrinsic impedance of electromagnetic waves in quartz

$$= \sqrt{\frac{\mu}{\epsilon}} = \sqrt{\frac{\mu_o}{4.5\ \epsilon_o}} = 178\ \Omega$$

$k_1 = 2$ cm. $= \frac{1}{50}$ meter

$\epsilon_o = 8.854 \times 10^{-12}$ Farad/meter

$\epsilon_r = 4.5$ (relative dielectric constant in the transverse direction of the optic axis).

$\alpha = 1.42 \times 10^{-23}$ Farad/volt[13]

$$\frac{C_E}{C + C_E} \simeq \frac{1}{2}$$

For a laser pulse of power $P_L = 10^6$ watts we obtain, from Eq. (2.20) $V_o = 1$ m volt. (per mega watt).

The input capacitance of the emitter follower could be made very small by the use of the stable wideband emitter follower using Fairchild transistors 2N917. The resultant input capacitance of the circuit, as discussed in reference (14) is 0.3 pf. A wide band pulse amplifier with a gain of 30 db was used in conjunction with the emitter follower. This amplifier is the slightly modified version of the amplifier described in reference (15). These circuits along with their batteries were housed in screened boxes to prevent interference from the electromagnetic pick up as seen in Fig. (2.14).

Results obtained with the device

The device was used to measure the power of the pulse from the ruby laser described above.

Initially Kerr cell was used as a Q-switch but the excessive electromagnetic pick-up from its thyratron unit submerged the signal, if any, from the power meter. This was in spite of the power meter being screened. For this reason the passive Q-switch alone was then used to obtain the giant pulse.

The signal from the power meter was observed on a dual beam Tetronix 555 Oscilloscope. The time base A was triggered by the photomultiplier signal and it simultaneously triggered the time base B which monitored the signal from the power meter.

When the electric vector of the laser beam was in the direction of the x-axis of the crystal and the electrodes were placed perpendicular to the latter axis, the signal obtained was at its peak value.

Since both the emitter follower and the preamplifier had very wide bandwidths no significant distortion of the laser pulse shape was observed. The measured value of the peak power was, however, smaller by a factor of four. This could be explained with reference to Equations (2.19) and (2.20). Since one of the electrodes was earthed, the output signal was thus halved as compared to that given by Eq. (2.18), since K_2 is reduced by this amount. The other cause of the discrepancy was the fact that in the above estimation of the output signal, C was assumed equal to C_E. Since both C and C_E had very small magnitudes, of the order of a picofarad, it was difficult to experimentally ascertain their value. The stray capacitance must add on to C and hence reduce the output voltage.

The output signal was confirmed to be proportional to the laser power, as predicted by Eq. (2.18). The Fig. (2.15) shows a plot of the peak laser power against the detector output signal. As can be seen it extrapolates to the origin.

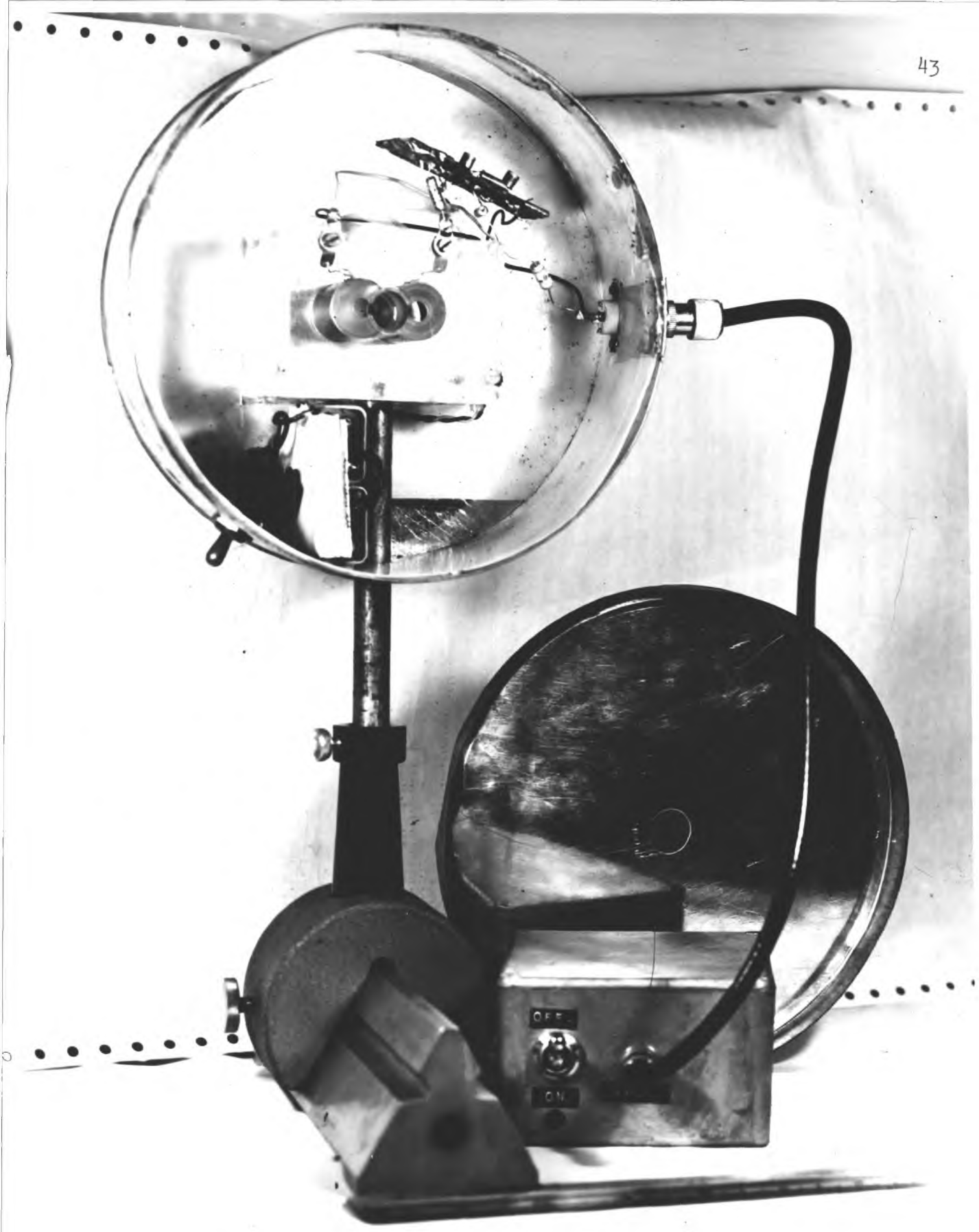

Fig(2,14) The Laser Power Meter.

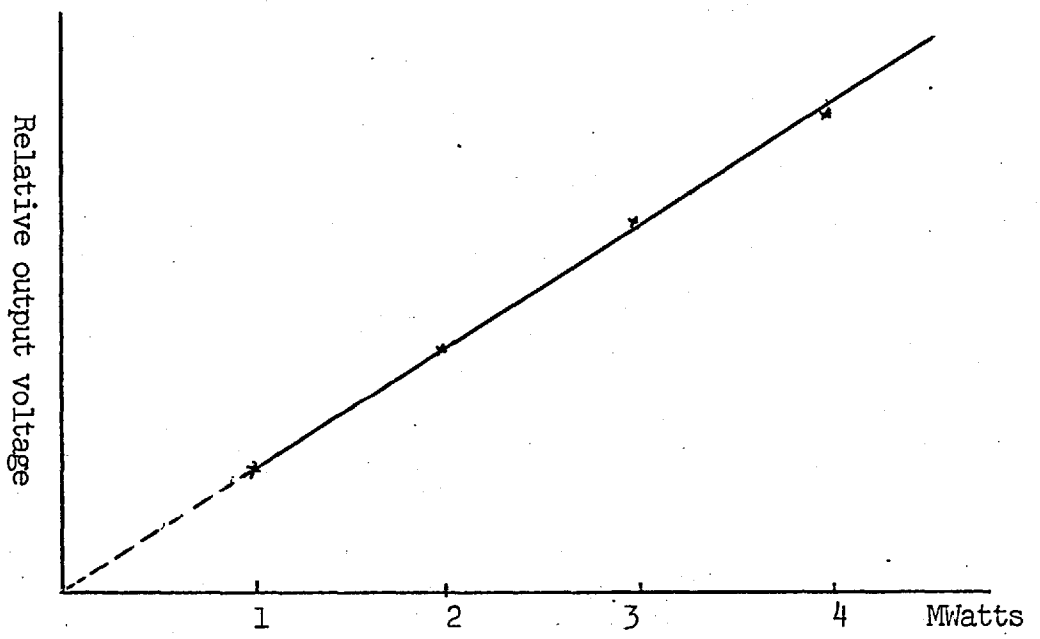

Fig (2.15)

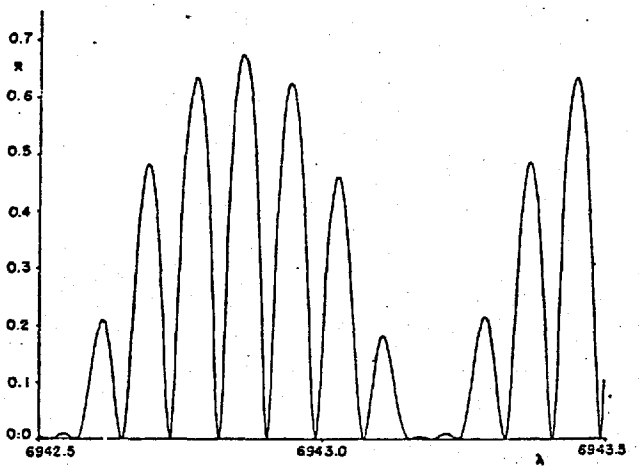

Fig (2.16) Reflectance against wavelength for the resonant reflector with 2-mm plates of Schott SF6 glass separated by 25-mm of air.

2.7 Dynamics of Q-modulation

Any theory of giant pulse production must predict and confirm the characteristics of the experimentally obtained output pulses. The total energy in the pulse, power output, the rise and fall times and any modulations due to mode interactions must be accounted for by that theory. Although the problem of cavity mode interactions is much more difficult to deal with theoretically, the rest of the characteristics can, however, be accurately explained by making some simplifying assumptions. Many authors have solved the problem analytically and numerically[17,18,19,20] and the general approach will be briefly outlined below.

The first simplifying assumption made is that the laser fluorescent line is homogeneously broadened. This is experimentally confirmed by Hellwarth et. al.[16]. Their results show that the ruby line is fairly homogeneously broadened for changes slow compared with 5 nsecs since the relaxation of Cr^{3+} ions between their $\bar{E}$ and $2\bar{A}$ levels (see Fig. (2.1)) in pink ruby occurs in less than 5 nsecs.

The second assumption is that the density of laser photons inside the active volume of the laser material is uniform. This assumption requires that the spatial distribution of the light energy inside the cavity does not change while the total cavity light energy is changing in time. This would be true only in a laser operating in a single transverse mode of the cavity. The simplified theory, however, does not explain the short time fluctuations such as occur from mode interference as seen in Fig. (2.9). The equations giving the rate of change of photon density in the cavity and the inversion in the ruby can be written down from the following considerations.

The fractional rate of increase in the photon number density Φ for a photon once passing through the laser medium is $\frac{\delta l}{t_1}$ where t_1 is the single transit time of the photon in the cavity and δl is the total gain in the laser medium. There is also a fractional loss rate for Φ given by $\frac{\gamma(t)}{\tau}$, where τ is the natural decay time of the cavity given

by $\tau = -\frac{t_1}{\frac{1}{2}\ell n\,(R_1 R_2)}$, R_1 and R_2 being the mirror reflectivities. Thus we get the rate equation for the photon density as

$$\frac{d\Phi}{dt} = \left(\frac{\alpha\ell}{t_1} - \frac{\gamma(t)}{\tau}\right)\Phi \qquad - (2.21)$$

The rate equation for the inversion N, where $N = N_2 - N_1$ is[20]

$$\frac{dN}{dt} = -2\,\Phi\,\sigma\,N\frac{\ell}{t_1} + R \qquad - (2.22)$$

where $\gamma(t)$ is the time varying loss term due to the Q-switch,

$\sigma \equiv$ peak absorption cross-section for the laser transition,

$R \equiv$ contribution to $\frac{dN}{dt}$ of the pumping and relaxation.

These equations normalized to the threshold inversion N_P at minimum loss and to τ are solved numerically[17] for the fast switching case where $\gamma(t)$ changes discontinuously. Here

$$N_P = \frac{t_1}{\tau\,\sigma\,\ell}$$

Since $\gamma(t)$ for saturable dyes also changes in a time much shorter compared to pulse build-up time, the same results are applicable for passive switch.

The energy of the pulse obtained from the solution of the normalized equations is obtained as[20]

$$E = \tfrac{1}{2}\,h\nu_o\,N_P\,(n_i - n_f) \qquad - (2.23)$$

n_i and n_f being the initial and final values of the inversion. E is the energy per unit active volume of material.

A simple calculation of the energy of the pulse in Fig. (2.9a) from the measured value of the rise time of the leading edge shows an agreement with experimentally measured value.

The rise time of the pulse = $\Phi/d\Phi/dt$ = 16 nsecs.

For the mirror separation of 46 cms. and 7.6 cms. long ruby, the single transit time t_l = 1.73 nsecs.

For mirror reflectivities 99.9% and 60%, the natural cavity decay time

τ = 6.64 nsecs.

The initial inversion/threshold inversion = $n_i = (\frac{1}{\Phi}\frac{d\Phi}{dt} + 1)$, ($t$ measured in units of τ) is

$$n_i = (\frac{6.64}{16} + 1) = 1.42$$

The energy utilization factor $\frac{n_i - n_f}{n_i}$ obtained from the calculations of Wagner et. al.[17] for the above value of n_i is 0.51

The threshold inversion = $t_l/_{\tau\sigma\ell}$ = 1.37×10^{18} cm^{-3}

for $\sigma = 2.5 \times 10^{-20}$ cm^{-2}.

The active volume of the ruby from the consideration of the focusing action of polished dielectric rod = 1.6 cm^3 for 3" x 3/8" dia. ruby rod.

Thus the expected pulse / active volume (cm^3) from Eq. (2.23) is

$$E = \tfrac{1}{2} \times 0.51 \times 2.8 \times 10^{-19} \times 1.37 \times 10^{18} \times 1.42$$

$$= 0.138 \text{ Joules/cm}^3$$

when $h\nu = 2.8 \times 10^{-19}$ Joules.

The total energy in the pulse = 1.6 x 0.138 = 0.22 Joules.
This value agrees quite well with the experimentally measured value.

The expected duration of the pulse (the time between half-intensity points, i.e. $t_r + t_f$) can also be obtained from Wagners results[17] by noting t_r and t_f in terms of cavity decay time corresponding to the above value of n_i = 1.42. These are

$t_r = 4.7\,\tau$ and $t_f = 5.1\,\tau$

i.e. $t_r + t_f$ = 65 nsecs.

The value obtained from the pulse in Fig. (2.9a) being 68 nsecs. shows a close agreement.

This agreement of theory with experiment is good only for long and weak pulses at low level of pumping. For higher initial inversion as for pulses in Fig. (2.9 b and c), the agreement is not so good. The possible reason being the simultaneous oscillation of a number of cavity modes due to inhomogeneously broadened R_1 line.

It is of interest to know the variation of power and energy with the output mirror reflectivity such that an optimum value can be chosen. Solutions of the equations (2.21) and (2.22) were obtained by Key[7] by an interpolation of the data of Lengyl[17]. For a 3" x $\frac{3}{8}$" ruby, the optimum value of the output mirror reflectivity was found to be about 60%.

The shape and width of the pulses shown in Fig. (2.4) can be explained if the loss term is assumed to vary from high to low value in a time slow compared to pulse build up time. Hellwarth[20] has solved the equations (2.21) and (2.22) with an analogue computer by assuming a form $1 + \exp(- wt)$ for $\gamma(t)$. By using various values of w, the results gave multiple pulses of different relative intensities. His results show a qualitative agreement with the pulses shown in Fig. (2.4).

2.8 The Laser Cavity Modes and their Selection

If the laser fluorescent light is being reflected axially between the mirrors forming the laser cavity, only those frequencies under the Doppler width will be able to form standing wave patterns leading to reinforcement which satisfy the following relation

$$\nu_n = n \frac{c}{2L} \qquad - (2.24)$$

where n is an integer and L is the separation between the mirrors. These frequencies form the axial modes of the laser. The two axial modes are separated by the frequency

$$\Delta\nu = \nu_n - \nu_{n-1} = \frac{C}{2L}$$

In the ideal case the cavity modes are orthogonal to each other, i.e. the oscillations of a single mode may be excited without exciting others. However, due to many factors such as introducing polarizable materials in the cavity and anisotropy of the laser material there is always a coupling of modes and the energy is transferred from one mode of oscillation to another.

The different modes of a resonant cavity may be regarded as almost independent oscillators. The quality factor Q of the oscillator is described by

$$Q = \frac{2\pi\nu_o E}{Pd} \qquad - (2.25)$$

where ν_o is the resonant frequency, E the energy and Pd the rate at which energy is dissipated in the oscillator.

The linewidth $\Delta\nu$ of the oscillator is $\frac{\nu_o}{Q}$ and hence the mode with low dissipation will have narrow line width. Wagner and Birnbaum[21] have shown that modes with more energy tend to grow faster and their growth rate increases with increasing Q. The modes near the line centre with the greatest supply of quanta, having the highest Q are therefore able to grow faster. Since all feed on the same supply of excited atoms, these modes are usually the only ones to survive.

The Q of each mode is determined by the formula (2.25), in which Pd consists of the sum of all losses from that mode. The reflection loss is usually the same for all modes while the diffraction loss is variable. For a plane resonator the diffraction loss is largest for the off-axis modes. This lowers their Q to the point at which their excitation becomes negligible and the laser is then described entirely in terms of the axial modes.

The losses of the axial modes are almost equal. For a cavity of

length L = 50 cm., the separation of the axial modes is 0.005 Å whereas the width of the ruby line R_1 is ~ 4Å at room temperature. Ordinarily quite a few of the modes lie so close to the top of the atomic line that they are excited simultaneously. However, even a small difference in the diffraction losses among modes of different types may provide a great discrimination in the excitation of these modes, and if a laser is operated sufficiently close to threshold, oscillations will occur only in modes of lowest loss.

The neighbouring modes may interfere and the beats between the resonance frequencies of two modes can be measured by means of photodetector of large bandwidth. The width of the single resonance is very narrow and is determined by the temporal width of the pulse. For a 50 nsecs pulse, $\Delta\lambda \sim 0.003$ Å. Thus the radiations of adjacent resonance frequencies are highly monochromatic.

The interference between light of frequencies ν_o and $\nu_o + \Delta\nu$ of equal amplitudes results in a signal proportional to $\cos^2 (2\pi \frac{\Delta\nu}{2} t)$. The time period of resulting oscillations can be obtained by setting

$$2\pi \frac{\Delta\nu}{2} t = \pi.$$

Thus $$t = \frac{1}{\Delta\nu} = \frac{2L}{C}.$$

For L = 50 cm., t = 3.3 nsec. This is confirmed by the experimental result shown in Fig. (2.9).

The pulse envelope pattern, however, does not tell about all the modes. This is confirmed by Bradley[22] who simultaneously obtained a Fabry-Perot interferogram. The latter usually contained many more lines than would be expected from the pulse envelope pattern. The single mode operation therefore cannot be safely inferred from the absence of beats. As mentioned earlier, if the laser is pumped near threshold, the spectrum is much 'cleaner' as can be seen in Fig. (2.9a). Moreover, for the same peak power fast switched giant pulses are spectrally cleaner than

slow ones.

During giant pulse operation different parts of the laser oscillate independently as found experimentally by Bradley[23]. Families of modes were found to exist, no family having more than four modes. No pair of modes was found to be separated by less than 3 $\Delta\nu$. This is explained by noting the action of the ruby end faces as mode selector. The observed widths of the modes indicated the mode life time to be between 2-8 nsecs.

The coherence of the radiation can be improved by making the laser operate in a single transverse mode of the cavity and restricting the number of axial modes to minimum. It is easy to achieve the former by inserting a pinhole in the cavity such that it limits the transverse action of the radiation field. Although it results in a reduction in output power and energy because of a small volume of the active material being used but it very much improves the spatial coherence of the output.

There exist many standard methods[24] for controlling the axial modes of giant pulse lasers. As pointed out above various sub-cavities in the laser cavity act to select the modes. For a 50 cm. long cavity, a 3" long ruby suppresses three out of every four cavity modes. The use of a properly designed resonant reflector has helped to achieve single mode operation when the laser is pumped near the threshold. A resonant reflector with two glass plates each 2 mm. thick with a spacing of 2.5 cms. of air was used in our experiment. A plot of reflectance against wavelength is shown in Fig. (2.16). In the design[25] it is ensured that at least one reflection maximum falls over the peak of ruby line.

The bleachable dye used as a passive Q-switch also acts as a mode selector. As explained by Sooy[26], the long build up time with passive switch enhances small differences in mode losses. The passive switch takes several hundred complete transits of the cavity to open compared with several tens for a Kerr cell.

In our experiment a combination of passive switch and Kerr cell with

the resonant reflector as the output mirror proved most effective in obtaining a comparatively pure spectrum. Although the laser was pumped much above the threshold, the use of the above combination of Q-switches still provided output with a reasonable degree of coherence. This is confirmed by the reasonable quality of holograms obtained with this radiation as discussed in Chapter 6.

References

1) Maiman, T.H. Nature 187, 493 (1960).

2) D'Haenaus, I.J., Asawa, C.K. J.A.P. 33, 11, 3201, (1962).

3) Edwards, J.G. Applied Optics 6, 837 (1967).

4) Brandervie, R.A., Hitt, J.S. and Feldman, J.M. J. Appl. Phys. 34, 3415 (1963).

5) Feldman, J.M. J. Appl. Phys. 37, 674 (1966).

6) Aisenberg, S., Missio, D.V., and Selberg, P.A., J. Appl. Phys. 35, 3625 (1964).

7) Key, M.H. Ph.D. Thesis, 1966, University of London.

8) G. Fonda-Bonardi, Lasers and Applications, 1962. P. 96. Edited by W.S.C. Chang.

9) Haswell, W.T., Hitt, J.S. and Feldman, J.M. Proceedings I.E.E.E. 52, 93, (1964).

10) Maiman, T.H., Hoskins, R.H., D'Haeneus, I.J., Asawa, C.K., and Evtuhov, V. Phys. Rev. 123, 1151-1157 (1961)

11) Kamal, A.K. and Subramanian, M. P. 601, Proc. of the symposium on Optical Masers, New York Polytechnique press, N.Y. 1963.

12) Nye, J.F. "Physical properties of crystals" (London) Oxford University Press, 1957, P.116.

13) Cady, W.G. "Piezo electricity" P.722, McGraw Hill, 1946.

14) Fairchild Application Report No: APP-41/2.

15) Fairchild Application Report No: 158.

16) McClung, F.J. and Hellwarth, R.W. Proc. I.E.E.E. 51, 46 (1963).

17) Wagner, W.G. and Lengyel, B.A. J.A.P. 34, 2040 (1963).

18) Wang, C.C. Proc. I.E.E.E. 51, 1767 (1963).

19) Vuylsteke, A.A. J. Appl. Phys. 34, 1615 (1963).

20) Hellwarth, R.W. Hughes Research Lab. Rep. 300 (March 1964).

21) Wagner, W.G. and Birnbaum, G. J. Appl. Phys. 32, 1185, (1961).

22) Bradley, D.J. Appl. Phys. Letters, P.150 (1966).

23) Bradley, D.J. Nature P.1281, 199 (1963).

24) McClung, F.J. and Weiner, D.
I.E.E.E., J. of Quantum Electronics 1, 94, (1965).

25) Watts, J.K., Appl. Optics 7, 1621 (1968).

26) Sooy, W.R. Appl, Phys. Letters 7, 36 (1965).

Chapter 3

Holography and Holographic Interferometry

3.1 Introduction

The recording of information about an object or an event on a two dimensional plane had been a partial record. The photographic plate 'senses' only the square of the amplitude of the waves carrying useful information and does not respond to their phase, consequently it builds only a partial picture of what it sees. However, with the advent of holography the record of 'holos' or 'the whole' about any object, the situation has changed. The record consists of the interference pattern between the coherent wave field from the object and a coherent reference wave on a two dimensional photographic plate. When illuminated by a coherent wave resembling the original reference wave, the coded message unfolds itself giving rise to real and virtual images of the object in its true perspective.

On the advent of the lasers, a powerful source of coherent light, technique of holography received a tremendous boost and found its application in many diverse fields. The most highly developed of these applications is the optical microscope which has been used as a small-object measuring device. This is now being used to obtain three-dimensional coloured photographs of short-lived biological specimens to be studied at leisure. The application of holographic techniques to the area of optical data processing, computing, and data storage is receiving much attention. In particular, the researchers are trying to use full band-pass and storage capacities of sources and detectors. In engineering holographic interferometry is being increasingly used in checking and controlling the slightest deformation of ball bearings and similar products. It is also showing promise in areas of vibration and stress analysis and turbulent studies. Lastly but not the least, it has contributed significantly in plasma diagnostics by almost replacing and improving upon the conventional optical interferometers.

The purpose of this chapter is the exposition of the basic principles of holography and holographic interferometry. In this context general requirements and conditions for obtaining holograms will be examined. The requirement of a certain degree of coherence imposes a restriction on the choice of a particular experimental set-up that can be used. A set-up has been looked for which places minimum demands on this parameter of the laser output. Image forming characteristics of the various set-ups differ considerably and impose many restrictions on the resolution and magnification of the reconstructed image. A qualitative analysis of various systems in the light of their image forming characteristics and their requirement of a certain degree of coherence etc. has been undertaken. It has helped in selecting the most suitable system for our application where the main criterion is to extract maximum information about the object under study with the least demands on laser and other optics. But before proceeding to this undertaking a brief survey of the historical development of the science of holography is given. This will act as a guide to the path to be followed in the rest of the chapter.

3.2 Historical development of holography

As the intermediate step of holographic process is the recording of the interference between the partially coherent reference beam and diffracted beam from the object, one can interpret Young's classical double slit experiment as an earliest example of hologram formation. Since both the slits receive light from the same point source, the light emerging from these slits is partially coherent with respect to each other. The fringe pattern they give rise to is due to interference between these two beams and is the simplest form of hologram. If one illuminates this fringe pattern by a sufficiently coherent beam resembling the beam from one of these slits, it reconstructs the beam which originated from the other slit.

The same principle was applied by Zernike[1] in his phase contrast

microscope devised in 1935, in which a coherent background wave is allowed to interfere with the term to be recorded on film before the actual recording process. The result is an interference pattern which stores the amplitude and phase information necessary to reconstruct an image of the original object. This is the principle used by Gabor[2] in his two step photographic process. The first step of the Gabor process is the recording of the interference between diffracted radiation from the object and a coherent background wave. The reconstruction in this process was accomplished by then illuminating the properly processed hologram with a similar coherent illumination and recording the radiation field on a photographic film in a plane removed from the hologram.

3.2.1 The object that could be used in the Gabor process of holography was such that it allowed most of the coherent illumination through unaffected (reference beam) and diffracted part of it (object beam). The radiation from the object was the Fresnel (near-field) diffraction term. The reference beam was coaxial with the diffracted waves. The hologram of a single object point is the Fresnel diffraction pattern which is the zone-lens term, i.e. identical to the Fresnel zone plate. This on reconstruction gave rise to two focussed images at $\pm f$, where f is the focal length of the zone plate (section 3.3.3). The main disadvantage of the Gabor process was that the undesired twin image which appeared with the same amplitude and opposite phase shift as the reconstructed focussed image acted as a disturbing background.

3.2.2 Although many attempts were made by Gabor and others[3-4] to remove this twin image in the reconstruction, they were not successful. Leith and Upatnieks[5] utilized the result from communication theory concerning the equivalent real representation of a complex signal and succeeded in effectively producing an angular separation of the real and virtual images in their respective planes. In this way they avoided the conjugate or twin image causing a deterioration of the desired image term.

The basic principle in this formation of the hologram employs an

off-axis coherent reference beam which acts as a non-zero carrier frequency to store the necessary information. In the reconstruction, a zeroth-order effect on axis, and two off-axis first-order images are obtained. If either of the off-axis images is perfectly focussed upon and detected, it yields a good reconstructed image without interference from the other image. Most of the experimental details differ in the manner in which the object and reference beams are brought to meet on the photographic plate.

3.2.3 Recently many workers[6,7] have shown that the limitation of the Fresnel hologram of the twin image deteriorating the desired image term can be eliminated if one goes to the far-field of the object and thereby mix a characteristic Fraunhofer diffraction pattern with a coherent background to form the hologram. Although the twin image is still on axis and is still out of focus when viewed in the focal plane of the focussed image, the deteriorating effect is reduced because the energy density of the twin image is much less than that of the focussed image.

To obtain the Fraunhofer diffraction pattern, the point of observation must be at an infinite distance from the illuminated object. However one can approximate to this situation and specify the far-field condition as follows.

If the distance from the source plane to the plane of diffracting aperture is Z' and from the plane of the diffracting aperture to the plane of observation is Z, as shown in Fig. (3.1), then the condition for getting Fraunhofer hologram is

$$|Z'| >> \frac{(\xi^2 + \eta^2)_{max}}{\lambda} \quad \text{and} \quad |Z| >> \frac{(\xi^2 + \eta^2)_{max}}{\lambda} \qquad - (3.1)$$

where ξ and η are the coordinates of a general point in the plane of the diffracting aperture and λ is the wavelength of the incident radiation.

Due to the above condition, in practical situations it is only possible to make measurements of small particle distributions, this constituting the main limitation of the method.

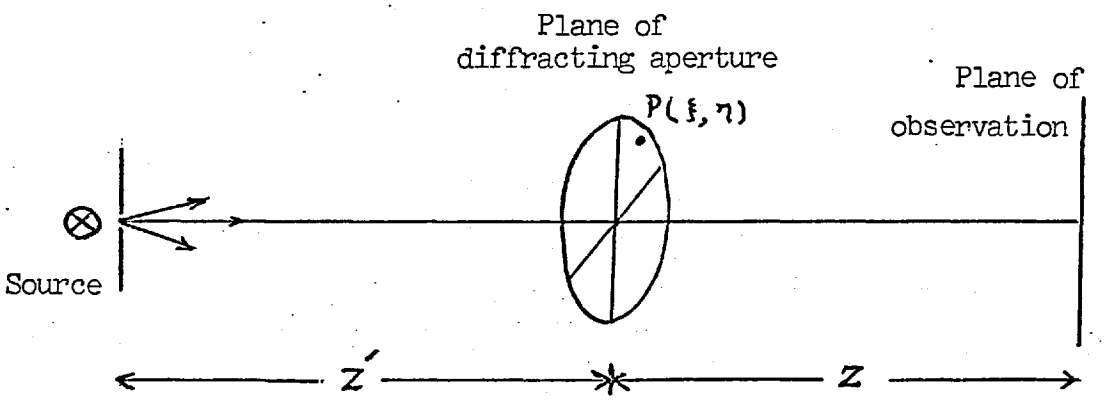

Fig (3.1) Arrangement for obtaining Fraunhofer hologram.

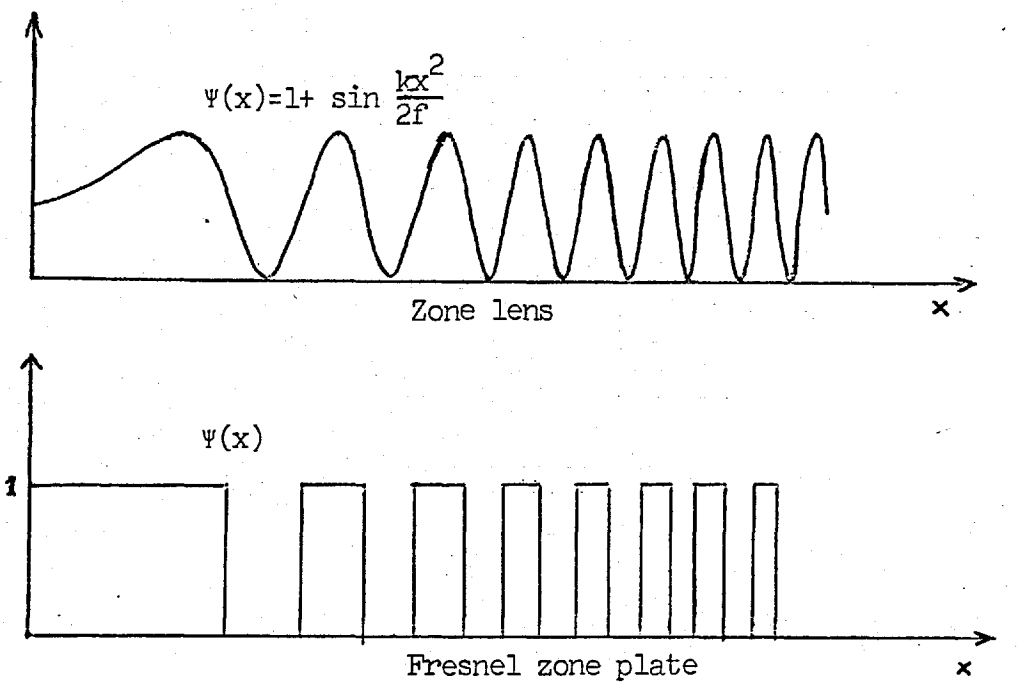

Fig (3.3) Comparision of Fresnel Zone Plate with a zone-lens.

3.2.4 A method utilizing the Fraunhofer diffraction pattern but with a higher resolution capability has been proposed[8]. To form such a hologram, an exact Fourier transform of the object is mixed with the coherent background. This is achieved by having the planar object and a coplanar point reference source on one Fourier Transform plane of a lens which the photographic plate is on the other Fourier Transform plane. The reason for the higher resolution capability of this hologram process is that the fringe pattern has a constant average frequency and is less demanding of the spatial frequency of the photographic emulsion.

Holograms have also been formed with X-band radiation[9] and reconstructed with visible radiation. Hologram formation and reconstruction with microwaves and other centimeter waves have also been reported[10]. Moreover the holograms can be formed and reconstructed by laser beams having more than one spectral component[11] resulting in coloured reconstructed images.

3.2.5 Some experimental arrangements have also been used which allow the formation of holograms with incoherent quasi-monochromatic radiation[12,13]. This is possible because from the theory of partial coherence, when the object and background illumination are derived from a primary incoherent source the field at the object position is partially coherent allowing for an interference pattern to be found. Another technique that utilizes a scatter-plate system[14] with perfect optical component allows the formation of the hologram of phase objects with almost white light. On reconstruction with a coherent illumination, one obtains a reasonably good image. This will be discussed in detail in the next chapter.

3.3 The process of hologram formation and reconstruction.

To obtain a hologram one has to consider many factors such as a) the nature of the quasi-monochromatic illumination, b) the manner of folding in of the reference and object beams, c) the characteristics of the photographic emulsion, d) the stability of the system during the time of exposure of the photographic emulsion etc. Before proceeding to

investigate in detail the effect of coherence, spectral content and spectral spread of the radiation on the hologram it would be profitable to examine the process of hologram formation. Then we will describe the nature of fringe distributions of which various kinds of holograms comprise of. Since image forming properties of holograms depend on the quality of these fringes, the influence of various factors such as characteristics of illumination etc. on the quality of the reconstructed image can be determined by the study of the former.

3.3.1 Formation of the hologram

The illumination is assumed to be quasi-monochromatic. It is characterized by the condition that the spectral width of the radiation ($\Delta\nu$) is very small compared to the mean frequency (ν') i.e.

$$\Delta\nu \ll \nu' \qquad - (3.2)$$

In addition it is assumed that all path differences satisfy the condition

$$\Delta\ell \ll \frac{c}{\Delta\nu} \qquad - (3.3)$$

The reference beam in each situation is assumed to be a plane wavefront inclined at an angle θ to the normal at the photographic plate. The object beam can either be a plane wavefront or a spherical wavefront. The former can always be treated as a limiting case of the latter when its radius of curvature tends to infinity.

Case (I). The spherical object wave from a point source.

The constant amplitude of the plane reference wave = A_o. The amplitude of the reference wave at the photographic plate has a phase term added to it equal to $e^{j\kappa(\theta x)}$ and hence its complex amplitude at a distance x from the point O, as seen in Fig. (3.2a) is

$$A_o\, e^{j\kappa(\theta x)} \qquad \text{where} \quad \kappa = \frac{2\pi}{\lambda}$$

The complex amplitude of the object wave at O

$$= A\, e^{j\kappa(P^2/2Z)}$$

Since the illumination is assumed to be coherent the amplitudes at the photographic plate are additive. The total amplitude at the emulsion is therefore

$$= A_o\, e^{j\kappa(\theta x)} + Ae^{j\kappa(P^2/2Z)} \qquad - (3.4)$$

and the total intensity is thus

$$I = \left|A_o\, e^{j\kappa(\theta x)} + A\, e^{j\kappa(P^2/2Z)}\right|^2$$

$$= A_o^2 + A^2 + A_oA\, e^{j\kappa(P^2/2Z - \theta x)} + A_oA\, e^{-j\kappa(P^2/2Z - \theta x)}$$

$$= A_o^2 + A^2 + 2\, A_oA \cos k\left(\frac{P^2}{2Z} - \theta x\right) \qquad - (3.5)$$

The density of photographic emulsion after development is

$$d = \gamma \log_{10} I \qquad - (3.6)$$

where γ is the slope of the H- and D- curve of the photographic emulsion. Since the density of the emulsion is defined as

$$d = \log_{10} \frac{1}{T} = \log_{10} \frac{1}{t^2} \qquad - (3.7)$$

where T and t are the intensity and amplitude transmission factors respectively. One obtains from Eqs. (3.6) and (3.7) the expression

$$t = I^{-\gamma/2} \qquad - (3.8)$$

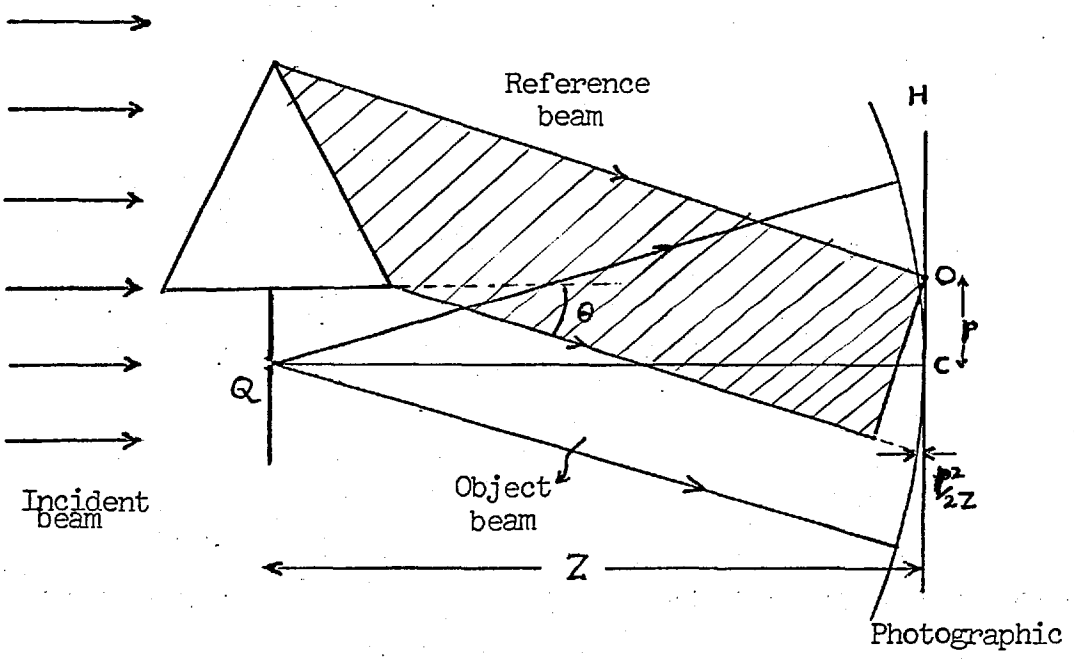

Fig (3.2a) Formation of the hologram.

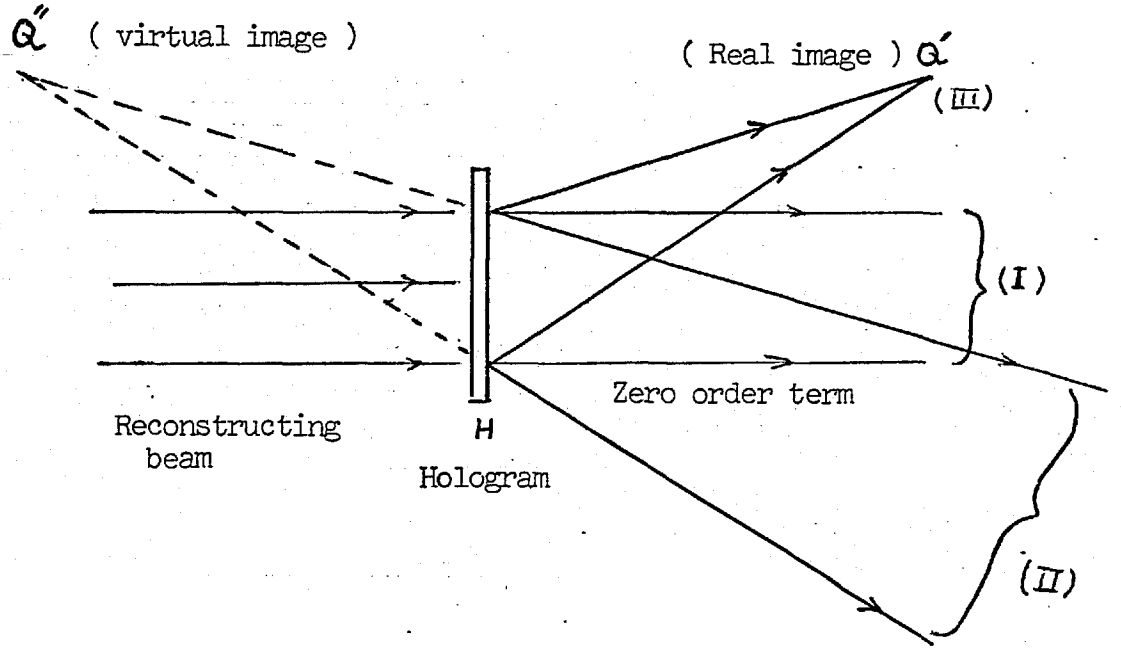

Fig (3.2b) Reconstruction of the hologram.

If the amplitude of the reference wave was much larger than that of the object wave in the process of formation of the hologram, then on substituting Eqs. (3.5) in (3.8) one can write for the amplitude transmission factor through the hologram

$$t = A_o^2 - \frac{\gamma}{2} A^2 - \frac{\gamma}{2} A_o A\, e^{jk(P^2/2Z - \theta x)} - \frac{\gamma}{2} A_o A\, e^{-jk(P^2/2Z - \theta x)} \quad - (3.9)$$

neglecting all powers of $\frac{A}{A_o}$ greater than two.

3.3.2 Reconstruction

Now if the hologram is illuminated with a coherent plane wavefront incident normally from the left, then eq. (3.9) would determine the terms emerging on the right side of the hologram. The Fig. (3.2b) shows the following terms

(I) The constant $(A_o^2 - \frac{\gamma}{2} A^2)$ represents the zero order term, i.e. the part of the beam which goes through undeviated.

(II) Apart from a constant factor it consists of the term

$$e^{jk\, P^2/2Z} \qquad e^{-jk\theta x}$$

$e^{+jk\, P^2/2Z}$ represents a diverging lens and $e^{-jk\, \theta x}$ acts to deflect the diverging rays to an angle w.r.t. the forward direction. This causes it to appear to originate from the point Q" which acts as a virtual image of the object point Q.

(III) Similarly, the term $e^{-jk\, P^2/2Z}$ acts as a converging lens and $e^{+jk\, \theta x}$ deflects these converging rays to the opposite direction of the normal w.r.t. term (II). This then forms the real image Q' of the object point Q.

Thus on illuminating the hologram with a coherent wave, the real and virtual images of the object point are reconstructed. These images are displaced w.r.t. the zero order term and hence do not overlap with each other as was the case with Fresnel hologram (sec. 3.2.1). These images can be seperately recorded on a photographic film or a screen.

This is true of every object point of an extended three-dimensional object and one obtains real and virtual images of the object in three dimensions.

Case (II). Object beam as a plane wavefront

This is the limiting case to the situation discussed above when $Z \to \infty$. The Eqn. (3.9) can then be written as

$$t = -2A_o^2 + \gamma A^2 + \gamma A_o A e^{-j\kappa \theta x} + \gamma A_o A e^{+j\kappa \theta x}$$

$$= -2A_o^2 + \gamma A^2 + 2\gamma A_o A \cos(\kappa \theta x) \qquad - (3.10)$$

The intensity distribution given by Eq. (3.5) corresponds to a grating in this case. If the hologram is illuminated by a plane wave, as seen from Eq. (3.10), one obtains a zero-order term and two terms corresponding to first order of the spectrum of the grating inclined at angles $\pm \theta$ from the normal.

3.3.3 Hologram as a linear superposition of zone-lenses.

The side-band hologram of a point object is a Fresnel diffraction pattern which resembles the Fresnel zone-plate and is termed as zone-lens. The zone-plate can be considered to be a special case of the hologram of the point source. When a zone-plate is arranged before a point source it duly reconstructs the image of the point source together with the symmetrically placed point on the far side of the original source. In common with the zone-plate the hologram acts as both a positive and negative lens. This accounts for the formation of real and virtual images. The effective focal length of the hologram varies with the wavelength λ and with a parameter representing the linear size of the hologram on the photographic plate and can be expressed as

$$f \propto \frac{L^2}{\lambda}$$

This is similar to the focal length of the zone plate

$$f_1 = \frac{S_1^2}{\lambda}$$ where S_1 is the radius of the first zone ring.

However, the difference between a zone-plate and the hologram is that the former has not only a primary focus, but also higher order foci corresponding to powers which are odd integral multiples of the primary power whereas the hologram has only one focal length. As pointed out by Rogers[20], this seems to arise from the practice of constructing zone-plates with abrupt changes from black to white at a sharp boundary, analogous to a square topped wave. The latter has a larger number of Fourier-coefficients and thus the sharper the boundaries in a zone-plate, the greater the numbers of orders obtained. The zone-lens produced by a continuous tone photographic process does not have sharp alternations but ones more closely conforming to sinusoidal vibrations, the exact form being

$$\psi(x) = 1 + \sin\left(\frac{\kappa x^2}{2f}\right) \qquad - (3.11)$$

Thus the greater part of the diffracted energy is concentrated in first-order images. This is the reason that the intensity of reference and object beams are not kept equal as unusual degree of photographic contrast might give rise to higher order terms. For comparison the term representing the real lens is given below

$$\psi(x) = \sin\left(\frac{\kappa x^2}{2f}\right)$$

The Fig. (3.3) shows the diference between the zone-plate and a hologram of a point source (a zone-lens).

As will be discussed later, the holographic system to be finally selected for our work is a scatter-plate interferometer. The hologram produced in this system corresponds to both a side-band and a Fourier-

Fig (3.4a) The Zone - Plate.

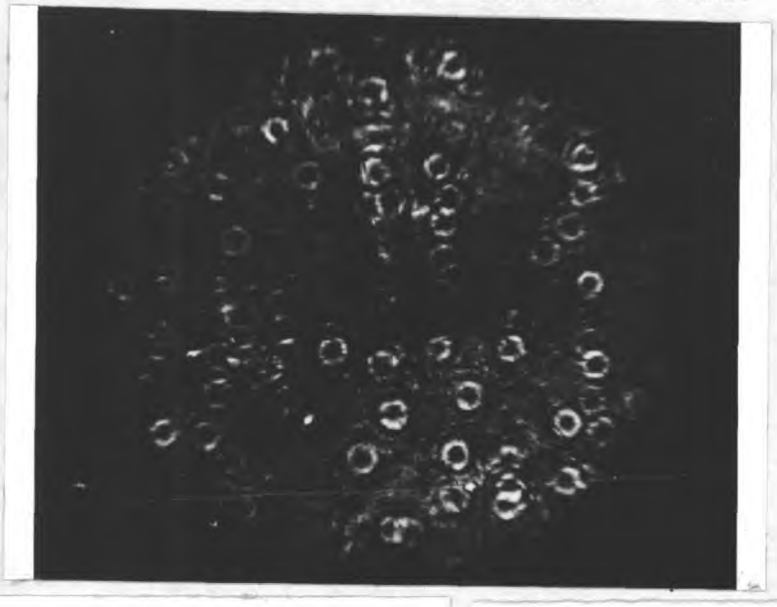

(b) Random distribution of zone-lenses.

X 100

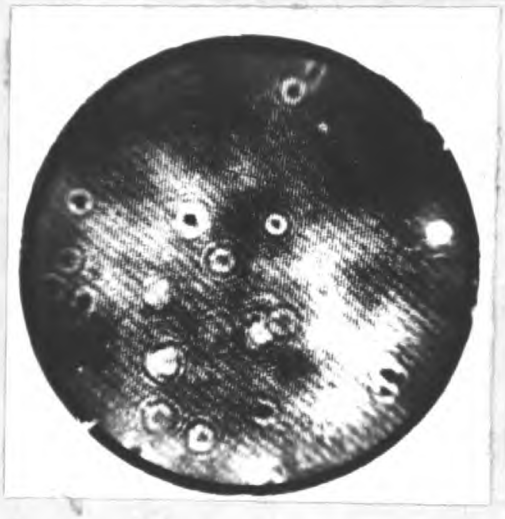

(c)

(d)

Fig (3,4) Fringe Patterns forming the hologram.
(c) Inside of the Moire Pattern hologram (See Fig(6.26))
(d) Inside of the hologram taken with diffused object beam.

transform holograms (secs. 3.2.2 and 3.2.4). Since the nature of hologram fringe pattern in each case will determine the resolution characteristics of the hologram, the Fig. (3.4) shows the kind of fringes obtained in each case.

3.4 Holographic Interferometry

To observe the phase changes in a wavefront caused by an object, a reference plane wave front is made to interfere with it. This produces the intensity modulations (fringes) corresponding to the phase modulation characterizing the object. An interferometer commonly used in plasma work for this purpose is the Mach-Zehnder system. One of the most useful applications of holography was in the field of interferometry which was first proposed by Stroke and Labyrie[15]. The double exposure technique was developed among others by Stetson and Powell[16] and holographic interferometry of transient events was first demonstrated by Heflinger et. al.[17]. Heflinger made quantitative measurements of the several fringes produced by disturbed air in the wake of a bullet. This technique has been improved by Jahoda et. al.[18] by introducing a background fringe pattern to the actual fringes thereby increasing the sensitivity by an order of magnitude bringing it at par to the value with Mach-Zehnder system. The background fringe pattern also allows the determination of the direction of fringe motion thereby indicating an increasing or decreasing value of the refractive index.

3.4.1 The Double-Exposure technique

Usually the holographic interferogram is made by a double exposure [14,16,17] of the photographic plate, one exposure with the disturbance to be recorded and the other without it. On subsequent development and reconstruction, the two wavefronts are reconstructed simultaneously giving the 'frozen-fringe' pattern, This being termed so because the relationship of the spacing of interference fringes and their orientation is fixed in relation to the reconstructed object. Although it is not possible to

make adjustments of the orientation and spacing of the interference fringe pattern, the three dimensional effects are still observable. The advantage of this method is that the interference effects are visible without the need to use the actual recording apparatus for reconstruction.

The live fringe pattern can also be observed if the hologram of the system without the disturbance is replaced in the position it originally occupied in the same apparatus. The reference wave incident upon it will produce a reconstructed virtual image from the hologram which coincides in position with the original object. The phase distributions in the two waves which now originate at the actual object and at the hologram should match exactly. If, however, there are phase changes resulting from changes in the object, these will show up as interference fringes which can be observed 'live' as the disturbance developes. In all these cases, the interference pattern is free from errors caused by imperfections in the optical system. The limitation of the 'live fringe' interferogram is that it can only be observed by utilizing the same apparatus. Any errors in replacing the hologram will produce background fringes which might add to the true fringe pattern.

3.4.2 Three-beam single-exposure technique

The above mentioned technique of frozen fringes uses two exposures of the photographic plate and needs two beams to form a hologram. Recently a technique of three-beam holographic interferometry has been proposed[19] which needs only single exposure of the photographic plate. This uses two reference beams instead of one as is customary. Depending on the location of the phase object, two configurations are possible, each having some distinct properties. When the object is placed in the central beam, one obtains, upon reconstruction, an interferogram having twice the sensitivity of all single-process interferometers. On the other hand if the object is located in one of the outerbeams, the reconstruction step would simultaneously yield an interferogram of the phase object in the first order of diffraction, and the original object wave in the second order.

In the set-up suggested by De, Manoranjan and Sevigny[19] the limitation of the technique was its requirement of high quality optics and the need of laborious alignment of the optical components. The requirement of using two conjugate diffusers forbid the use of opal glass. However, as shown by Tanner[36] the scatter-plate system completely relaxes these requirements and overcomes the limitations of the method by using a central reference beam in the scatter-plate system. The diffused illumination from the scatter-plate acts as a binary mash of dots having a random distribution and hence the diffuser acts as an amplitude scatterer - a condition imposed by the need of having two conjugate diffusers (see Ref. 19). However, when one wants to analyse both the first and second order reconstructions, much higher requirement is still placed on the resolution capability of the film, which should be about seven times the maximum significant spatial frequency of the signal.

In conclusion it must be mentioned that out of various holographic interferometric techniques that are available, two-beam double-exposure frozen fringe technique stands out as the most useful one. This is because of its simplicity, ease of operation and least requirements on the optical system. Using a background fringe pattern, the sensitivity of the technique matches that of Mach-Zehnder system but of course with all the additional advantages which holographic interferometry offers.

3.4.3 The process of holographic interferometery

To see in more detail how the two wavefronts are 'stored', let us consider a simple case of a plane wavefront Σ passing through the test region but in the absence of the disturbance (such as plasma) to be studied. This falls on a photographic plate H simultaneously with a coherent reference beam R which is inclined at an angle θ to the direction of Σ. Fig. (3.5).

Let A_R be the amplitude in H due to the wavefront Σ, and $A_O\, e^{j\kappa\theta x}$ be the amplitude in H due to the reference beam R. The exponential phase term $\exp(j\kappa\theta x)$ is introduced due to the constant angular inclination of the reference beam w.r.t. the photographic plate. Since the two beams

are assumed to be coherent, their amplitudes can be added to give us the intensity distribution on the photographic plate.

This gives

$$I_1 = |A_R + A_o\, e^{j\kappa\theta x}|^2$$

or $$I_1 = A_o^2 + A_R^2 + A_R A_o\, e^{j\kappa\theta x} + A_R A_o\, e^{-j\kappa\theta x}$$

Now if a test dephasing object in the path of Σ is introduced without displacing the photographic plate H, and again 'switching on' both the wavefront Σ and the reference beam R, the amplitude in H due to 'test beam' is $A_R\, e^{j\phi}$, where ϕ is the phase due to the disturbance in T. The intensity in the latent image produced by this second recording is

$$I_2 = |A_R\, e^{j\phi} + A_o\, e^{j\kappa\theta x}|^2$$

$$= A_R^2 + A_o^2 + A_R A_o\, e^{j(\phi-\kappa\theta x)} + A_R A_o\, e^{-j(\phi-\kappa\theta x)}$$

The total recorded intensity is

$$I = I_1 + I_2$$

$$= 2A_R^2 + 2A_o^2 + A_o A_R\, e^{j\kappa\theta x}\,(1 + e^{-j\phi}) + A_o A_R\, e^{-j\kappa\theta x}\,(1+e^{j\phi})$$

After development of the photographic plate and illuminating by a plane-parallel coherent beam, the amplitude transmitted by the hologram will consist of some zero-order terms independent of ϕ and θ and two other terms

$$\gamma\, A_o A_R\, e^{j\kappa\theta x}\,(1 + e^{-j\phi})$$

and $$\gamma\, A_o\, A_R\, e^{-j\kappa\theta x}\,(1 + e^{+j\phi})$$

The first term gives an image which shows interference between the object and the reference wavefront Σ. Thus one obtains an interferometer

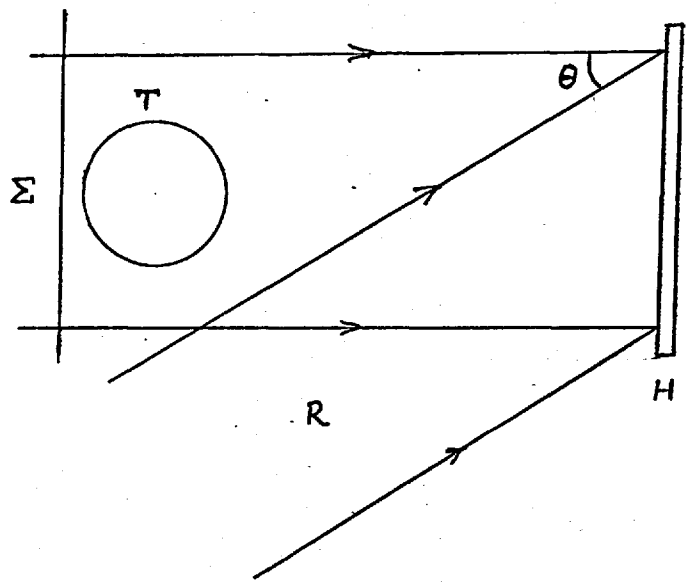

Fig (3.5) Formation of the holographic interferogram.

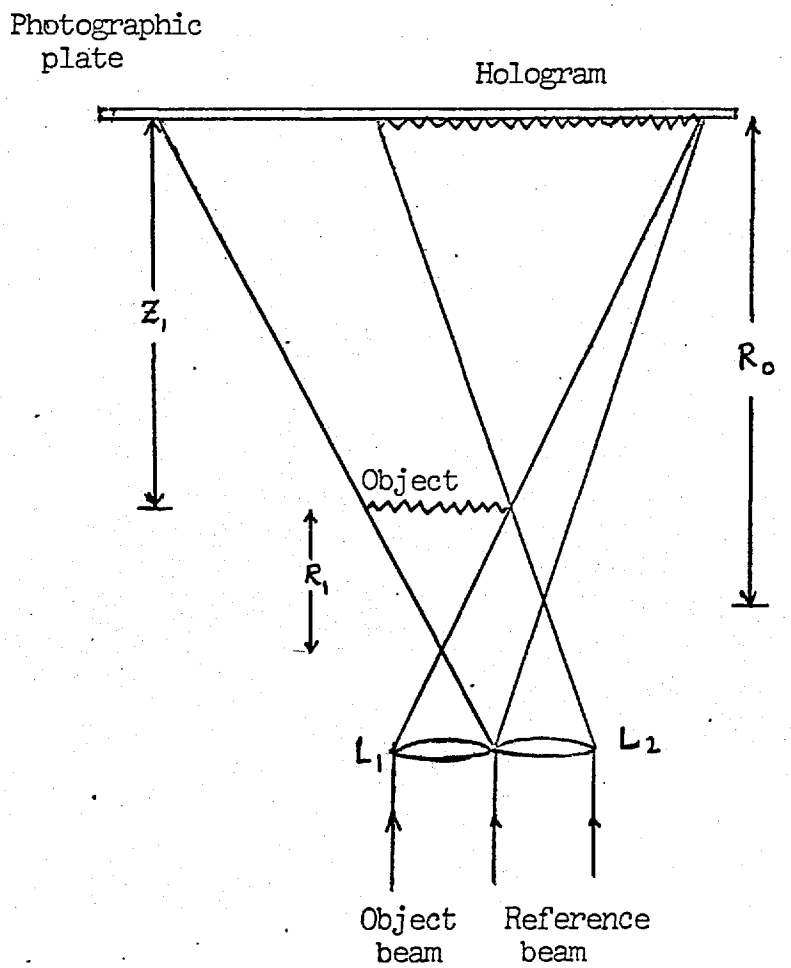

Fig (3.6) Spherical wave illumination for magnification analysis of a side-band hologram.

by recording two wavefronts successively. The other term merely gives an image conjugate to the first one.

The actual experimental layout of the interferometric system will depend on various factors such as the coherence length and the degree of spatial coherence of the light source, the size of the test region to be explored, the range of viewing angle giving certain extent of three dimensionality, the desired magnification of the reconstructed image and so on. Therefore before being in a position to decide upon the actual experimental system to be used, one has to consider the parametric dependence of the reconstructed image of a hologram on these factors. This will be the subject of the following sections.

3.5 Magnification considerations of side-band holograms with spherical wavefronts

As stated earlier, if the hologram is replaced in the original position as during the formation stage and illuminated by the same reference beam, it reconstructs a virtual image in the same location as occupied by the original object and of unit magnification. However, if either the wavelength of reconstructing illumination or the curvature of the beam and the distance of the hologram from the source of illumination is varied, a magnification of the reconstructed image w.r.t. the original object size results. Since the geometry of side-band holograms with spherical wavefront is quite often utilized for hologram formation of the plasmas and of other objects, it is necessary to establish quantitative relationships between the above mentioned parameters to enable one to calculate the position and size of the image in focus.

Magnification of holographic systems has been investigated by many authors[21,22,23]. In the following is summarized their general approach to the problem and the results obtained for various situations regarding different values of the above mentioned parameters.

Side Band holograms

The magnification of the system is defined as

$$m = \frac{\lambda_2 Z_2}{\lambda_1 Z_1} \qquad - (3.12)$$

where λ_1 and Z_1 are the wavelength and the distance between hologram and the planar object respectively in the planar object. All quantities with suffix 2 refer to the reconstruction stage.

Assuming monochronatic spatially coherent illumination both during formation and reconstruction stages, the focusing condition for the amplitude of reconstructed image is given by[24]

$$\mp \frac{k_1}{Z_1} \pm \frac{k_1}{R_o} + \frac{k_2}{Z_2} + k_2/R_2 = 0 \qquad - (3.13)$$

where the two signs correspond to real and virtual images. R_o and R_1 etc. are defined in the Fig. (3.6).

Substituting this in Eq. (3.12), magnification of the object is then

$$m = \frac{1}{(1 - \frac{Z_1}{R_o} \mp \frac{\lambda_1 Z_1}{\lambda_2 R_2})} \qquad - (3.14)$$

where +ve sign corresponds to real image.

Limiting Case I

Both the reference beam in the formation stage and the reconstructing beam are plane-parallel. This is described by R_o and $R_2 \to \infty$.

this gives $m = 1$ - (3.15)

Thus the magnification is independent of the wavelength used to construct and reconstruct the hologram.

Case II

When reconstruction alone is with plane wave, i.e. $R_2 \to \infty$

then $$m = \frac{1}{1 - \frac{Z_1}{R_o}} \qquad - (3.16)$$

again the magnification is independent of wavelength and the entire magnification is due to 1st step of the process. When $\frac{Z_1}{R_o} \approx 1$, m becomes very large but the image is formed at very large distance since $\frac{k_2}{Z_2} \approx 0$ as seen from Eq. (3.13)

Case III

The hologram constructed using plane parallel wave but reconstructed using spherical wave, i.e.

$R_o \to \infty$, and R_2 is finite

this gives $$m = (1 - \frac{\lambda_1 Z_1}{\lambda_2 R_2})^{-1} \qquad - (3.17)$$

where $\lambda_1 Z_1 = \lambda_2 Z_2$ m becomes very large but again Z_2 is very large as seen from Eq. (3.13) and hence the recording of the reconstructed image is limited by experimental considerations.

The above discussion was confined to the planar object and the lateral magnification m_{lat} (i.e. magnification transverse to the optic axis) was discussed. However, for a three dimensional object one has also to consider the longitudinal magnification m_{long}, i.e. along the optic axis. It has been shown[22,23,25] that the longitudinal magnification is given by

$$m_{long} = (\frac{\lambda_1}{\lambda_2}) m^2_{lat}$$

This causes distortion on magnification of the three dimensional object. This distortion can, however, be removed by making $m_{lat} = \frac{\lambda_2}{\lambda_1}$, which gives $m_{long} = m_{lat}$. Moreover to avoid distortion, m_{lat} should be independent of Z_1.

The Fig. (3.7b) shows two reconstructed real images obtained from the hologram of a toy bulldozer. The hologram was taken with the simple arrangement shown in Fig. (3.7a). To obtain the real image a portion of the hologram was illuminated by a beam with the same convergence as that

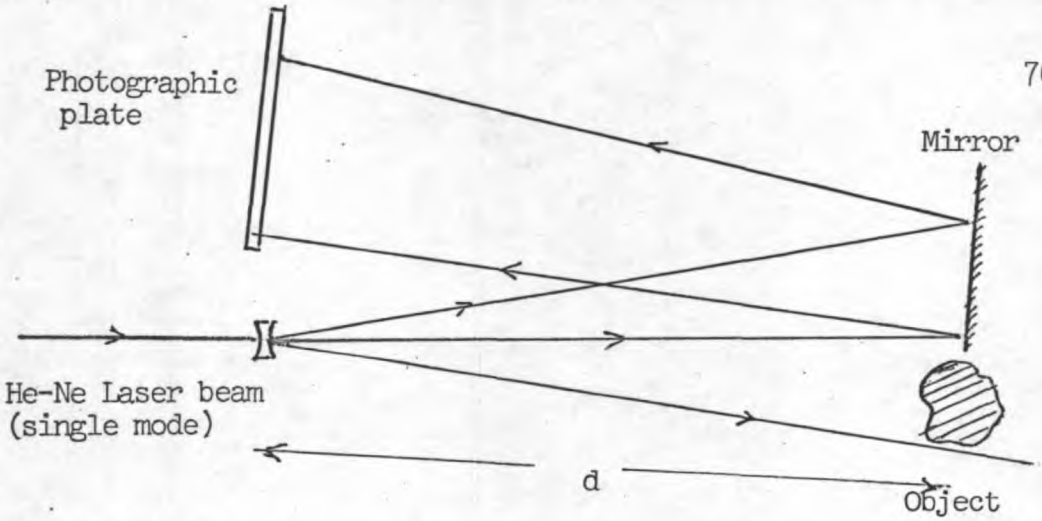

Fig (3.7a) $R_1 = d$, $Z_1 = d$, $R_o = 2d$, $\lambda_1 = \lambda_2$

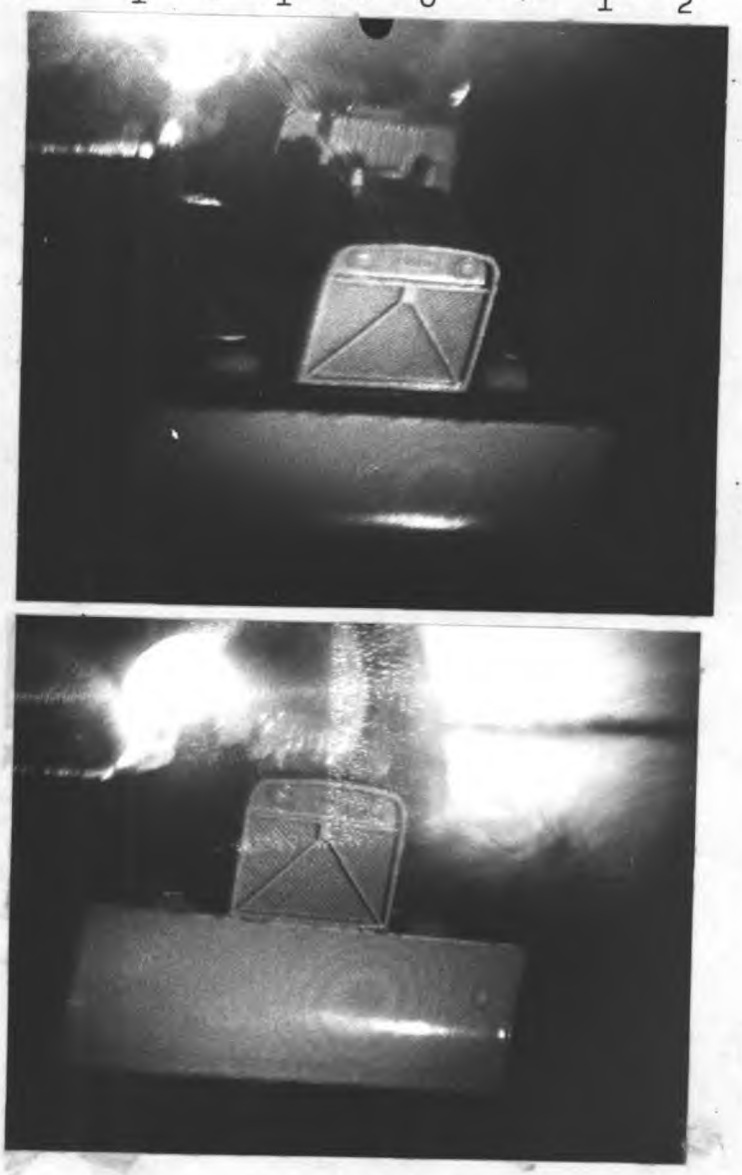

Fig (3.7b) The reconstructed images of toy object.

of the expanding beam looked upstream in Fig. (3.7a). Focused real image of unit magnification was obtained at the same distance from the hologram as during the formation stage, as predicted by Eq. (3.13). The image was photographed by simply placing the photographic plate at the position of the focused real image. Using different areas of the hologram, one can observe the images from different viewing directions showing the three-dimensionality of reconstruction. It must be noted that as seen from Eqs. (3.13) and (3.14) one obtains a virtual image at infinity of infinite magnification.

Fourier Transform hologram

The magnification in Fourier Transform type holograms (3.2.4) is given by

$$m = \frac{\lambda_2 Z_2}{\lambda_1 Z_1} \qquad - (3.18)$$

and is only wavelength dependent since no focusing condition needs to be satisfied as was the case for side-band holograms. Thus if a hologram is constructed using ruby laser output and reconstructed using He-Ne laser, there is a demagnification of $\lambda_2/\lambda_1 = \frac{6.328}{6.943} \approx 0.91$ provided $Z_1 = Z_2$ as is usually the case.

3.6 Effect of coherence on the image quality in wavefront reconstruction

The quality of the reconstructed image from a hologram depends on that of the recorded interference fringe pattern on the photographic plate. This in turn is dependent on various factors such as coherence of the illumination, the spatial frequency of the photographic emulsion, the photographic development process, the imaging optics and finally on the coherence of the reconstructing illumination. The influence of coherence of the illumination both in construction and reconstruction stages of the hologram will be discussed in this section.

In the discussion so far, the light was assumed to be quasi-monochromatic as defined by the equations (3.2) and (3.3), and also to be

perfectly spatially coherent. Hence perfect interference between reference and object beams was expected. It has, however, been shown in Chapter 2 that the output of the ruby laser has only a partial degree of coherence. This is due to the fact that the crystal amplifier in the ruby laser operates simultaneously in various axial and transverse modes of the cavity. The effect of multi axial mode operation is to broaden the frequency width of the output light and hence decreasing its temporal coherence. On the other hand the spatial coherence of the light is spoilt due to the laser operating simultaneously in many transverse modes of the cavity. It is interesting to note that the spatial coherence of the light in the cavity[26] owes its origin to the partially coherent or even incoherent light having sufficient number of transmissions through a periodic structure and accompanying diffraction at each mirror in the cavity. This happens even in the absence of the laser medium, and the only effect the active medium in the cavity has is to compensate - at least partially - for losses of light suffered in each transmission and reflection. The spatial coherence will be complete provided the number of reflections is sufficiently large, and only if a single mode survives, and presumably if also the effect of spontaneous emission is negligible. Since in the Q-pulse operation with short pulse widths, the condition of sufficiently large reflections is not met. Moreover the cavity operates in many modes. All these factors contribute to spoil the spatial coherence of the laser output.

3.6.1 The contrast of fringes as a function of the degree of coherence of illumination

To study the influence of coherence of illumination on the quality of the interference fringes, the former is specified in terms of a parameter which would be an experimental observable. This is termed as the complex degree of coherence γ_{12}. The rigorous description of the theory of partial coherence is given by many authors[27,28]. Here it will suffice to state that the total intensity I_P on a point P from two point sources having intensities as seen in Fig. (3.8), will be given by

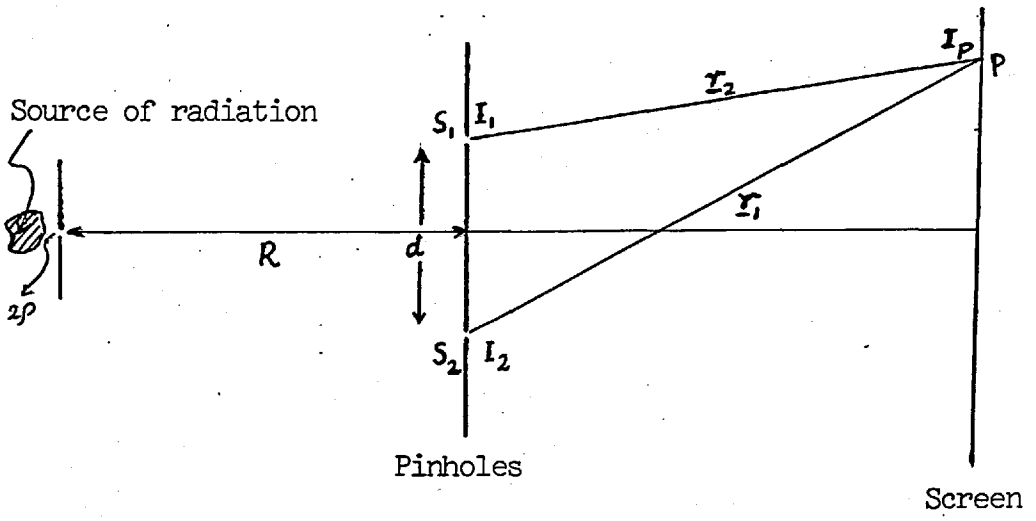

Fig (3.8) Measurement of modulus of complex degree of coherence with two-pinhole experiment.

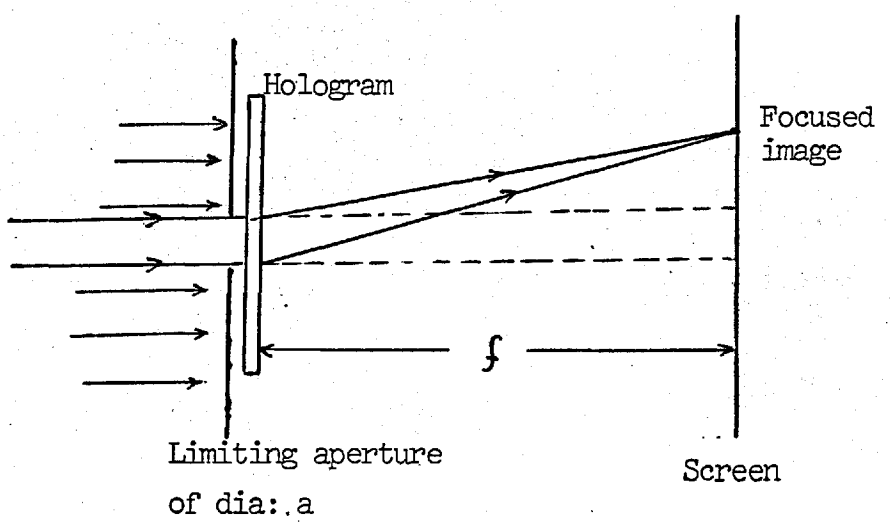

Fig (3.9) Diagram showing the hologram as a lens of a limited aperture for determining the spatial frequency of the speckle pattern.

$$I_P = I_1 + I_2 + 2\sqrt{I_1 I_2}\,|\gamma_{12}| \cos \Phi_{12} \qquad - (3.19)$$

where $|\gamma_{12}|$ is the modulus of γ_{12} and is termed the degree of coherence and Φ_{12} is the phase of γ_{12}

$$\Phi_{12} = 2\pi\nu'\tau + \beta_{12}\,, \qquad 2\pi\nu'\tau = \text{phase difference} = \frac{2\pi}{\lambda'}(|\underline{r}_1 - \underline{r}_2|)$$

and $\beta_{12} = \arg[\gamma_{12}]$.

The phase term β_{12} is related to the relative position of the central fringe to the origin when the pinholes are symmetrically displaced w.r.t. the optic axis.

The degree of coherence $|\gamma_{12}|$ has the values

$$0 \leq |\gamma_{12}| \leq 1 .$$

When $|\gamma_{12}| = 1$, the light is completely coherent and

$$I_P = I_1 + I_2 + 2\sqrt{I_1 I_2} \cos \Phi_{12}$$

whereas if $|\gamma_{12}| = 0$, the light is completely incoherent and the intensities are merely additive, so that

$$I_P = I_1 + I_2 .$$

For intermediate values of $|\gamma_{12}|$, the radiation is partially coherent and the resulting interference is given by Eq. (3.19).

Although the coherence effect in a radiation field are completely described by the complex function γ_{12}, in limiting cases it can be separated into two categories as spatial coherence and temporal coherence. The former results primarily from angular source size considerations and is expressed by $\gamma_{12}(0)$, and the latter results from considerations of the finite spectral width of the radiation and is expressed by $\gamma_{11}(\tau)$.

Here τ is the coherence time equal to $\frac{\Delta\ell}{c}$, $\Delta\ell$ representing the coherence length of the radiation.

To see the effect of the complex degree of coherence on interference fringes, the definition of fringe visibility is recalled, which is

$$V = \frac{I_{max} - I_{min}}{I_{max} + I_{min}} \qquad - (3.20)$$

Assuming $I_1 = I_2 = I$, eq. (19) becomes

$$I_P = 2I(1 + |\gamma_{12}| \cos \Phi_{12})$$

which gives $V = |\gamma_{12}|$

If we have the situation $|\underline{r}_1 - \underline{r}_2| << \Delta\ell \; (= \frac{c}{\Delta\nu})$, the visibility of fringes measures the degree of spatial coherence. Moreover, one would observe interference fringes only when the two beams travel within the limit of temporal coherence, i.e. when $|\underline{r}_1 - \underline{r}_2| < \Delta\ell$.
Thus it can be seen that light of higher degree of coherence will produce fringes of better contrast, which in turn will determine the quality of the reconstructed image.

3.6.2 Considerations from microscopic point of view

In most of the different types of holograms the interference pattern is the linear superposition of Zone-lens type fringes (3.3.3). The effect of coherence on the imaging properties of the hologram can be determined by the former's influence on zone-lens fringes. This problem has been treated by Reynolds et. al.[24,29] using the theory of partial coherence for a mathematically simple case of Fraunhofer hologram of an opaque particle in a clear aperture illuminated by quasi-monochromatic partially coherent radiation. Both their computational and experimental results indicate the following.

For a given coherence length and aperture size the effect of spatial

coherence on the hologram is to reduce its effective size. As the coherence across the aperture decreases, the outer rings of the zone-lens hologram are lost. Since the zone-lens acts like a lens in the reconstruction stage, when illuminated by a plane wave, it will focus the beam to a diffraction pattern whose central spot size is inversely proportional to the diameter of this zone-lens. Thus a reduction of the degree of spatial coherence will result in the poor resolution of the reconstructed image.

Usually the coherence length of CW gas lasers is of the order of tens of centimeters, and can easily be made to operate in single transverse mode. The only limitations to the quality of the hologram will be the film effects (which will be discussed in the next chapter). However, the coherence length of a non-mode controlled giant pulse ruby laser is only at the most one or two centimeters. Moreover unless mode controlled, its spatial coherence will not be very good as the laser operates with a complex time dependent mode pattern. This is also a strong function of the quality of the ruby crystal. Thus both the temporal and spatial coherence of the ruby will present problems in actual carrying out of the experiment and will degrade the fringe pattern on the hologram which will in turn deteriorate the quality of the reconstructed image. These will also place quite stringent restrictions on the geometry of the experimental set-up that can actually be employed. The ruby output can of course be improved by proper mode-selection procedures but they are usually not very easy to utilize and work only at the expense of the energy and power of the output radiation. This problem can be bypassed or at least very much relaxed by the use of proper holographic set-up (see Chapter 4) which is fortunately possible for phase objects and relaxes the requirements of temporal and spatial coherence to quite a large extent.

3.6.3 Considerations from macroscopic point of view

To show quantitatively the influence of a certain frequency spread in hologram forming and reconstructing illumination and also of their

spatial coherence on the reconstructed image, many authors[30,31,32] have carried out the analysis of the process. If the optical path differences involved are comparable to the coherence length, the frequency spread will contribute in the image terms during reconstruction of the hologram. If ν and ν' are the frequencies of illumination during formation and reconstruction stage and have a finite bandwidth $\Delta\nu$ and $\Delta\nu'$ respectively, the wavefront emerging from the hologram has the following two terms as shown by Mandel[30].

1) A spread of directions of propagation $\theta(\nu/\nu')$ leading to a transverse blurring or defocus of the reconstructed (virtual) image. This is approximately given by

$$2\ell \left(\frac{\nu_o}{\nu_o'}\right) \left(\frac{\Delta\nu}{\nu_o} + \frac{\Delta\nu'}{\nu_o'}\right) \qquad - (3.21)$$

where $\ell \equiv$ width of the plane-wave reference beam utilized in the formation and reconstruction process. ν_o and ν_o' are the mid-frequencies of the writing and reading beams.

2) A spread of wavefront retardation leading to a longitudinal defocus of reconstructed image. This is approximately given by

$$2\left[c\eta(x,y,\nu_o) - \theta(x + \tfrac{1}{2}\ell)\right] \left(\frac{\nu_o}{\nu_o'}\right) \left(\frac{\Delta\nu}{\nu_o} + \frac{\Delta\nu'}{\nu_o'}\right) \qquad - (3.22)$$

where $\eta(x,y,\nu)$ is the retardation function due to the object and c is the velocity of light.

Thus it can be seen that the contribution of both $\Delta\nu$ and $\Delta\nu'$ are added together, so that the loss of resolution cannot be avoided simply by using the same light beam for recording and reading the hologram.

e.g. If the spectral line-width of ruby output = 0.5 A^o (corresponding to a coherence length of 1 cm) then $\Delta\nu = 3 \times 10^{10}$ c/s

$\nu = 4.3 \times 10^{14}$ c/s $\qquad \frac{\Delta\nu}{\nu} \simeq 7 \times 10^{-5}$

If reconstructed with He-Ne laser illumination, then

$$\Delta\nu' \simeq 500 \text{ mc/s} \quad \text{and} \quad \frac{\Delta\nu'}{\nu'} << \frac{\Delta\nu}{\nu}$$

Thus for a beam of 5 cm. width (ℓ = 5 cm.) the defocus would amount to 7×10^{-4} cm. which is about ten wavelengths.

But if a hologram is constructed with light in a broad spectral band of say $\Delta\lambda$ = 50 A^{o} then $\frac{\Delta\nu}{\nu} \sim 7 \times 10^{-3}$ and the defocus would be 0.7 mm. Thus the reconstructed image would appear blurred. If the radiation has many closely spaced frequency components as in Argon laser or else the hologram is made with white light of a certain bandwidth as with scatter-plate system (see chapter 4), only then is the blurring serious.

The quantitative analysis carried out by Bertolotti et. al.[31] shows the influence of spatial coherence on the characteristics of holograms. They employed partially coherent field only for the recording of the hologram while reconstruction was carried out with perfectly coherent light. The reconstructed wave in the direction ϕ is expressed as

$$\psi(\phi) = \int_{-\infty}^{+\infty} \gamma(\xi) \; e^{-2\pi i(\nu/c)\,(\theta-\phi)\xi} \; d\xi \qquad - (3.23)$$

where θ is the angle between reference and object beams during hologram formation,

$\gamma(\xi)$ is the degree of spatial coherence, and

ξ is the coordinate in the hologram plane.

When $\gamma(\xi) = 1$, $\psi(\phi)$ becomes a Dirac function $\delta(\phi-\theta)$,

i.e. the light is diffracted only in the direction $\phi = \theta$.

If $\gamma(\xi) \neq 1$, there is diffracted light around a mean value $\overline{\phi} = \theta$.

The r.m.s. of ϕ is obtained as

$$\Delta\phi = \frac{c}{2\pi\nu} \left\{ \frac{\int_{-\infty}^{+\infty} \left|\frac{d\gamma(\xi)}{d\xi}\right|^2 d\xi}{\int_{-\infty}^{+\infty} |\gamma(\xi)|^2 \, d\xi} \right\}^{\frac{1}{2}} \qquad - (3.24)$$

The limits are justified because the coherence area of a typical partially coherent field is generally much smaller than the dimensions of the photographic plate. Thus using Eq. (3.24) one can calculate the angular spread of the reconstructed image due to distribution of spatial coherence of the radiation on the photographic plate.

In conclusion it can only be remarked, that it is possible to obtain a hologram with partially coherent light. However, the reconstructed image will have a good quality as regards resolution and contrast only if the degree of partial coherence of illumination both in formation and reconstruction stages is high. This requires that all the path differences are well within the coherence length and also the degree of spatial coherence γ_{12} is greater than 0.88 (P.509 of Ref.27), which specifies 'almost coherent' radiation.

3.7 Holography using diffuse illumination

When a diffusing screen such as a ground glass is introduced between the source of illumination and the object, the hologram obtained has very distinct and useful properties. Firstly, the hologram when reconstructed also recreates the diffuser screen which acts as a luminous background to the object. Hence the virtual image can be viewed with the naked eye as if being viewed through a window because light from all points of the object reaches the eye. If the diffuser had not been used in making the hologram, the reconstruction has to be observed using an eye-piece or other optical aids.

Another interesting property of the diffuse-illumination hologram is that, since each point of the object illuminates the entire hologram recording plate, very small areas of the holograms are able to reconstruct the entire object. As the illuminated area becomes smaller, resolution is lost since this area of the hologram constitutes the limiting aperture of the wavefront reconstruction imaging process. The most important property of such a hologram is that the local imperfections in the optical elements no longer degrade the image quality. In other types of holograms

any dust particles or scratches etc. on the photographic plate or other elements of the optical system cause annoying diffraction patterns in the reconstructed image due to the coherence of the illumination. In the diffuse illumination holograms such imperfections are completely removed from the holograms.

Since in such holograms, each point of the object spreads its effect over the entire hologram plate, any scratch or damage to any piece of the hologram does not cause any noticeable deterioration of the reconstructed image.

To make diffuse illumination holograms a large design angle has to be used. This necessitates the use of very fine grain, high spatial frequency film of low speed. The other limitation is encountered using ruby laser as a source of light of short coherence length. One has to ensure the reference beam path to be reasonably equal to the path through the diffuser and the object. Although the depth of the object need not be shorter than the coherence length as long as the above condition is satisfied.

To understand how the diffuser works, it must be mentioned that the light impinging on the object is no longer a well-defined wavefront, but instead has a phase and an amplitude which vary randomly from point to point. It is represented by $e^{i\,\psi_1(x,y)}$ where $\psi_1(x,y)$ is a random function and the diffuser acts as a phase object. Although the diffused light behaves as if it were incoherent, it retains the properties necessary for the hologram formation process. The phase and amplitude relations although being random functions are time invariant, in contradistinction to the case of incoherent illumination. However, if the diffuser is moved or rotated, thus essentially placing different pieces of ground glass behind the object, this ensemble averaging effectively destroys the coherence of the radiation. This is indeed the method of obtaining light of partial spatial coherence by passing coherent beam through a rotating ground glass screen.

Having seen the advantages of diffuse illumination holograms, it is

imperative that a system is chosen which incorporates in itself a diffuser. A system in which a scatter-plate does the dual function of providing diffuse illumination and also acting as a beam splitter is described in the next chapter. This system is ideal for use with ruby laser as it requires minimum conditions of both the spatial and temporal coherence of the radiation.

There is one more aspect of diffuse illumination in coherent field, namely the speckle effect, which merits consideration and is discussed in the following.

3.8 Speckle Effect

When surfaces are illuminated by coherent field of a laser, speckle patterns are observed. Since this effect contributes in degrading the quality of reconstructed images of a hologram, it is important to understand its cause and the parametric dependence of the speckle size and its spatial frequency.

Speckling is not a property of laser light itself but is present only when phase variations are introduced into the wavefront by transmission through or reflection from an optically rough object. Thus the diffuse illumination from a ground glass is not uniform but is speckly.

If a hologram is formed with diffuse illumination, when reconstructed it recreates the speckle effect with the object beam. The spatial frequency of the speckles is proportional to the angular aperture of the illumination. The hologram size illuminated for reconstruction is effectively an aperture acting as a spatial filter cutting off the higher frequencies. The density of speckling (or spatial frequency of speckles) is proportional to the cut-off frequency (f_c) of the imaging system[33] where,

$$f_c = \left(\frac{m}{1+m}\right) \cdot \frac{a}{f} \frac{1}{\lambda}$$

where m ≡ magnification of the system

$f/_a$ ≡ f-number of the hologram acting as a lens to give a focused

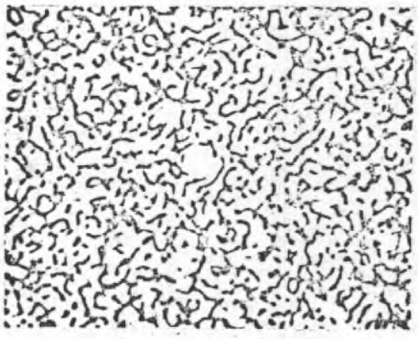

Fig (3.10) Speckle Pattern.

(a)

(b)

Fig (3.11) The reconstructed image from a transparency.

image. Fig. (3.9).

$\lambda \equiv$ mean wavelength of the light source.

As the aperture size a is decreased, spatial frequency of speckles decreases and speckle size increases. The Fig. (3.10) shows a typical speckle pattern obtained by exposing the photographic plate by object beam alone. If the reconstructed image is an interferogram, with the interference fringes having a spatial frequency of p lines/mm., then to obtain a reasonable speckle-free image, the spatial frequency of the speckles should be much larger than that of the interference fringe pattern. This determines the smallest area of the hologram that can be utilized to give a good image having sufficiently clear fringes for practical use. The need to limit the aperture of the hologram arises from the requirement of angular resolution of the interference fringe distribution in a non symmetric plasma (or any other phase object). To estimate the typical size of the hologram aperture, let us assume a spatial frequency p = 20 fringes/cm. (a reasonable figure in plasma work).

If $f_c \simeq 10\ p$ to give good speckle free reconstruction, then

$$f_c \simeq 200 \text{ lines/cm.},$$

for $\lambda = 0.63 \times 10^{-4}$ cm. and unit magnification (m = 1)

when f = 25 cms., we get a = 6.3 mm. as the minimum diameter of the aperture size for hologram illumination.

To obtain a better angular resolution, if one has to resort to using a smaller area of the hologram, difficulty may be encountered in reading the fringes due to speckling of the reconstructed image. The Fig. (3.11) shows the reconstruction from a hologram of a transparency obtained by using relaxation oscillation output of a ruby laser in the scatter-plate system. The Fig. (3.11a) was reconstructed using about twice the area of the hologram than that in Fig. (3.11b). The latter has roughly half the speckle frequency compared to the former.

3.9 Considerations for the choice of a practical system for holography.

As pointed out in the preceeding discussion, the choice of a particular system for holographic interferometer depends mainly on the following considerations.

3.9.1 The coherence of the ruby light output

If ruby operation is not in single transverse mode or the wavefront is not uniphase, then the degree of spatial coherence will be less than unity and the interference fringes will have poor contrast. One can either resort to control the mode structure of laser output, at a price to be paid in terms of loss of energy and power, or choose a holographic system which will have minimal demands on coherence. If a diffuser is incorporated into the system between the source of illumination and the object, then the wavefront is completely randomized, and interference at photographic plate takes place between randomly related elements of the original wavefront. This therefore requires the uniphase operation of the laser so that the degree of spatial coherence is maximum to allow each element of the wavefront to interfere with any other.

Moreover the presence of many axial modes causes the coherence length to be reduced and presents problems in alignment of optical components to obtain reference and object beams whose path difference is shorter than the coherence length of the laser. For ordinary giant pulse laser operation without any mode control, coherence length is only of the order of a centimeter or so and it is very easy to exceed this length with diverging beams and especially with a diffuser in the system. As discussed later, the final arrangement uses a scatter-plate system with a ruby laser operating in many axial modes but with an improved spatial coherence by using a pinhole mode selector (2.8).

3.9.2 The spatial frequency of the available photographic emulsion

This determines the design angle, or the angle between the reference

and the object beams by the relation

$$2\,d \sin\theta = \lambda$$

where d ≡ fringe separation.

If p is the spatial frequency of the emulsion then the maximum value of θ is given by

$$\theta = \sin^{-1}\left(\frac{\lambda}{2} \cdot \frac{1}{d_{min}}\right) = \sin^{-1}\left(\frac{p\lambda}{2}\right)$$

If a large design angle is desired, allowing a larger range of viewing angles, then high resolution plates have to be used. The exposure time of the emulsion goes up as p^2 for moderate p, since the number of resolvable points per unit area in two dimensions goes up as p^2. Thus a larger light energy would be needed to produce a given exposure. For very fine-grain emulsions used in holography, the penalty may be even higher in practise than in theory, the exposure time going up as p^4. Recently sufficiently fast high resolution plates have been developed and their characteristics will be discussed in the next chapter.

3.9.3 The desired range of viewing angle

This is limited by the coherence length of the laser. As the angle subtended by the photographic plate on the object determines the field of view, the path differences of various rays reaching the former should be within the coherence length.

3.9.4 Vibrational stability of the system

Any vibrations in any of the components of the holographic set-up during the exposure time would cause a loss of resolving power of the reconstructed image or the image itself might be completely lost due to the loss of diffraction pattern. This poses severe problems with He-Ne laser holography where exposure times are relatively long, but the system is generally free from vibrations during the exposure time with

pulsed lasers. In either case the lateral tolerance can be taken to be quarter of the fringe spacing in order to retain a sharp set of fringes at the photographic plate. If the angle between the reference beam and the scattered light from the object is θ, then the lateral tolerance δx, is[34]

$$\delta x \leq \frac{\lambda}{4 \sin \theta}$$

To calculate the longitudinal tolerance δZ, it must be realized that the change of angle between the reference beam and the scattered light from the object reaching the bottom of the photographic plate must be such as to cause less than quarter period shift in the fringes. This gives,

$$\delta Z \leq \frac{\lambda}{4 \sin 2\theta \tan \theta} = \frac{\lambda}{8 \sin^2 \theta}$$

Thus it can be seen that a larger design angle reduces both these tolerances. These tolerances are of the order of a fraction of the wavelength of light being used.

Although the system is free from vibrations in the duration of the ruby laser pulse, in a double exposure hologram any vibrations in the duration between the two exposures can alter the behaviour of the hologram reconstruction. The effect of these vibrations is distinct from the ones where the vibration is during the exposure time of the hologram. The reason is that in the former each of the two 'holograms' of the double exposure would be perfect but only displaced with respect to each other due to any motion between the two exposures. Hence it will produce a background fringe pattern in the field of the desired interferogram; while in the latter case, it is the actual diffraction pattern constituting the hologram that is lost. This is the reason that the tolerances on vibration are so severe in this case. In the double exposure case, it is virtually impossible to destroy the diffraction pattern by superposing on it a pattern slightly displaced by vibrations, except in the case when

the diffraction pattern constitutes a grating. Indeed it is the superposition of a slightly 'distorted' pattern on the 'undistorted' one which produces the interferogram. Only the basic precautions of not knocking against the set-up etc. are required to avoid the formation of the background fringe pattern in the field of the interferogram.

Sometimes it is desirable to produce such a background pattern to increase the sensitivity of measurements of the fringes caused by the disturbance in one of the exposures. Moreover it allows the determination of the direction of fringe shifts. This will be discussed in section (6.5.4) where an actual situation is described.

It can therefore be safely concluded, that the choice of the actual set-up will be partly determined by its capability to resist vibrations - or its immunity to them. A system with the minimum number of optical components and all mounted on one optical bench, if possible, would thus seem to be the best choice. The most suitable set-up for holographic interferometry is thus the one which satisfies all the above criteria of stability, coherence requirements etc. The scatter-plate interferometer originally described by Burch[35] has been adapted for such an application and is the simplest and least demanding of all the holographic set-ups. This will be described and discussed in the next chapter.

References

1) A.H. Bennett, H. Jupnik, N. Osterberg and O.W. Richards, "Phase Microscope", John Wiley & Sons Inc. New York 1951.

2) D. Gabor, "Microscopy by Reconstructed Wave-Fronts", Proc. Roy. Soc. (London) A197, 454 - 487 (1949).

3) D. Gabor, "Microscopy by Reconstructed Wave-Fronts, II", Proc. Phys. Soc. B64, 449 - 469 (1951).

4) H.M.A. El-Sum, "Reconstructed wavefront microscopy". Ph.D Thesis, Stanford University, 1952 (Dissertation Abstracts 4663, 1963).

5) E.N. Leith and J. Upatnicks, "Reconstructed wavefronts and communication theory", J. Opt. Soc. Am. 52, 1123 (1962).

6) B.J. Thompson, "A New Method of Measuring Particle Size by Diffraction Techniques", J. Appl. Phys. 4, 302 - 307 (1965), Suppl. I.

7) J.B. DeVelis, G.B. Parent Jr. and B.J. Thompson, "Image reconstruction with Fraunhofer holograms", J. Opt. Soc. Am. 56, 423 (1966).

8) G.W. Stroke and D.G. Falcones, "Attainment of High Resolutions in Wavefront Reconstruction Imaging", Phys. Letters 13, 306 - 309 (1964).

9) R.P. Dooley, "X-Band Holography", Proc. IEEE 53 (11), 1733-1735 (1965).

10) D.E. Duffy, "Optical Reconstruction from Microwave Holograms", J. Opt. Soc. Am. 56, 832 (1966).

11) K.S. Pennington and L.H. Lui, "Multicolour wavefront reconstruction", Appl. Phys. Letters 7, 56 - 57 (1965).

12) G. Cochran, "New Method of making Fresnel Transforms with Incoherent Light", J. Opt. Soc. Am. 56, 1513 (1966).

13) A. Lohmann, "Wavefront Reconstruction for Incoherent Objects", J. Opt. Soc. Am. 55, 1555 - 1556 (1965).

14) J.M. Burch, J.W. Gates, R.G.N. Hall and L.H. Tanner, 1966a Nature, London, 212, 1347-8.

15) G.W. Stroke and A.E. Labeyrie, Phys. Letters 20, 157 (1966).

16) K.A. Stetson and R.L. Powell, J. Opt. Soc. Am. 56, 1161 (1966).

17) L.O. Heflinger, R.F. Wuerker and R.E. Brooks, J. Appl. Phys. 37, 642 (1966).

18) F.C. Jahoda, R.A. Jeffries and G.A. Sawyer, Appl. Opt., 6, 1407 (1967).

19) De Manoranjan and Leandre Sevigny, Appl. Opt. 6, 1665, 1967.

20) G.L. Rogers, Nature 1950, 166, 237.

21) G.W. Stroke, An Introduction to Coherent Optics and Holography, Academic Press Inc. N.Y. and London, 1966.

22) R.W. Meier, "Magnification and third-order aberrations in holography", J. Opt. Soc. Am. 55, 987-992 (1965).

23) E.N. Leith, J. Upatnick and K.A. Haines, "Microscopy by wavefront reconstruction", Ibid p.981 - 986.

24) J.B. DeVelis and G.O. Reynolds, "Theory and Applications of holography", 1967, Addison-Wesley Inc. (pp. 77 - 78).

25) D. Gabor, Proc. Roy. Soc. (London) A 197, 483 (1949).

26) E. Wolf, Physics Letters 3, 166 (1963).

27) M. Born and E. Wolf, "Principles of Optics" (2nd ed.), Pergamon Press, New York (1964).

28) M.J. Beran and G.B. Parrent Jr. "Theory of Partial Coherence", Prentice-Hall Inc., Englewood Cliffs, N.J. (1964).

29) G.O. Reynolds and J.B. DeVelis, "Hologram coherence effects", J. IEEE Trans. AP - 15, 41 (1967).

30) L. Mandel, "Wavefront reconstruction with light of finite coherence length", J. Opt. Soc. Am. 56, 1636 (1966).

31) M. Bertolotti, F. Gori and G. Guattari, "Coherence requirements in holography", J. Opt. Soc. Am. 57, 1526 (1967).

32) M. Lurie, "Effects of partial coherence on holography with diffuse illumination", J. Opt. Soc. Am. 56, 1369, (1966).

33) P.S. Considine, "Effects of coherence on imaging systems", J. Opt. Soc. Am. 56, 1001 (1966).

34) G.L. Rogers, J. Sci. Instr. 43, 677, (1966).

35) J.M. Burch, Nature 171, 889 - 90, (1953).

36) L.H. Tanner, J. Sci. Instr. 2, 288, 1969.

Chapter 4

Scatter-plate System for Holography - and Related Experimental details

4.1 Introduction

The hologram is essentially made by providing part of the illumination as a coherent reference wave which interferes in the plane of the photographic plate with the object beam. Techniques of holography mainly differ in the method by which the beam splitting is achieved.

It is easy to achieve these rays by straight forward division of amplitude or division of wavefront. As first pointed out by Lieth and Upatneiks [12], one can also use a partly diffusing "scatter-plate" as a beam splitter to an advantage when taking holograms of smooth transparent or reflecting objects. The unscattered portion of the transmitted light then serves as a reference beam and the scattered portion provides a conveniently diffuse illumination for the object, thus avoiding the need of a separate diffuser.

The use of a diffuser imposes the restrictions that a laser with output having large coherence length must be used. This being so because the diffuser makes the rays pass at a variety of angles causing the rays reaching the photographic plate to have large path differences which may exceed the coherence length of the laser. Moreover, if the output of the laser has many transverse modes, the degree of spatial coherence may be fairly low giving rise to a loss in contrast of interference fringes on the photographic emulsion and hence a poor quality of reconstructed image.

As mentioned earlier these problems can be resolved either by mode controlling the ruby laser output or by choosing a system which relaxes the requirements of coherence. Since the methods of controlling the modes work only at the expense of considerable loss of power and energy of the output pulse, it would therefore be preferable to follow the latter course. Scatter-plate system introduced by Burch [1] as a transmission interferometer and later adopted by Burch et al. [2] for holography of pure phase objects allows the use of partially coherent light. The conditions are completely relaxed only in the case of perfect optical components being used in the system. The method is described and analysed for its image forming characteristics. The estimation of various tolerances is made within which the system can work with minimum demands on coherence. Finally details of various aspects of actual experimental setup are given.

4.2.1 Description of the optical setup.

The general layout of the system is given in Fig. (4.1). The output beam from the ruby laser is expanded to fill the aperture of the scatter-plate 5 which is placed in the focal plane of lens L_3. Displacement of lens L_2 in its own plane provides a ready means of placing the focus F of the unscattered reference beam anywhere within the field of view of the system. The scatter-plate S allows part of the incident light to be transmitted, and scatters the remainder in a random fashion over the whole aperture of the lens L_2. Lenses L_3 and L_4 image the scatter-plate S onto the photographic plate S^I, so that both the scattered and unscattered

light originating at any given point of S will be recombined at a conjugate point in S^1. If there are no large path differences between the alternative paths - which are well within the coherence length of the ruby laser output - the resultant amplitude at S^1 will be determined by the phase differences between each of the possible paths in the scattered beam and the path in the unscattered beam. An object O with an absorbing or phase shifting distribution will effect the interference pattern at S^1 according to the differential effect of absorption or phase shift on the scattered and unscattered beams. A true distribution due to the object alone will be obtained if the unscattered beam is unaffected by the object and acts as a constant reference beam. This is easily achieved by offsetting the reference beam to be clear of the object region as shown in Fig. (4.1a). A collimated beam incident obliquely at the scatter plate forms a point image at F which is clear of the object O.

4.2.2 One can arrange the system either with a symmetrical or a non-symmetrical configuration. In the former case the seperation of lenses L_3 and L_4 is equal to 2f where f is the focal length of each lens. The scatter-plate and the photographic plate are both at the focal planes of the two lenses, and the other focal planes of each lens coincide and contain F. The object O is located in and around the plane of F, which is the Fourier-Transform plane of the lenses L_3 and L_4 with respect to S and S^1 respectively. Light scattered by a point of the object lying in or near the plane of the reference point F then spreads over the whole area of the hologram. Since collimated light is being used in this case for the reference beam, its use in the reconstruction will provide the image with unit magnification.

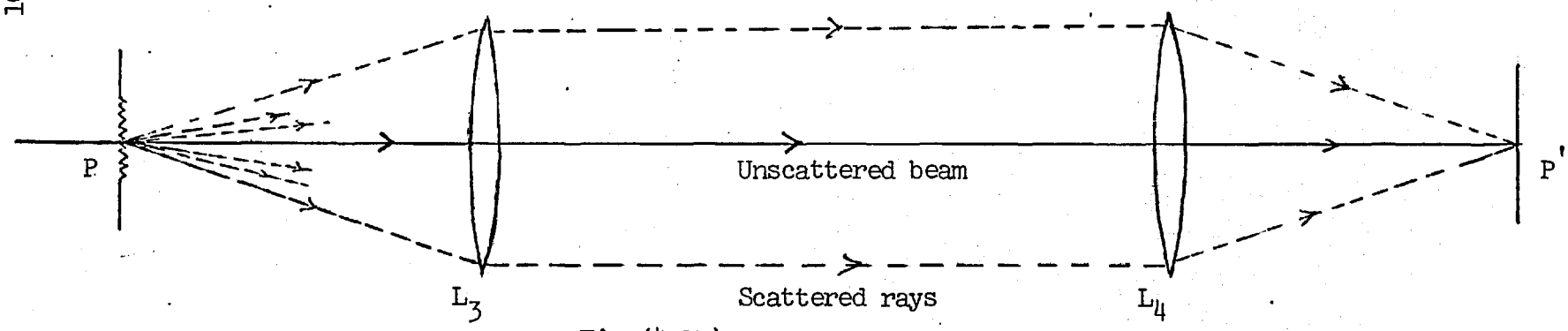

Fig (4.1b)

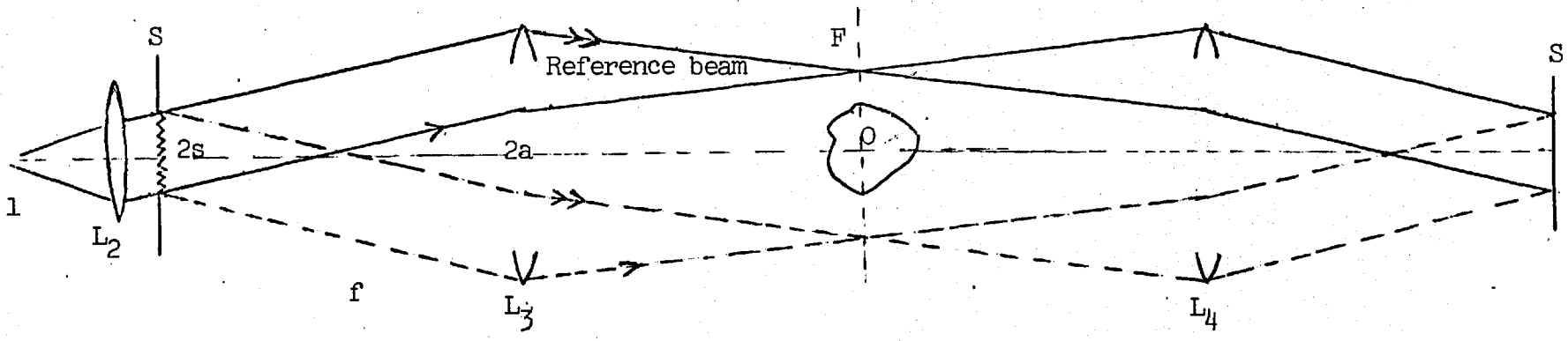

Fig(4.1a) Scattered Plate Arrangements.

In the non-symmetric configuration, the lenses L_3 & L_4 are no longer seperated by a distance 2f and the magnification of the reconstructed image depends on the wavefront curvature of the illuminating beam. As discussed later, the symmetric configuration is an optimum one for resolution and contrast of the image.

4.2.3 The Criteria determining the size of the optical system and the required size of the hologram are established by considering a) the coherence length of the ruby laser output, b) the object size and c) requirements of the axial resolution of the reconstructed image.

The collimated reference beam filling the aperture cross-section of the scatter screen of dia 2s will completely pass the lens aperture of diameter 2a, if the incident beam makes angle equal to or smaller than $\frac{a-s}{f}$, when f is the focal length of the lenses. The reference beam will be focused in the plane of F at a distance (a-s) from the axis. Thus the maximum diameter of the central transverse plane of the object which can be fully illuminated is 2(a-s).

4.2.4 The extent to which points spaced axially can be resolved in the reconstructed image will depend primarily on the degree of angular convergence of the illumination. At a point in the plane of F, the semi angle of the cone of maximum convergence is $s/_f$, and is directly proportional to the size of the scatter-plate, 2s. Better discrimination is obtained if the size of the scatter-plate is increased retaining the same focal length lenses. But if the aperture of the lens diameter 2a is not increased at the same time, increasing the size of the scatter-plate will necessitate an inward shift of the

position of the reference point F reducing the size of the object field 2 (a-s). Thus a compromise between the field size and depth discrimination must be made.

4.2.5 To determine the extent of the field of view in the reconstruction that this system affords, it can be seen that the extreme sets of collimated rays illuminating the object are those that originate from the extreme points on the scatter-plate. This gives an angular field of $\frac{2s}{f}$. Thus eventually one has to settle for small f - value lenses to allow a large range of viewing angles and large depth discrimination.

4.3.1 Effect of lenses L_3 and L_4 on image formation and reconstruction.

The scatter-plate system is supposed to have minimal demands on coherence and should be able to produce hologram of a pure phase object even with incoherent light. But this is true only with perfect optical components which are free of aberrations. There are two distinct problems which must be taken into account. The first deals with the influence of lens aberrations on the formation of the hologram and consequent criteria of a certain degree of coherence as a result of these aberrations. The second is that of the influence of these lens aberrations on the quality of the reconstructed image of a) a hologram and b) a holographic interferogram. The two problems are discussed in the following.

4.3.2 Effect of Lens aberration on hologram formation.

The two of the five monochromatic aberrations that are of importance in this case are spherical aberration

and coma. For the ideal working of the system, all the scattered rays originating from a point on the scatter-plate should converge to a conjugate point on the photographic plate. Due to the spherical aberration, these rays however will not meet at a common point. If the illumination is incoherent or partially coherent from spatial point of view with a certain coherence interval, it becomes necessary to examine the criteria for these rays to produce interference fringes on the photographic plate for the given degree of coherence.

As seen in Fig (4.1b), even if p is illuminated with incoherent light of zero coherence interval, the rays will still be able to interfere at p' in perfect optical systems, as they originate from the same point source. For the analysis of the imperfect system we consider the effect of lens L_4 in Fig (4.1). The longitudinal spherical aberration of L_4 is given by

$$\text{Long s.a.} = F_p - F_m$$

where F_p and F_m are the paraxial and marginal focal lengths respectively. If θ_m is the angle the marginal rays make with the axis, then the maximum spread of the rays on the photographic plate is given by, as seen in Fig (4.2):

$$\delta x = (F_p - F_m) \tan \theta_m \qquad (1)$$

Thus only some of the rays which are im the paraxial region will be able to interfere with each other and produce a hologram. This in turn will on reconstruction, recreate only the paraxial region of the object field. The non-paraxial rays from a single point on the scatter-plate will not interfere with each other. These will however, interfere

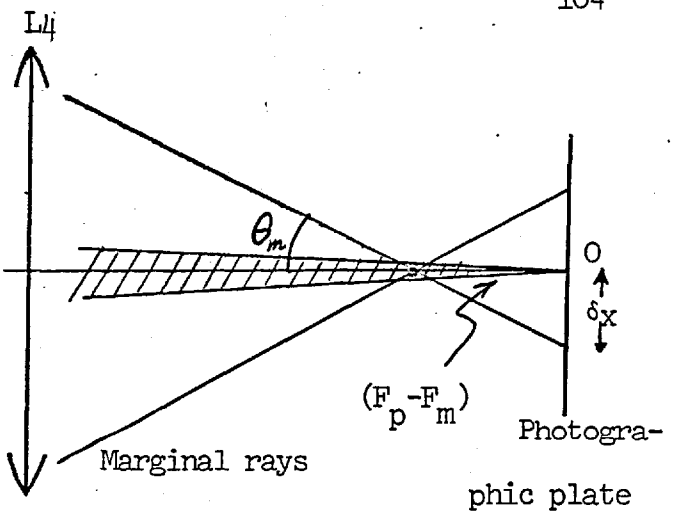

Fig (4.2)

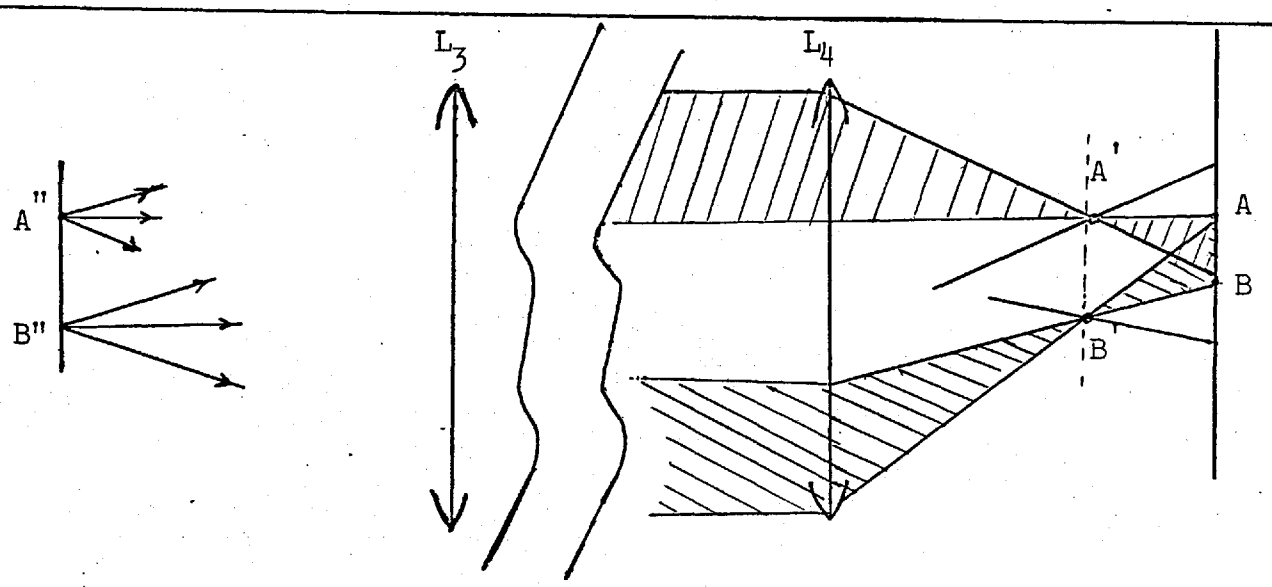

Fig (4.3)

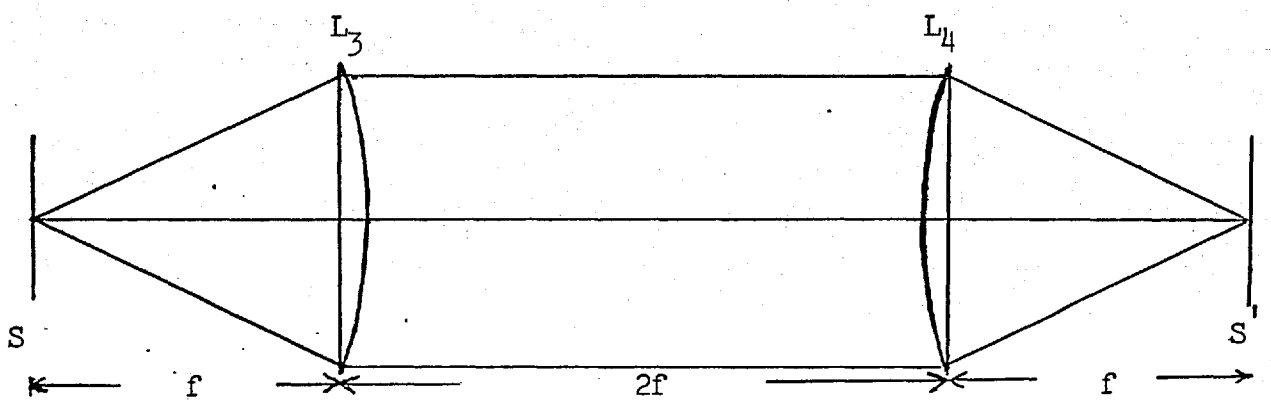

Fig (4.4)

with rays from adjacent scattering points as seen in Fig (4.3). The radius of the circle around the point P on the scatter-plate having such scatterers will depend on the value of the spherical aberration. Since such points are very close to each other, we can assume

$AB \simeq A'B' \simeq A''B''$.

where A" and B" are the two points on the scatter-plate giving rise to the two image points A' and B'. As can be seen in Fig (4.3), only part of the rays in each of the light cones starting from A" and B" are able to overlap. Thus on reconstruction only the shaded region of the object field will be reconstructed. If we demand that the image in at least half the cone angle should be reconstructed the rays within it must be able to interfere with each other. To do this they must i) overlap with each other and ii) the overlap region must be due to the points A" and B" lying within the coherence interval x_c of the radiation.

A larger spherical aberration will allow the same overlap of illumination from points A" and B" with larger seperation. This is because both $(F_p - F_m)$ and θ_m get larger and hence δx will also get larger. When x_c is smaller than δx, the rays will be able to cause interference only within an element x_c and will merely fog the photographic plate outside this region. Thus for a given coherence interval larger spherical aberration of L_3 will merely cause a larger spread of the beams and hence a larger waste of light. This would effectively reduce the contrast of the interference fringe pattern on the photographic plate and hence a poor quality of the reconstructed image. Moreover, it must be mentioned again that this partial overlap and interference

of a limited portion of the cone of illumination will cause only a limited region in the object field to be reconstructed. Although these regions will be complimentary to those recreated by paraxial rays but the overall contrast and resolution of the reconstructed image will be smaller than that obtained in the case of aberration free optics. As pointed out earlier, this loss of contrast is mainly due to the overlap between rays being partial and consequently a fogging of the photographic plate causing a higher 'noise' level.

As a typical example, the spherical aberration of a plane convex lens is considered for the system used with normal ruby laser operation. From thin lens formula (3), the spherical aberration for the lens having focal length = 25 cms and diameter = 6.3 cms, is calculated to be 0.42 cms. Thus using Eq. (1) we have

$$\delta\chi = \text{(longitudinal spherical aberration)} \times \tan\theta = 0.42 \text{ (cms)} \times 0.12 = 504\mu$$

Typical measurements of Collins et.al. (4) indicate a coherence interval of 50μ in the output of a ruby laser without any mode control. Thus it can be seen that a reasonably large amount of radiation will fall outside the coherence interval and hence will be wasted. This will contribute to the noise level of the interference

fringes due to adjacent points and will thus degrade the contrast.

4.3.3 It must be mentioned in passing that a similar action will happen even in the case of aberration free lenses if there is a certain defect of focus. One can easily estimate the amount of the allowed defect of focus for a given coherence interval. Again assuming overlap to be at least for half of the total spread of rays, the defect of focus that can be tolerated is

$$\delta z = x_c / \tan \theta_m \qquad (2)$$

where θ_m = angle the marginal rays make with the axis.

δz = defect of focus in the direction of beam propagation.

For $x_c = 50\mu$ and $\tan \theta_m = 0.12$
we get $\delta z = 416\mu$

The condition is considerably relaxed if the spatial coherence of the ruby laser is improved. Although Collins et. al.'s value is only a typical one, other workers (5) have indicated that there is a partial degree of spatial coherence over the entire surface of the emitted wavefront. However, the value of the parameter for the complex degree of coherence is much less than unity. Although one gets interference fringes even with a defect of focus larger than the value estimated above, the contrast of these fringes is generally poor.

4.3.4 The effect of coma is very similar to that of the spherical aberration discussed in the previous sections. The effect of the spherical aberration was a longitudinal defocus of the rays passing through the outer zones of

the lens. This resulted in a symmetrical spread of the rays reaching the photographic plate around the axial ray. In the case of coma there is a transverse spread of the rays but only to one side of the axial ray. Moreover this transverse spread is not uniform but is three times larger for tangential rays as compared to that for sagittal rays. This merely adds to the problem discussed above as it causes the spread of the rays to be larger than that with spherical aberration only. For a fixed coherence interval, the amount of light spilling over this interval is larger with a consequent reduction of contrast of the interference fringes. However looking carefully it turns out that the contribution of coma to the angular spreading of the rays by spherical aberration is very small. The radius of the comatic circle is an index of this contribution (3) and for the lens mentioned above is only 3μ. This is very small compared to the spread of 540μ due to the spherical aberration of the same lens and can thus be neglected.

4.3.5 Although one would like to have a light source having a large degree of spatial coherence, a simpler first alternative would be to choose lenses with smaller aberrations. Each lens is characterized by its shape factor . The minimum spherical aberration and coma occur for lens with a shape factor q = + 0.7. The third-order theory shows (3) that the plano convex lens with q =+ 1 is very near to the minimum value of spherical aberration. Thus the scatter-plate system will have minimum aberrations when two such lenses are used with the plane surface of each facing the scatter-plate and the photographic plate as shown in Fig. (4.4).

4.3.6 Influence of the imaging optics on the quality of the reconstructed image.

In this section the influence of imaging optics on the resolution of the reconstructed image will be examined. Moreover any distortions introduced in the image by lens imperfections will also be considered. The problem depends on the nature of the object under study. For transparent diffusing or scattering objects, one can obtain both a hologram and an interferogram whereas for a pure phase object the latter has to be employed to render it visible.

Since holographic system using a double exposure technique acts as a common path interferometer, any aberrations in the optics have no contribution to the reconstructed interferogram as the aberrations do not change between the two exposures. Thus no matter how poor the quality of the lenses may be, the reconstructed interferogram will be completely free of distortions as it is produced only by the change of refraction index in the object region between the two exposures. Since we have a transparent, non-scattering object, the lenses are merely being used to 'channel' the reference and the object beams to their proper course. The lens L_4 is NOT focusing the object onto the photographic plate and hence its transfer function does not enter into the discussion of the resolution of the reconstructed image.

As regards the contrast of the interference fringes in the interferogram of the object, it would depend on the relative intensity of illumination in the two exposures, being maximum when it is equal in both cases.

4.4.1 Effect of the photographic emulsion on the reconstructed image of holograms.

Since the hologram is a photographic record of the interference pattern produced by the interaction of coherent reference beam and the object beam, characteristics of the photographic emulsion and the photographic processing involved is bound to effect this record. Consequently the characteristics of the reconstructed image will be influenced by the emulsion. In general the emulsion will influence the holographic process in the following manner.

1) The spatial frequency of the photographic emulsion sets the limit to the frequency of information which it can store and has an upper cut off frequency beyond which it does not register the information.

2) The emulsion does not respond equally to various frequencies of information and the curve giving this characteristic response versus frequency is the transfer function of the emulsion.

3) The emulsion processing determining the γ of the photographic emulsion also effects the resolution of the reconstructed image.

Many workers (6,7,8) have described the behaviour of photographic emulsions in terms of simple models. A simplified model by Kelly [6] explains the essential features of emulsion effects and its results are briefly described in the following.

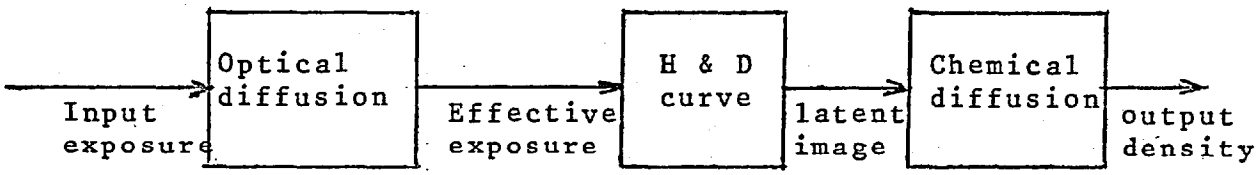

Kelly's film model

Fig. (4.5)

Light falling on an unexposed photographic emulsion is not only absorbed, reflected, and transmitted, but also scattered. It is therefore necessary to distinguish between (a) the optical image which would be measured by a microphotometer in place of the film, and (b) the optical image which usually renders the grain developable; the latter is a somewhat 'blurred' version of the former. The images may be regarded as respectively, the input and output of the first stage of the proposed model. Since first stage effects precede the formation of the latent image, they do not depend in any way on the subsequent chemical development; this is why the output from the first stage is called the effective exposure. The optical diffusion term is dependent on the spatial frequency of the plate. The transfer function of optical diffusion influences the amplitude transmittance of the hologram. As shown by Van Lighten [9] this merely causes small alterations in amplitude, phase and resolution properties of the reconstructed image and is not very important.

The second stage of the model represents the conversion of exposure to emulsion density using the conventional H-and D-characteristics of the emulsion. The third stage represents the space-dependent effects of the development process namely the chemical diffusion. This is made uniform over the plate by its continuous agitation during the development process.

Van Lighten [9] has derived quantitative expressions for the reconstructed images showing the influence of the various terms of the Kelly's model. These expressions for the zero-order background term and the real and virtual images R_1 (Y) and R_2(Y) respectively are given below.

$$R_o\ (Y) \propto K^{-\gamma/2}$$

$$R_1\ (Y) \propto -\frac{\gamma}{2} K^{-\gamma/2} \int_{-\infty}^{+\infty} \sigma\ (v)\ T(v - mK_1)\ e\ iv(y - m/z|)\ dv$$

$$R_2\ (Y) \propto -\frac{\gamma}{2} K^{-\gamma/2} \int_{-\infty}^{+\infty} \sigma\ (v)\ T\ (v + mK_1)\ e + iv\ (y - m/z|)\ dv$$

$$- (3)\ dv$$

Y being the coordinate in the image plane.
K is the effective exposure time. The other terms are defined in the above mentioned reference. The basic assumption involved in the above derivation is that the intensity of the reference beam is larger than that of the object beam.

4.4.2 Effect of γ of the photographic process.

The factor $K^{-\gamma/2}$ appears in all three images in Eq. (3). This means that as long as the linear portion of the H-& D-curve is used, the exposure influences all three images equally. In R_1 and R_2 γ appears as a linear multiplier factor. Consequently as γ increases, the energy contained in R_1 and R_2 is higher and hence the background image R_o can be made weaker than the real and virtual images.

When $\gamma = -2$, its contribution disappears from all the image terms and the ratio of intensity between reference and the object beams becomes unimportant. However, when γ is chosen arbitrarily, the intensity of the reference beam should be higher than that of the diffracted beam from the object so that the images R_1 and R_2 should have more intensity than R_o.

4.4.3 Effect of film processing on image resolution.

The photographic emulsion is assumed to be processed in the linear range of H & D curve. But if the contrast of intensity distribution of the hologram exceeds the dynamic range capacity of the film, i.e. the maximum and minimum value of exposure of the emulsion exceeds the linear portion of H & D curve, then the density at extremes will reach values such that photographic clipping will occur. This causes a loss of information stored on the film. The transfer function of the film will exhibit a lower resolution limit due to clipping.

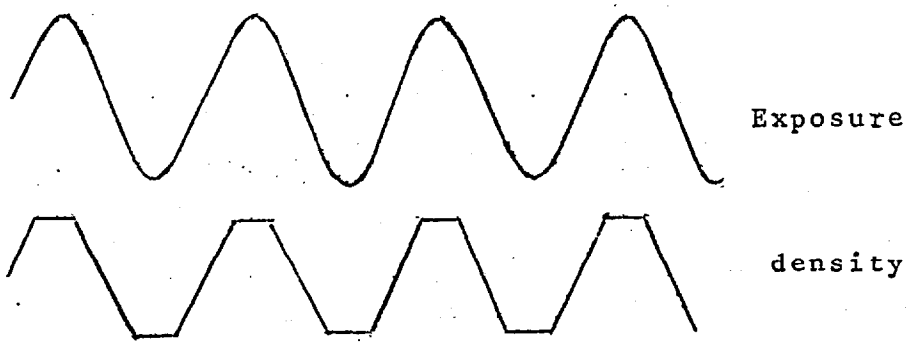

Fig. (4.6)

4.5 The Scatter-plate.

Since the scatter-plate is being used both as a beam-splitter and a diffuser, the unscattered portion of the incident light serves as the reference beam while the uniformly scattered light illuminates the object. As pointed out previously, the intensity of the reference beam should be higher than that of the object beam in order to maintain a linear relationship in the modulation. Although the hologram reconstructs the images for a large range of the intensity ratio of the reference and object beams, a ratio of five or six is the optimum value (10). Since in our work, the object (plasma) does not absorb the radiation, the same ratio will be required between the unscattered beam passing through the scatter-plate and the scattered beam which just fills the area containing the object. Only very finely grounded and polished glass could provide such a ratio of intensity, while the coarser ones scattered almost all the light. One big disadvantage of such a diffuser is that its diffused illumination is not uniform over the whole aperture but is preferential in the forward direction as shown in Fig. (4.7a). This can be

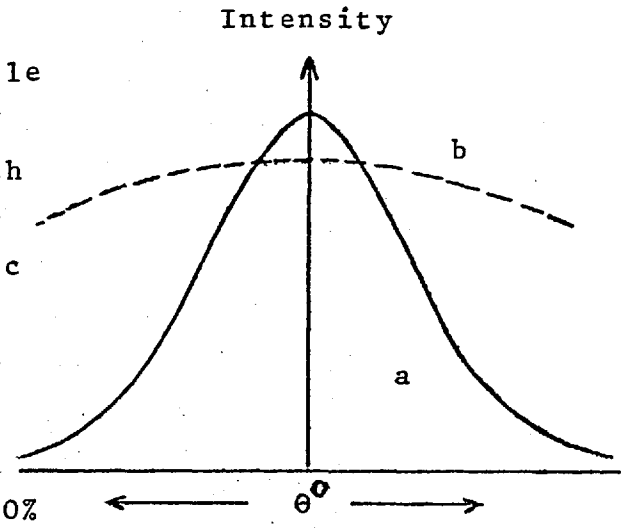

Fig. (4.7)

corrected by placing a variable density filter in the path of the diffuse object beam. Such a filter can be made by exposing a fine grain photographic plate by this illumination and processing to a unit density. When replaced in its original position this graded density filter allows 10 to 20% of the incident radiation and produces a uniform field. However, one of the disadvantages of such a filter is that on reconstruction of the hologram, this filter is also recreated as a background to the object. As suggested by Gates [11], a glass plate smoked with a very thin layer of ammonium chloride acts as a diffuser with a very uniform scattered field shown in Fig. (4.7b). If the plate is lightly smoked, the scattered field is weak but a ratio of about five between unscattered and scattered light can be obtained by properly fuming the plate. If the unscattered light reaching the photographic plate exceeds the desired value, the ratio can always be adjusted by inserting neutral density filters in the path of the reference beam. Such a diffuser was initially used. However, it has the disadvantage that the smoked plate works as a diffuser only for a few hours after which it looses its scattering property.

The above situation was improved by following a much better procedure. The hologram obtained using a diffuser as a scatter-plate will reconstruct the distribution of

illumination in the object field as well as the object if any. The hologram made in the same apparatus without any object using He-Ne laser can therefore be used as a scatter-plate. The amplitude modulating holograms, as obtained after development of the photographic material, allow only a small fraction of the incident energy to go to the wanted image, which is usually only a few percent. This difficulty was avoided by bleaching the hologram (see section 4.7.2). This gave a phase changing structure, almost completely free from absorption, allowing all the incident energy of illumination to go to the reconstructed images. The resulting bleached hologram produced the same uniform scattered field as that of the original scatter. It had the added advantage that it did not absorb the incident light. The hologram produced twin reconstructions when illuminated by the incident radiation whereas only one of these reconstructions acted as the object beam. Thus to obtain an intensity ratio of five between the reference and the object beams, the intensity ratio in the process of formation of the hologram-scatter-plate' had to be adjusted to about 2.5.

The resulting phase hologram-scatter-plate is a permanent sturcture consisting of a thin layer of gelatin. Since it has very little absorption, it remains undamaged even for large intensities of incident radiation from pulsed ruby laser.

4.6.1 Photographic materials for use in holography.

The main criteria for selecting photographic plates for holography is the design angle between the reference

and object beam. This fixes the spatial frequency limit of the emulsion. The emulsions should thus exhibit a high resolution but also high sensitivity in order to reduce the necessary exposure times or intensities respectively. This minimizes the requirements for mechanical stability of the experimental arrangement. High resolution and high sensitivity are to a certain extent contradictory properties. If the grainsize d is large ($d > 0.1\mu$), the emulsion is more sensitive but scatters considerable amounts of light in the layer producing a somewhat diffuse image. Moreover, a reduction of the resolution is caused by the grainness of the image. If the grainsize is reduced ($d < 0.1\mu$) it reduces the scattering and grainness but also causes a loss of sensitivity. Although some photographic emulsions having high resolution existed before, these were extremely slow. Recently Agfa-Gevaert have developed emulsions especially for holography which meet the two requirements. The following table gives the list of various emulsions currently in use in holography.

4.6.2 Agfa-Gevaert Limited.

Ruby Laser wavelength 6943Å

plate	optimum exposure	spatial frequency	thickness of emulsio
8E 75	200 ergs/Cm^2	3000 lines/mm	7μ
10E 75	50 ergs/Cm^2	2800 lines/mm	7μ (on plate)
14C 75	3 ergs/Cm^2	1500 lines/mm	5μ

(The number at the left of the letter E (or C) indicates the speed, while that at the right side indicates the spectral response).

He-Ne laser wavelength 6328Å

8E70	200 ergs/Cm^2	3000 lines/mm	7μ
10E70	50 " "	2800 " "	7μ
14C70	3 " "	1500 " "	5μ

Argon laser wavelength 4880Å and 5145Å

10E56	50 ergs/Cm^2	2800 lines/mm	7μ

4.6.3 Kodak Limited.

649-F	1500 ergs/Cm^2	2200 lines/mm
V1061-F	375 " "	1000 " "
V1043-F	-	-
Kodalith Pan	50 ergs/Cm^2	200-500 lines/mm

The letter F indicates a near infra red sensitization of the emulsion. Agfa-Gevaert plate type 10E75 is about 30 times faster than 649-F for the same ruby laser exposure. Since Kodak V1061-F is about half in resolution than 649-F, it is therefore four times as fast compared to the latter.

4.6.4 To get an idea how the laser power that is required tc produce a given exposure is related to the sensitivity of the emulsions mentioned above, a typical example is considered. The photographic plate 10E75 with a size 9 x 12 Cm^2, needs light energy of ~ 50 x 110 = 5500 ergs

for optimum exposure. For a laser pulse of 55 n secs duration, this corresponds to a power of 10 K Watts. This is much less than the power of about 1 M Watt easily obtainable from ordinary Q-switched ruby lasers. A narrow pulse width for better time resolution is obtained only at higher pumping energies and hence larger output powers. Thus even very high resolution plate 8E75 will be amply sensitive to the available light energy.

4.7 The Photographic process.

4.7.1 Development.

The parameter of interest in observing the reconstructed image of a hologram is the amplitude transmission defined as the ratio of the amplitude of the reconstructing wave after and prior to penetration of the photographic layer. The curve of amplitude transmission T_a vs exposure E is thus a better representation of a hologram than the density vs log (exposure) representation of H- and D-curve in normal photography. This is because the holographic process requires linearity between the exposure and the resulting amplitude transmittance of the hologram (10, 12, 13).

The slope of T_a vs E curve is different for different developers for a particular emulsion. Friesem et. al.[14] have plotted these curves for D11, D-19, Dektol 1.1 and other developers for 649-F plates. The slope and linear range of these curves differ by considerable amounts for various developers. It was found that D-19 with a developement time of 5 minutes gave the best results, with

quite a steep slope of T_a - E curve and only a small amount of chemical fog.

Fixing. It was done in the usual manner in Hypam fixer for a period of about 2-3 minutes.

4.7.2 Bleaching.

As indicated in section 4.5. , hologram is bleached to get a phase modulating structure. The holograms of phase objects are also bleached where it is desirable to obtain a higher brightness in the reconstructed images. The bleaching process removes the dense silver from the hologram and leaves the gelatin with no light absorbing medium present. The emulsion then merely has variations in gelatin height proportional to the original density of silver. Any wavefront passing through this emulsion then experiences a phase shift depending on the differences in gelatin thickness and also on the differences, if any, in the refractive indices of the tanned and untanned areas. In 649-F type bleached emulsion, these refractive indices changes are negligible compared to the height differences. Thus the phase changes produced by the emulsion will depend principally on its height.

4.7.3 The dense silver can be removed or bleached from the plate by several bleaches or reducers. The criterion for a better bleacher is that it produces a larger height of the gelatin (called relief image). Altman [15] has measured the height of relief images for Kodak Bleach Bath R-9 and R-10. The height of the relief image for

bleaching with R-10 solution was 3 μ when the silver density was 4.0. The process of bleaching described by Altman [15] causes the resolution of the images to degrade very much although the brightness of the image is very good.

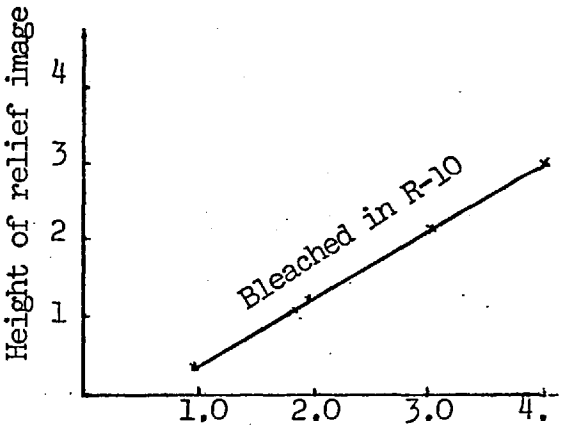

Fig. (4.8)

4.7.4 A modified formula by Russo et. al.[16] and also used by the author gave an image of much better resolution. The procedure and the formula of the Kodak bleach bath R-10 and the modification to it is decribed below.

Original Kodak Bleach Bath R-10.

1 Part solution A
1 Part solution B
10 Parts of water

Solution A.

Distilled water 500 ml
Ammonium bichromate 20 grams
Concentrated sulfuric acid 14 ml
Distilled water to make 1 litre

Solution B.

Sodium chloride 45 grams
Distilled water to make 1 litre

Modifications.

1 Part solution A, one tenth part solution B, 10 parts water.

4.7.5 Procedure.

1. The sample was developed in D-19 b (or D-19) developer for 5 minutes at 20°C with continuous agitation.
2. Washed in running water for 10 minutes (18-21°C)
3. Bleached in modified Kodak Bleach Bath R-10 for 2 minutes at 20°C.
4. Washed for 4 minutes in running water at 18-21°C.
5. Fixed in Hypam rapid fixer for 5 minutes at 20°C.
6. Washed for 15 minutes in running water at 18-21°C.
7. Dried in still air at room temperature (to avoid cracking the gelatin).

This procedure using the modified bleacher gave a resolving power of 1200 lines/mm (against 750 lines/mm without unmodified formula).

It was experienced by the author that in some cases, if the hologram was bleached before fixing, the image in the reconstruction was lost and one got only a diffused field. However, if the bleaching was performed after fixing and drying the hologram, good images could be obtained in the reconstruction. This could be due to the fact that in a plate already fixed and dried, the profile of the gelatin remains, most probably, unchanged by bleaching. In this latter case, the resolving power was also improved.

4.8 Conclusions.

The following conclusions about the practical aspects of the system can be drawn from the discussion so far.

1) The diameter 2S of the scatter-plate and the aperture 2a of the lenses L_3 and L_4 (Fig. 4.1), should be chosen so that (2a-2S) is greater than or equal to the object size to be explored.

2) The lenses L_3 and L_4 are chosen to be plane convex for the spherical aberrations to be minimum. The system being arranged as shown in Fig. (4.4), with the plane surfaces of the lenses facing the scatter-plate and photographic plate respectively.

3) The scatter-plate can be made by obtaining a hologram in the scatterplate system of an ammonium chloride smoked plate acting as a uniform scatterer. One obtains a pure phase modulating structure by bleaching this hologram which acts as a non-absorbing scatterer with the desired properties.

4) The system will give good holograms of pure phase objects with unmode controlled ruby laser. If, however, the wavefronts are deviated or distorted by introducing a cylindrical glass tube (plasma tube)(see 6.5.3), the spatial coherence of the ruby laser needs to be improved. As mentioned in Chapter 2, this can be done by using a pinhole mode selector.

5) Agfa-Gevaert plates 10E 75 are the most suitable for use with ruby laser and the developer D19-b (or D-19) has best performance as regards the slope of amplitude transmittance vs exposure characteristics of the hologram.

REFERENCES.

1. Burch J.M. Nature, 171, 889 (1953)
2. Burch, J.M., Gates, J.W., Hall, R.G.N., and Tanner (1966) a, Nature, Lond. 212, 1347-8.
3. Jenkins and White, Fundamentals of Optics (2nd Ed.) McGraw Hill (1951).
4. Nelson, D.F., and Collins R.J. "Spatial Coherence in the output of an optical maser", J. Appl. Phys. 32, 739-740 (1961),
5. Galanin M.D. et. al. "Coherence and directionality of ruby laser radiation". Soviet Phys. J.E.T.P. 16, 249-251 (1963).
6. Kelly, D.H. J. Opt. Soc. Am., 50, 269 (1960).
7. Clark Jones, R., J. Opt. Soc. Am., 48, 934 (1958).
8. Hendenberg, L.O., Arkiv. Fysik, 16, 417 (1960).
9. Vanligton, R.F., J. Opt. Soc. Am., 56, 1, (1966).
10. Kozma, A. J. Opt. Soc. Am., 56, 428, (1966).
11. Gates, J.W.C., Private Communications.
12. Leith, E.N., and Upatnieks, J. J. Opt. Soc. Am. 53, 1377, (1963).
13. Friesem A.A., and Zelanka, R.J.S., J. Opt. Soc. Am. 56, 542, (1966).
14. Friesem A.A., Kozma, A, and Adams, G.F. Appl. Optics, 5, 851, (1967).
15. Altman, J.H., Appl. Optics, 5, 1689 (1966).
16. Russo, V., Sottini, S., Appl. Optics, 7, 202 (1968).

Chapter 5

Refractive Index of a Plasma and the Construction of an Unstabilized Z-Pinch Device

5.1 Introduction

The holographic interferometry is intended to be used to measure electron densities and their distributions in a plasma. This is possible because in a plasma with sufficient degree of ionization the electrons are mainly responsible for the refractive index. In this Chapter various other factors which contribute to the plasma refractive index are described, and an estimation is made of their relative contribution as compared to that of free electrons. In the rest of this chapter the construction and operation of a particular plasma device suitable to be used for holographic interferometry is described. The choice of an unstabilized Z-pinch was made due to its amenability to quantitative measurements. It is imperative to perform side-on measurements because of the excessive refraction of the probing beam in end-on configuration. The conventional interferometry fails to be applied to this geometry due to its excessive demands on the optical quality of the plasma tube. This is exactly where the holographic technique comes to the rescue by completely dispensing with the necessity to use good quality optics. The actual application of this technique to the Z-pinch plasma will be described at length in the next chapter.

5.2 Refractive Index of a Plasma

When the plane polarized ruby laser radiation enters the plasma it comes across free electrons, ions and bound electrons in the various levels of the neutral atom. If there is no magnetic field in the plasma and the effect of collisions between plasma particles is neglected, then the index of refraction of the plasma due to all components is given by[1]

$$\mu = 1 - \underbrace{\frac{n_e e^2}{2 m \varepsilon_o \omega^2}}_{\text{electronic}} + \underbrace{2\pi \alpha_m N_m}_{\substack{\text{atoms or molecules} \\ \text{in ground state}}} + \underbrace{2\pi \sum_i N_i \alpha_i}_{\substack{\text{ions and} \\ \text{excited atoms}}} \qquad - (5.1)$$

where $\alpha \equiv$ polarizability at the laser wavelength per unit of volume.

$N \equiv$ number density of various particles.

n_e and m being the density of the free electrons and the mass of the electron respectively.

5.2.1 Refractive index due to free-electrons

If the non-electronic contributions are neglected, then the refractive index of the plasma due to free-electrons is

$$\mu = 1 - \frac{n_e e^2}{2 m \varepsilon_o \omega^2} \qquad - (5.2)$$

setting

$$\frac{e^2 n_e}{\varepsilon_o m} = \omega_p^2 \qquad - (5.3)$$

we obtain $\mu = 1 - \frac{\omega_p^2}{2\omega^2}$ $\qquad - (5.4)$

Inserting the numerical values of e, m and ε_o, we obtain the refractivity of the plasma due to free electrons as

$$(\mu - 1)_e = - 4.48 \times 10^{-14} \; n_e \; \lambda^2,$$

where n_e in cm^{-3} and λ in cm.

The Eq. (5.4) defines three ranges of operation determined by n_e and λ. These are:-

Case I $\quad \omega > \omega_p$

In this case the refractive index is real and the wave is able to

propagate through the plasma. The reason is that the time period of the incident radiation is smaller than the time period of the readjustment of the plasma. The inertia of the plasma will prevent it from making any appreciable response in the period of the incident radiation

Case II $\omega < \omega_p$

The period during which the electric field changes is long in comparison with that required for the plasma to readjust itself by the motion of the charged particles. Currents are then set up in the plasma so as to exclude the electric field thereby reflecting the incident wave.

Case III $\omega = \omega_p$

This gives the cut off electron density beyond which the plasma becomes opaque to the radiation

we have $$\sqrt{\frac{n_e e^2}{m \varepsilon_o}} = \omega$$

or $$n_{ec} = \frac{m \varepsilon_o}{e^2} \cdot \frac{4 \pi^2 c^2}{\lambda^2} = 2.32 \times 10^{21} \text{ cm}^{-3} \text{ for } \lambda = 6943 \text{ Å} \quad -(5.5)$$

The condition for propagation of the waves through the plasma is then

$$n_e \leqslant n_{ec} = \frac{1.12 \times 10^{13}}{\lambda^2} \text{ cm}^{-3}, \quad (\lambda \text{ in cm})$$

5.2.2 The effect of collisions

In the above discussion the effect of collisions was assumed to be negligible. This implies the plasma to have an infinite conductivity. But all laboratory plasmas have a finite resistivity and the electron-ion collisions modify the value of the refractive index. This is because the collisions of electrons with positive ions and neutral atoms is equivalent to a viscous damping of the electrons proportional to the electron velocity. In this case the refractive index is given as[2]

Fig (5.6) The Plasma Tube.

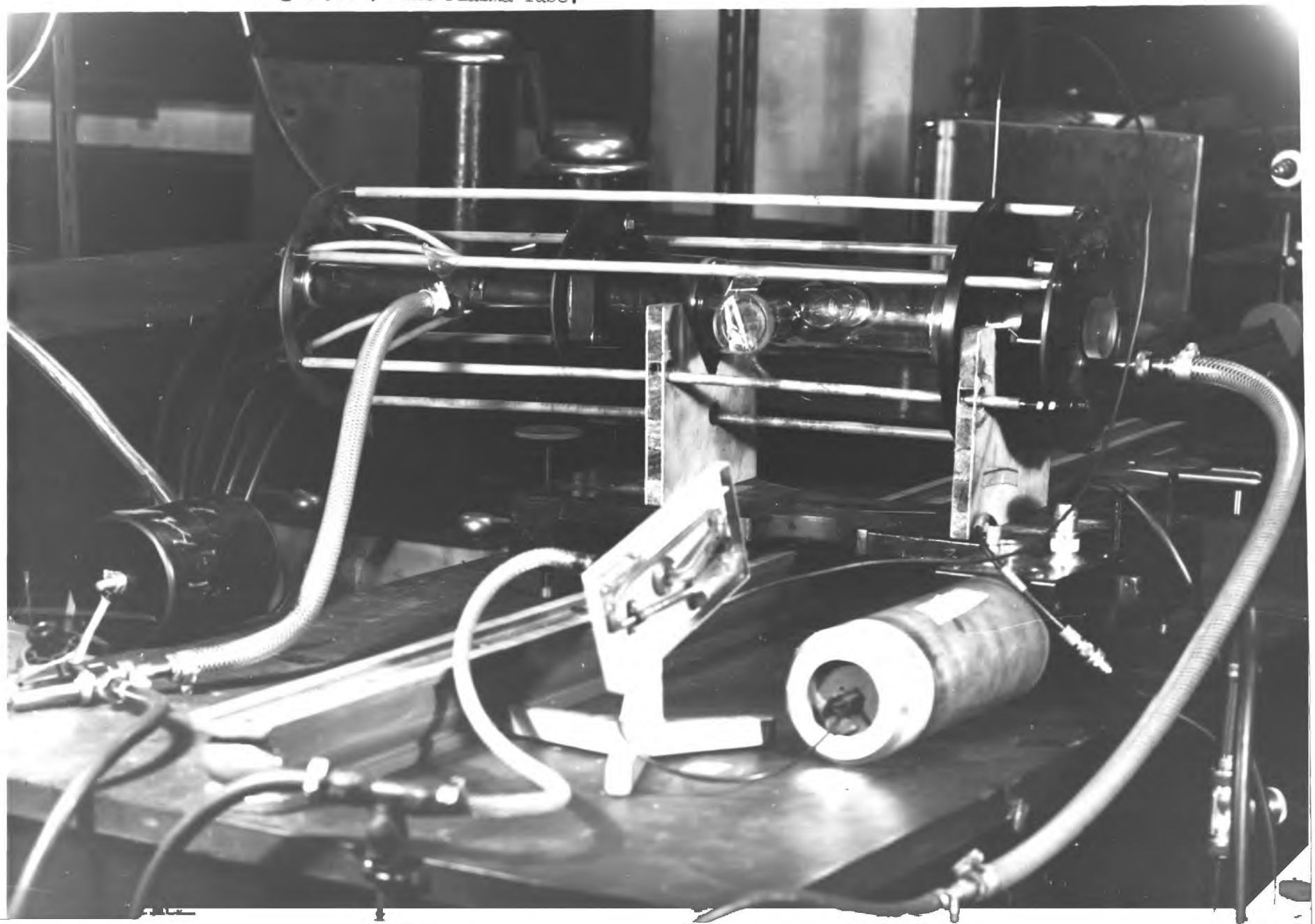

Fig (5.7) Block Diagram of the Electrical System of the Z - Pinch.

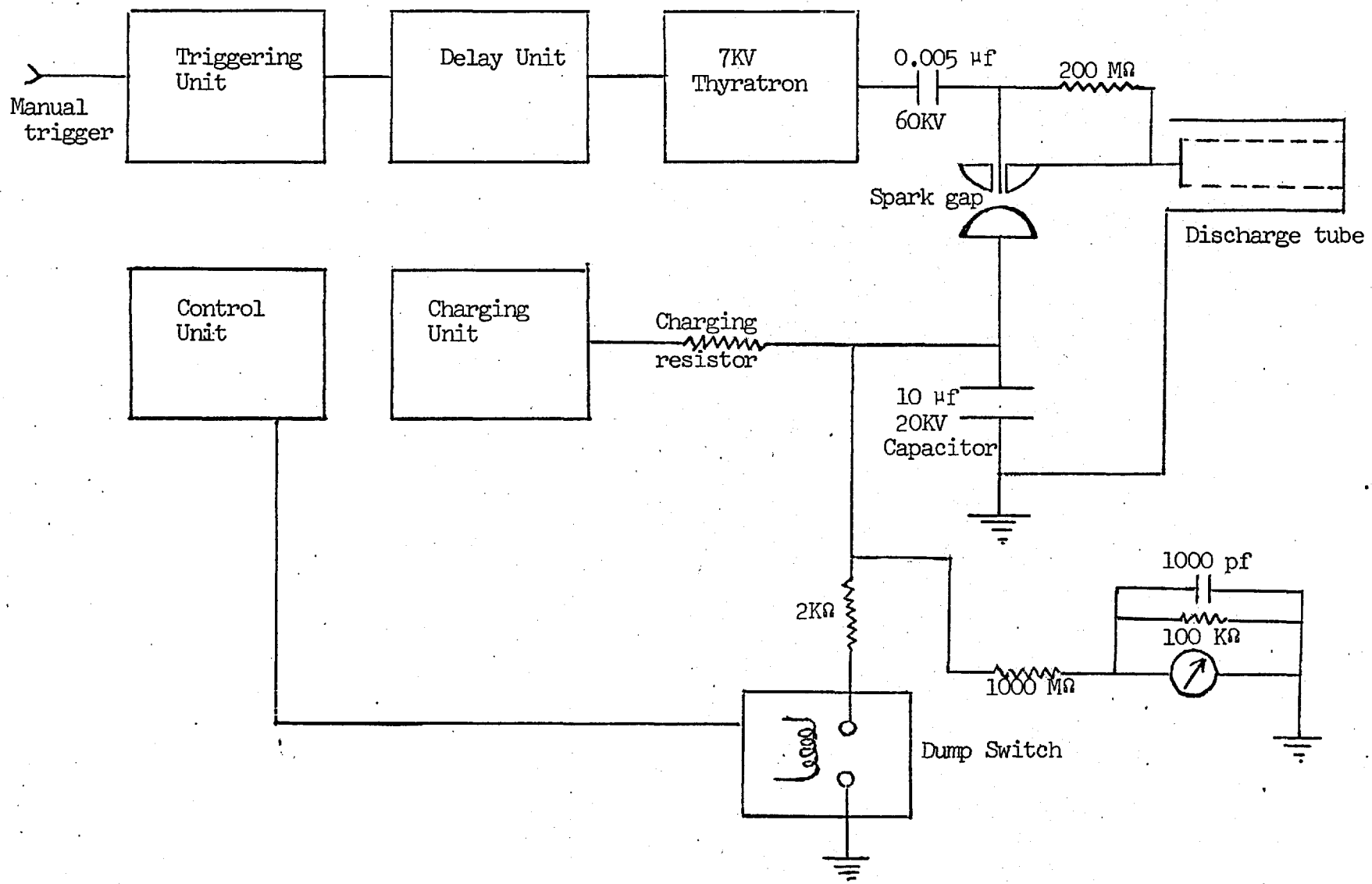

5.4.3 The Vacuum System

A powerful Edward's rotary pump was used to evacuate the discharge tube. Pressure less than 1 mtorr could be achieved after an initial period of degassing the system. Gas inlet valve was provided at the other end of the tube, so that cross flow of gas could ensure uniform pressure in the tube.

5.5 Operation of the device

5.5.1 Preliminary measurements

It was desired to obtain preliminary information about the behaviour of the new device. When at first operated in Helium at 200 mtorr at 10 KV, the discharge was very irreproducible and difficult to break down. At 15 KV maximum working voltage, the break down was more consistent. Simple observation as to whether the 'pinch' is being formed, is to visually observe the discharge through green goggles. The many-fold increase in luminosity of the plasma at maximum compression causes the eye to retain the image of the plasma coherence as a cylindrical rod along the tube axis. The diameter of this rod as can be roughly estimated visually is about one centimeter. If the pinch does not occur, as at low voltages, then this 'rod' can not be seen, but the whole tube is almost uniformly luminous.

The same observations can be better performed when the eye is replaced by a photomultiplier tube and the signal observed on an oscilloscope screen. Instead of observing the 'total' non-spatially resolved light output, much better picture of the dynamic behaviour of the plasma was obtained by collecting the light through a 3" long narrow tube with 2mm internal diameter and the inner walls of the tube being blackened. This tube was placed radially outside the discharge tube so that it collected most of the light from a small section of the luminous shell as it collapsed toward the axis. At the other end of this narrow tube was attached a fibre optics light pipe which carried the light to a photomultiplier.

The measurements showed that at 15 KV, 200 mtorr filling pressure of He, three distinct 'pinches' could be observed. Fig. (5.8) shows the temporal behaviour of the light output and current waveforms. The second pinch occurs just 2 μ sec after the first, while the third appears after 9 μ sec from the second. The first and second pinch follow so closely in succession because as the reflected shock wave strikes the current sheath and causes it to expand, the current in the tube is still near the peak value. The self magnetic pressure of the plasma is still large enough to compress the current sheath. This causes the luminosity to suddenly rise again. At this stage the current has dropped to about half of the peak value and the kinetic pressure of the plasma plus the reflected shock cause the sheath to expand till the luminosity drops to minimum.

The break-down in He was quite irreproducible. However, when the gas was preionized using a high frequency tisla coil, it became better behaved. The time of the first pinch was 3.8 μ sec after the initial breakdown of the gas under the above mentioned conditions. This agreed quite well with the predictions of the snowplough model as discussed in Chapter 8.

5.5.2 Electrical monitoring of the discharge

The measurement of current and voltage across the plasma tube leads to some useful information about the discharge. For a satisfactory pinch to form initial $\frac{dI}{dt}$ must not be either too small or too large. If it is too small, the rate of contraction of the plasma will be smaller than the speed of sound and the amplitude of instabilities may grow large enough to destroy the inward motion of the plasma before the pinch. In the latter case, the constriction of the plasma may be delayed due to too rapid build up of self magnetic field even before the gas is sufficiently ionized.

By independent observations of the plasma through the light output from the discharge it was indirectly ensured that the initial rate of increase of the discharge current was reasonable to allow the pinch

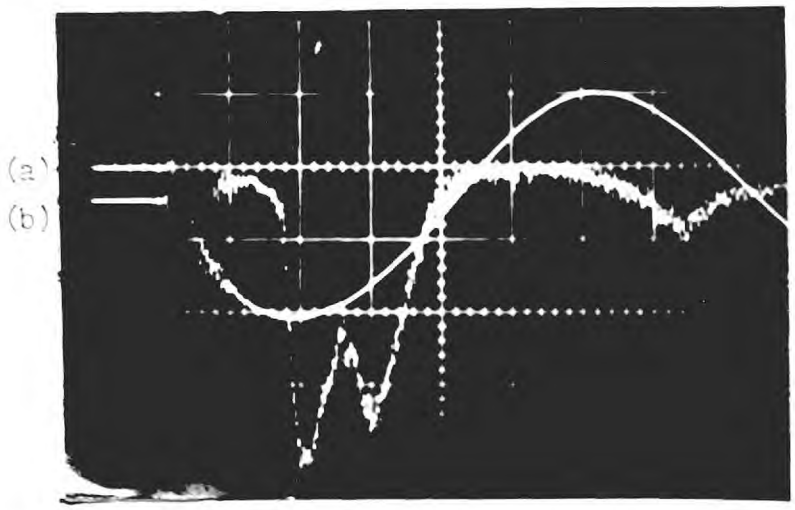

Helium 200 mtorr 10 μf 15 KV

Fig (5.8) a) Light output b) Current.

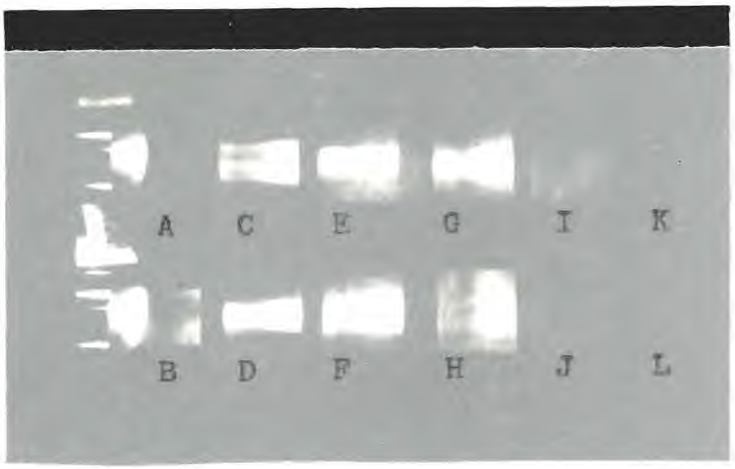

Fig (5.11) Framing Camera photographs of the discharge as in Fig 5.

to occur. Fig. (5.9) shows the voltage, current and light output traces. The instantaneous voltage across the discharge tube was measured using a 250 Ω tapping on a resistive potentiometer. The voltage trace for a given charging voltage and initial filling pressure was extremely reproducible and needed to be measured only once. The current flowing through the discharge tube was recorded as a function of time on an oscilloscope using a Rogowski coil linking one of the six return conductor rods. The output of the Rogowski coil was integrated by a simple RC circuit to give current. It was ensured that RC >> time period of the discharge circuit.

Normally the current and voltage waveforms yield the information about (i) the duration of any delay in breakdown, and (ii) the time to pinch. The current waveform however, did not show any indication of the time to pinch. This is due to the fact that the distribution of circuit inductance determines the shape of current and voltage waveforms. The device can be represented by the equivalent circuit shown in Fig. (5.10). The dynamic behaviour of the sudden discharge from the voltage V_o is represented by

$$i = CV_o \frac{a^2 + b^2}{b} \ell^{-at} \sin bt \qquad - (5.20)$$

where $a = \frac{R}{2L}$

and

$$b = \frac{R}{2L} \sqrt{\frac{4L}{CR^2} - 1}$$

The ringing frequency $= \frac{1}{2\pi\sqrt{LC}}$

From fig. (5.9) and Eq. (5.2), one obtains the maximum value of total circuit inductance = 0.725 μh

and the resistance R = 0.048Ω.

To see the relative influence of the plasma inductance L and the external circuit inductance L_e on the current and voltage waveforms,

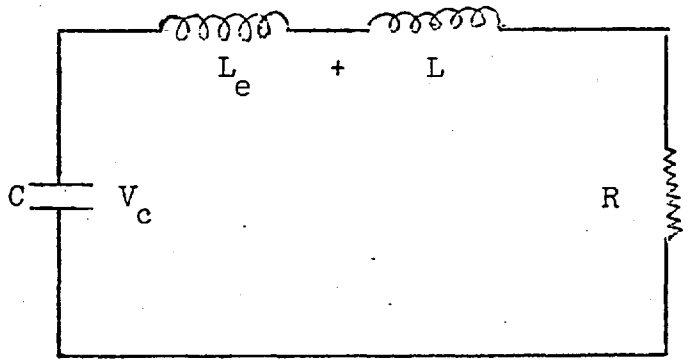

Fig (5.10)

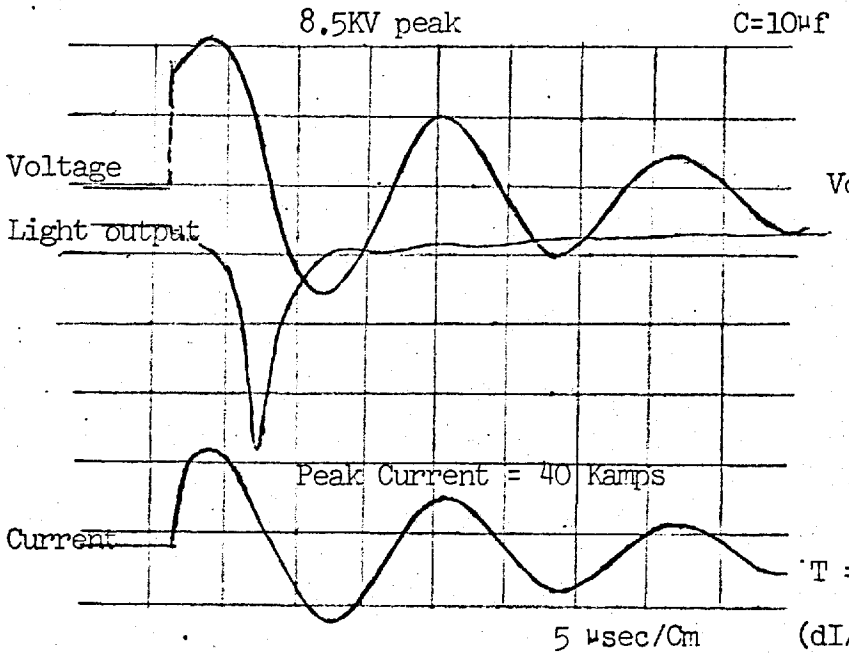

Fig (5.9)

consider the capacitor bank voltage V_c during the short interval of time at the pinch as

$$V_c = L_e \frac{dI}{dt} + V \qquad - (5.21)$$

$$= L_e \frac{dI}{dt} + \frac{d(IL)}{dt} + IR \qquad - (5.22)$$

where V is the voltage across the tube terminals. The tube resistance is smaller than the value quoted above as the latter includes the circuit resistance as well.

Thus

$$V_c = L_e \frac{dI}{dt} + L \frac{dI}{dt} + I \frac{dL}{dt} \qquad - (5.23)$$

At the short moment of pinch, an insignificant amount of charge leaves the capacitor bank, so that V_c can be considered constant. Also near the pinch $I \frac{dL}{dt}$ is always large. Thus the relative values of L and L_e will determine the shape of current and voltage oscillograms at the time of pinch. The plasma inductance can be calculated from the following expression[10]

$$L = 5 \times 10^{-10} \ell \left(1 + 4 \ell n \frac{r_o}{r}\right) \qquad - (5.24)$$

where r is the radius of the pinched column in cms (obtained from framing camera photographs, section 5.5.3),

$r_o \equiv$ radius of the outer return conductor in cms, and

$\ell \equiv$ the tube length in cms.

For $r = 0.25$ cms $\quad r_o = 9.5$ cms $\quad$ and $\quad \ell = 46$ cms

we obtain $L = 0.382$ μh.

This gives $L_e = 0.725 - 0.382 = 0.343$.

Thus L and L_e are very nearly the same and hence each has some relative influence on the current and voltage oscillograms near the pinch. When doing holographic measurements it was therefore decided to ensure

the moment of pinch by observing light output from the discharge mostly in the continuum region. This was easily done by placing a red filter (Wratten No: 29) at the tip of the light output. This is because most of the light emission from He and Argon plasma is in the visible and ultraviolet region of the spectrum.

5.5.3 Framing Camera Photographs

To determine the radius of the discharge at the maximum compression, the plasma was photographed using image converter camera. The camera used was a Telford Type T.E.12 image converter equiped with a 1 Mc/s framing unit. This imaged eight to twelve frames or one polaroid film, with a 50 nsec exposure time and a separation of 0.5 μ sec. between the frames.

The shutter of the camera was controlled by a 40 volt pulse from a timing unit. The timing of this pulse was adjusted to correspond to the time when the plasma light output picked up by a photomultiplier began to be observed on the oscilloscope. Fig. 5.11 shows a photograph of various stages in the discharge. The sequence of the exposures is marked from A to L. A progressive contraction of the plasma can be observed. The boundaries of this contracting column mark a distinct luminous "shell" which is moving inward. In the frame marked C luminosity at the axis shows that the gas is ionized while the shell has not yet reached the axis. This confirms the observations of Nation[11] who also observed an axial luminosity before the collapse of the current sheath.

After about 2.5 μ secs from the time of the pinch, the tube is filled by the plasma showing a uniform luminosity across the shole cross-section. Photographs with least exposures showed distinctly the diameter of the pinched column although the other frames were then under-exposed. A compression ratio of twelve could be observed in He at some pressures, which corresponds to a diameter of 6 mm. Assuming fully ionized gas and 100 per cent trapping, the electron density of 7×10^{17} cm^{-3} can be expected. With argon even higher electron den-

sities can be obtained because of its lower ionization potential. As seen in the next chapter, the diameter at half-height points (of electron density distributions) with argon is as small as 2.6 mm.

References

1) Griem, H.R. Plasma Spectroscopy, 1964, McGraw-Hill Book Co.

2) M.A. Heald and C.B. Wharton, "Plasma Diagnostics with Microwaves", Wiby, New York, 1965.

3) G.J. Parkinson, A.E. Dangor and J. Chamberlain. "Time Resolved Measurements of Electron Number Density and Electron Temperature Using Laser Interferometry at 337 μm. wavelength". 1968 Int. Report, Imperial College, London S.W.7.

4) C.W. Allen, 1955, "Astrophysical Quantities", University of London, Athlone Press, P.86.

5) A.E. Dangor, Ph.D. Thesis, 1969. University of London.

6) M. Born and E. Wolf. Principles of Optics. 2nd Edition. 1964. Oxford, Pergamon Press.

7) T.A. Hall. Ph.D. Thesis, 1968. University of London.

8) Wort, D.J.H. 'Refraction of Microwaves by a plasma cylinder'. Research Report CLM-R27 (1963).

9) S.J. Fielding, Ph.D. Thesis (in preparation), London University.

10) S. Glasstone and R.H. Lovberg. "Controlled Thermonuclear Reactions". 1966. P.250. Van Nostrand Co. Inc. London.

11) J.A. Nation, Ph.D. Thesis, 1960, University of London.

12) Jenkins, F.A. and H.A. White, 'Fundamental of Optics'. New York: McGraw-Hill, 1957.

Chapter 6

Holographic Interferometry of the Z-pinch Plasma

6.1 Introduction

The applicability of holography to plasma diagnostics depends on the fact that when a light wave passes through a plasma, it experiences both phase and amplitude distortions. The phase distortions are rendered visible by such optical techniques as interferometry, schlieren and shadow photography. The changes in amplitude can result from absorption and from scattering. Almost all the holographic diagnostics performed so far have been directed at measuring the phase changes leading to information about the electron densities in the plasma. However, the amplitude changes caused by absorption of the light by the plasma hold out a bright future for temperature measurements as well. This will be discussed in Section 6.2.2 and Appendix I. In this chapter the measurements of phase changes and associated experimental details are described. Before we proceed to do this, it will be useful to briefly review the work reported so far in the literature about the holographic diagnostics of plasmas.

6.2 A review of previous work on holographic diagnostics of plasmas.

Although the science of holography acquired a strong base at the advent of the laser in 1960, it has only recently begun to be applied to plasma diagnostics. Ostrovskaya et. al.[1] were the first to point out in 1966 the possibility of such an application. Later some results of investigations were published by Jahoda et. al.[2,3] and independently by Eaidal et. al. and others[4-9]. The work by these authors has mainly been aimed at developing the technique rather than the actual investigation of any particular plasma.

6.2.1 Phase Changes

Holographic interferometry was first successfully applied for the

investigation of the plasma produced by laser spark by Kakos et. al.[5]. Initially the hologram was obtained using Gabor single-beam method[11] requiring single exposure by using the unabsorbed part of the laser beam that produced the spark[1]. By this method the accuracy of the electron density calculations was not better than 50%. The quality of the hologram was improved by Kakos et. al.[5] by using two-beam holography rather than the single-beam method mentioned above. They obtained interferograms using the double exposure technique. A thin glass wedge was introduced in one of the two exposures to produce a background fringe pattern allowing a higher sensitivity of measurements. The estimation of the electron densities from a knowledge of the fringe shifts could be made with an accuracy of about 20%

Some investigations of a fully ionized deuterium plasma in a θ-pinch Scylla-I device have been reported by Jahoda et. al.[2,3]. A scatterer was used before the plasma position to give a diffuse object beam which enabled a three-dimensional image to be obtained within the viewing angle during reconstruction.

Very recently some more work has been reported by Jahoda[12] where measurements performed on a coaxial gun configuration called snowplough are described. In these experiments a current sheath collapsing to form a plasma focus has been studied. Holographic interferograms at different times show the motion of current sheath. In all these experiments mode controlled ruby laser operating in uniphase single axial mode was used. The other experimental features are mostly the same as described in Ref. (2).

6.2.2 Amplitude Changes

If the hologram is made in the linear range of the emulsion such that the transmission at each point of the hologram depends linearly upon the exposure, then the brightness distribution over the reconstructed image agrees quite well with that over the object itself. This property

makes it possible to employ the holographic method for plasma absorption measurements. Since the reconstructed image from the hologram is insensitive to the incoherent plasma radiation, this method has therefore definite advantage over the usual absorption methods.

Preliminary studies of Ostrovskaya et. al.[8] have shown that quantitative measurements of absorption coefficient are feasible with holographic method. They used a step filter attenuator having a transmission ratio of outermost step equal to 1:20. The transmissivity coefficient of the reconstructed images of these step filters agreed very well with that of the step filters themselves. Although the brightness of the reconstructed image varied for holograms with different exposure times, the transmissivity of the images of the step type filter attenuators remained almost constant.

Various factors such as non-linear properties of the photoemulsion, light scattered in the emulsion, various illumination conditions on the hologram created by various object points etc. cause error in the brightness ratios. The scattering of light in the emulsion in the above mentioned work caused a background brightness amounting to about 5% of the brightness of the transparent filter steps. Knowing these factors one can thus correct for the transmissivity coefficient. The measurement of the plasma absorption coefficient can therefore be performed with an accuracy which is satisfactory for most purposes and compares with that of the other methods. To date only Zaidel et. al.[8] have made temperature determinations of a laser spark plasma this way be measuring the absorption of the coherent laser light in the presence of high but incoherent self-luminosity at the same wavelength.

The absorption coefficient by free-free transitions in plasmas is appreciable only for radiation in the infra red region[18]. This presents practical difficulties in making the hologram as no photographic material with reasonable resolution exists for exposures by wavelengths beyond 1.2 μ. However, there is appreciable resonance absorption in the visible

even at not very large densities. The two examples where corresponding lasers also exist allowing such measurements are

Argon laser	4880 Å	Argon plasma	4880 Å
"	5145 Å	"	5145 Å
Ruby laser	6943 Å	Nitrogen plasma	6942.9 Å (N_{II})

In the nitrogen plasma, the line N_{II} 6942.9 Å has a width of ~ 5 Å at electron density of 10^{18} cm^{-3} and the ruby line falls within the profile of the former. The theoretical and experimental considerations are further discussed in Appendix I.

6.3 Choice of the Operating Conditions

The main consideration in the choice for any particular gas is the instability break up time as the pinched plasma is more stable in some than in others. The smaller the speed of sound in the plasma at any temperature the more slowly the instability break up of the pinched plasma occurs. Xenon, Argon and Helium are commonly used because of the slower speed of sound in these gases. Since the holographic interferometric measurements were to be performed side on, with a small path length, maximum values of electron densities were required to get sufficient fringe shifts. Both Helium and Argon were tried in the preliminary run.

Since the bremsstrahlung emission from a plasma is a strong function of electron density ($\propto N_e^2$) and depends only weakly on the temperature ($\propto T^{-\frac{1}{2}}$), measurement of the continuum provided an estimation of relative electron densities at various pressures in Helium and Argon. Figures (6.1), (6.2) and (6.3) show the continuum light output versus pressure. These graphs also show the times of peak light output at maximum compression for these pressures. As discussed in Chapter 8 these times agree very well with the predictions of the snowplough model.

In the above, the peak light output was assumed to indicate the moment of maximum compression. This is not necessarily generally true.

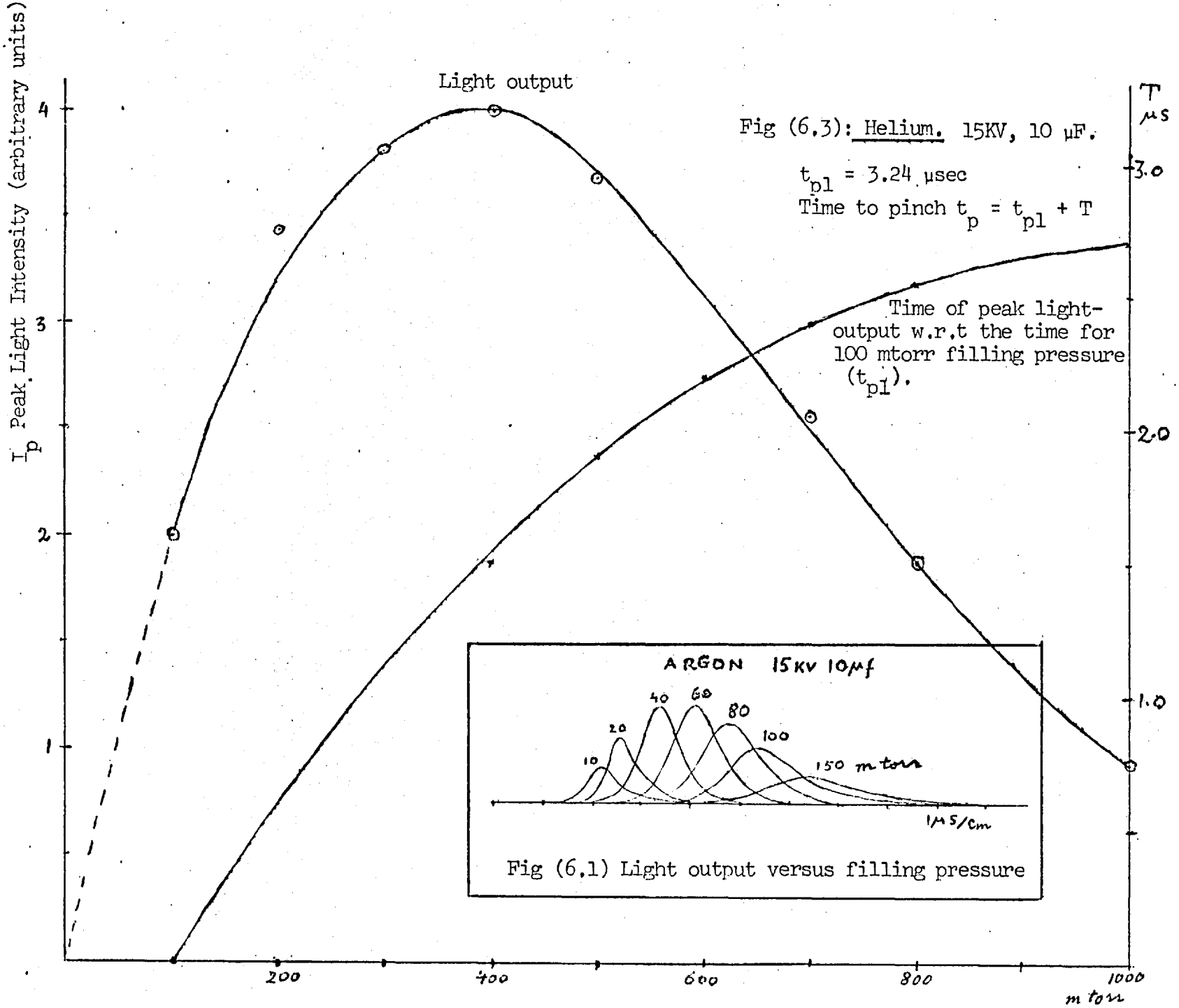

Fig (6.1) Light output versus filling pressure

Fig (6.2): ARGON. 15KV, 10 μF

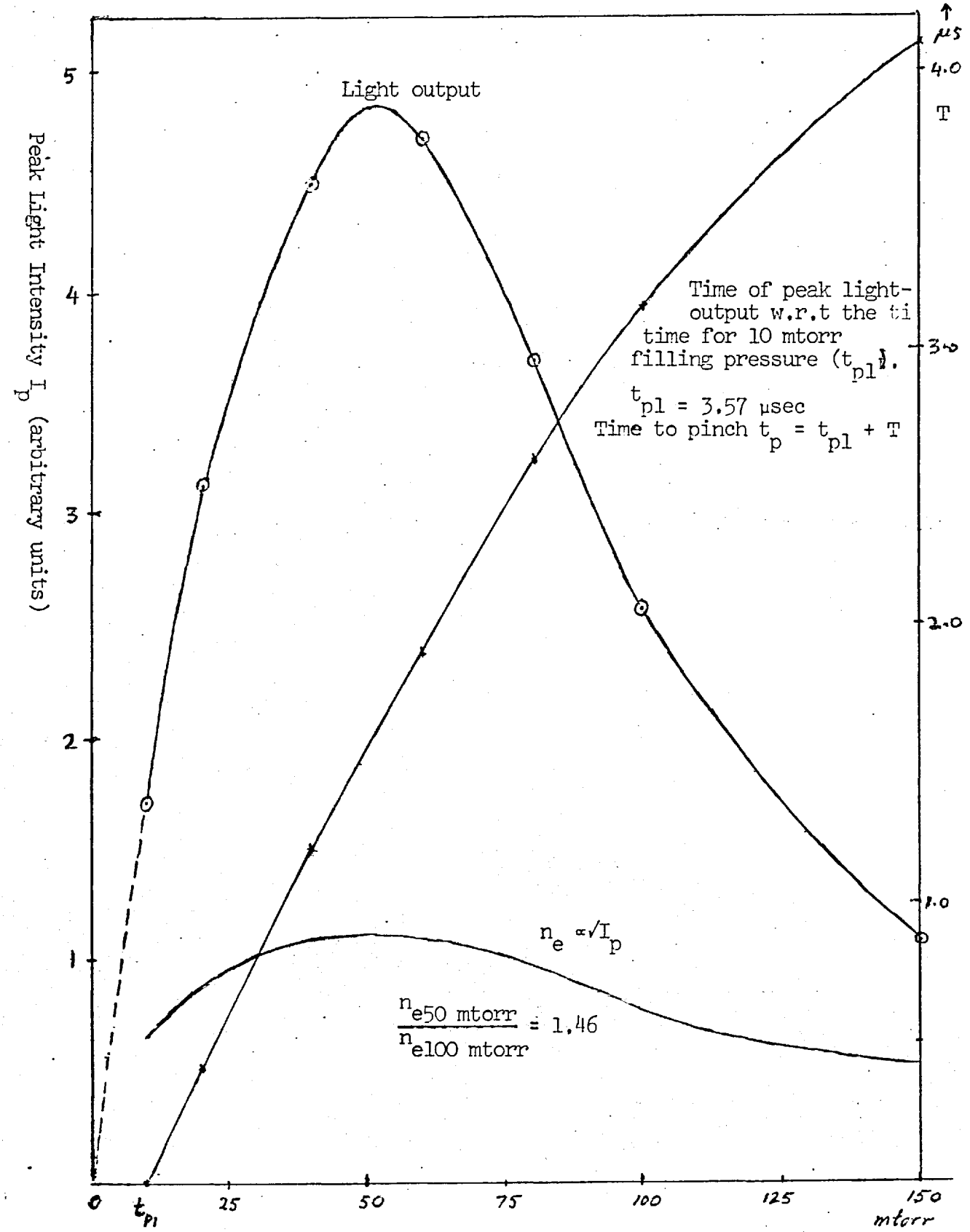

As mentioned in Section (8.2.2), a shock wave moving ahead of the plasma shell produces an axial luminosity much earlier than the time of maximum compression. The light output is, however, maximum at the pinch because of the larger emissivity due to a larger volume of the emitting plasma than that due to shock wave produced axial luminosity.

The relative intensity of the signal was an order of magnitude larger with Argon as compared to Helium indicating larger values of electron density at the pinch with the former gas. This is confirmed by the interferograms showing smaller fringe shifts in Helium plasma. The other difficulty using Helium was the fact that the initial breakdown of the gas was very jittery and it caused a lot of difficulty in timing the ruby pulse at a desired moment in the plasma life time. This, however, was found to be resolved when the gas was preionized using high frequency teslacoil. Break-down with Argon was found to be much more reproducible.

The continuum light output from the plasma shows a strong pressure dependence indicating a similar dependence for the electron density as seen in Figs. (6.2) and (6.3). The electron density peaks for a certain pressure. Such behaviour was also observed by Burgess et. al.[29] in an unstabilized Z-pinch discharge. This effect is explained in terms of shock theory and is discussed in Section (8.2.2). The working pressures were selected to be those which produced optimum fringe shifts in the interferogram, a requirement imposed to fecilitate the measurements on the latter.

6.4 The experimental set up of the system

To perform the holographic interferometric experiment on the Z-pinch plasma, the system with its various components needed to be assembled together.

The laser, the Z-pinch devide and the scatter-plate set up for holography have all previously been described separately. The Fig. (6.4)

shows the arrangement in its final configuration.

6.4.1 The Ruby Laser

The laser has been described in Chapter 2. Due to the claim of the scatter-plate system to work with almost incoherent light, the ruby laser was initially not mode controlled.

The coherence length of the light output from the ruby was roughly estimated by utilizing an equivalent Michelson interferometric arrangement. This was achieved by reflecting the collimated laser beam expanded to larger cross-section from the two surfaces of a slightly wedged glass block placed at 45° to the beam. The reflected light producing interference fringes was photographed. The path difference between the two interfering beams is $2\,d\cos\theta = 1.41\,d$ for $\theta = 45^{\circ}$, where d is the thickness of the glass block. By using different thickness blocks, one gets the coherence length as the optical path length for which interference fringes are no longer obtained. The reason for using a single glass block is that for short coherence lengths of the ruby it provides an easy substitute of Michelson interferometer. To measure the coherence length of the output from a mode controlled laser, one has to use a Michelson interferometer where the length of one of the arms can be varied by any desired amount. With our un-mode-controlled laser, interference fringes could not be observed beyond d = 1 cm., indicating a coherence length of about 1.4 cms.

A simple method of estimating the degree of spatial coherence of the laser output is to measure the contrast of the interference fringes when d is much smaller than the coherence length. The contrast of these fringes then directly gives the degree of spatial coherence. A photodensitometer trace of these fringes was taken at various locations of beam cross-section on the exposed photographic plate. The contrast was found not to be uniform across the beam cross-section but varied from region to region. It confirmed the observations of Evtuhov and Neeland [13] and Nelson and Collins[14] which show that ruby radiates in clusters

of coherent spots of the order of 100 μ to 850 μ diameter of each spot. Our measurements showed a variation of the degree of spatial coherence between 0.1 and 0.3, indicating that the light output is only partially coherent.

Another important parameter that deserved attention is the duration of the output pulse. If the pulse width is large, the rapidly varying plasma can no longer be assumed to be stationary in the duration of the pulse. This would result in a loss of contrast of the interference fringes due to their being smeared out by the plasma motion. Careful measurement of the pulse duration showed the width at half-power points to be more than 180 nsecs. Interferograms of Helium plasma taken with this broad pulse show smeared out fringes of low contrast.

The broad pulses obtained under various operating conditions are shown in Fig. (2.4). The pulse widths are much larger than what is expected under fast switching conditions. The measurements by Key[31] on the same laser as being used for this experiment had indicated a half width of ~ 70 nsecs for 100 cm. cavity. A shorter pulse would be expected for our cavity length of 50 cms. Not only was the pulse width much larger but also the output contained many pulses of comparable intensity. To account for such a wide discrepancy between the expected and the observed pulses, a systematic survey was undertaken of all the diverse factors that determine the pulse characteristics. The main conclusions are listed in the following along with the steps taken to remedy the situation.

i) The light signal was being measured using an EMI 9698B photomultiplier and Tetronix 555 oscilloscope with G-type preamplifier unit. The resultant rise time due to the photomultiplier, the cables and the load and the scope was 69 nsecs. For a measured pulse width of ~ 200 nsecs, the actual width is thus 188 nsecs. It is evident therefore that the measuring system is not responsible for the above effect. The photomultiplier was operated in the linear range to avoid any saturation of the output signal.

(ii) As shown by the computations of Key[31], the product (power output x half width of the pulse) is roughly constant. The input energy to the pump was increased much above the threshold, but the output remained almost constant. This clearly indicated that the flash tube energy was not properly coupled to the ruby. An examination of the aluminium cavity liners revealed their surface conditions to be very bad. The stainless steel liners were coated with silver because the former has an absorption maximum near the ruby absorption peak. But as discussed in Chapter 2, more stable coating was obtained by aluminizing the liners. This improved the situation but not enough to account for the large pulse widths.

(iii) As mentioned in Chapter 2, $\lambda/4$ switching using a Kerr cell is not the most efficient way for Q-spoiling. The Q is partially spoiled and the rest of the light is able to cause depletion of upper levels not allowing the population inversion to rise appreciably. The expected pulse widths for the levels of over inversion obtained by $\lambda/4$ switching are much shorter than those obtained in our experiment. It was, however, found that the thyratron was discharging much more slowly due to a fault in its electrical circuit. The slow switching of the cavity losses from low to high Q condition produced single and multiple pulses of much larger pulse widths (Section 2.7). Pulses of normal width were obtained by eliminating the defect.

(iv) One can obtain very short pulses of less than 5 - 6 nsecs duration by using Pulse Transmission Mode (PTM) double switching technique[32]. The practical problem such as the availability of good quality Glan-Thomson prism to be used as the output coupling element prevented this technique being tried. However, reasonable short pulses (~ 30 nsec) were obtained by using dye solution as a passive Q-switch. To control the timing of the output pulse, the passive Q-switch was used in conjunction with the Kerr cell. When the dye cell was kept between the ruby and the Kerr cell, the larger light power transmitted by the dye on its

being 'ruptured' was too large to be controlled by the Kerr switch. The output was thus highly jittery as it depended on the saturation of the dye which is an irreproducible phenomenon. However, on keeping the dye between the Kerr cell and the 99.9% reflecting mirror, it allowed the Kerr cell to exercise control of the timing of the output pulse. By this method well timed single pulse of about 30 - 40 nsec. duration was obtained and is shown in Fig. (2.5). This gave sufficient time resolution for the study of the fast discharge.

6.4.2 The Scatter-Plate System

As seen in Fig. (6.4), the ruby laser beam was expanded by a diverging lens L_1 and then collimated by lens L_2. This beam then entered the scatter plate system, whose components were all arranged on a single optical bench which was a square base Hilger and Watts bench. It need not be especially heavy for resisting vibrations as is usually the requirement for gas laser holography. The scatter-plate was the bleached hologram of an ammonium chloride scatter (see Section 4.5) and made in the same system with He-Ne laser. It allowed part of the beam unscattered and scattered the rest which just filled the aperture of the lens L_3. Both L_3 and L_4 were plane-convex lenses (see Section 4.3.5) with a diameter of 6.3 cms., and a focal length of 25 cms each. They were positioned such that they imaged the scatter-plate on to the photographic plate with unit magnification.

The unscattered portion of the offset beam acted as the reference beam and narrowed down in size as it passed the test region. Since most of the measurements were performed at or near the maximum compression, the reference beam could be allowed to be focused within the plasma tube at about 2 cms off the tube axis, a region almost free of the plasma. The diameter of the test region is (2a - 2s), a and s being the radii of L_3 and the scatter-plate respectively.

To adjust the ratio of intensities of the reference and object beams,

Fig (6.4) Experimental Setup for holography of the Z-pinch plasma.

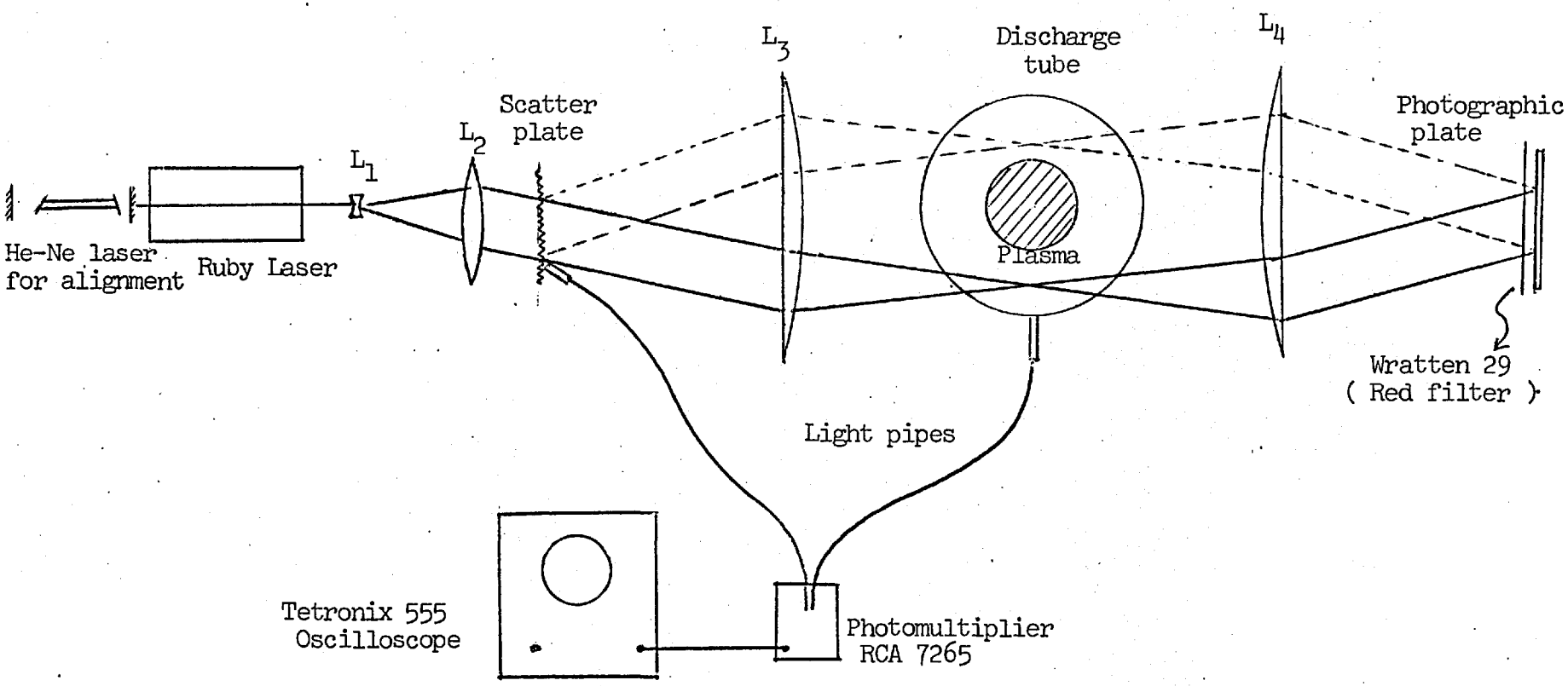

Fig (6.4a) The Experimental Setup for the holography of the Z- Pinch Discharge.

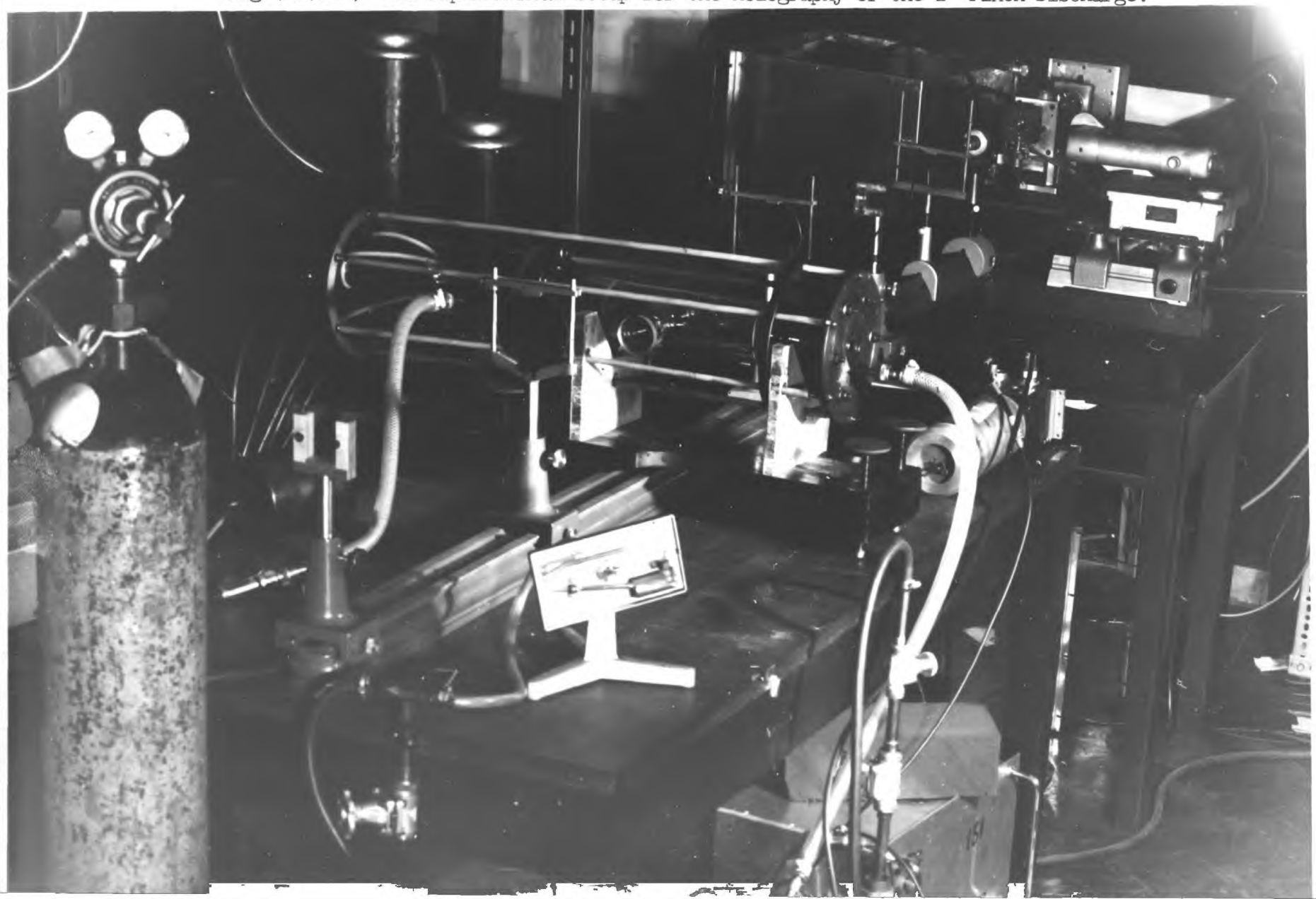

neutral density filters of appropriate attenuation were inserted into the path of the reference beam just outside the plasma tube. If these filters were inserted at the focused beam, where the energy density was high, it usually damaged the filter and subsequently distorted the beam wavefront. Care was taken to avoid such a situation after experiencing it once.

Each Agfa plate 10E75 size 5" x 4" was cut into four pieces. These were held in a plate holder made to the appropriate size. The plate was actually locked into the holder to avoid any motion due to vibrations between the two exposures. Since the hologram size was the same as that of the scatter plate, i.e. 1" diameter, two exposures could be made on each piece of the plate by simply raising the plate holder to the new position for each exposure. A photograph of such a plate is shown in Fig. (6.5). The photographic emulsion is also sensitive to the blue and green regions of the spectrum. The light from the plasma which is predominantly in the blue and violet parts of the spectrum causes a fogging of the plate. This was avoided by using a gelatin filter, Wratten 29. This has a passband with the lower cutoff at 6100 Å, and was placed directly at the photographic plate.

In some circumstances the laser light signal is strong enough to over expose the plate. One can not avoid this by operating the laser at lower power output as it tends to increase the half-width of the pulse at the cost of time resolution of the measurements. A simple solution was to attenuate the laser light by inserting neutral density filters near the photographic plate. This had an added advantage in that it reduced the plasma light in the red region passing through the Wratten 29 filter.

6.4.3 Electronics

The Fig. (6.6) shows the block diagram of the electronics used to control and operate the whole system. Here the Tetronix 555 oscilloscope was used to serve also as a long delay unit.

Fig (6.6) BLOCK DIAGRAM OF ELECTRONICS

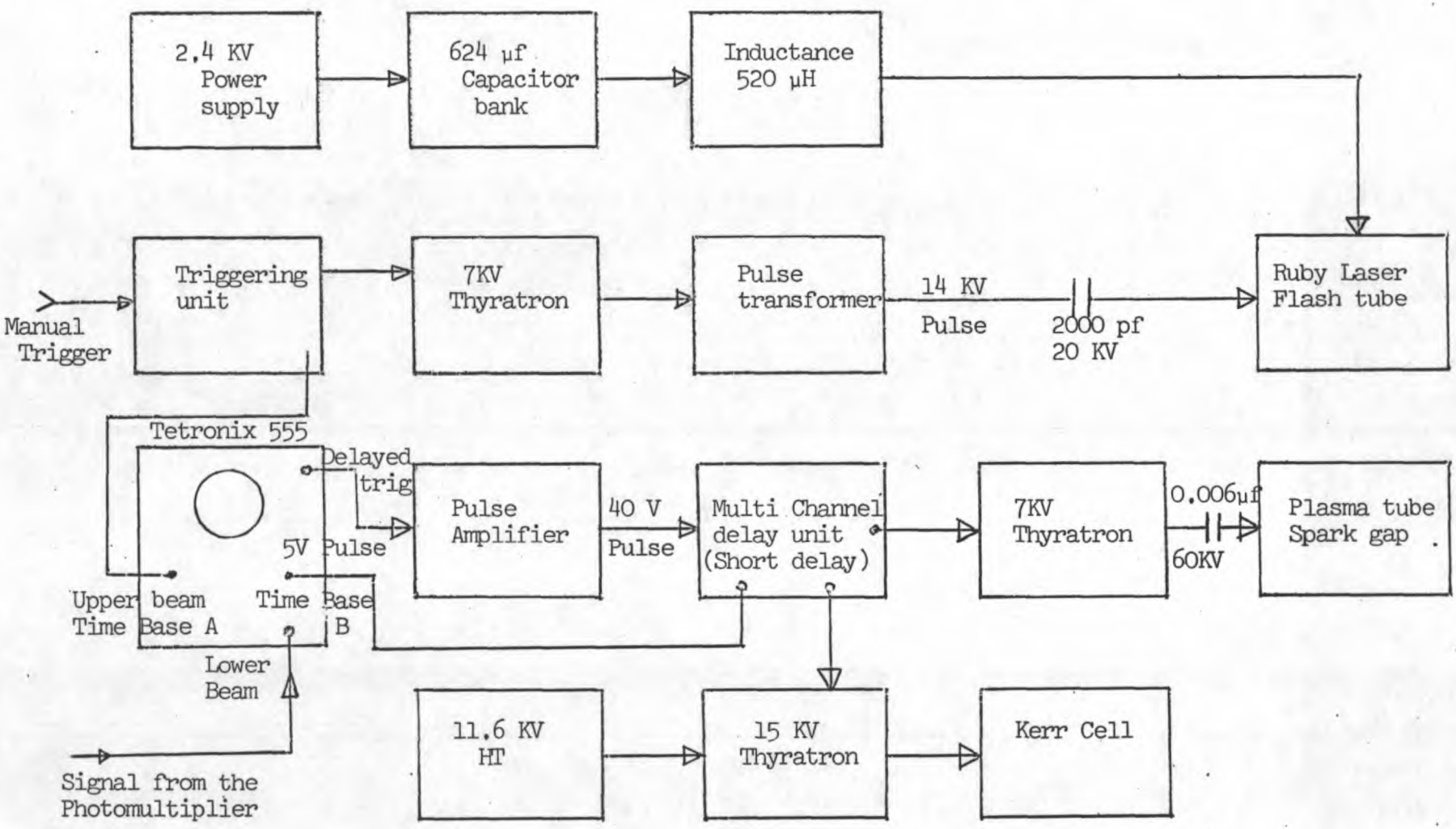

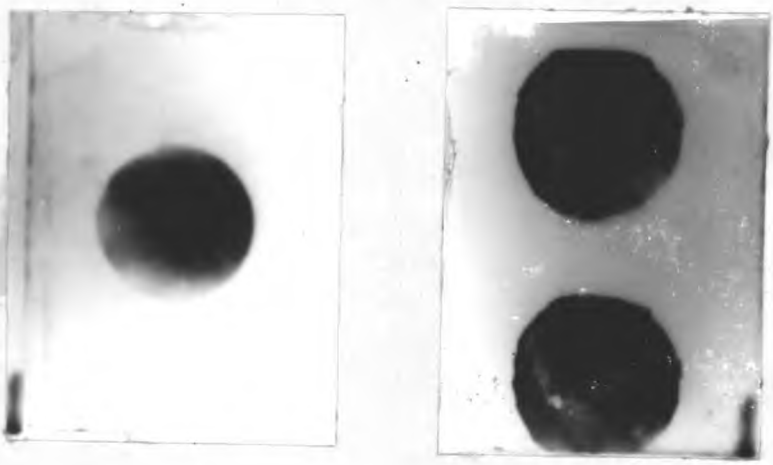

(a) (b)

Fig (6.5) Photographs of the holograms (to the scale)
(a) Single hologram on the plate (b) Two holograms on the same plate.

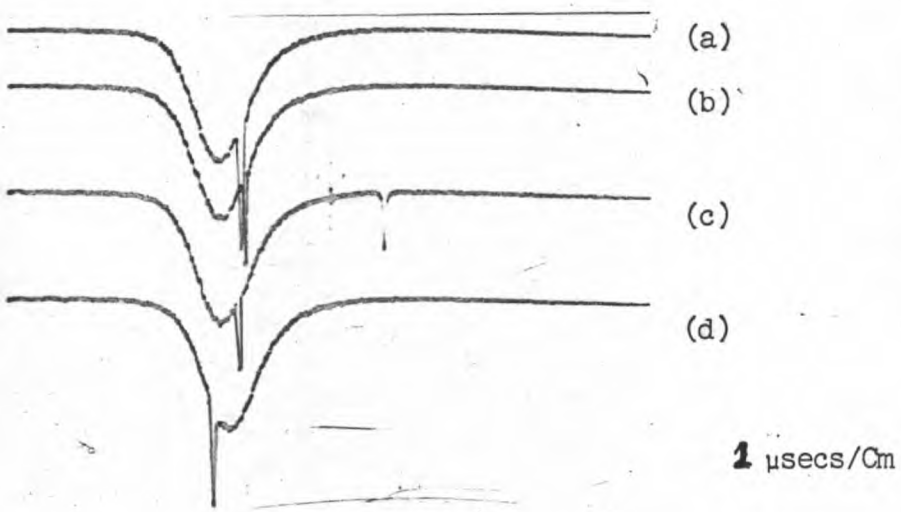

Fig (6.7) Plasma Light output traces modulated by Ruby Laser pulses.

This is due to the fact that the Kerr cell has to be opened at the time when the light output from the flash tube is maximum corresponding to maximum population inversion in the ruby. This happened at about 1.4 msec after the initiation of the flash tube current. No delay unit could be obtained which would provide a pulse after such a long interval. A pulse from the triggering unit triggers the time base A of the oscilloscope at the same time the flash tube is triggered by a simultaneous pulse from the triggering unit. A +5v volt pulse is obtained from the 'delayed trigger unit' of CRO, whose delay w.r.t. input pulse is given by the product time base A X helipot setting of 'delayed trigger unit'. This can provide delays ranging from 20 nsec to 50 seconds. The +5v pulse was amplified to +48v by simple switching circuit using fast transistors, providing a rise time of 20 nsec.

It was observed that this pulse amplifier was triggered much earlier than the provided delay. This was traced to be due to the strong electromagnetic pickup from the pulse transformer being used to trigger the flash tube. However it was eliminated when the +5v input to the pulse amplifier was fed through a coaxial cable coiled round a ferrite ring damping the high frequency pickup. The +48 volts output from the pulse amplifier triggered the multichannel short delay unit which provided trigger pulses for the rest of the system as shown in Fig. (6.6).

6.4.4 Monitoring the timing of the event under study.

To study the behaviour of the plasma at, before or after the maximum compression, it was essential to monitor the timing of the laser pulse with respect to the plasma. As shown in Fig. (6.4), this was done by feeding the plasma continuum light and the laser light to the same photomultiplier through two fibre optic light pipes. The relative signals from these two sources could be adjusted by inserting neutral density filters at the entrance tips of the light pipes. The photomultiplier used was RCA 7265 and care was taken to operate it in its linear range.

Fig. (6.7) shows the ruby laser pulse modulated on the light output from the plasma whose maximum indicates the time of maximum compression. It also shows the reproducibility of the plasma. One of the traces shows double pulsing of the ruby which happens if the input energy to the flash tube exceeds the threshold of the dye solution beyond which it gives more than one pulse. In such a situation one obtains a differential interferogram with only a single exposure.

6.5 EXPERIMENT

The formation and the reconstruction of the hologram will be discussed separately.

6.5.1 Formation

The system can be checked by making an interferogram by double exposure technique of a bunsen burner flame. This affords a source of easily generated phase variation with sufficient refractive index change to observe many interference fringes in the field of view. Moreover, the problem of timing the laser pulse at a fixed moment does not arise as the disturbance is not a transient one. Furthermore, unlike the plasma containing device with optically imperfect walls, the flame is a pure phase object and does not deviate or distort the wavefronts passing through it except in the presence of large refractive index gradients. This helps in checking the optical system for its ability to form holograms with a poor degree of coherence. The hologram of this disturbance can be made even with relaxation oscillations of the ruby laser output lasting about 0.4 - 0.6 msec. because any change in the disturbance is very slow as compared to the duration of the light output from the ruby.

Having ensured the workability of the system by obtaining the hologram of pure phase object, the plasma tube was introduced midway between the lenses L_3 and L_4 (Fig. (6.4)). The He-Ne gas laser simulating the path of the ruby laser beam was used for alignment of the system.

The tube was placed such that the reference beam at point P (Fig. (6.4)) passed about 2 cm. off the tube axis. The electron density distributions obtained by gas laser interferometry (Chapter 7) indicate densities about two orders of magnitude smaller at 2.0 cms off axis as compared to the axial values. It is therefore reasonable to assume that the reference beam is clear of the plasma region.

The timing of the laser Q-spoiled pulse was adjusted to coincide with any desired moment w.r.t. the peak plasma light output. The photographic plate with red filter (Wratten 29) placed on to it was introduced into the plate holder with near darkness in the room. One advantage of working with high resolution plates used in holography is that they are not very fast and hence it allows one to work under subdued light in the room without fogging the emulsion.

Finally the laser and plasma capacitor banks were charged, and an exposure of the plate made at the proper operating conditions. Another exposure of the same plate was made without the plasma in the tube, with the same laser energy. A few minutes period was allowed between the two exposures for the cooling of the ruby by the air being blown through the cavity. To obtain maximum contrast of the interference fringes of the reconstructed interferogram, the intensity of the two exposures was kept nearly the same. Moreover the intensities were adjusted such that the density of developed emulsion was nearly unity, thus having an amplitude transmission factor of ~ 10%. This ensured operation in the linear dynamic range of the emulsion. The plate was then developed, fixed and dried. A double exposure hologram of the plasma was thus obtained.

Holograms were taken at 50, 100 and 150 mtorr pressures of argon. For each pressure a range of timings was covered w.r.t. the peak compression. The electron density increased to sufficient level to allow fringes to form only about 1 μsec. before the pinch.

6.5.2 Reconstruction

The hologram was reconstructed using coherent radiation of He-Ne

laser. Since we are interested in frozen fringe pattern obtained by double exposure hologram, it can be reconstructed without the use of the set-up employed during formation. For visual reconstruction, it was simply held just in front of the eye in the diverging beam of the gas laser. One observed the images on the far side as if looking through a window. However, to perform the measurements on the recorded event the reconstructed image has to be photographed. The Fig. (6.8) shows the arrangement used for recording the reconstructed image.

To obtain an image of the same size as the object itself the lens L_4 has the same focal length as in formation stage. However, there will be a demagnification of the image size in proportion to the ratio of the two wavelengths, i.e. λ_2/λ_1 where λ_2 is the reconstructing wavelength. The hologram and the photographic plate (or a screen) are each at the Fourier transform plane of the lens L_4.

The hologram was illuminated by a collimated beam whose diameter was controlled either by using telescopic arrangements of different magnifications, or by inserting apertures of the desired size in the expanded beam. A practical difficulty that was encountered in photographing the images was the effect of zero order term. This is usually brighter by an order of magnitude than the images themselves, because an intensity ratio of about five was maintained between the reference and the object beams during the formation stage. This term thus caused a strong fogging of the photographic plate at and around O often masking part of the images leading to difficulty of measurements. This was avoided by inserting a small screen anywhere in the path of this term preventing it from reaching the photographic plate. Since the reconstruction was carried out by the red wavelength of He-Ne laser, panchromatic plates (HP3, Ilford) were used to record the reconstructed image.

As seen in Fig. (6.4), the cylindrical plasma column lies in the horizontal plane. The reconstructed image of the double exposure hologram will show contour fringes of the plasma, unless background straight

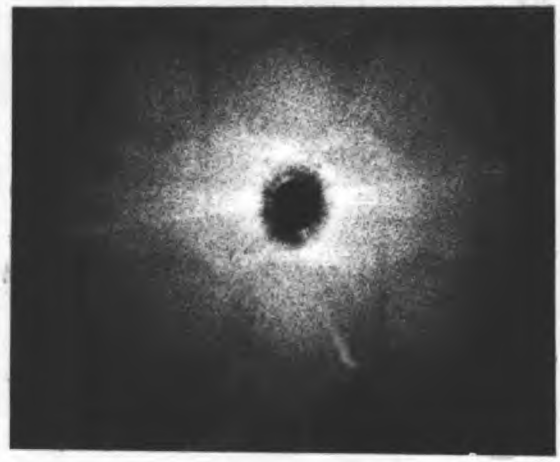

Reconstructed twin images of the sausage instability in the Z-pinch discharge.

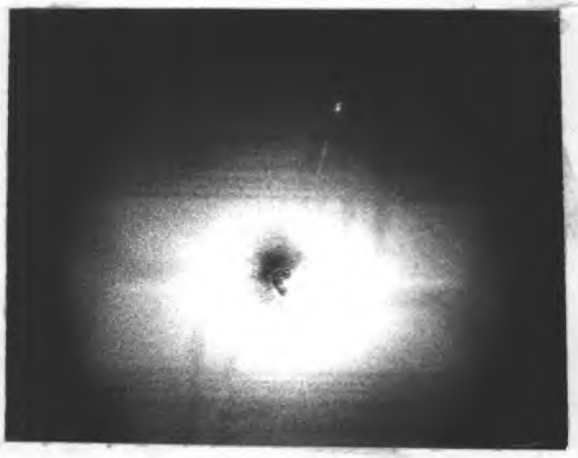

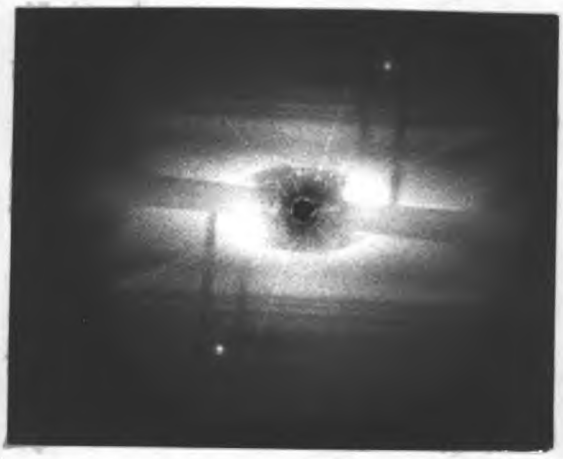

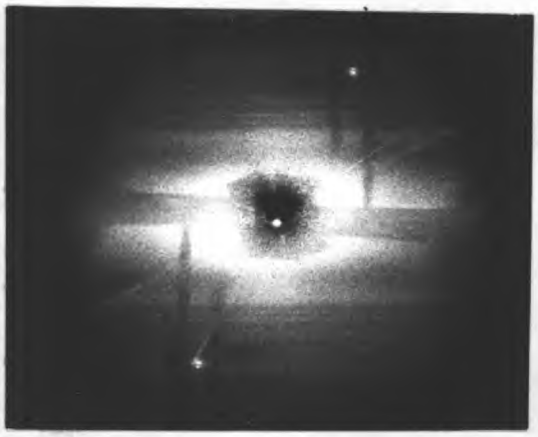

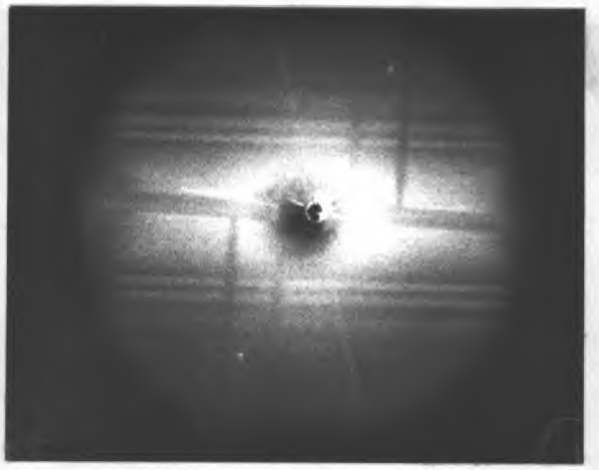

Fig (6.9) Reconstructed interferograms of the Z-pinch discharge. The black spot in the centre shows the position of the referencebeam with twin images on each side.

fringe pattern is introduced by inserting a wedge (Section 6.5.4) during one of the exposures. In Fig. (6.8), these fringes will lie at the screen on a plane coming out of the paper. Fig. (6.9) shows reconstructed interferograms of the plasma at different operating conditions.

6.5.3 Improvement of spatial coherence for the amelioration of the interference fringe pattern.

The poor quality of the interference fringe patterns as seen in Fig. (6.9) is due to the following reasons.

1) The spatial coherence of the ruby laser was very poor (Section 6.4.1). One can ideally obtain good holograms using scatter-plate system with almost incoherent light. But it requires a perfect optical system which sharply images each point of the scatter-plate on to the photographic plate. On insertion of the glass tube into the system, this is no longer possible as various rays are strongly deviated from their path due to refraction by tube walls. It must be emphasized that unlike the case of the Mach-Zehnder interferometer, these deviated rays do not distort the interference fringe pattern of the plasma. These merely determine the quality of the hologram in terms of its ability to reconstruct images of reasonable contrast. The situation can be remedied by improving the spatial coherence of the radiation.

2) As pointed out earlier, the illumination across the field of view was very non-uniform. Due to large contrast of the photographic paper (Bromide paper) the situation is further worsened.

3) Since the diameter of the lenses L_3 and L_4 was only 6.3 cms., it allowed a working region of less than 4 cms. diameter.

All these limitations were removed (a) by using larger plano-convex lenses (10 cms. diameter and 55 cms. focal length). The f-value of the lenses was kept nearly the same as for those used above so that the same scatter-plate could be used to fill the lens aperture by the

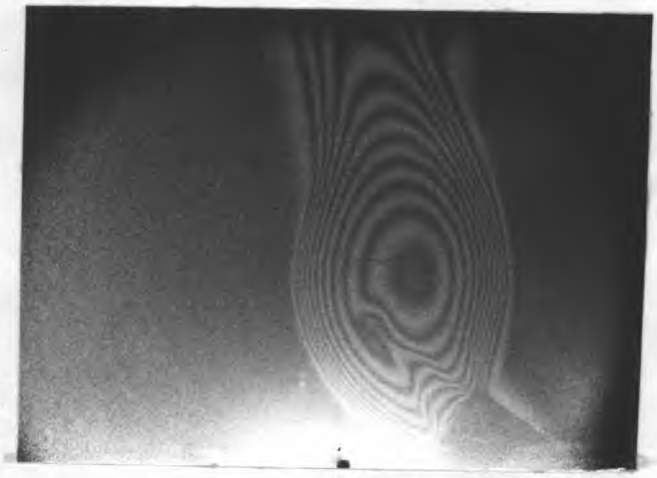

(a)

(b)

Fig (6.10) (a) Without the mode-controlling aperture
(b) With the mode-controlling aperture.

scattered light; (b) the use of larger lenses allowed a larger test area to be examined and also improved the uniformity of the field of view; and (c) by improving the spatial coherence of the radiation by inserting a 1.5 mm. diameter aperture into the laser cavity near the 99.9% reflecting mirror. Correct positioning of this aperture was ensured by first passing a He-Ne laser beam along the ruby axis and then introducing the aperture onto the beam. This pushed up the threshold for relaxation oscillations from 660 Joules to 910 Joules input energy to the flash tube. The Fig. (6.10) shows the bunsen burner flames interferograms for both with and without mode controlling aperture into the cavity. These photographs show a considerable improvement in the quality of the interferograms with the above modifications to the system. From the considerations of Van Cittert-Zernike theorem (p.508, Ref.33), an aperture of 1 mm. diameter would further improve the spatial coherence of the laser output. This, however, required much higher input energies to reach the threshold of laser operation and therefore could not be used.

6.5.4 Sensitivity of fringe shift measurements.

At or near the pinch, the plasma radius was quite small and hence very narrow closely packed interference fringes were obtained. Initially no background fringe pattern was introduced to increase sensitivity of measurements. Due to this reason contour fringes of the plasma were obtained. Accurate measurements of the location of the centre of the fringe, and the tailing off of the outermost broad fringe could be made by taking photodensitometer traces of the negative of the reconstruction. In this way at least a quarter fringe shift could be ascertained.

At much earlier times than the pinch the fringes were broader than at the pinch. Their sensitivity was increased by producing a background fringe pattern by using an air wedge. The required wedge angle to produce fringes with 1 mm. separation by causing a change of air pressure by one atmosphere is estimated as follows.

The number of fringes for a path length L and a refractive index

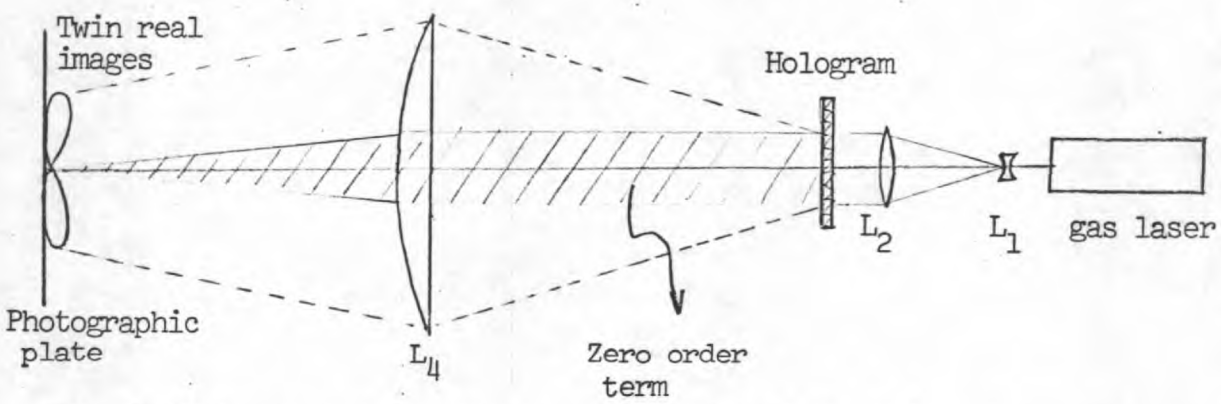

Fig (6.8) Arrangment for the reconstruction of the hologram.

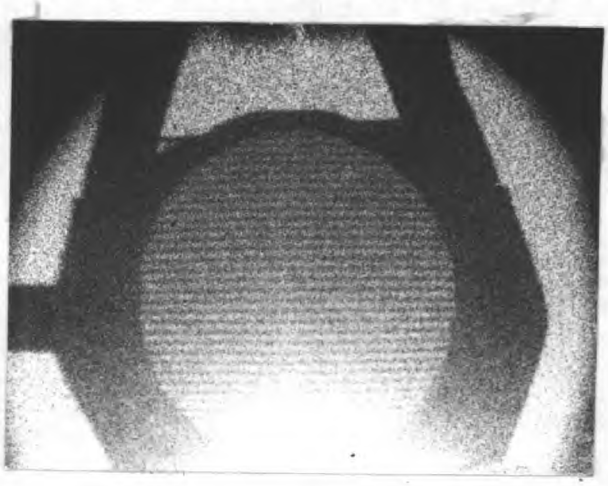

Fig (6.11) Reconstructed image of the background fringe pattern obtained with an air wedge.

Fig (6.12) Reconstructed image of the wedge pattern modulated with phase disturbance.

change $d\mu$ is

$$\delta = \frac{L}{\lambda} d\mu = x \frac{\tan \theta}{\lambda} d\mu$$

where x is the fringe spacing and θ is the wedge angle.

For $\delta = 1$, $x = 1$ mm., $\lambda = 0.7 \times 10^{-4}$ cms. and $d\mu = 0.0002716$ for a change of one atmospheric air pressure at room temperature, we obtain $\theta = 68.6^{\circ}$.

The wedge was made of brass tube of an internal diameter of 5 cms., with one end milled to an angle of 70°. Two glass plates were araldited to the ends to give a vacuum-tight seal. To obtain a hologram, the reference beam passed outside the wedge, while the object beam traversed the glass wedge. Air was let into the wedge for one of the two exposures. By simply controlling the pressure change a straight fringe pattern with any desired spacing could be produced. With a reasonable contrast of the fringes, sensitivity as high as $\lambda/8$ could be obtained. The Fig. (6.11) shows the straight fringe pattern, while the Fig. (6.12) shows a phase disturbance modulated on the straight pattern.

6.5.5 Fringe Localization

Since the disturbances producing plasma fringes and wedge fringes are located at different positions in the system, it is necessary to consider the plane of localization of the interference fringes produced by each and to examine as to how they overlap. Gates, in a recent paper[34], has shown the ability of scatter-plate system to discriminate against the depth of field. If the two disturbances are situated at p and q in Fig. (6.13a), then they can be focused independently by focusing the camera lens with the aperture open to maximum to give a limited depth of field. This can be done by utilizing the arrangement shown in Fig. (6.13b) for reconstructing the hologram. However, if the reconstructed image is photographed with a small camera aperture, the result is the plane projection of the effect of both disturbances integrated in

a fixed direction. Fig. (6.14) shows both the integrated interferogram and also the independent fringe patterns due to each of the two flames. In each there is only a small disturbance due to the other. The same applies to the wedge fringes and the fringes due to plasma. The disadvantage of using a small aperture used to increase the depth of field is that it produces speckle pattern in the reconstructed image. However this effect was not too serious.

If only contour fringes are being observed with the plasma tube being in the mid plane between L_3 and L_4 (Fig. (6.4)), the optical arrangement can be considered to give Fourier Transform type hologram (Section 3.2.4). Thus on reconstruction the fringes can be considered to be localized at the plane passing through the point O and perpendicular to the collimated reconstructed wavefront (say A'A") originating from the region of illumination A on the hologram as shown in Fig. (6.13).

6.5.6 Errors in the measurement of fringe spacings.

1) As can be seen in Fig. (6.13), if the region A of the hologram is illuminated with the reconstructing laser light, the rays A'A" will generate the corresponding image which can be photographed by placing a photographic plate at O.

Similarly the region B will generate the image in the direction of the rays B'B". These images are localized in the Fourier transform plane O of the lens L_4, but as pointed out in Section (6.5.5), these lie in the plane perpendicular to the collimated rays A'A" or B'B" etc. Since the recording photographic plate at O is always normal to the collimated rays originating from the central point P_o of the hologram format (Fig. 6.13), the images corresponding to A'A" etc. are at an angle to the recording plane. If the reconstructed plasma interferogram are contour fringes, then the observed fringes on the recording plane will be the projection of those in the images normal to A'A" etc. as can be seen in Fig. (6.15). The true fringe separation can be estimated from the

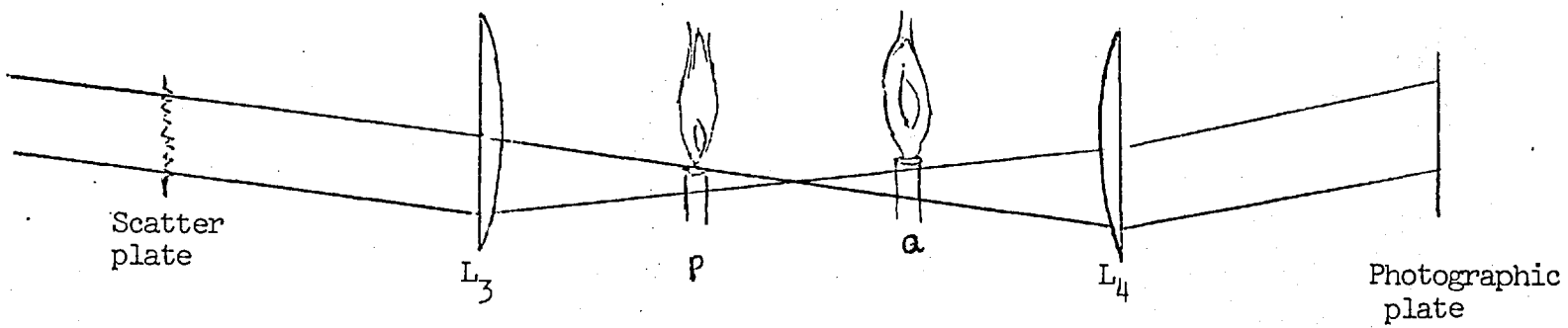

Fig (6.13a).

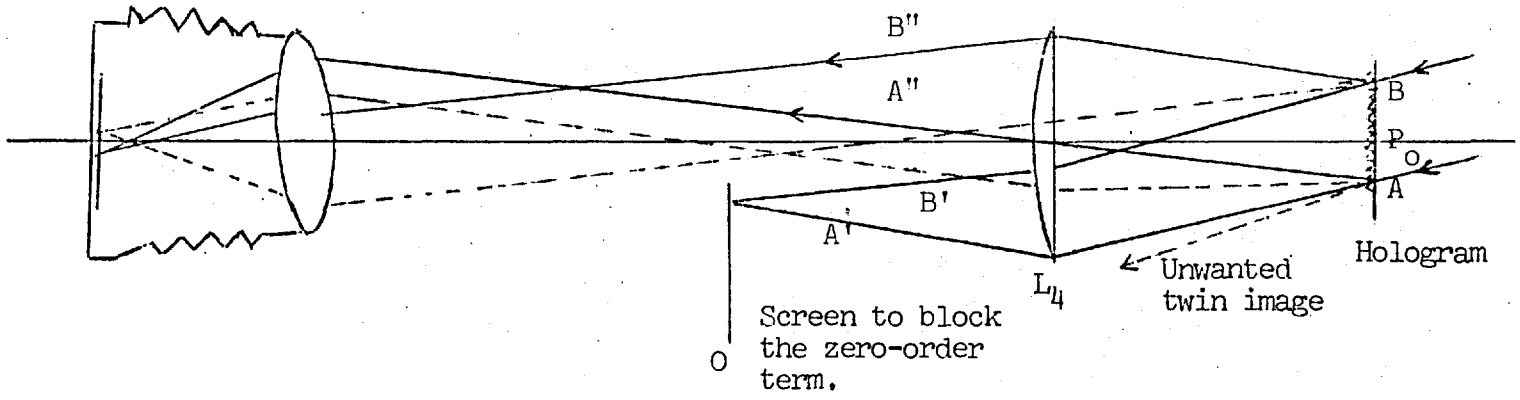

Fig (6.13b).

(a)

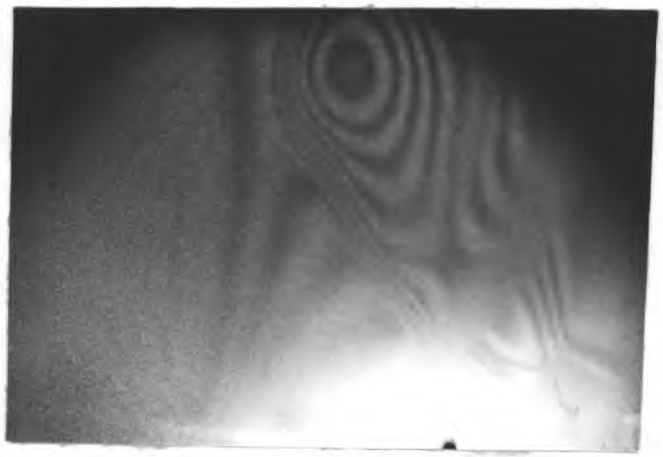

(b)

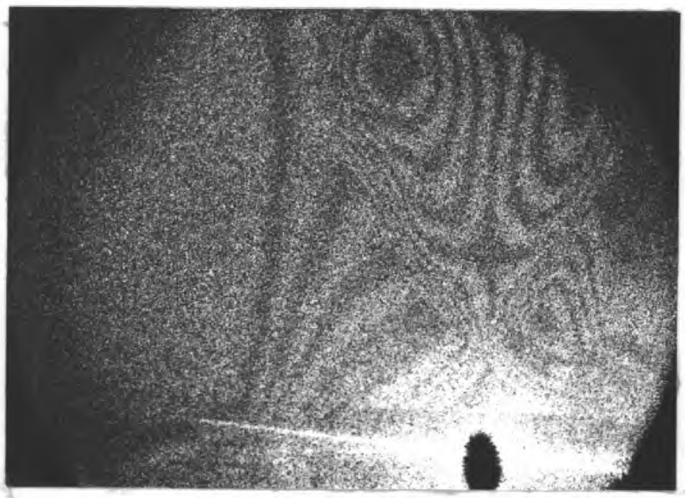

(c)

Fig (6.14) (a) & (b) Spatially resolved flame interferograms (c) Integrated interferogram obtained by increasing the depth of field for viewing the reconstructed images of the hologram.

observed values as follows.

If x is the actual separation between two fringes and y is the observed separation, then as seen in Fig. (6.15), $y = x \sec \theta$.

The maximum value of θ is given by $\theta_m = {}^a/_f$, a being the radius of the hologram format.

For our experimental situation $\theta_{max} = \frac{1.25 \text{ cm}}{25 \text{ cm}} = 0.05$ radians

$= 2.85^\circ$

Hence the maximum value of y is

$$y_{max} = 1.0014\ x$$

This is only 0.14% larger than the actual value of the fringe spacing. Even for a larger angular range of (say) 20°, y_{max} is only 1.54% larger than x. It is therefore safe to neglect this error.

2) In the above example only a small area of the hologram was considered to be illuminated for reconstruction. In this situation the speckle pattern becomes troublesome, acting as a background noise to the actual fringes. The consideration that the speckle frequency should be at least six times larger than the fringe frequency (Section 3.8) made it necessary to use a larger area of the hologram for reconstruction. Various points within this area will reconstruct the images from their corresponding directions and there will be an angular spread of $\pm \delta\theta$ of the planes of fringe localizations around some average position. $\delta\theta$ is determined by the radius of the region being illuminated and the focal length of the lens L_4. If the plasma distribution is radially symmetric, then the fringe spacings in all the planes of fringe localization will be equal. Since the plane of observation remains fixed, the projection of actual fringe spacings from the various planes of localization on to the plane of observation will produce a broadening of the observed fringes. The amount of this broadening can be estimated by determining ${}^{dy}/_y$ as a function of $d\theta$. Since we have

$$y = x \sec \theta \quad . \text{ (Fig. 6.15)}$$

$$dy = x \tan\theta \sec\theta \, d\theta$$

Therefore $dy/y = \tan\theta \, d\theta$.

The typical values of θ and $d\theta$ in our scatter-plate arrangement for 1 cm. radius of the hologram being illuminated near the edge of the hologram are

$$\theta = a/f = \frac{1.25 \text{ cm}}{25 \text{ cm}} = \frac{1}{20} \text{ radian}$$

$$d\theta = \frac{1 \text{ cm}}{25 \text{ cm}} = \frac{1}{25} \text{ radians}$$

Thus $dy/y \simeq \frac{1}{500} = 0.5 \times 10^{-2}$

Thus dy (the amount of fringe broadening) is only 0.5% of y (the fringe spacing).

3) It has been pointed out earlier (Section 6.5.2), that if a different wavelength is used for reconstruction than that used for the formation of the hologram, the reconstructed image is magnified by a factor λ_2/λ_1. In our case λ_1 = 6943 Å and λ_2 = 6328 Å, giving $\lambda_2/\lambda_1 = 0.91$. Hence the observed fringe spacings were multiplied by 1.1 to obtain the correct values.

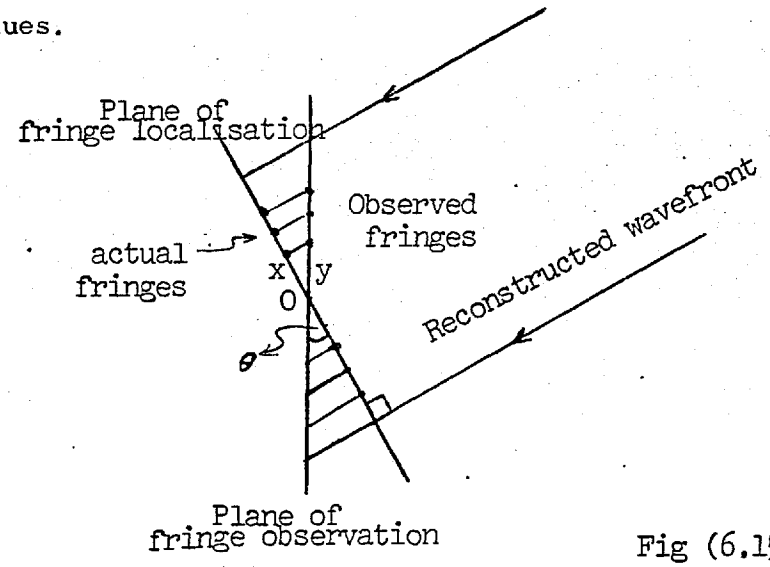

Fig (6.15).

6.6 Abel Inversion of the observed fringe distributions

Using holographic interferometry, one can examine both symmetric and asymmetric plasma distributions. In the former case, the interference fringe pattern will be essentially identical irrespective of the direction of observation. While in the latter case it is no longer the same but varies depending on the degree of asymmetry of the plasma. The symmetric distribution is easy to analyse and can be made to yield radial distributions of electron densities by well known technique of Abel Inversion. However the asymmetric distribution does not lend itself to an easy solution and hence has not yet been attempted. Unlike the first case, where there is only one unknown, i.e. the radial distribution of the refractive index, there are two unknowns in the second case, namely the shape of the asymmetric plasma column and the distribution of the refractive index. Since most of the holographic measurements were made at or before the maximum compression (the first pinch), the plasma column was invariably symmetric. Only in a few cases, where the hologram was taken in the expanding phase of the plasma column, could a slight asymmetry be observed. The symmetric case will therefore be dealt with first. The out line of the procedure that can be used to obtain refractive index distributions in an asymmetric plasma with the help of holographic interferometry will be discussed later.

6.6.1 Cylindrically symmetric distribution

If a plane wavefront of ruby laser light traverses the plasma in the x-direction (Fig. (6.16)), the optical path difference at a height y from the centre w.r.t. no plasma situation is given by (C.G.S units)

$$\delta(y) = \int_{-\ell}^{+\ell} \{\mu(\lambda) - 1\} \, dx$$

$$= \frac{e^2 \lambda^2}{2\pi \, c^2 m} \int_{-\ell}^{+\ell} N_e(r) \, dx \qquad - (6.1)$$

this corresponds to nth fringe counting from the boundary of the plasma

column, if $\delta(y) = n(y)\,\lambda/2$.

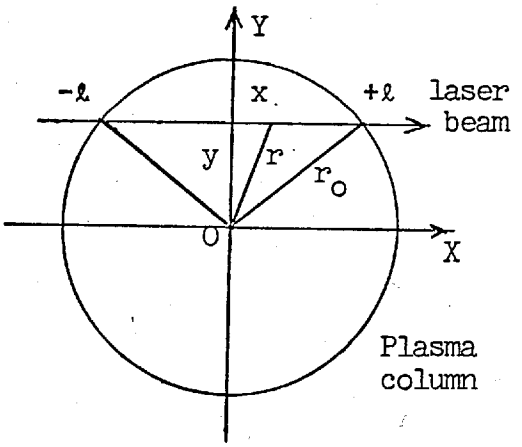

Fig (6.16)

One thus gets

$$n(y) = \frac{e^2 \lambda}{\pi c^2 m}\, 2 \int_y^{r_o} \frac{N_e(r)\, r\, dr}{(r^2-y^2)^{\frac{1}{2}}} \qquad - (6.2)$$

This is similar to the relation of observed intensity at a height y in optically thin plasma, in terms of the radial emission coefficient[15]. This can therefore be solved by using Abel inversion technique[16,17] giving

$$N_e(r) = \text{const} \int_r^{r_o} \frac{n'(y)\, dy}{(y^2-r^2)^{\frac{1}{2}}}$$

where $\text{const} = \dfrac{e^2\lambda}{\pi^2 c^2 m}$ $\qquad - (6.3)$

The holographic interferogram of the cylindrical plasma column gave contour fringes lying symmetrically on both sides of the axis of the cylindrical tube. Fringes were counted inward up to the centre and

Fig (6.17).

(a) ≡100 mtorr argon 15KV 0.3 μsec after the pinch
(b) ≡50 mtorr " " 0.3 μsec after the pinch
(c) ≡50 mtorr " " 0.5 μsec after the pinch

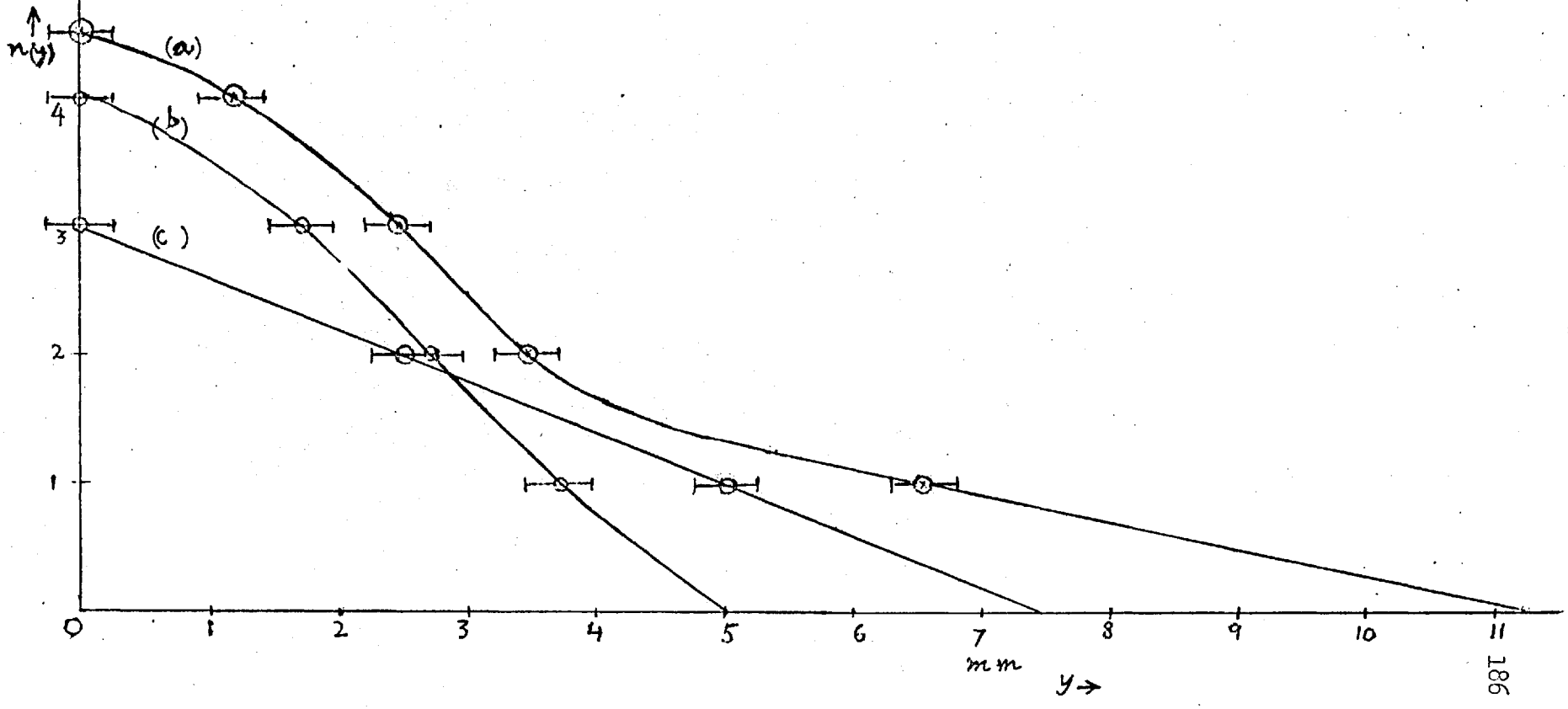

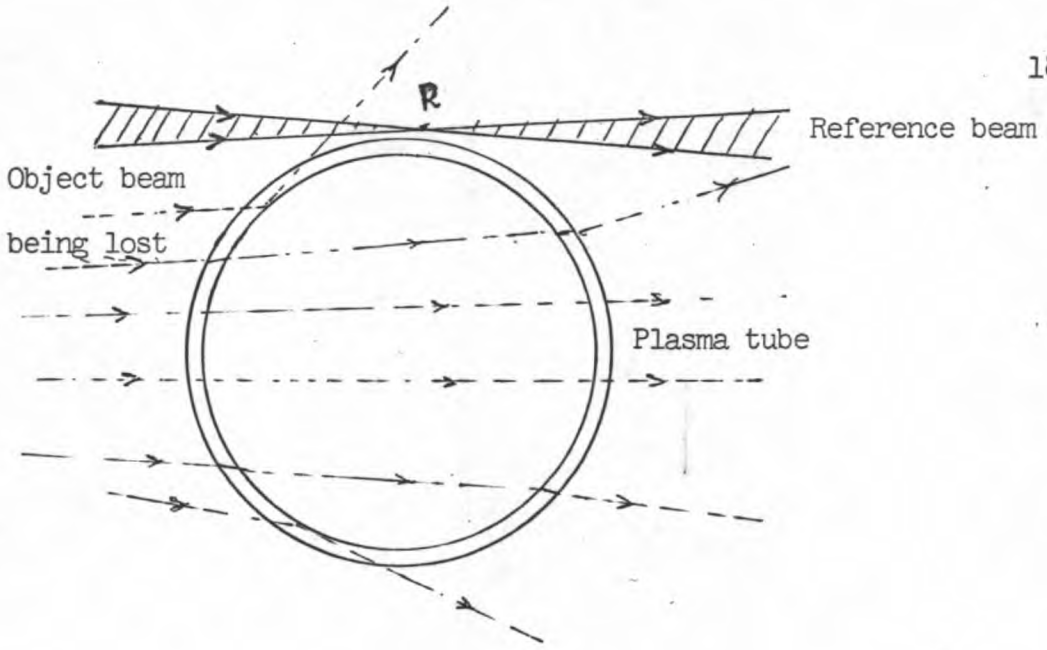

Fig (6.18a)

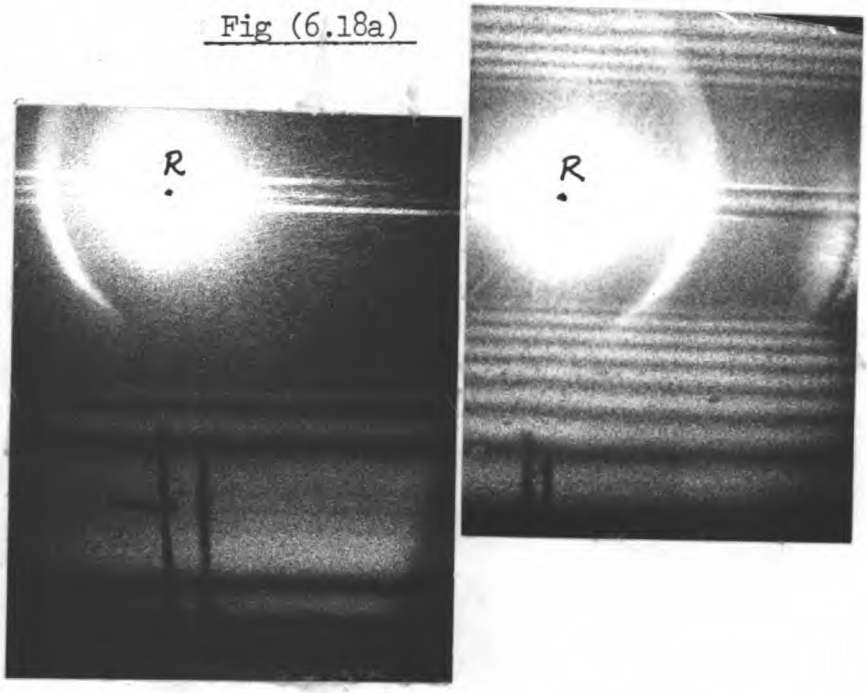

Object beam being lost due to internal reflection at the periphery of the tube

R ≡ Reference beam (just outside the glass tube)

Fig (6.18b) Reconstructed image from a doubly exposed hologram.

plotted against the distance y from the axis of symmetry. Distributions of n(y) versus y for different times w.r.t. the pinch are shown in Fig. (6.17) for some of the operating conditions. These were extrapolated to intersect the abscissa, thus defining the radius of the pinched column. These distributions were Abel inverted using the computer program of Fielding[18]. This program used the area elements of Ref.(16). The radius was divided into twenty-five equal segments and corresponding fringe shifts were fed as input. The output comprised absolute values of electron densities as a function of radius.

To check the accuracy of the computer program, it was operated on a known distribution whose Abel inversion can be calculated theoretically. The elliptic or circular distribution can be easily Abel inverted with the help of Eq. (6.3).

Experimentally such a distribution was obtained by taking a double exposure hologram of the cylindrical plasma tube by changing filling pressure of air between the two exposures. If the fringes are plotted against their respective position w.r.t. the tube centre, one obtains an elliptic distribution depending on the choice of the axes. The Figs. (6.18) and (6.19) show the reconstructed image of the interferogram and the plot of the fringe distribution respectively. The Abel inversion of this elliptic distribution is calculated as follows.

Setting y = n(x), i.e. the number of fringes, the equation of an ellipse is written as

$$\frac{n^2(x)}{b^2} + \frac{x^2}{a^2} = 1$$

or $n(x) = \pm b \left(1 - x^2/a^2\right)^{\frac{1}{2}}$

which gives $n'(x) = \mp \frac{b}{a^2} x \left(1 - x^2/a^2\right)^{-\frac{1}{2}}$

Substituting this in Eq. (6.3) and solving the integral, the Abel

inverted distribution is obtained as

$$N(r) = \pm \frac{1}{\pi} \frac{b}{a} \left[\tan^{-1} \left(\frac{a^2 - r_o^2}{r_o^2 - r^2}\right)^{\frac{1}{2}} - \frac{\pi}{2}\right]$$

Since $y = n(x) = 0$ at $x = r_o$, we set $a = r_o$, which gives

$$N(r) = \pm \frac{1}{\pi} \frac{b}{a} \left[0 - \frac{\pi}{2}\right] = \mp \frac{b}{2a} .$$

Thus the Abel inversion of an elliptical distribution is a straight line with zero slope (horizontal). For a circular distribution a = b and we obtain $N(r) = \frac{1}{2}$, which is independent of the radius of the circle. The Fig. (6.19) shows the plot of the output of the computer program using experimentally obtained distribution as the input. It agrees quite well with the expected shape. However, it shows oscillations corresponding to steep gradients of the fringe distribution. This can be understood by examining the circular case where y (no. of fringes) is related to abscissa x as $y^2 = r_o^2 - x^2$ or $dy = -\frac{x}{y}\, dx$. Near the tube boundary where x is large and y very small, x/y is large and any error in x results in large error in y. To check this, accurately calculated values of y for the circular case were fed as the input fringe shifts. The resulting inverted profile is a much smoother straight line, also shown in Fig. (6.19).

Another shape which corresponds closely to the distribution of electron densities in our plasma is the gaussian. Its Abel inversion yields a gaussian and it was considered apt to check the computer program using this function as well. The inverted profile was obtained to be an almost perfect gaussian. Any slight scatter in the points was usually due to the errors in the input fringe shifts and not due to the error in the program.

An Abel inversion technique suggested by Bockasten[19] was also used for its simplicity. In this method, the Abel inversion integral is approximated analytically by substituting third degree polynomial for

Fig (6.19): A change of air pressure by 398 mtorr in the 3" dia: tube at 6328 Å producing 17 fringes on either side of the tube axis.

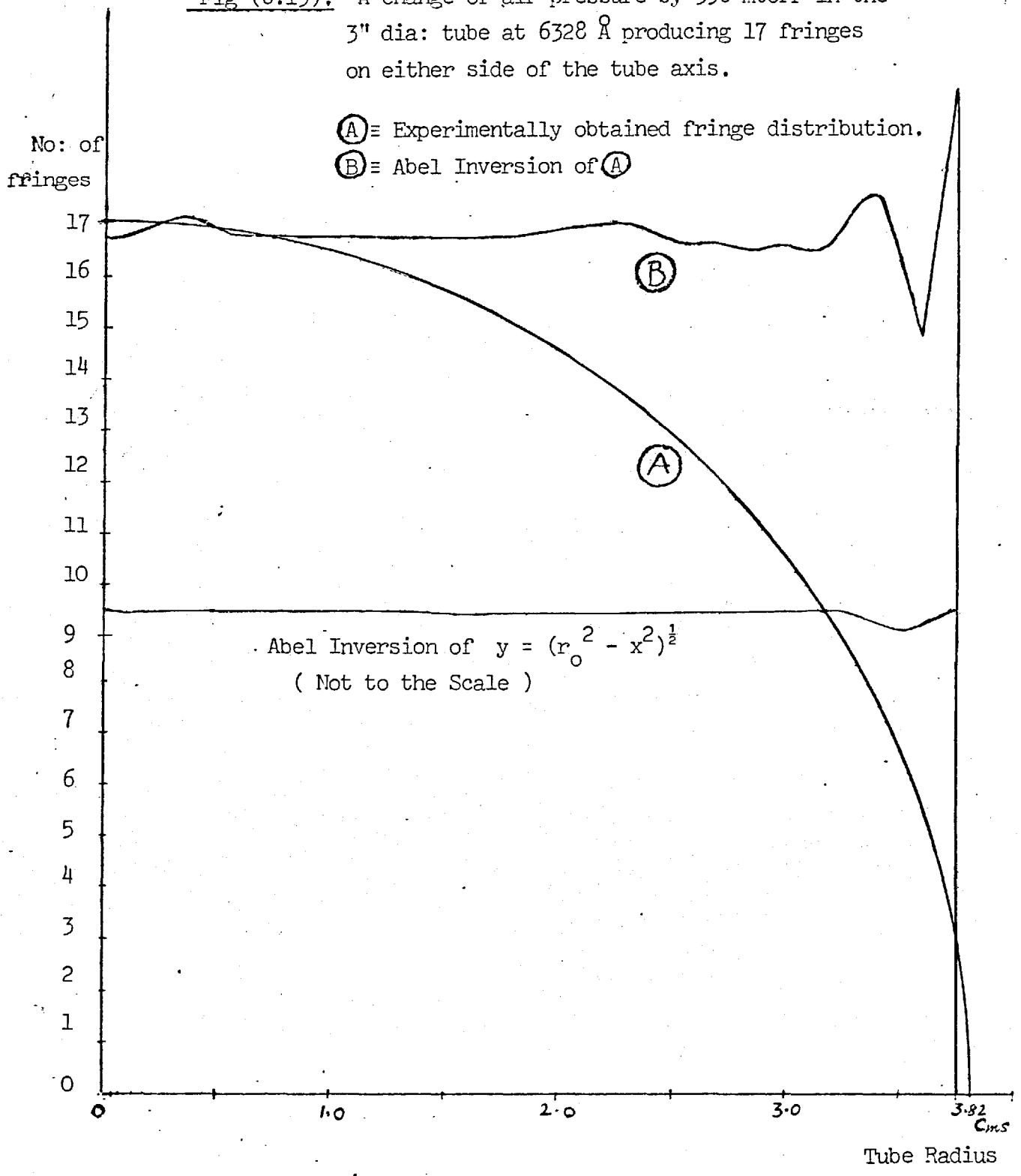

the experimentally obtained fringe distributions. The results obtained with this method agree very closely with those from the computer program using area elements. One great advantage of the method of Bockasten is that it is also able to yield axial values of the electron densities while the former method provides only off-axis information. For instance, the program using area elements gave for 50μ filling pressure of argon a value of $n_e = 0.60 \times 10^{18}$ cm.$^{-3}$ at 0.35 mm. from the axis: The Bockasten's program, however, provided the additional information about the axial electron density to be 1.02×10^{18} cm.$^{-3}$. Since the gradient of electron density is usually large near the axis, one may expect a substantial difference between the axial value and the first off-axis value provided by the first program. A simple outline of Bockasten's program for Abel Inversion is given in Appendix II.

6.6.2 Asymmetric distribution of refractive index

By reconstructing the hologram from different viewing directions, the varying fringe patterns of the interferogram reveal the asymmetry, if any, in the refractive index distribution. The problem of quantitative evaluation of this distribution is very complex. The Abel Inversion technique can not be used for such cases as it is essentially based on the assumption of circular symmetry. There are two unknowns in this situation, namely the geometrical shape of the plasma and its refractive index distribution.

The geometrical shape of the plasma, however, can be known by its simultaneous optical photography. The cross-section of the pinched column, e.g. in the presence of some kink or helical instabilities, can be approximated to an ellipse. In such simple situations one can obtain an average refractive index at the fringe positions in the contour interferogram knowing the respective path lengths. Reconstructing the interferogram from a sufficiently large number of viewing angles, an array of the optical paths of known average refractive index can be

created. By an ensemble averaging procedure at the points of intersection of these paths, one can obtain a distribution of the refractive index. The accuracy of such a calculation will essentially depend on the number of fringes obtained from each direction of observation and the total number of the directions of observation.

Since in our work, no such plasma distribution was observed, a detailed analysis for such a situation was not pursued. However, the above outline is sufficient to indicate the usefulness of holographic interferometry to unravel the distribution of refractive indices in an asymmetric plasma.

6.7 Results obtained with holographic interferometry.

The operating conditions of the discharge initially selected were those which would produce maximum path length changes between the two exposures of the hologram. This was done by using the continuum light output signal versus pressure curves shown in Figs. (6.2) and (6.3) and discussed in Section (6.3).

To obtain time resolved interferograms of the plasma at different stages of the discharge, the time correlation was achieved by collecting simultaneously the plasma continuum signal and the laser pulse signal in the same photomultiplier as shown in Fig. (6.7). Since plasma compression takes place very rapidly, it is only 1.0 μ sec before the pinch that one begins to obtain contour fringes.

The results obtained by Abel Inversion of the fringe distributions at various conditions of filling pressures and timings are presented in graphical form in Figs. (6.20) to (6.23). The Figs. (6.20) and (6.21) show the distributions of electron densities at 100 mtorr filling pressure of argon. The distributions are plotted for the following timings.

(i) At the pinch

(ii) 150, 200, 250 nsecs before the pinch

(iii) 1.0 μ secs. before the pinch.

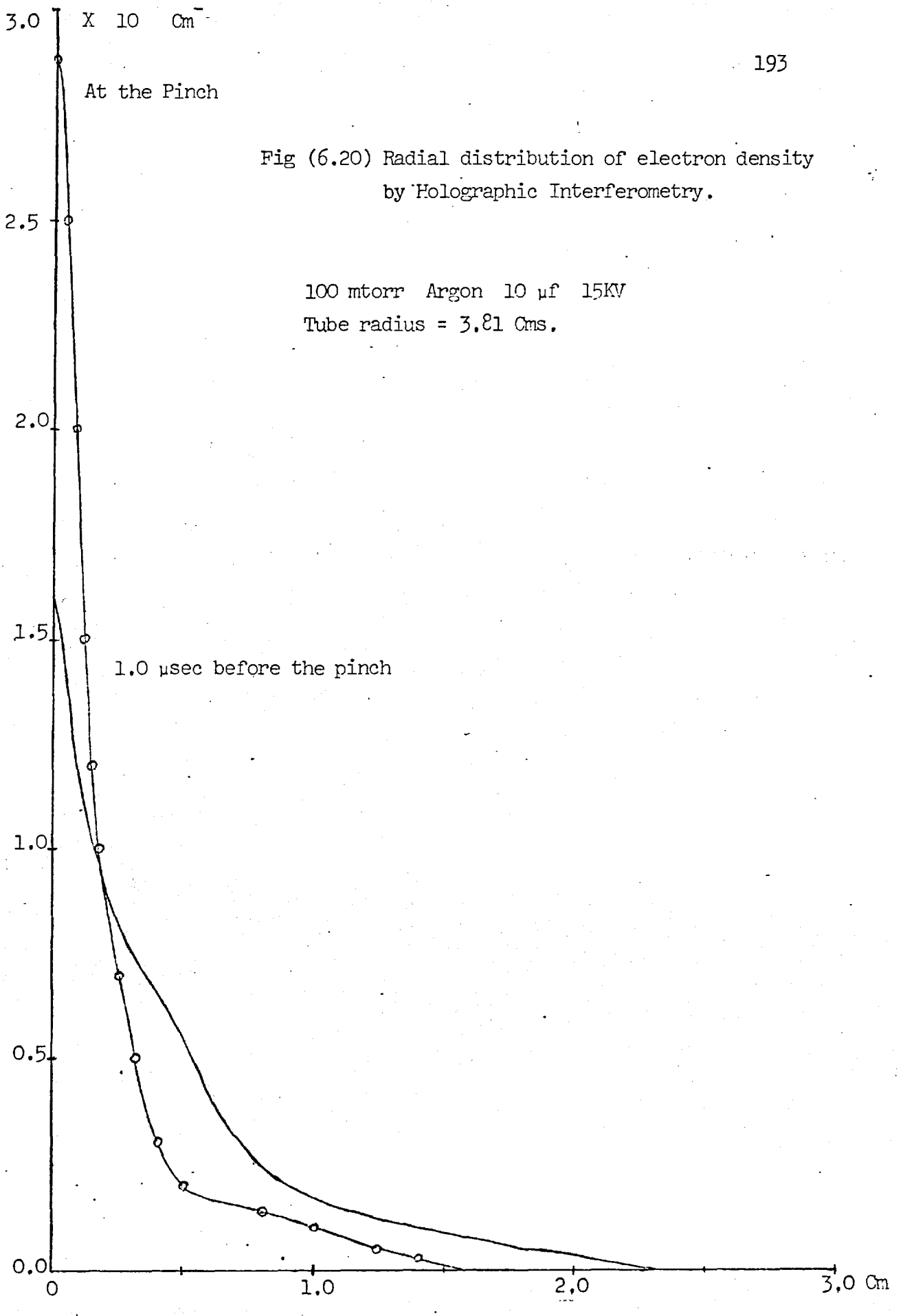

Fig (6.20) Radial distribution of electron density by Holographic Interferometry.

100 mtorr Argon 10 μf 15KV
Tube radius = 3.81 Cms.

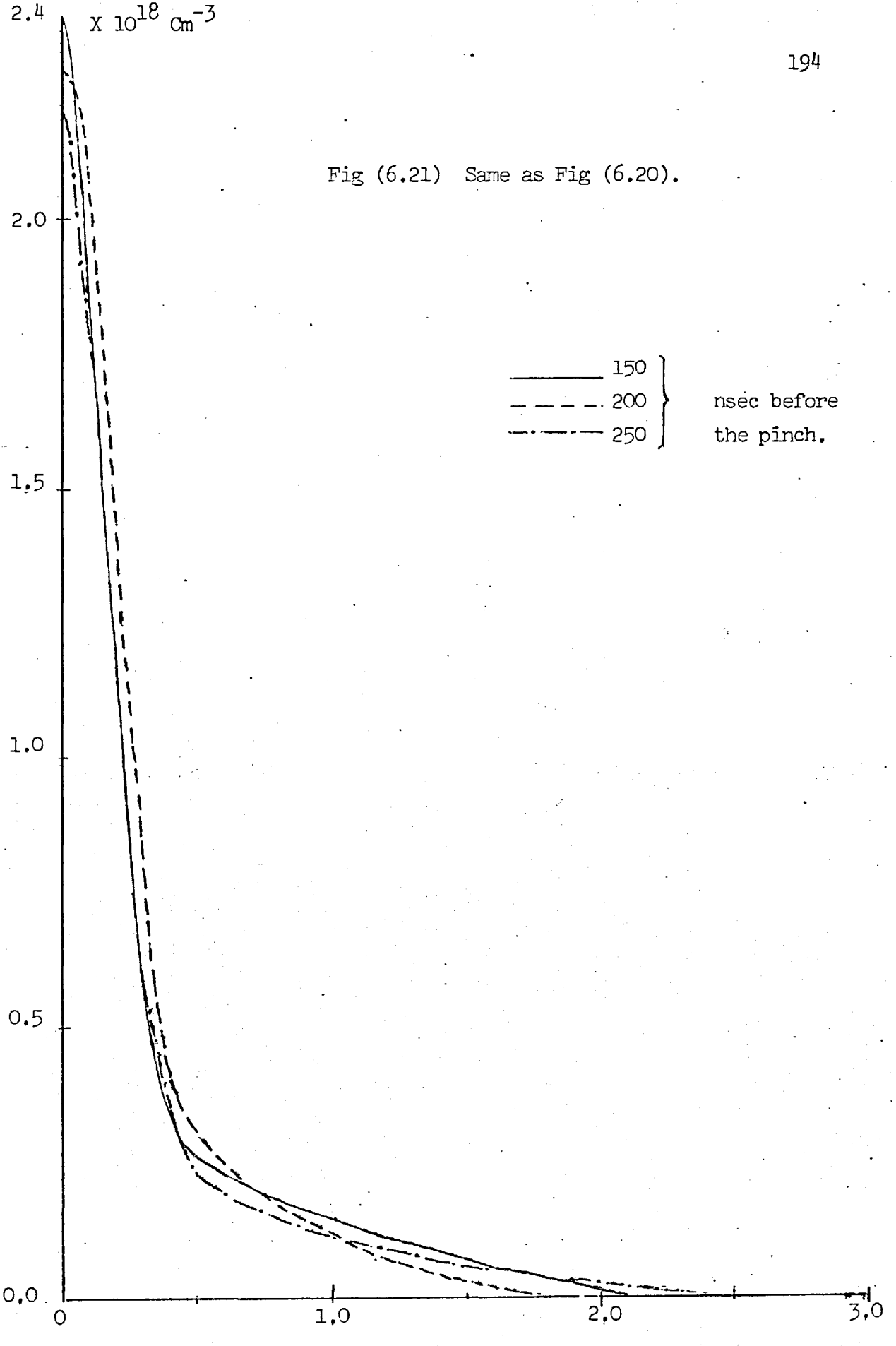

Fig (6.21) Same as Fig (6.20).

Fig (6.22) Radial distribution of electron density by Holographic Interferometry.

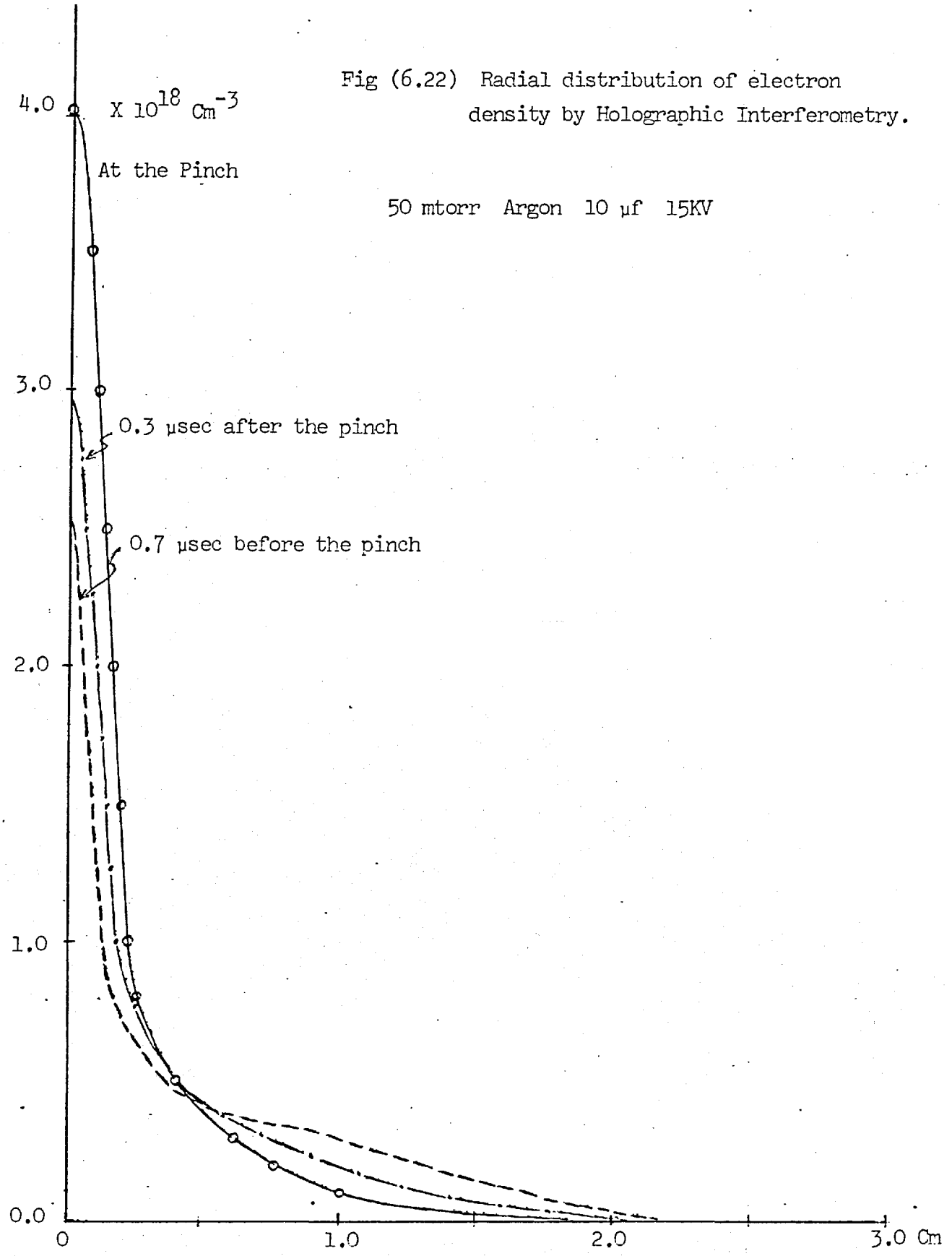

If one defines an effective diameter at half-height, the value for the above pressure at maximum compression is 2.6 ± 0.2 mm., while at about 200 nsecs earlier it is 4.2 ± 0.4 mm.

The uncertainty in the radius is due to the fact that the ruby laser giant pulse has a half-width of about 40 nsec. The discharge is very fast and speeds up as it approaches the tube axis. As seen in Fig. (6.23) the rate of increase of electron density is about five times larger near the time of pinch than what it was only 1 μ sec earlier. Thus the values near the axis will be an average over 40 nsec exposure time. This speeding up of the electron density build up rate is qualitatively explained by the shock wave model (Ref. 20) which shows that the shock in the cylindrical geometry accelerates as the radius decreases. As shown by Payne[20] this results from the momentum equation which states that a decrease in the area of the shockfront will cause an increase in the shock velocity. This is further discussed in Chapter 8.

The presence of not too inconsiderable electron density at the axis before the time of maximum compression agrees with the observation of Nation[21]. He reported the onset of axial luminosity prior to the arrival of the current sheet. This of course is true if the luminosity is associated with a region of hot dense plasma. The onset of axial luminosity is consistent with the assumption of a shock wave moving ahead of the current sheet and this essentially gives rise to the observed electron densities before the pinch in the present case.

Fig. (6.22) shows the electron density distribution at 50 mtorr filling pressure of Argon at

(i) the time of maximum compression
(ii) 0.7 μ sec before the pinch, and
(iii) 0.3 μ sec after the pinch.

The peak electron density at maximum compression is about 1.45 times larger than that at 100 mtorr filling pressure of argon. This agrees very well with the qualitative estimate on the basis of continuum light

Fig (6.23) Peak Electron Density vs time at and before the Pinch.

100 mtorr Argon 10 μf 15KV

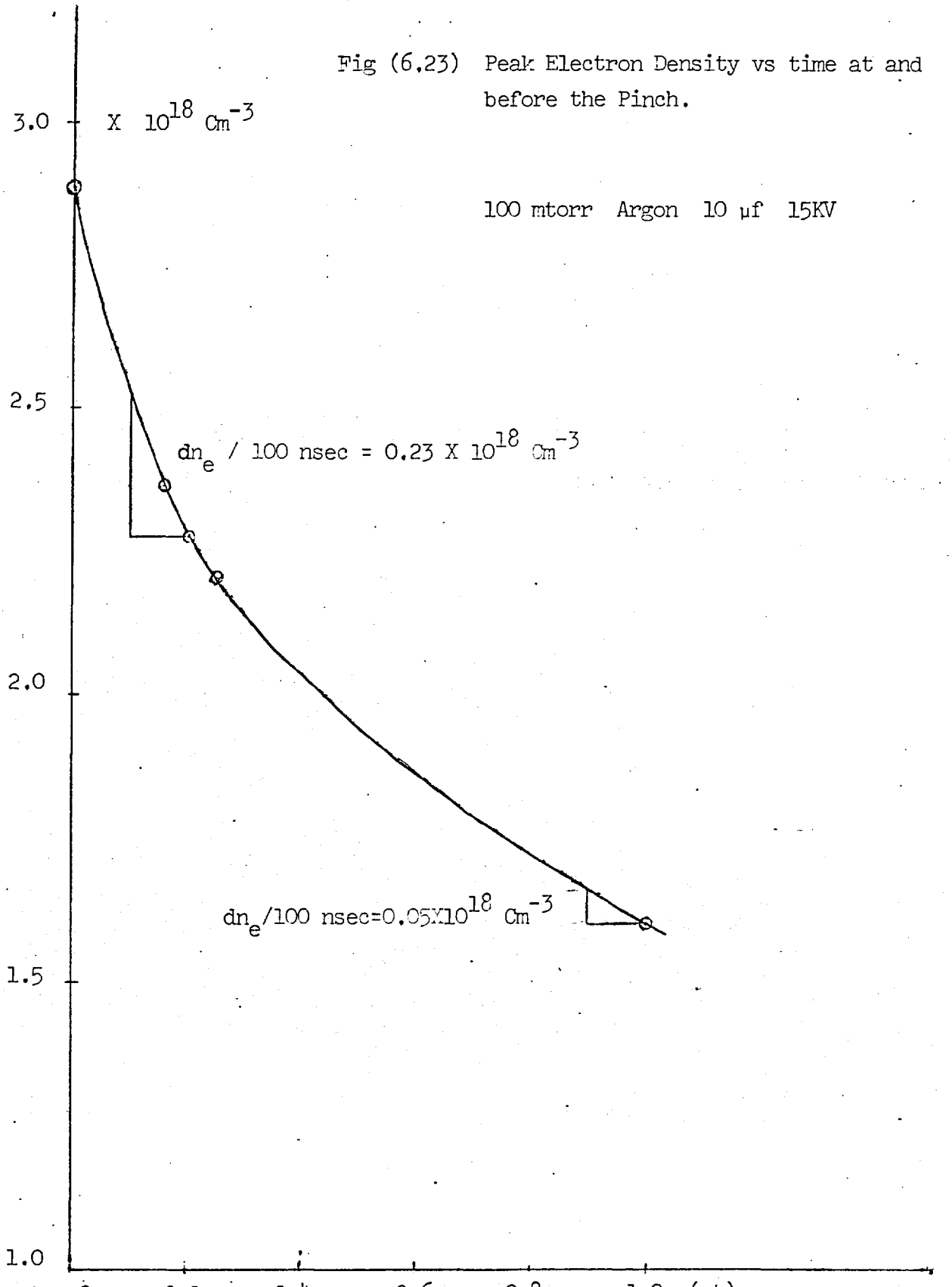

output as seen in Fig. (6.2). The time to pinch in the two cases of 100 mtorr and 50 mtorr filling pressures agree with the predictions of the Snowplough model as discussed in Chapter 8.

The holographic interferometry makes it possible to perform the differential measurements on the plasma. The curve in Fig. (6.22) showing the distribution at 0.3 μ secs after the pinch was derived from such a hologram. The Fig. (6.7c) shows the position of two ruby pulses within the life-time of the same discharge. The second pulse occurs when the light output from the discharge is almost zero, indicating a very low electron density. Thus the interferogram gives 'almost' absolute value of electron density. Any difference from the absolute value is certainly less than the experimental error in reading the interference fringes. The 'reference exposure' in other holograms is made with the neutral gas in the tube at the corresponding working pressure. The refractive index of argon at a pressure h mtorr at room temperatures is $\mu \sim 1 + 3.8 \times 10^{-12}$ h. This at 100 mtorr is

$$\mu = 1.000\,000\,000\,38$$

Thus the electron density measurements can be considered to be absolute, i.e. with respect to vacuum.

6.8 Errors due to the refraction of the probing beam

The large values of electron densities at maximum compression obtained both at 100 mtorr and 50 mtorr filling pressures coupled with strong pinching cause large refractive index gradients to be produced. This is liable to refract the probing rays and consequently produce a distorted interference pattern upon reconstruction of the hologram. The amount of deviation has been estimated in Chapter 5 on the assumption of parabolic distribution of the refractive index. This assumption is justified as seen in Figs. (6.20) to (6.22).

It is only at the base of the profile that the shape differs from

parabolic due to the broadening of the wings, but the densities there are always an order of magnitude smaller than the peak values. When the maximum value of electron density at the axis is ~ 4×10^{18} cm^{-3}, the maximum deviation in side-on measurements is $\psi_{max} \sim 6.2'$. However, when the hologram is reconstructed in the same system, the deflected ray will be reconstructed and will retrace its path to the original position of the plasma boundary as seen in Fig. (5.4). The effective displacement of this deflected ray from its true position in the plane of fringe localization is ψr_{cms}, where r is the radius of the original plasma column. For r = 0.2 cm.,

$$\psi_{max}\, r = \frac{1}{3} \text{ microns}$$

Thus any error due to refraction of the beam in side-on measurements using holographic interferometry even for large electron density can easily be discounted.

6.9 Miscellaneous

6.9.1 The Electromagnetic T-tube

Before the measurements on Z-pinch were started, an electromagnetic T-tube was used as a plasma source to perform the holographic interferometric measurements. The shock tube was originally being used by Chowdhury[22] as a light source for spectroscopic measurements of shift to width ratios of spectral lines. The energy density being fed into the T-tube was only 625 Joules and the diameter of the cylindrical section was 1.6 cms. This is small compared to T-tubes used by McLean and Ramsden[23] where larger optical paths were available.

Unfortunately, at the time of measurements, no optical wedge was available to produce background fringe pattern for increasing the sensitivity of measurements. For this reason only contour fringes in the T-tube were obtained. Due to small refractive index change provided by the T-tube, it was difficult to perform accurate interferometric

measurements. Moreover, the breakdown of the gas and the ejection of the plasma into the arm of the tube was very jittery. It was due to these reasons that detailed measurements of electron densities on T-tube could not be carried out. The following therefore only briefly describes the holographic measurements and the results of these measurements.

The T-tube consisted of two electrodes made of heavy alloy. A brass-back strap was attached to one of the electrodes and ran parallel to the cross-arm. The magnetic field of the current through this back strap interacted with discharge current between the electrodes to apply a Lorentz force on the plasma in the perpendicular direction to both the magnetic field and the discharge current. The expansion tube was originally cylindrical and caused internal reflection of the laser light near the edges. For this reason it was replaced by a square section tube of internal dimensions of 1.5 cm square. A copper piston was also introduced at the end of the expansion tube to serve as a reflector for the incident shock. The condenser bank consisted of a single capacitor of 2 μf and charged to 25 KV.

The scatter-plate arrangement was employed to take holograms. The horizontal T-tube was illuminated side-on by the diffuse object beam, the reference beam passing just outside it. The interferograms were taken at various filling pressures of Helium gas at 25 KV charging voltage. The timing of the laser pulse was also varied to perform measurements at various positions of shock front in the tube. The value of electron density obtained at 1 mm. of Hg. filling pressure was

$$\bar{n}_e \sim (0.8 \times 10^{17} \pm 50\%) \text{ cm}^{-3}$$

More accurate values could have been obtained if an optical wedge had been available to produce a background fringe pattern.

The shock velocity was measured by collecting continuum light from the plasma by two lightpipes through very narrow pinholes and placed at

known distances w.r.t. each other and the electrodes. These signals were fed to the same photomultiplier and observed on an oscilloscope. The knowledge of the temporal separation of the two distinct peaks of light allowed a calculation of the velocity. The Fig. (6.24) shows the two traces of optical signal operating in air and in Helium. The velocity of the incident shock at 25 KV operating voltage was $v = 3.0$ cms/μsec. for 1 mm. of Hg. of Helium, and $v = 2.5$ cms/μsec. for 2 mm. of Hg. of Helium. These measurements helped to evaluate the electron densities of the plasma behind the incident shock using the results of computations by Chowdhury (pp.39 of Ref.22). He has solved the equations describing the equilibrium state of the gas behind the incident and the reflected shocks with the Saha equation and the equation of State. The parameters of the shocked gas, e.g. electron density and temperature etc. are calculated in terms of initial filling pressure and the shock velocity. For shock velocity of 3.0 cms/μsec. at 1 mm. filling pressure of Helium, the electron density (at incident shock) of 1.88×10^{17} cm^{-3} is predicted. This is higher than the value obtained by holographic interferometry. The discrepancy in the above values of electron density can be roughly accounted for by noting that the shock front in the incident shock might not be coincident with the luminous front thus leading to errors in velocity measurements.

In conclusion, it must be mentioned that by holographic interferometry the measurements on shock tube can be simplified as no compensating tube is required in the reference arm. Furthermore, off-set interferometry[24] can be performed by simply reconstructing the hologram at different angles of observation.

6.9.2 Holographic Moiré Pattern

The conventional Moiré technique utilizes two screens with a regular pattern of fine lines or dots with the event between them, and has only recently received attention for refractive index measurements[25],[26]. Holographic interferometry can be used to see Moiré fringes of pure phase

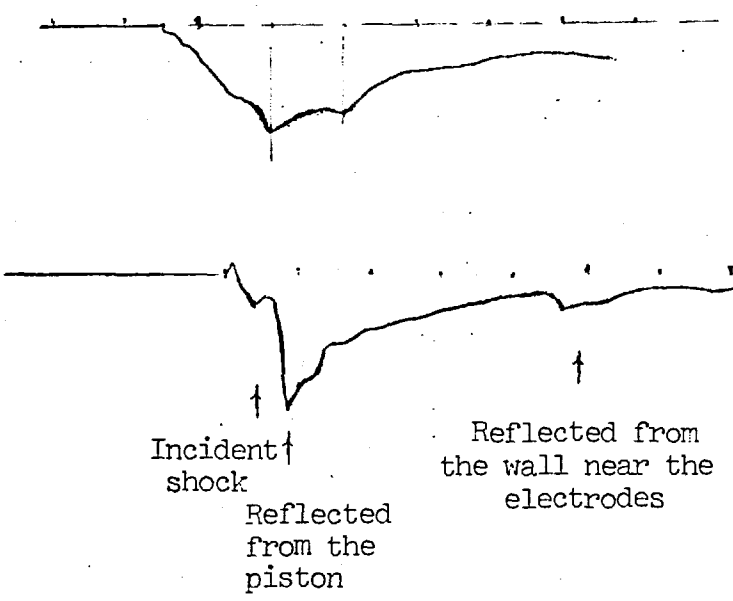

Fig (6.24) Light output from the T-tube.

Fig (6.26) Reconstructed Moire Pattern of a gas flame.

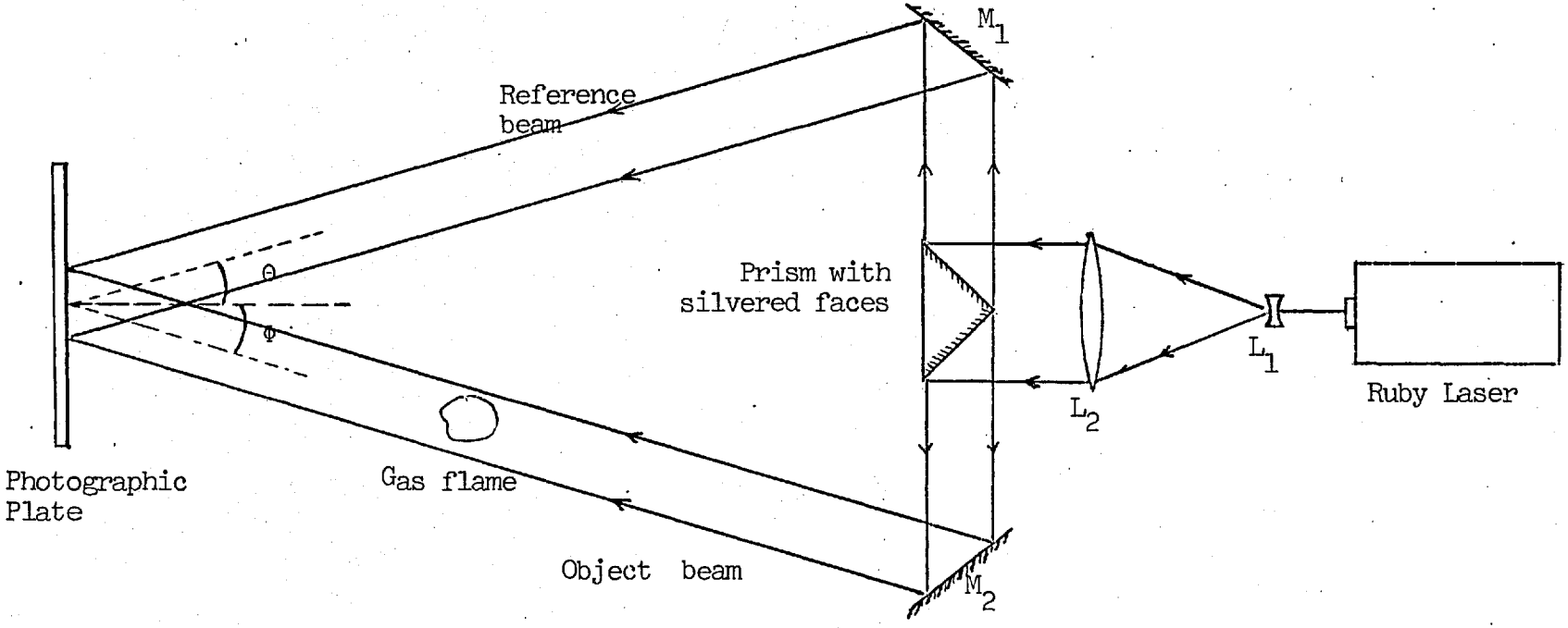

Fig (6.25) Arrangment for obtaining Holographic Moire Pattern.

objects such as gas flames, high pressure gas flows in aerodynamics and plasmas etc. This is possible because of the fact that when two collimated coherent laser beams are introduced on a high resolution photographic plate, one obtains a diffraction grating. Moire patterns will be displayed if two sets of such gratings are super-imposed by means of double exposure holography.

In an attempt to study the plasma in the above mentioned T-tube, the arrangement shown in Fig. (6.25) was used to obtain two collimated beams from the ruby laser. The path lengths of these two beams reaching the photographic plate were within the coherence length of the laser output. The spatial frequency of the resultant grating in the plane of the photographic plate surface is given by

$$\text{spatial frequency} = (\sin\theta + \sin\phi)/\lambda ,$$

where θ and ϕ are the angles, the collimated reference and the object beams make with the normal to the plate, and λ is the wavelength of the laser light. Both θ and ϕ were equal to 4^{o} and the resultant grating made with ruby wavelength (λ = 6943 Å) had 200 lines/mm.

In a preliminary check of the system a bunsen burner flame was introduced in one of the two exposures of the double exposure hologram.

The advantage of such a hologram is that the interference pattern of the phase object can be viewed with white light. The pattern can be seen by simply reflecting the white light roughly at the angle θ and observing the reflected light at the angle ϕ, both the angles being the same as during the formation stage. Fig. (6.26) shows a photograph of the pattern with white light illumination.

When the square section glass tube was introduced into the object beam, the very bad optical quality of the glass completely spoilt the collimation of the beam. This did not allow a grating to be formed and hence the Moire pattern for the plasma could not be obtained. However, the pattern obtained with the flame demonstrated the workability of the

idea which would certainly be utilized in situations where the collimation of the beam is retained after passing through the test region.

In passing it must be mentioned that Moiré beats can be easily produced using the arrangement shown in Fig. (6.25). If one of the mirrors M_1 (say) is slightly rotated about a vertical axis, during one of the two exposures, it will result in a slight change of the grating spacing. The superposition of the displacement due to phase object on the Moiré beat will result in a finite fringe interferogram.

6.9.3 Schlieren photography and shadowgraphy using holography.

Recently these two techniques have been applied to plasmas[27] to provide information complementary to that of interferometry. Application of holography to produce schlieren photographs and shadowgraphs has been suggested by Tanner[28]. The hologram is merely used to freeze the event and study it in the usual arrangements for these techniques. However, the schlieren technique was previously widely used because it was experimentally less demanding than interferometry. Since schlieren pictures are harder to evaluate than interferograms and lead to density gradients rather than to density, there is no reason to produce schlieren pictures especially when holography inverts the relative ease in favour of interferometry. The other disadvantage of producing schlieren pictures using holograms is that the hologram subtrate adds a source of noise. The same applies to producing shadowgraphs. Due to these reasons these techniques were not utilized for the study of the plasma.

6.10 Conclusions

In this chapter are presented the results obtained by holographic interferometry of a Z-pinch plasma. In addition to the development of the technique, the emphasis has been on its actual application to a particular plasma. The use of scatter-plate system has been shown to allow the measurements with the simple ruby laser with multimode operation. However, when wavefront distorting elements are present in the system,

the need for improving the spatial coherence arises. Again the use of a simple pinhole mode selector is shown to be sufficient to achieve the desired results.

The results for circularly symmetric plasma distribution are obtained by side-on measurements. The use of holographic interferometry is particularly helpful in this configuration. The errors in the results are mainly due to the inability to use background fringe pattern when the contour fringes are already very narrowly packed. However, since one can still measure to quarter of a fringe this error is not large. This diagnostic method has the advantage over cw laser interferometers (see the next chapter) that the deviation due to refraction of the beam is negligible in this case.

It can thus be concluded that the holographic interferometry is an asset to plasma diagnostics especially in situations where other diagnostic techniques are difficult to apply.

References

(1) G.V. Ostrovskaya et. al. J.E.T.P. Lett., 4, 83 (1966).

(2) F.C. Jahoda et. al. Applied Optics, 6, 1407 (1967).

(3) F.C. Jahoda. 8th International Conference on Phen. Ioniz. Gas, Vienna (1967), p.509.

(4) A.N. Zaidal et. al. Sov. Phys. - Tech. Phys., 11, 1650, (1967).

(5) A. Kakos et. al. Phys. Letters, 23, 81 (1966).

(6) Yu.I. Ostrovskii et. al. 'Holographic Plasma Diagnostics with Lasers', Rep. for the First Intern. Congress on Laser Applications, Paris, (1967).

(7) A.N. Zaidal et. al. 8th Int. Conf. on Phen. Ioniz. Gas, Vienna (1967) p.508.

(8) G.V. Ostrovskaya and A.N. Zaidal. Phys. Letters, 26A, 393 (1968).

(9) Yu.V. Ashcheulov et. al. Phys. Letters, 24A, 61 (1966).

(10) L.O. Heflinger, R.F. Wuerkerand R.E. Brooks. 'Holographic Interferometry', J. Applied Physics, 37, 642 (1966).

(11) D. Gabor. Proc. Roy. Soc. 197, 454 (1949).

(12) F.C. Jahoda. Report LA-3968 (1968).

(13) V. Evtuhov and J.K. Neeland. Appl. Optics 1, 517-520, (1962).

(14) D.F. Nelson and R.J. Collins. J. Appl. Phys. 32, 739-740, (1961).

(15) H.R. Griem. Plasma Spectroscopy p.176, McGraw Hill Book Co. New York (1964).

(16) W.J. Pearce 'Optical Spectrometric Measurements of High Temperatures' p.125. University of Chicago Press (1961).

(17) W.E. Gericke. Z. Astrophys., 53, 68, (1961).

(18) S.J. Fielding. Ph.D Thesis. London University. (1969).

(19) Kjell Bockasten. "Transformations of observed Radiantes into Radial Distributions of the Emission of a Plasma". J. Opt. Soc. Am. 51, 9, (1961).

(20) R.B. Payne, J. Fluid Mechanics 2, 185 (1957).

(21) J.A. Nation. (1960). Ph.D Thesis, London University.

(22) S.S. Chowdhury. (1969) Ph.D Thesis, London University.

(23) S.A. Ramsden and E.A. McLean. Nature 194, 761 (1962).

(24) R.H. Huddlestone and S.L. Leonard. Plasma Diagnostic Techniques, p.454. Academic Press, New York. (1965).

(25) Y. Nishijima and G. Oster. J. Opt. Soc. Am. 54, 1 (1964).

(26) G. Oster, M. Wassermann and C. Zwerling. J. Opt. Soc. Am. 54, 1 (1964).

(27) V. Ascoli-Bartoli, S. Martellucci and E. Mazzucato. Proc. 6th Int. Conf. Ionization Phenomena in Gases, Paris, 1963, Vol.4, p.105 (North-Holland, Amsterdam, 1964). Phys. Rev. 107, 345 (1957).

(28) L.H. Tanner. J. Sci. Inst. 43, p.81 (1966).

(29) D.D. Burgess, A.E. Dangor and J.E. Jenkins, Brit. J. Appl. Phys. 18, 1281 (1967).

(30) A.E. Dangor and S.S. Chowdhury. J. Quant. Spectrosc. Radiat. Transfer, 9, pp.705-711 (1969).

(31) M.H. Key. (1966). Ph.D Thesis, London University.

(32) A.A. Vuylsteke, Theory of Laser Regeneration Switching. J. Appl. Phys. 34, 1615-1622, (1963).

(33) Born M. and Wolf E. (1964), Principles of Optics. 2nd Edition. (Oxford: Pergamon Press)

(34) J.W.C. Gates. J. Sci. Instr. 1, 989 (1968).

Chapter 7.

Electron density measurements with Michelson Interferometer using He-Ne laser beam.

7.1 Introduction.

It was desired to make a check on the measurements of electron densities and their distributions by an independant method. In recent years CW laser interferometry, first experimentally demonstrated by Ashby and Jephcott [1], has proved to be a convenient and quite accurate technique for plasma density measurements. Unlike spectroscopic methods, it involves no assumptions about local equilibrium conditions in the plasma and yields with fair accuracy the change in optical length due to plasma in the path of the laser beam.

Since the first application by Ashby and Jephcott, many variations in the method have been effected to improve its versitality. The choice of a particular configuration depends on such factors as its frequency response, sensitivity and immunity to strong deviations of the laser beam by large refractive index gradients in the plasma. Before it is possible to decide on a particular configuration for our application, it is necessary to examine various systems for their range of operation with reference to the above mentioned characteristics. This is done in the next section which leads to the choice of the Michelson interferometer to be used for side-on measurements of electron density distributions in the

Z-pinch discharge.

7.2 Review of Methods for Electron density measurements using He-Ne laser;

The various systems of electron density measurements using CW lasers can be divided in the following three categories.

a) Ashby-Jephcott type (multiple beam transit type)
b) Transmission Fabry-Perot " " " "
c) Single and double transit type.

There are in turn two sub-divisions each for a) and b). These being i) Cavity with plane-parallel mirrors and
ii) Concave resonator.
The Table(7.1) describes the essential features of each system and these are shown in Figs. (7.1) and (7.14).

a) The Ashby-Jephcott type.
In this system the laser is used simultaneously as the source and the detector. When the reflected light from the reference cavity containing plasma is fed back into the laser cavity, the amplitude of the laser oscillation changes. Interference occurs between the reflected beam and the cavity field and the whole laser intensity is thus strongly dependent on the phase of the reflected beam. The phase information contained in the returning signal shows up as amplitude modulation on the laser output.

The main limitation of the Ashby-Jephcott type interferometer is its inherently low frequency response. The parameters that determine the time response of this interferometer are discussed by Gerardo et. al. [9] and by

TABLE (7.1)

S.No	The Configuration	Diagram No.	Interference wavelength	Detection wavelength	Sensitivity = (Half-fringe)	Frequency response	Depth of modulation	Spatial resolution	References
(a)	Ashby-Jephcott type	Fig(7.14)			$\bar{n}_e$/fringe $= \frac{1.12\times10^{13}}{L\lambda}$ Cm^{-3}				
i)	Plane-parallel reference cavity	(a)	0.63μ	0.63μ	$\bar{n}_e = \frac{0.89\times10^{17}}{L}$	3 Mc/s	1/e at 150 Kc/s	same as dia. of the laser beam	(1),(2).
			3.39μ	0.63μ	$0.165\times10^{17}/L$	"	<5% at 1Mc/s	"	"
			3.39μ	3.39μ	"	7 Mc/s	"	"	(3)
			1.1523 μ	1.1523 μ	$0.46\times10^{17}/L$	~3 Mc/s	-	"	-
ii)	Concave resonator	(b)	3.39 μ	3.39 μ	$4.8\times10^{15}/L$ for $(d/r = \frac{1}{2})^*$	7 Mc/s	generally poor	Poor compared to (a)	(4)
			1.1523 μ	1.1523 μ	$1.25\times10^{16}/L$	-	"	"	"
iii)	Plane - parallel reference cavity with M_3 made to oscillate.	-	3.39 μ	3.39 μ	$3.4\times10^{13}/L$	1 Mc/s	-	-	(5)
(b)	Transmission Fabry- Perot								
i)	Plane-parallel reference cavity	(c)	Any laser wavelength	Interference wavelength	$0.89\times10^{17}/L$	~15 Mc/s	In practice poor finess (2-3)	Same as dia. of the laser beam	(2),(6)
ii)	Confocal resonator	(d)	"	"	"	Band width f= c/2LF	Finess F = 20-30	"	(7)

	(Continued)								
(c)	Single and Double Transit types								
i)	Mach-Zehnder system (single transit)	(e)	"	"	$\bar{n}_e = 1.12 \times 10^{13} / L\lambda$ (for half-fringe)	Almost infinite	fringes cosine terms	Very large by using pinholes	(2)
ii)	Michelson interferometer (double transit)	Fig(1)	"	"	$= 0.56 \times 10^{13} / L\lambda$ (for half fringe)	"	"	"	(8)

* $$\Delta \bar{n}_e = \frac{1.12 \times 10^{13}}{L\lambda} \left\{ \Delta q + \frac{\Delta m + \Delta p}{\pi} \cos^{-1} \left(1 - d/r \right)^{\frac{1}{2}} \right\}$$

r ≡ radius of curvature of each mirror,
d ≡ Length of the cavity $M_2 - M_3$

For the case $d/r = \frac{1}{2}$, the minimum density measurable by changes in m or p is $\frac{1}{4}$th of that measurable by changes in q.

TABLE (7.1)

Dangor [10]. They show that the time response depends upon the quality factor Q of the reference cavity. It determines the maximum rate at which the power transmission through the cavity can be altered. In addition, the rate equations for the He-Ne laser have to be considered since the laser acts not only as source but also as detector. If the loss factor of the laser cavity is suddenly altered, it takes a finite time to obtain a new stationary operation of the laser. On the basis of such considerations Gerardo et. al. find the time response to be nearly independent of all parameters except the transmission coefficient through mirror M_2. Increasing this transmission improves the frequency response. But, on the other hand, in a small-gain laser such as the 6328Å, He-Ne laser, it is necessary to use a mirror M_2 of high reflectivity in order to obtain laser action at all. Consequently this imposes a limit on the maximum attainable frequency response. When using a high-gain laser, such as the 3.39μ He-Ne laser, a low quality factor (small reflectivity of M_2) can be tolerated and better frequency response can therefore be expected. Although a many-fold increase is obtained as seen in Table 7.1 , it is still slow as compared to the rates involved in the fast Z-pinch described in the last chapter.

A disadvantage of plane parallel reference cavity in the Ashby-Jephcott system is that the multiple reflections cause the off-axis rays in the cavity to be lost from the system. This results in the degradation of the modulation of the resultant fringes. This problem is

ASHBY- JEPHCOTT ARRANGEMENT.

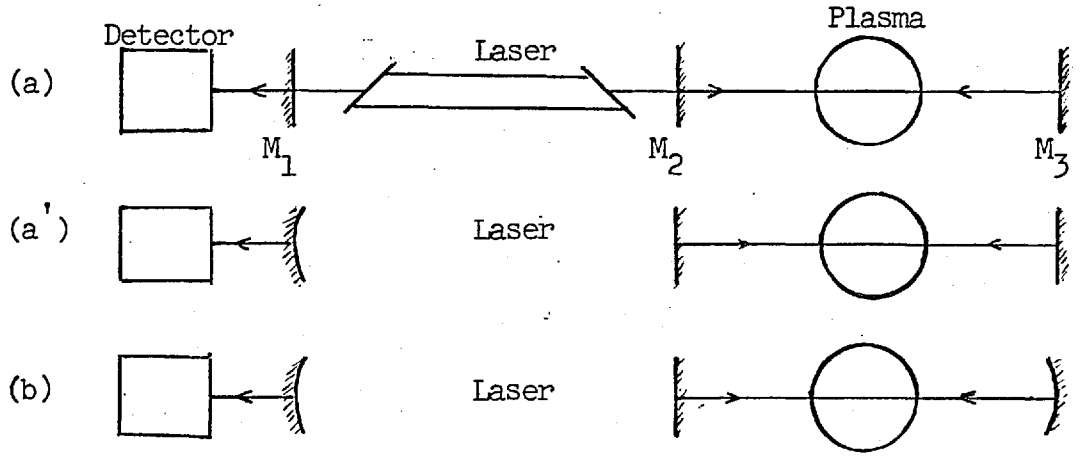

TRANSMISSION FABRY- PEROT.

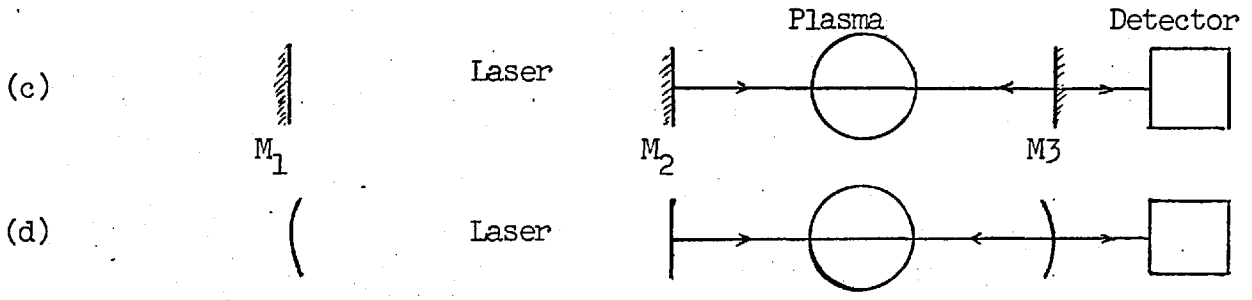

MACH- ZEHNDER SYSTEM.

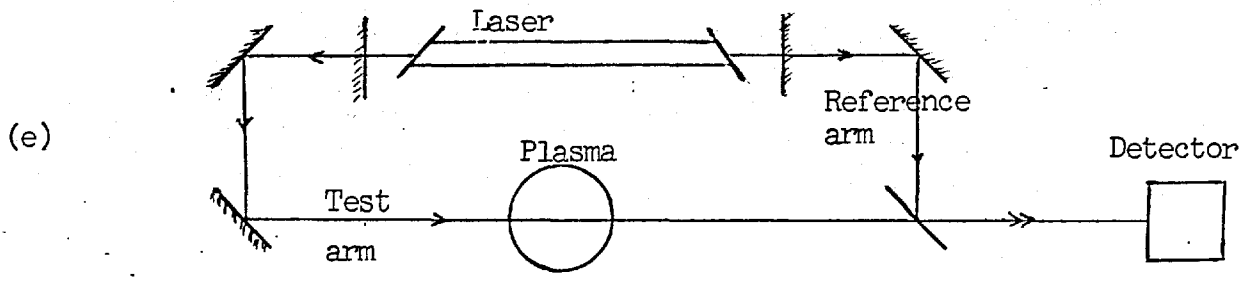

Fig (7.14) Various interferometric arrangments using cw-lasers.

resolved by the use of concave resonator. This system was suggested by Gerardo et. al.[4] for its improved sensitivity compared to that of the plane-parallel system. This is because the light ray entering the reference cavity M_2 M_3 makes S double traversals before it retraces itself to the entrance point.

The minimum detectable electron density variation corresponding to the observation of half a fringe is given by:

$$= \frac{0.56 \times 10^{13}}{S\ L}\ Cm^{-3}$$

However, the use of transverse modes of the reference cavity for improving the sensitivity results in a degradation of the spatial resolution.

b) Transmission Fabry-Perot system.

In this system the laser is no longer used as detector and the reference and the laser cavities are decoupled. The laser output through mirror M_2 is approximately constant i.e. independent of optical path changes in the reference cavity. This results in a significant improvement of the frequency response of the system over that of the Ashby-Jephcott arrangement. The transmitted signal through M_3 will also vary with the plasma changes as the laser radiation is resonantly supported in the reference cavity. Since the quality factor can now be made considerably smaller, the time response can be made equal to the time required for the light to make a few traversals through the reference cavity. For slow discharges

the use of concave confocal resonator is preferred over the plane-parallel cavity. This is because the former has very high finesse due to the mirror surfaces being coincident with the surfaces of constant phase of the radiation. The high finesse is, however, obtained at the cost of frequency response and is not necessary for the study of fast discharges. An advantage of the spherical cavity is its relative insensitivity to mirror misalighment with consequently a higher tolerance to deflections of the beam inside the davity caused by electron density gradients in the plasma.

Another limitation of the confocal system, is its lack of spatial resolution. The use of GEC laser tube type XL 614 with M_1 and M_3 both having a radius of curvature of 2 meters resulted in a beam of $1mm^2$ cross section in single mode output. The holographic measurements indicated a pinched coherence with a radius of 2mm at maximum compression at 50 filling pressure of argon. Thus the laser beam is unable to provide sufficient spatial resolution. Narrow apertures could not be introduced into the cavity because of the resulting diffraction of the beam foiling the intended purpose and also because of the considerable loss of already meagre power output.

c) Single and double transit types.

The only other systems which can be utilized for electron density measurements of the fast unstabilized Z-pinch are Michelson and Mach-Zehnder interferometers. The former is a double pass system while there is only one traversal of the beam through the latter. Thus the Michelson system produces twice the number of fringes as

compared to Mach-Zehnder interferometer for the same plasma electron density change. The time response of both the systems is extremely fast being just the time taken by the beam to traverse the plasma and is limited only by the detector bandwidth.

The problem of beam deviation by large refractive index gradients in the plasma is also resolved by using a lens to image the plasma on the detection system as discussed in Section (7.4). The use of very narrow aperture at the image plane limits the effective beam diameter to the diameter of the aperture thus providing good spatial resolution. The Michelson system being identical to Mach-Zehnder in all respects with the exception of its sensitivity being double to that of the latter is finally chosen to perform the measurements of electron density distributions and is described in the rest of the chapter.

7.3 Michelson interferometer using He-Ne laser.

Since in this system the laser is only a source of light and is in no way coupled to the plasma cavity, it was possible to use Spectra Physics laser Model 132. This could not be used with Fabry-Perot system; as it has mirrors with radii of curvatures which could not form a simple cavity which would lend itself to easy mode analysis (see 7.2). The laser had an output of 1m watt of radiation at 6328Å. This output power is sufficient to produce reasonable signals even when very narrow apertures are inserted into the system.

Time-resolution of this system is determined by the

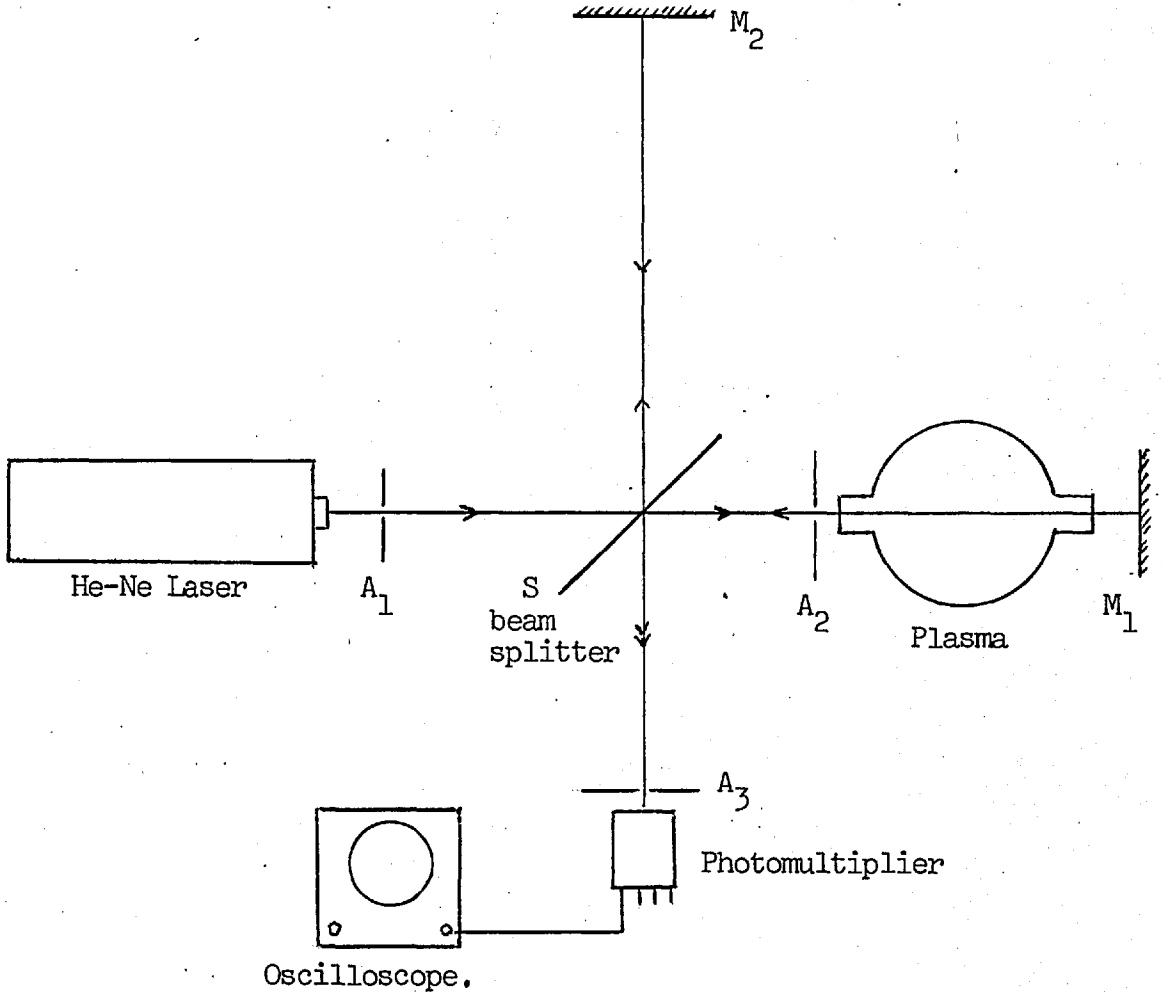

Fig (7.1) Cw-laser interferometer using Michelson System.

double transit time of laser beam through the plasma and by the response time of the detector. The former is in any situation only a few nanoseconds while the latter can also be as low as 15 n sec. The fringe modulation is independent of the laser and is not reduced even at very high frequencies. Also it does not require many transits of the laser beam through the cavity to have a reasonable fringe finesse as is the case in Fabry-Perot system, since in the present case the fringes are cosine square terms.

Figure (7.1) shows the actual experimental setup. The laser has a beam diameter of 0.8 mm and a beam divergence of 1.0 milli radians at $\frac{1}{e^2}$ points of the intensity distribution. A beam splitter S reflected about 50% of the light to the mirrors M_2 and allowed the rest of the light to proceed to mirror M_1 through the plasma tube. Reflected light from M_1 and M_2 was made to overlap and fed to the RCA 7265 photomultiplier which had a S20 photocathode. It had a quantum efficiency of 4% at 6328Å. An interference filter of about 70% transmission was used at the entrance of the photomultiplier and had a bandwidth of 5Å around the He-Ne wavelength. The apertures A_2 and A_3 further limited the stray optical pickup from the plasma.

The tube previously used for holographic interferometric measurements had no side windows. It was noted that the poor optical quality of the glass tube distorted the laser beam wavefronts and caused non-uniform refraction across the tube diameter. It was therefore decided

to fix side arms of 1" inner diameter to the tube to hold the quartz windows with an 'O' ring seal when the tube is evacuated. The windows could get 'dirty' after firing a few dozen or so shots of the plasma and were easily detachable for cleaning their surfaces. Fig. (7.2) shows the tube with the side arms attached to it.

The above arrangement was chosen due to the ease of obtaining a vacuum tight seal by just pushing the windows against the 'O' rings. Although the windows were not exactly parallel the laser beam retraced its path when reflected by the mirror M_1. With the Michelson interferometric arrangement one can afford to use windows which are not necessarily very good optical flats. This is because the laser beam makes only a double transit through the plasma tube.

The lengths of the arms SM_1 and SM_2 were adjusted such that the angular width α of the central spot of the interference pattern was more than the beam divergence E of the laser beam. In such a case the intensity of the emergent beam from the interferometer is almost uniform across its cross-section and will vary between a maximum and a minimum depending on the difference in the optical path length of the two beams. α is given by

$\alpha = \sqrt{\lambda/d}$ where d is the difference in the arms lengths SM_1 and SM_2. For α to be at least five times larger than E (= 1 milli radian), SM_1 and SM_2 should be within 2.5 cms of each other. The other consideration which places a restriction on the difference of SM_1 and SM_2 is the coherence length of the laser. The output

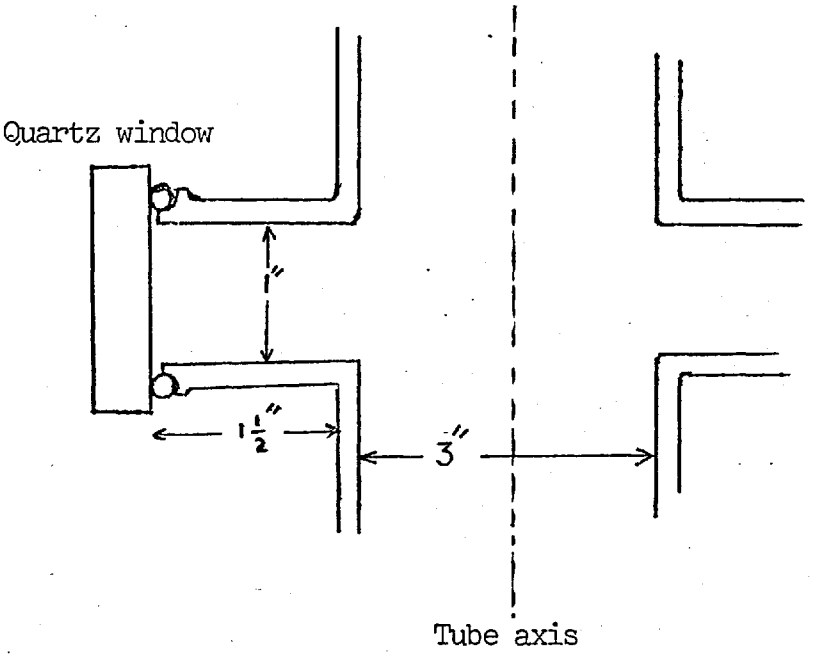

Fig (7.2) Side arms for affixing windows to the tube.

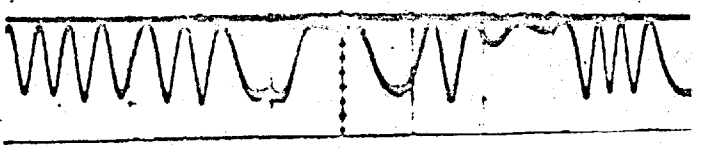

Fig (7.3) Trace showing depth of modulation of the fringes.

from the He-Ne laser has a Doppler width of 1700 Mc/s which includes three longitudinal modes of the cavity spaced 500 Mc/s apart. The coherence length of the radiation is thus 20 Cms which is far larger than the limit placed by the considerations of beam divergence.

The mirror M_1 was plane with dielectric coatings for a reflection of 99.9% at 6328Å It was mounted on a piezo-electric tubular resonator which was energized at 10.2 KC resonant frequency from a high frequency oscillator. This helped in the alignment of the mirrors by providing fringes due to the change of the path length of the arm SM_1. The frequency of these fringes depends on the velocity of the mirror during its vibration and could be controlled by changing the driving voltage. The mirror M_2 which was also plane with 99.9% reflectivity was fixed. The fringe modulation depended on the relative intensities of the two beams in the region of overlap. The arm SM_1 had as much as 20% more losses due to four additional reflecting surfaces as compared to the arm SM_2. This could be compensated if the beam splitter had a reflectivity of 0.45. In this manner fringes with almost 100% modulation could be achieved. Fig. (7.3) shows such fringes obtained by vibrating the mirror M_1.

The band width of the system was essentially determined by the response time of the detection system. The RCA 7265 photomultiplier has a rise time of 2n sec. A 75 Ω terminated cable could be used because of the laser being able to provide sufficient signal even when

most of the light was wasted due to the use of very narrow pinholes (see sec. 7.4). The Tetronix 555 scope was used with a type K plug in preamplifier unit and had a rise time of 12 n sec. This amounted to a bandwidth of 30 Mc/s. This is about 30 times larger than the upper limit for Ashby and Jephcott system (sec. 7.2). It must be emphasized that the frequency bandwidth of the Michelson system itself is almost infinite and the limitation is entirely due to the response time of the detection system.

7.4 Electron Density measurements of Unstabilized Z-pinch using Michelson system.

The purpose of these measurements was to check and compare the results obtained by holographic interferometry. By the latter method, one obtains a spatial distribution of refractive index at one particular instant averaged over the very short duration of a ruby laser giant pulse. The use of CW He-Ne laser gives the temporal behaviour of the refractive index averaged along the path of the narrow laser beam. To obtain the distribution of the refractive index, one has to scan across the whole width of the plasma column and then to perform an Abel Inversion on the measured distribution at a particular time during the life of the discharge.

The discharge was operated under the same working conditions of charging voltage and filling pressure of the gas as during the measurements of holographic interferometry. These are 15 KV; 50 mtorr and 100 mtorr filling pressure of argon.

A preliminary discharge showed a large background stray optical pickup which completely masked laser light from the interferometer. Completely wrapping the plasma tube with black paper and further covering it with black rags and also housing the photomultiplier in a similar 'cage' the optical pickup disappeared completely. Fig (7.4) shows an initial record of the interference fringes on a very slow time scale. This indicates the occurence of the pinch after about 6.5μ sec from the onset of the discharge. There is then an expansion of the plasma, instabilities set in and thereafter the plasma column withers away. However one can still observe some gross effects which neither lend themselves to an easy interpretation nor do they offer any useful information about the after glow as the method lacks sensitivity at this range of wavelength. Fig. (7.4) also shows a fall off of the amplitude of the fringes at and near the pinch. This effect is better shown in Fig. (7.5). It made the measurements of fringe shifts impossible at or near the pinch.

The possible reasons for such an effect can be the following

1) The large gradients of refractive index in the plasma at or near the time of pinch may refract the beam by an amount such that it no longer interferes with the reference beam. Since an aperture of the same diameter as that of the laser beam is used to admit the latter to the photomultiplier, any deflection greater than this amount would cause the dc level of signal to drop to half its original value. This is because the reference beam is still undeviated. This distance between mirror M_1 and the aperture A_3 is two meters. Thus a deviation of 1.0 m radian (as discussed later) will cause the beam to be deflected by 2mm from the

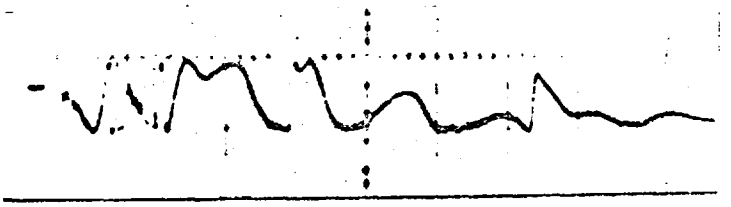

Fig (7.4) He-Ne Laser Interferogram. 15 KV 50 mtorr argon

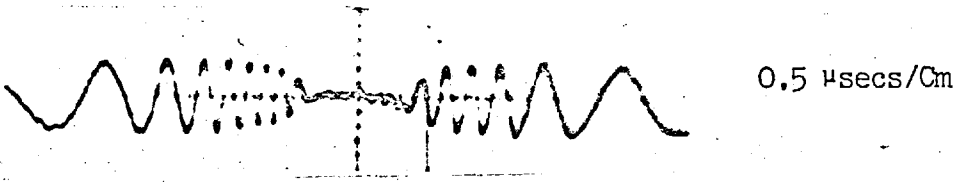

Fig (7.5) He-Ne Laser Interferogram. 15 KV 50 mtorr argon

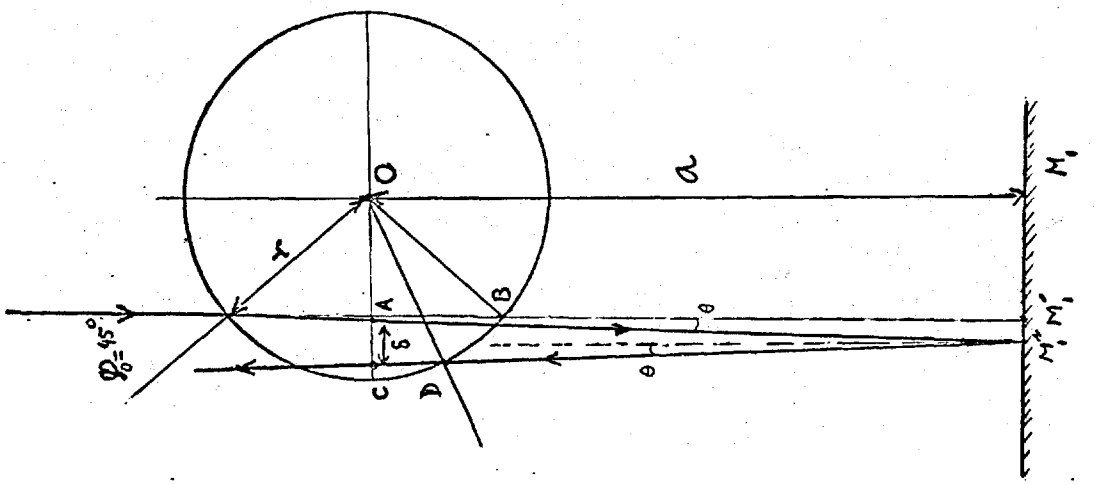

Fig (7.7)

aperture A_3.

This effect can be eliminated by using a lens for imaging the mirror M_1 on to the aperture at the entrance of the photomultiplier. Any rays refracted by the plasma will on reflection by mirror M_1 be focused by the lens on to the aperture.

2) The diameter of the pinch at maximum compression is less than one centimeter. The probing beam with a diameter of 0.8 mm at $\frac{1}{e^2}$ points is bound to have large refractive index gradients across its cross-section. This will cause a variation of phase across the beam when it combines with the reference beam at the region of interference. The effective amplitude of the fringes will decrease due to the random addition of phases over the wavefronts. This is perhaps the reason for the loss of modulation of the observed fringes at or near the maximum compression.

Alternatively, the gradients of refractive index across the beam cross-section can be considered to cause a velocity gradient over the cross-section. This will produce a tilting of the wavefront with respect to the reference wavefront hence producing wedge fringes (11, 12) at the region of interference. The spacing d of the wedge fringes is given by $d = \frac{\lambda}{2\theta}$, which for a deviation of 0.5 milli radians amounts to ~ 0.63 mm for the He-Ne laser wavelength. Thus if the pinhole size is 0.6 mm, there will be a complete loss of modulation due to the averaging of the intensity by the presence of a dark and a bright fringe in the region of interference.

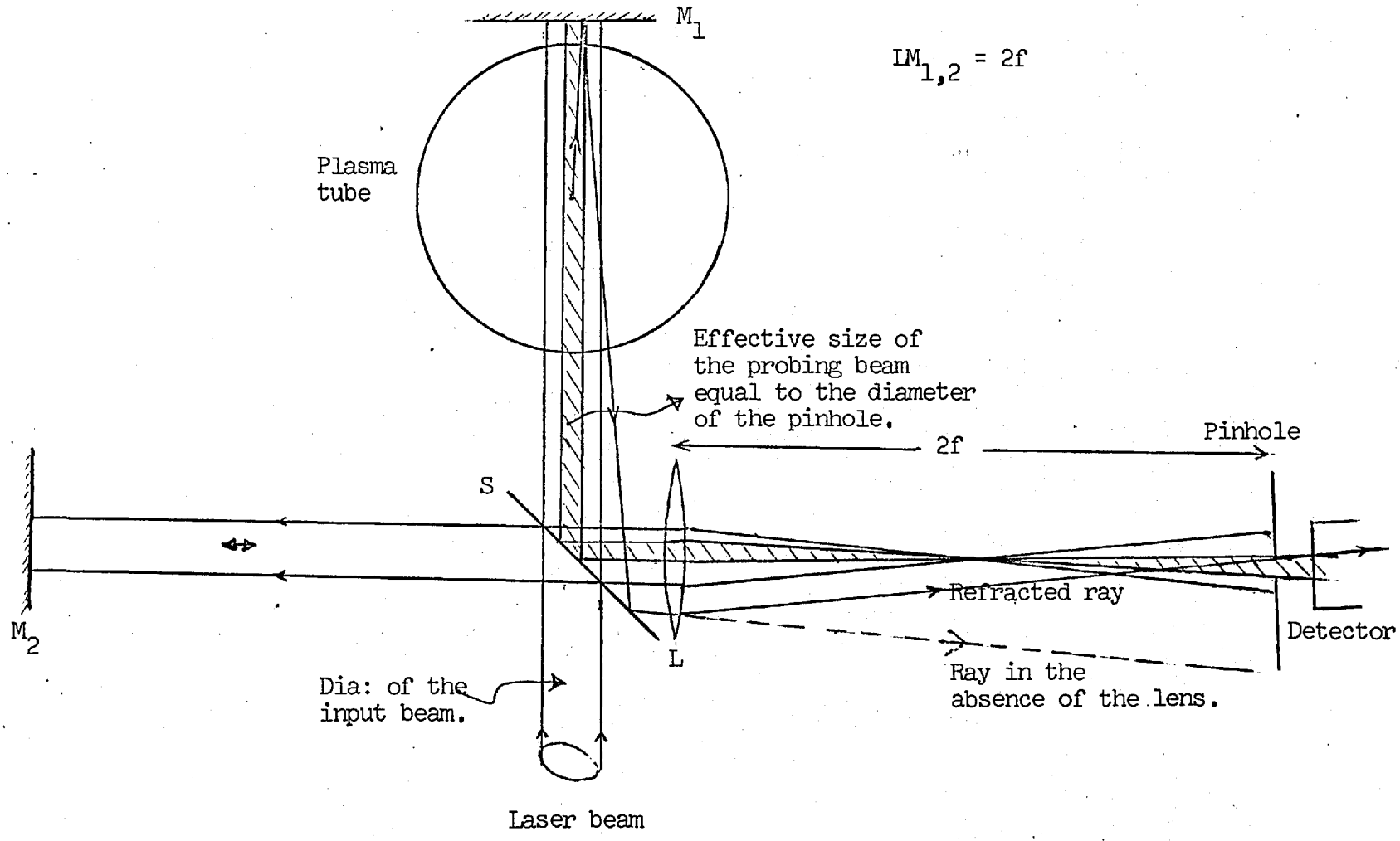

Fig (7,6) Diagram showing the effects of Lens L.

If a pinhole with a size less than half (or smaller) than the fringe spacing is used at the position of the aperture A_3, then the phase across it will always be uniform. It will thus admit only a portion of the wedge fringe hence avoiding any loss of modulation. A pinhole with a diameter of 0.3 mm was tried but under certain operating conditions one could still observe the loss of fringe modulation. This is understandable if one recalls the maximum deviation calculated on the assumption of a parabolic distribution of refractive index at the maximum electron densities measured using holographic interferometry. For 4.0×10^{18} Cm^{-3} as the max: electron density, $\psi_{max} = 1.44$ m radian. The spacing of the wedge fringe would then be 0.22 mm and there would be plenty cause to expect trouble. However, the use of 0.11 mm diameter aperture improved the situation completely, since the aperture size is equal to the width of a bright (or dark) fringe. Such a narrow pinhole was made by carefully piercing a streched aluminium foil with a needle and measuring the pinhole size with a travelling microscope. The arrangement using pinholes is shown in Fig. (7.6).

It must be noted that the pinhole apart from its usefulness for improving fringe modulation is very helpful for obtaining very good spatial resolution of the measurements as the effective width of the probing beam is the same as the pinhole diameter. The attempts at reducing the diameter of the beam to obtain better spatial resolution by placing pinholes before the plasma

tube were a failure. This is because for narrow pinholes, the diffraction becomes severe and there is a considerable divergence of the beam thus foiling the intended purpose. The angular radius of the diffraction spot is given by:

$\theta = 1.22 \frac{\lambda}{b}$, where b is the diameter of the circular aperture. For the aperture A_2 of 0.3 mm diameter, $\theta \sim 2.4$ radians. This does not allow the spatial resolution as the beam at the plasma tube after being reflected from M_1, thus traveling a distance of 30 Cms, is 0.72 mm wide. This apart from the loss of spatial resolution causes a degradation of fringe modulation.

7.5 Errors in the observed fringe shifts due to the refraction of the beam.

There are two main sources of error in the measurement of the fringe shifts.

1) The first is because of the fact that the deviated ray after its reflection from M_1 will traverse a different path in the plasma. This is shown in Fig. (7.7). The effect essentially depends on the size of the plasma column, the value of the angle of deviation and the distance of M_1 from the plasma axis.

As shown earlier (sec. 5.3.2.), the maximum deviation ψ_{max} is given by $\psi_{max} = \sin^{-1} K$, where $K = \frac{naxis}{n_c}$ (7.1)

The value of naxis as measured by holographic interferometry is $\sim 4.0 \times 10^{18}$ Cm^{-3}. Also the critical electron

density for 6328Å wavelength is $n_c = 2.78 \times 10^{21}$ Cm^{-3} This gives $\psi_{max} = 1.44$ m radians. This corresponds to the ray which is incident on the cylindrical plasma column with $\phi_o = 45^o$. As seen in Fig. (7.7), the error in the geometrical path length for this ray in the return trip through the plasma is

$$\Delta = 4\,AB - 2\,(AB + CD)$$
$$= 2\,(AB - CD) \qquad (7.2)$$

AB for the ray with maximum deviation (as discussed above) is $AB = \frac{r}{\sqrt{2}}$

and $$CD = (OD^2 - OC^2)^{\frac{1}{2}}$$
$$= \left[r^2 - \left(\frac{r}{\sqrt{2}} + \delta\right)^2\right]^{\frac{1}{2}}$$
$$= \left[r^2 - \left(\frac{r}{\sqrt{2}} + 2\,a\,\theta\right)^2\right]^{\frac{1}{2}} \quad \text{as } \theta\ (=\psi_{max}) \text{ is small and } \delta = 2\,a\,\theta$$
$$= \left(\frac{r^2}{2} - 4\,a^2\theta^2 - 2\sqrt{2}\,r\,a\,\theta\right)^{\frac{1}{2}}$$

Neglecting the second term as it represents the second order effect, one obtains

$$CD = \left(\frac{r^2}{2} - 2\sqrt{2}\,r\,a\,\theta\right)^{\frac{1}{2}} \qquad (7.3)$$

Using typical values

$r = 0.4$ cm, as obtained from holographic interferometric measurements.

$a = 15$ Cms and $\theta = 1.44 \times 10^{-3}$ radians

we obtain CD = 0.235 Cm

Also AB = r $/\sqrt{2}$ = 0.283 Cm

Thus Δ = 0.956 mm

The "true" path length = 4AB = 2x5.656 mm.

Thus the % error = $\frac{\Delta}{4AB} \times 100 = 8.45\%$

The error for the incident rays with different ϕ_o values can be determined if the angle of deflection θ is known. Again for a parabolic distribution the angle of deflection is given by Wort [13] as

$$\theta = \frac{\pi}{2} - 2\psi_o + 2\alpha \qquad (7.4)$$

where $\alpha = \frac{1}{2} \sin^{-1}\left[-\frac{1-K-2\sin^2\phi_o}{\sqrt{(1-K)^2+4K\sin^2\phi_o}}\right]$

As can be seen $\theta = 0$, for both $\phi_o = o$ and $\frac{\pi}{2}$.

i.e. for the rays passing along a diameter and the ray passing tangentially to the column.

Thus, from the above it can be seen that the error in the path length through the plasma can become quite large. In the above example, the number of fringes when AB = 2.83 mm was 4.9 when performing Michelson interferometry. To obtain the true fringe shifts, one has to consider optical path changes rather than the geometrical paths calculated above. Again using Wort's [13] result for the parabolic distribution, the optical path through the plasma is given

as

$$P = r_o \left\{ \cos \phi_o + \frac{1-K}{2\sqrt{K}} \operatorname{Tanh}^{-1} \left[\frac{2\sqrt{K} \cos\phi_o}{1 + K} \right] \right\} \qquad (7.5)$$

The value of ϕ_o for the incident beam following the geometric path AB in Fig. (7.7) is $= 45^o$.

This for the deviated ray after reflection from the mirror M_1 is ϕ_d. It can be calculated with reference to Fig. (7.7).

$$\phi_d = \angle C\ D\ O = \sin^{-1} \left(\frac{OC}{OD}\right)$$

$$= \sin^{-1} \left(\frac{r_o/\sqrt{2} + \delta}{r_o} \right)$$

$$= \sin^{-1} \left(\frac{1}{\sqrt{2}} + \delta/r_o\right) = \sin^{-1} \left(\frac{1}{\sqrt{2}} + \frac{2\ a\ \theta}{r_o}\right)$$

$$\phi_d = \sin^{-1} \left(\frac{1}{\sqrt{2}} + \frac{2\ a\ \psi_{max}}{r_o}\right) \qquad (7.6)$$

$$\text{as } \theta = \psi_{max}.$$

In the above example $\psi_{max} = 1.44$ m radian

$$a = 15 \text{ Cms}$$

$$r_o = 0.4 \text{ Cms}.$$

we obtain $\phi_d = \sin^{-1} \left(0.707 + \frac{2 \times 15 \times 1.44 \times 10^{-3}}{0.4}\right)$

$$= \sin^{-1} (0.815) = 54.6^o$$

The optical path for the case $\phi_o = 45^o$ from Eq. (7.5) is

obtained as $P = 1.414\ r_o$ for $K = 1.44 \times 10^{-3}$ obtained from Eq. (7.1).

The optical path for the returning beam for $\phi_o = \phi_d = 54.6^o$ is $1.158\ r_o$. Thus the % deviation from the 'true' optical path = 9.1%.

As can be seen this is only slightly larger than the error in the geometrical path.

The above estimation of the error in the optical path of the ray with maximum deviation ($\phi_o = 45^o$)is used to correct for the observial fringe shift. The number of observed fringes = 4.9. The actual number of fringes is thus = 5.3. There is, however, another source of error which produces fringe shifts in the opposite direction and is described below.

2) The other source of error is the fact that in the event of refraction, the deviated rays travel outside plasma a larger distance than they would otherwise. This additional path contributes to the fringe shifts. The amount of error can be easily estimated by calculating this additional path ΔP with the help of Fig. (7.7).

$$\Delta P = 2\left[\sqrt{a^2 + \left(\frac{\delta}{2}\right)^2} - a\right]$$

$$= 2\left[\sqrt{a^2 + (a\,\theta)^2} - a\right]$$

$$= 2a\left[\sqrt{(1+\theta)^2} - 1\right]$$

Since θ is small, neglecting higher order terms one can write

$$\Delta P = 2a\left(1 + \tfrac{1}{2}\theta^2 - 1\right)$$

$$= a\theta^2$$

For the errors in the fringe shifts due to this effect to be sufficiently small we should have $\Delta P \lesssim \lambda/10$. For the above discussed example,

$$\Delta P = 15 \times (1.44)^2 \times 10^{-6} = 31.0 \times 10^{-6} \text{ Cms.}$$

Thus $\frac{\Delta P}{\lambda} = 0.49$ when $\lambda = 0.63 \times 10^{-4}$ Cms.

Thus ΔP for $\phi_o = 45$ ($\psi_{max} = 1.44$ m rad.), the path $\Delta P \simeq \lambda/2$ thus producing extra half fringe. This must be subtracted from the previous error to obtain a net error due to two effects. The net error in the fringe shift = 0.50 - 0.41 = 0.09. Hence there is a net 1.8% error introduced in the fringe shift measurements. For other values of ϕ_o this error is still smaller, as the deflection is smaller for both smaller and larger ϕ_o. Moreover for smaller ϕ_o, the percentage error is small since a larger number of fringes are produced. It must be emphasized that such errors do not influence the peak value of electron density as $\theta = 0$ for $\phi_o = o$. It should be pointed out that both these effects would be more acute with Fabry-Perot system because a larger number of transits are required to obtain fringes with reasonable finesse.

The improved system as shown in Fig. (7.6) was used to make a scan of the plasma after having ensured the contribution of various errors to be minimal. The discharge was operated in all the measurements at 15 Kv (10μ f) and at 50 mtorr & 100 mtorr filling pressure of

argon. Under these conditions the discharge is extremely fast as seen in Fig. 7.8 (b) where one can observe a fringe shift/100 n sec. It further shows the reproducibility of the pinch as can be seen from the turnover point indicating the time of maximum compression. It is reproducible to within $\pm$ 25 n sec. Fringe shifts can be counted simply from one crest to another or from one trough to the other. Any fractional fringe shifts can be added at the beginning of the trace and also at the end near the turnover. This is possible because the fringes are cosine square terms, but it becomes difficult when the modulation is not uniform. However an estimate to within $\frac{1}{4}$th of a fringe can easily be made as can be seen in Fig. (7.8a).

The scan was made by lifting the tube in steps of 0.52 mm while near the pinch axis, and 1.04 mm when away from the axis. The most simple way of shimming was by introducing 3 and 6 Fortran statement computer cards respectively under each leg of the structure supporting the tube, each card having a standard thickness of 0.178 mm. This avoided the use of all difficult alternatives.

7.6 Results obtained with the interferometer.

The Fig. (7.8) shows the interference fringes of the scan at 50 mtorr pressure of argon. The number of fringes versus the height of scan position measured from the tube centre was plotted for various times w.r.t. the pinch. To obtain the electron density distributions, the fringe distributions were Abel inverted using the computer programs described in Chapter 6 (see 6.6.1).

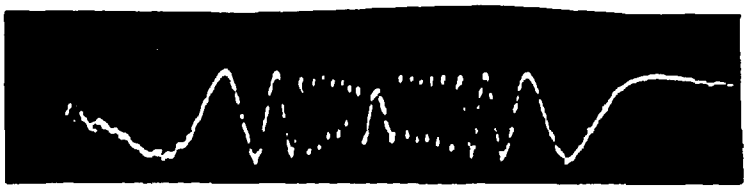

(a) 1 μsec/Cm

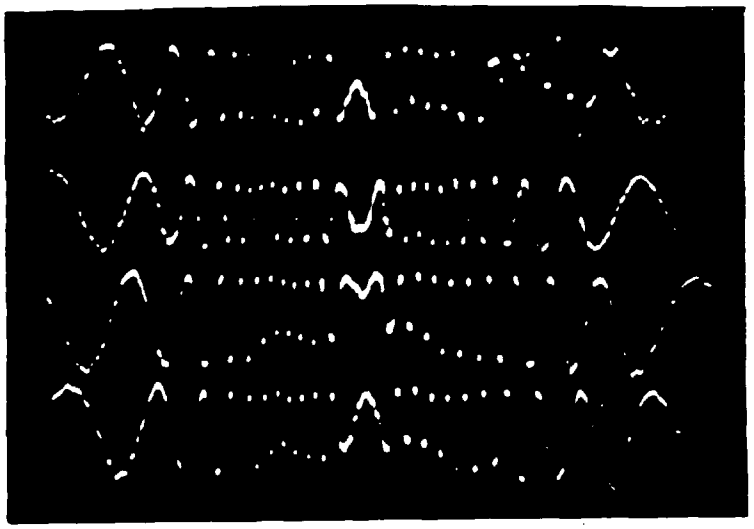

(b) 0.5 μsec/Cm

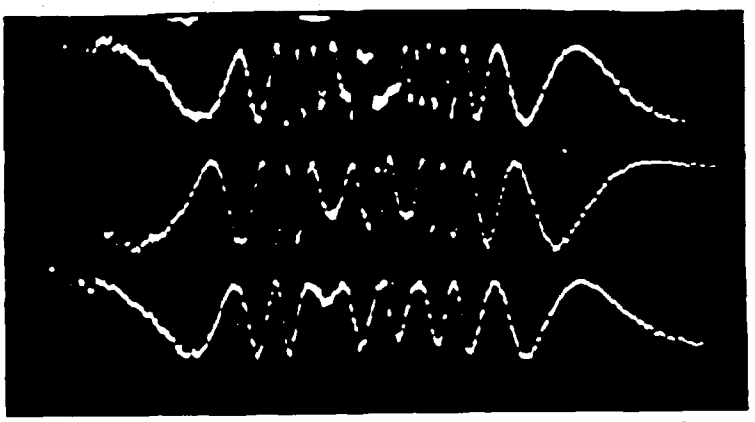

(c) 1.0 μsec/Cm

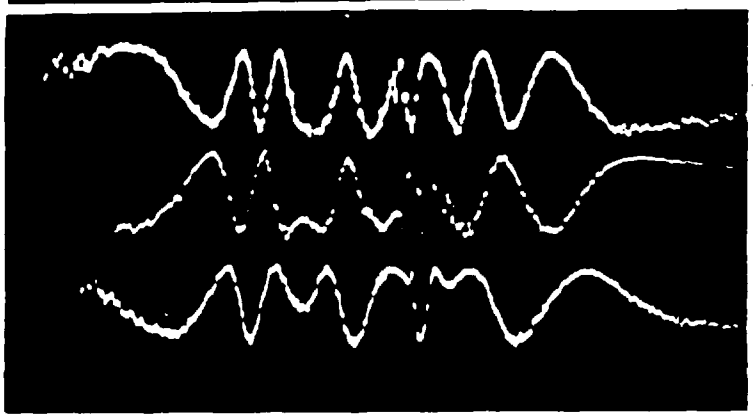

(d) 1.0 μsec/Cm

Fig. [illegible] He-Ne Laser Michelson Interferograms of the Plasma.

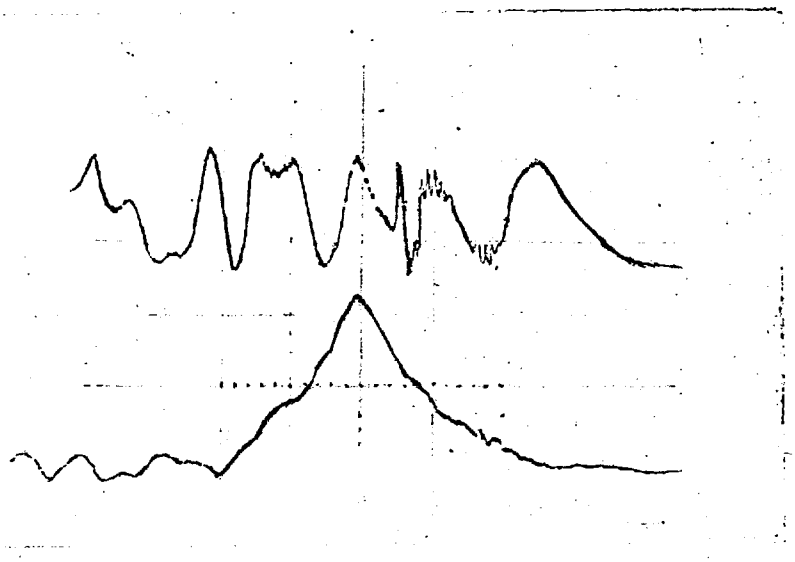

Fig (7.9)

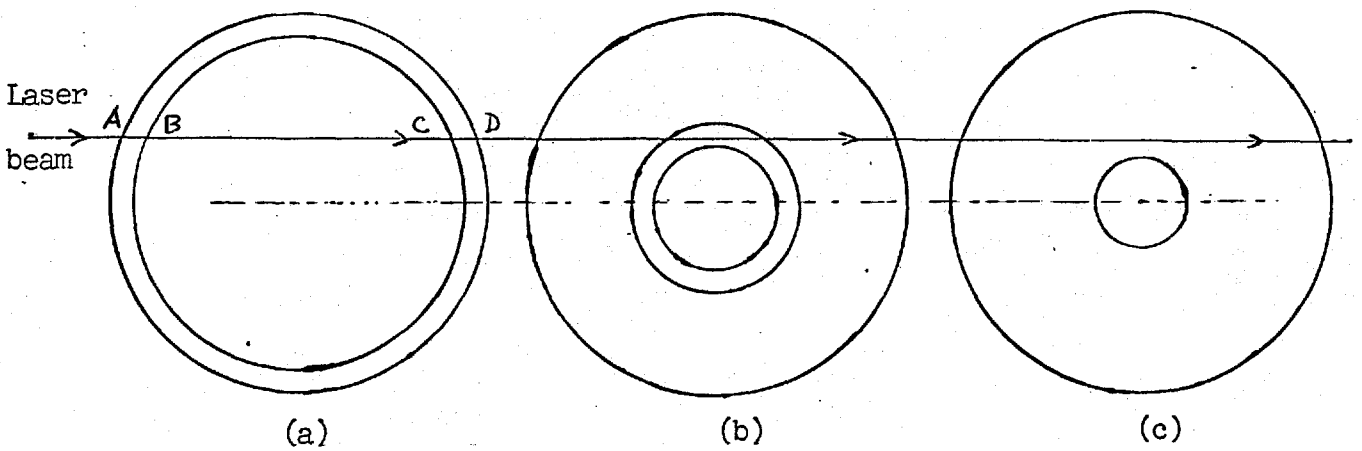

Fig (7.10)

Before the actual results are presented, some useful and interesting observations may be made about the fringes in fig. (7.8).

The time of maximum compression was ascertained by two independent means. Assuming the electron density to be maximum at maximum compression, the spatial position of the laser beam when the maximum number of fringes were obtained determined the axis of the cylindrical plasma column. The turn over at this fringe pattern shows the time of pinch. The other method to determine this time was by using simultaneous measurement of light - output on the same time base. The maximum of the light output trace shown in Fig. (7.9) indicated the pinch. As fig. (7.9) shows, it is otherwise impossible to identify the turnover when it occurs at the natural turning point of the fringe i.e. at the crest or trough.

When the laser beam is moved further from the tube axis, more than one turning points can be seen but not necessarily any at the maximum compression. This can be understood with the help of Fig. (7.10) when the collapsing shell begins to move in, as in Fig. (7.10a), the refractive index along the beam is increasing due to

i) a build up of the ionized particle density due to ionizing shockwave in advance of the shell as experienced by BC and

ii) due to a 'fattening' of the current sheath itself by snowplough effect registered at AB and CD. But as the shell passes by the beam, the optical path along the beam begins to decrease. This is the cause of the first turning point. If the current sheath is not a 'leaky piston',

Fig (7.11) Plot of the height of the laser beam from the axis versus the duration between the first and second turnover points.

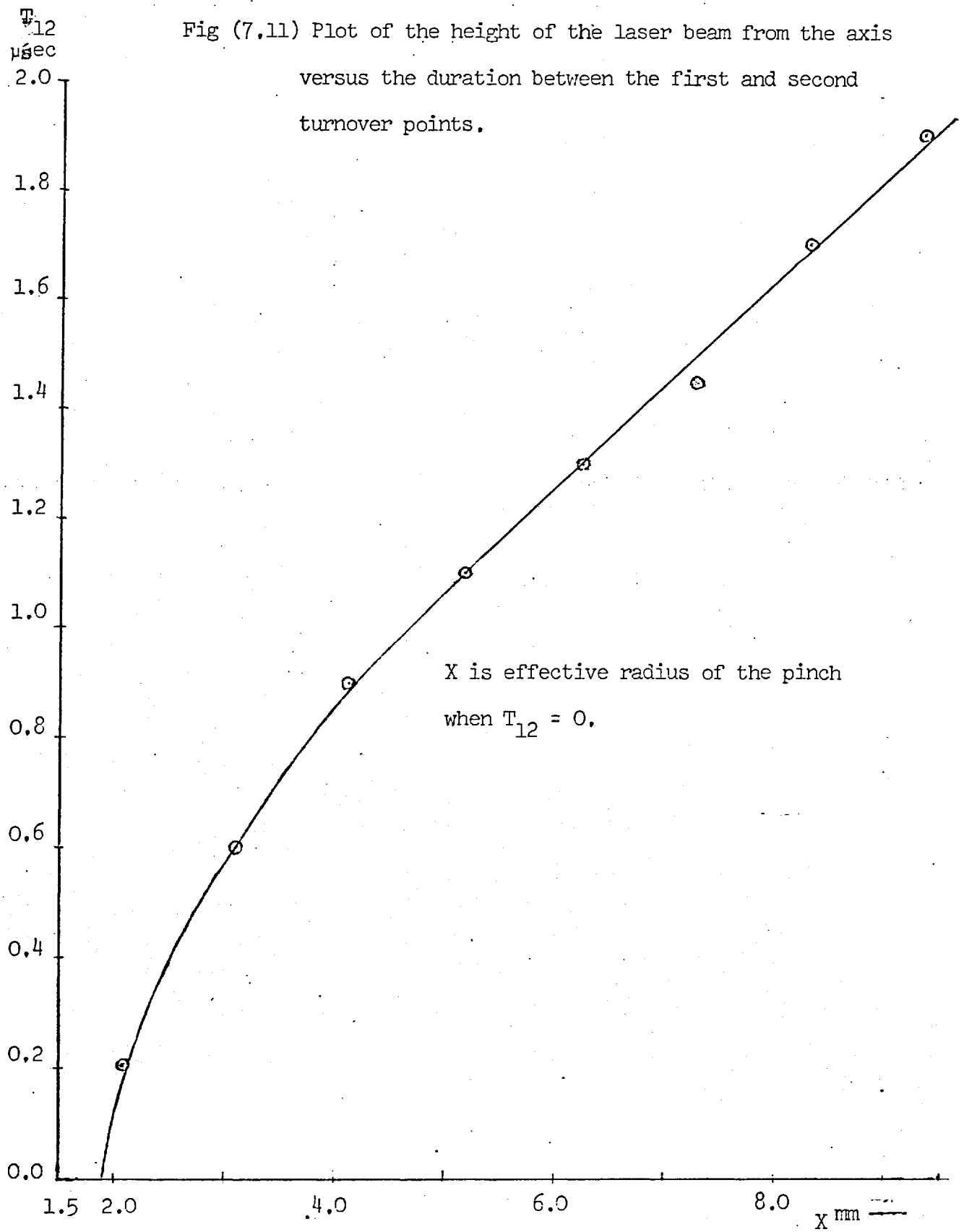

then there is almost vacuum outside it and thus the laser beam looses all contact with the plasma. It is unable to register the moment of maximum compression shown in Fig. (7.10c). Here the light output trace is helpful to establish the time of pinch.

As the plasma expands, possibly again as a diffuse shell, the beam registers a sharp turnover corresponding to an increase of refractive index along the beam. This corresponds to the second inflexion point on the fringe trace. The further expansion of the plasma shell causes the optical path length along the beam to decrease due to the decrease of electron densities. This change is registered as the third turnover point.

The fig. (7.11) shows a plot of the height of the laser beam from the axis versus the duration between the first and second turnover points. Extrapolating the curve to zero time gives the effective radius of the pinched column. This agrees very well with the estimate of the radius from the half width of electron density distribution. The curve in Fig. (7.11) gives a radius of 1.8 mm at the pinch for 50 mtorr pressure of argon.

Another interesting observation can be made with reference to fig. (7.9). The light output trace was obtained by collecting light through a 3" long tube with 1 mm internal diameter used to define the solid angle of observation. This light was conveyed to the photomultiplier by a light pipe connected at the other

end of the narrow tube. In a non-simultaneous measurement the tube occupied the same position as the laser beam which produced the lower trace. In fact this beam was used to align the pipe in the correct position. As the current shell with marked luminosity had passed the line of sight, there was a drop of the light output in the solid angle of observation. However, due to many fold increase of luminosity at the pinch the general level of light increases due to reflections from the tube walls.

It can be seen that the time this shell has taken to reach the tube-axis (to pinch) is 1.0μ sec. The shell travelled a distance of 7.26 mm in this time. Thus the average velocity ≃ 7.26 mm/μ sec. The speed of sound in the gas ahead of the shell at 20°C = 0.332 mm/μ sec., giving the average velocity of the shell as ~ 22 Mach. This velocity is an average value because the true velocity increases as the shell approaches the tube axis. This estimate of the velocity will be helpful in understanding the dynamics of the pinch as discussed in the next chapter.

The figs. (7.12) and (7.13) show the plots of radial distribution of electron densities at the following operating conditions.

a) 15 KV 50mtorr of argon at the pinch, 0.5μ sec and 1.0μ sec earlier than the time of maximum compression.

b) 15 KV 100 mtorr of argon at the pinch.

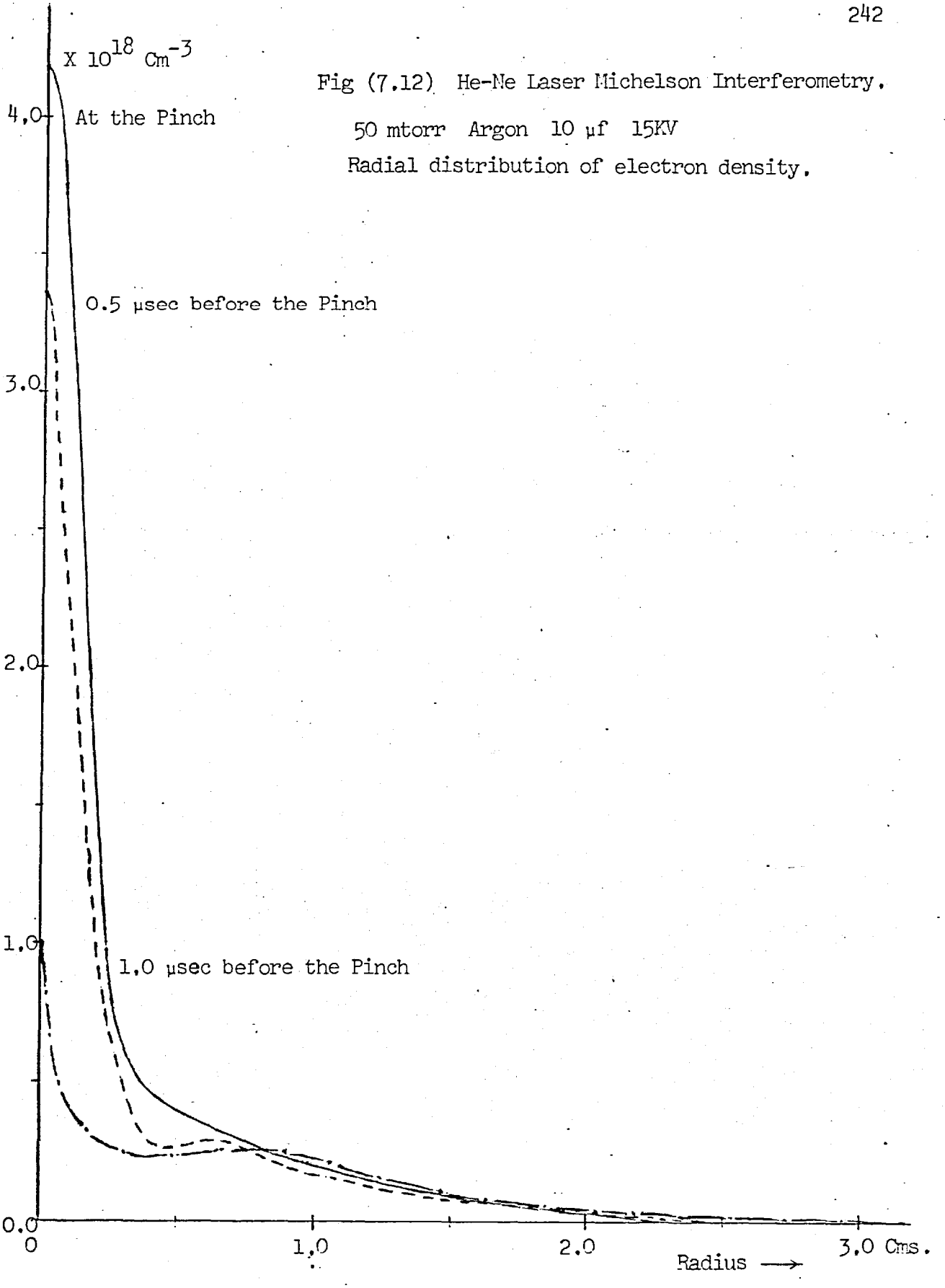

Fig (7.12) He-Ne Laser Michelson Interferometry.

50 mtorr Argon 10 μf 15KV

Radial distribution of electron density.

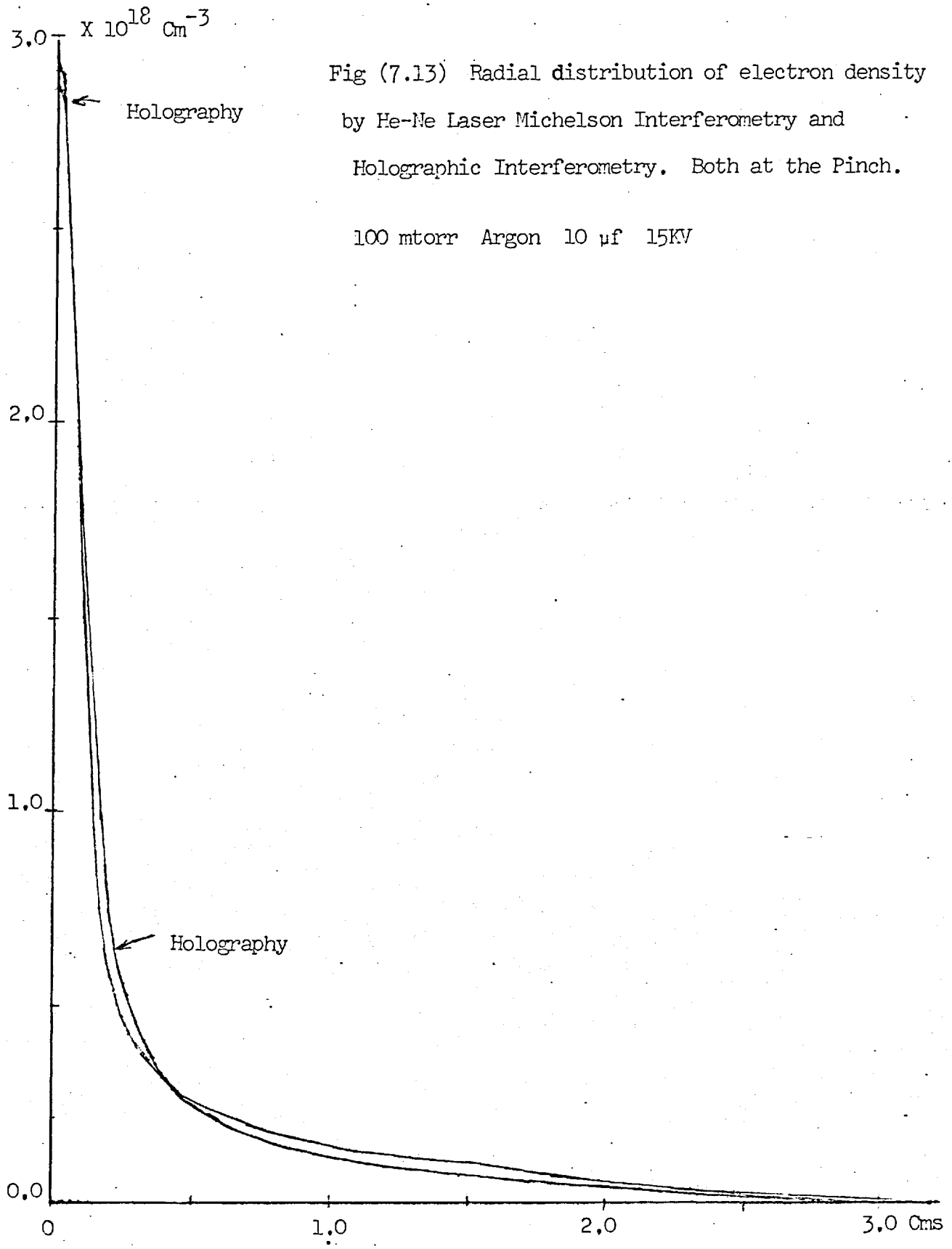

Fig (7.13) Radial distribution of electron density by He-Ne Laser Michelson Interferometry and Holographic Interferometry. Both at the Pinch.

100 mtorr Argon 10 μf 15KV

The peak value in a) is $(4.16 \pm 0.2) \times 10^{18}$ Cm^{-3} and the radius at half-height is ~ 1.8mm. At a time 0.5 μ sec earlier than the pinch wings can be seen indicating a shell to be moving inward. One can also observe quite an appreciable electron density at the axis even 1.0 μ sec earlier than the pinch. The Abel inversion with the computor program using area elements (6.6.1) gave a value of electron density of $(0.59 \pm 0.05) \times 10^{18}$ Cm^{-3} at 0.35 mm from the axis. Unfortunately this program does not give axial values. The second program using polynomial coefficients, however, supplemented this information showing an electron density of $1.02 \times 10^{18} Cm^{-3}$ at the axis. Fig. (7.13) shows the plot of the electron density distribution at the pinch for 100 mtorr pressure of argon. It also shows a curve obtained by holographic interferometry at the same operating conditions. The two are identical within the limits of the experimental errors.

To assign any figures for the accuracy of the measurements, one has to consider the sensitivity of the interferometer to measure fractional fringe changes. As mentioned earlier it is possible to measure up to a quarter of a fringe with Michelson interferometer. For large fringe shifts as at or near the axis, the percentage error is quite small usually less than ± 10% as the number of fringes is large. The same applies to fringe distribution obtained from holographic interferometry. Although in the latter the sensitivity of fringe shift measurements was also $\frac{1}{4}$th of a fringe, the error in specifying fringe

positions for narrow contour fringes at the pinch amounts to more than ± 10%. However, the difference between the two curves in fig. (7.13) is only a minor one considering that the peak value of the electron density at the axis is almost exactly the same.

7.7 Discussion.

The results obtained by the two methods of electron density measurements i.e. holographic interferometry and Michelson system are given in Table (7.2) for comparison at various operating conditions. It can be seen that at the time of maximum compression, the value of electron density and radius of the pinched column as obtained by the two methods agree very closely. The small differences are due to the experimental errors as discussed earlier.

Each method of electron density measurement has its own advantages. Both are easy to operate depending on the availability of appropriate laser in either case. Usually the main limitation of CW laser interferometry has been the time response of the system. But as the work presented in this chapter shows that the Michelson system has a very high frequency response and is only limited by the detector.

The major problem with the Michelson system at very high electron densities is that of refraction of the beam causing errors in the measurements of fringe shifts. In the present work, fortunately, the distribution of refractive index could be approximated as parabolic. This allowed the correction to the fringe shifts to be made easily as the maximum deflection could be obtained

Pressure	Time w.r.t the pinch	$n_e \times 10^{18}$ Cm^{-3}		Radius at half-height Cm	
mtorr	μsecs	Holographic Interferometry	Michelson system	Holographic Interferometry	Michelson System
50	0.0	4.02	4.16	0.2	0.19
	-0.5	-	3.36	-	0.18
	-0.7	2.58	-	0.15	-
	-1.0	-	1.02	-	0.12
	+0.3	3.0	-	0.19	-
100	0.0	2.88	2.93	0.18	0.13
	-0.2 ± 0.05	2.28 ± 0.08	-	0.26	-
	-1.0	1.6	-	0.45	-

+ve and -ve signsindicate the time after or before the pinch respectively.

TABLE (7.2)

by solving the problem analytically (section 5.3.2). However, in situations where the radial distribution is a more complicated function, one has to resort to ray tracing using numerical techniques to estimate the amount of deviation that various rays suffer. Although the situation is less complicated in Michelson system as compared to other CW laser interferometers which involve multiple transits through the plasma, it can be avoided altogether by using holographic interferometry. This is because as mentioned in (5.3.2) the deviated ray retraces its path on reconstruction and hence the effective error is relatively much smaller.

The time resolution of the holographic method depends on the width of the laser pulse. It can be made as small as 10-15 sec by fast switching techniques and to about 6 μsecs by using a slightly more difficult method of PTM operation of the ruby (6.4.1). The other advantage of holographic interferometry is that one obtains instantaneously the electron density distribution at a particular moment throughout the plasma without resorting to scanning techniques which depend on reproducibility of the discharge.

In conclusion it must be remarked that the above two diagnostic methods have provided sufficient information about the electron densities and their distributions in the discharge under various operating conditions. The next chapter describes the processes involved in the unstabilized Z-pinch collapse.

References.

1. Ashby, D.E. T.F. and D.F. Jephcott, Appl. Phys. Letters, 3, (1963) p. 13.
2. Wheeler C.B., and A.E. Dangor, Boc. 26th Agard Energetics Meeting, Pisa, (1965).
3. Baker, D.A. and J.E. Hammel and F.C. Jahoda, Rev. Sci., Inst. 36, 395 (1965).
4. Gerardo, J.B. and J.T. Verdeyen, Proc. I.E.E.E. 52, (1964), p. 690.
5. Hooper E.B. and G. Bekefi, J. Appl. Phys. 37, 4083, (1966).
6. Fox A.G., and T. Li, Bell. Systems Tech. J. 40, 453, (1961).
7. Sinclair, D.C. Spectra Physics Laser Tech. Bulletin, No. 6, Mountain View California (1968).
8. Deuchars, W.M, D.E. Kidel, J. Irving and A.C.C. Warnock, Appl. Phys. Lett. 7, 30 (1965).
9. Gerardo, J.B. J.T. Verdeyen and M.A. Gusinow, J. Applied Phys. 36, 2146, (1965).
10. Dangor, A.E. Ph.D. Thesis 1969, University of London.
11. Brossel, J. Proc. Phys. Soc. 59, 224; 1947.
12. Tolansky, Multiple Beam interferometry, Pergamon 1947.
13. Wort, D.J.H., 'Refraction of Microwaves by a plasma Cylinder' Research Report CLM - R27(1963).
14. Nation, J.A., Ph.D. Thesis, 1960, University of London.

Chapter 8.

Discussion of the Experimental Results and Conclusions

8.1 Introduction.

In this chapter an attempt will be made to explain the following experimental observations presented in the last two chapters.

i) the time to pinch for various initial conditions
ii) the presence of appreciable axial electron densities well before the pinch. Also the related phenomenon of axial luminosity before the arrival of current sheet at the axis.
iii) the rapid increase of the rate of build up of axial values of electron densities near the time of pinch and
iv) peaking of the electron density at a certain filling pressure.

The behaviour of the Z-pinch discharge has been studied by many authors [1,2,3]. The exact nature of the processes involved in the discharge is complex and its study involves various simplifying assumptions. In spite of this in many cases good agreement is obtained between the theoretical predictions and the experimental results, while in other cases there is at least qualitative agreement. It will be shown that the plasma temperature can be estimated by a simple consideration of energy balance in the discharge.

8.2 The mechanism of the pinch collapse.

There are various models which explain the mechanisms of the pinch discharge. These being

i) the single-particle model
ii) the adiabatic model
iii) the snowplough model
iv) the shockwave model

The first two models are not applicable in the case of fast discharge as used in the present work. In this discharge the velocity of collapse is larger than the velocity of sound and hence the gas is not compressed adiabatically. Also for the single-particle model to be valid, the mean free-path of the particles must be large to allow the particle to move freely. In our experiment with electrondensity larger than 10^{17} Cm^{-3}, the mean free path for collisions between neutral atoms was much less than the dimensions of the tube. This model is therefore unable to describe the pinch dynamics correctly.

8.2.1 The Snowplough Model.

The snowplough model is a special case of the shockwave model and involves various simplifying assumptions. The latter is able to explain most of the features of the discharge and will be discussed later. The snowplough model is able to predict the time of the first pinch with reasonable accuracy and is discussed first for its simplicity. First proposed by Rosenbluth [1], the snowplough theory assumes that all the neutral gas particles which come into contact with the current sheet are

ionized by electron-atom collisions and hence adhere to it due to space charge forces. It therefore assumes that no shockwave can propagate ahead of the current sheet.

The main properties in the rapid contraction phase of the discharge are due to the skin effect in the distribution of current. During the initial stages of the implosion, because of a marked skin effect, the central region of the gas column is heated only slightly, so that the gas pressure is small and does not play any appreciable role. The gas pressure becomes important only during the last stage where there is strong compression.

To obtain the time to pinch, the equation of motion of the contracting plasma column acting as a magnetic piston is solved. The plasma pressure can be neglected at the start of the compression. The equation of motion then is

$$-\frac{d}{dt}\left(M\ \frac{dr}{dt}\right) = 2\pi\ r\ p \qquad (8.1)$$

where P is magnetic pressure $= \frac{B_\theta^2}{8\pi} = \frac{I^2}{200\pi r^2}$

where I is in amperes, r in cms, p in dynes/Cm^2 and B in gauss. M is the mass per unit length of the sheet. If P_o is the initial density of the gas, then

$M = \pi\ (r_o^2 - r^2)\ P_o$, r_o being the radius of

the plasma tube. Thus the snowplough equation becomes

$$-\frac{d}{dt}\left(\pi p_o (r_o^2 - r^2)\frac{dr}{dt}\right) = \frac{I^2}{100\, r} \qquad (8.2)$$

The current I can be obtained from the circuit equation. In our experiment the current was sinusoidal and the pinch occured in a time short compared to the discharge quarter period. Thus the current I can be replaced by

$$I = I_o \sin \omega t \simeq I_o \omega t \qquad (8.3)$$

Anderson et. al. [2] have solved the equations (8.2) and (8.3) and obtained the time of the first pinch as

$$t_p = 1.5\left[\frac{100\pi\, p_o\, r_o^4}{I_o^2\, \omega^2}\right]^{\frac{1}{4}}$$

$$= 1.5\left[\frac{100\,\pi\, p_o\, r_o^4}{\left(dI/dt\right)_o^2}\right]^{\frac{1}{4}} \qquad (8.4)$$

where $(dI/dt)_o$ is the initial rate of current rise.

Although the result given in Eq. (8.4) shows more than qualitative agreement with the experimental results, there are following two potential causes of descripency between the two. These also show the limitations of the snowplough theory.

1) In the above calculations the plasma pressure is

taken to be zero during the entire compression. The first consequence of this is that the radius of the pinch at maximum compression is predicted to be zero. This obviously does not pertain to the actual situation. Also the equation (8.2) shows that the acceleration at r = o becomes infinite. Thus the theory cannot be used beyond the time of the first pinch.

Since the capture of the gas by the converging plasma shell is an inelastic process accompanied by heating, the plasma pressure term can not be neglected. The electro-dynamic force by compressing the current sheet produces a shock wave (see 8.2.2.). The inward moving shock heats up the gas. The energy which is delivered to the gas by the electrodynamic force is partly associated with directed motion and partly with thermal motion. From the standard results of shockwave theory (14), it is known that in the case of a strong shock, in a monoatomic gas, the energy is equally divided between directed and random motions. Thus in the final stages the kinetic pressure of the plasma is important as it becomes of the order of magnetic pressure and will have appreciable influence on the development of the discharge.

Leontovich and Osovets [4] have obtained the solution of the equation of motion including the pressure term by numerical integration. The difficulty of this calculation is that gross assumptions have to be made regarding the form of the pressure term as its radial distribution is not known. Moreover, it is assumed that the pressure varies according to the laws of adiabatic

compression. In practice this is not true due to the effects of showkwaves, ohmic heating, ionization and radiation. The general conclusions of Leontovich and Osovets are, however, still valid. Their results show that when the initial pressure is not zero, the plasma column contracts to some non-zero minimum radius. Also the time of first pinch is shown to be prolonged only slightly for higher pressures, there being an increase of only a few per cent.

2) The time to pinch given by snowplough model as given by Eq. (8.4) is measured from the moment the current sheet leaves the walls of the containing vessel. One, however, measures experimentally the time to pinch from the moment of gas breakdown. This is not necessarily the same as t_p in Eq. (8.4). This is because there elapses sometime before the magnetic field is able to exert sufficient pressure for the current sheet to move. In actual comparison of snow-plough theory with experiment, this wall hang up time must be taken into account. Lundquist [5] has shown that the magnetic field will exert sufficient pressure on the current sheet for the latter to be able to move when

$$BR\,\sigma\sqrt{\frac{4\pi}{p}} \sim 1 \qquad (8.5)$$

where p is the gas density, $R \sim \frac{nev}{j}$, v being the velocity of the collapsing shell, j and n the current and particle densities respectively. σ is the conductivity of the plasma and B the magnetic field. Because in the early stages of the discharge the conductivity is low,

there will thus be an associated wall hang up time and is given by Osovets [6] as

$$t_w \propto p_o^{\frac{1}{8}} / V_c^{3/4} \qquad (8.6)$$

where p_o is the initial gas density and V_c is the condenser voltage. As shown by Nation [3], the wall hang up time becomes a significant fraction of the time to pinch only at very low bank voltages. For the large bank voltage of 15 Kv in our experiment, this time is completely negligible.

One more important cause for a delay in the start of the compression is that the conductivity in the early stages is small. The snowplough model assumes the gas to be preionized with hundred percent ionization thus causing the current to flow in a very thin sheet due to skin effect. In our experiment no such preionization was carried out hence causing a lower conductivity than assumed. The B_θ field is able to leak in the current sheet and thus has to compress itself. The effect of slower compression with decreasing preionization was confirmed experimentally by Hain et. al. [8].

The above mentioned effects on the pinch time could have been important at low bank voltages and high filling pressures. These, however, were negligibly small in our experimental conditions. The results shown in Fig. (6.3) agree within the limits of experimental errors with the prediction of the snowplough theory given by Eq. (8.4).

8.2.2. The Shock wave Model.

Although the snowplough model discussed above predicts reasonably accurately the time for the first pinch, it does not explain any of the phenomena mentioned in sec. (8.1). These are explained by shockwave model, first proposed by Allen [7], which in contrast to snowplough model, assumes that the gas particles after reflection from the magnetic piston generate compression waves. These shockwaves are large amplitude plasma ion oscillations which are established in fast discharges at not too low pressures where the ionic mean free path is greater than the width of the discharge chamber. If the conductivity of the current sheet is large, then the magnetic field is excluded from the sheet. The pressure acting on the sheet will be $B_\theta^2/8\pi$. For large currents the ratio of this pressure to the initial pressure of the gas will be very large and the shock wave will be in a strong shock limit. For this case the parameters namely the shock velocity, the density ratio and temperature ratio of the shocked gas to the unshocked gas are obtained from conventional shockwave theory. As shown by Allen [7] there is a density ratio of four for a monoatomic gas in the strong shock limit. Also the temperature of the shocked gas is much higher than that of the unshocked gas. Assuming a one-dimensional shock, the velocity of the shockwave is shown to be $4/3$ times larger than that of the current sheet. For a 3" radius tube the shock wave will reach the axis about

2 μ sec earlier than the current sheet if the latter has a speed of ~ 10^6 cm/sec. The large temperatures produced by the shock wave cause appreciable ionization in the gas. This is the possible reason for the presence of large axial electron densities before the arrival of the current sheet on the axis (see Fig. 6.28 & 29) and Fig. 7.12. The large ionization caused by the shock wave is accompanied by a luminosity of the gas. Simultaneous measurements of axial luminosity using light pipes and the interferometric measurements of electron densities showed a reasonably large light signal about 1μ sec before the pinch. These measurements confirm the results of Nation [3] who had also observed by high speed photography the axial luminosity before the arrival of current sheet. Under his experimental conditions the incident shock front was non-luminous. The shockwave on reflection produces the doubly shocked gas which has a temperature and particle density significantly higher than that behind the incident shock.

The rapid increase of the rate of electron density buildup at the axis as seen in Fig. (6.30) can also be explained on the basis of shock wave model. As shown by Chisnell [13], the shock in a cylindrical geometry will accelerate as the radius decreases. For a monoatomic gas with $\gamma = 5/3$. the Mach number of the shock wave is

$$M \propto R^{-0.225}$$

This is because a decrease in area of the shock front causes an increase in the shock velocity from the consideration of momentum balance. Also as the shock gets to smaller radii fewer and fewer particles are engaged in shock propagation. As a result of this the energy per particle inside the shocked gas increases causing a larger degree of ionization. Both the acceleration of the shock and the larger degree of ionization are responsible for the effect mentioned above.

The effect of the electron density having a maximum at a certain filling pressure is also explained in terms of shock theory. Dangor et. al. [9] have solved the equations describing the equillibrium state of the gas behind the incident and reflected shocks with the Saha equation and the equation of state. Their results for the particle densities in the incident and reflected shocks in terms of initial density of the gas are given as

$$\frac{N_1}{N_0} = \frac{4 + 2\left[\alpha_1 \; I^1 + (1-\alpha_1') \; E_1'\right]}{K \; T_1 \; (1 + \alpha_1)} \qquad (8.7)$$

and

$$\frac{N_2}{N_1} = \frac{5}{2} + \frac{\left[\alpha_2 \; I^1 + (1-\alpha_2) \; E_2'\right]}{K \; T_2 \; (1+\alpha_2)} \qquad (8.8)$$

where suffices 1 and 2 apply to the quantities in incident and reflected shocks respectively. α is the degree of

ionization, I^1 and E' are the ionization and excitation energies of the neutral atom. The ratio of ionization energy to the thermal energy, $\frac{\alpha I}{KT}$, in the incident and reflected shocks is important in determining the variation of electron density with pressure. At low pressures the temperature is high causing the degree of ionization to be large. Since T decreases with increasing filling pressure, it causes both N_1/N_o and N_2/N_1 to increase with P_o. At high pressures, the temperature is small and varies only slightly, whereas α decreases strongly for these temperature changes. Thus the ratio $\frac{\alpha I}{KT}$ and hence N_1/N_o and N_2/N_1 are decreasing functions of P_o. This is the reason that the electron density, which is closely associated with the particle densities in the incident and reflected shocks, has a maximum at a certain filling pressure.

8.3 An Approximate Analysis of the Pinch.

A simple calculation was carried out on the z-pinch plasma discussed in the last three chapters to estimate the energy distribution between the random and ordered motions in the collapse phase of the discharge. It is also shown that by utilizing the measured parameters such as peak electron density, pinch radius and plasma current at the pinch, it is possible to estimate the plasma temperature at maximum compression.

The condenser bank parameters are

$C = 10\ \mu f$

$V_c = 15$ Kv

The total stored energy = $\frac{1}{2} CV^2 = 1.125 \times 10^3$ Joules
The filling pressure of argon gas = 100 mtor.
The density of argon atoms in the tube = $0.35 \times 10^{16} Cm^{-3}$
The peak current = 40×10^3 amps.
The current at the time of pinch = 14×10^3 amps.
Initial rate of rise of current ~ 0.6×10^{10} amps/sec.
The time to pinch $t_p = 6.7\ \mu$ sec.
This time agrees well with the calculated value using Eq. (8.4).
The total energy input to the discharge up to the time of pinch =

$$\int_0^{t_p} V\ I\ dt \sim 0.2 \times 10^3 \text{ Joules.}$$

The velocity of collapse measured from the framing camera photographs and light output measurements 8.7×10^5 Cms/sec. Assuming 100% trapping of the atoms by the current sheet, the total energy stored as kinetic energy during implosion is

$K \simeq n_o \times$ volume $\times \frac{1}{2} mv^2$

$\simeq$ 16 Joules.

The radius of the pinch column at half-height as obtained from experimental results shown in Fig. (6.28) $\simeq$ 1.3 mm.

The compression ratio $= \left(\frac{r_o}{r}\right)^2 = \left(\frac{3.81}{0.13}\right)^2 = 860.$

The ion density is therefore $= 0.35 \times 10^{16} \times 860$

$$= 3 \times 10^{18} \text{ Cm}^{-3}$$

The magnetic field at the boundary of the pinched column =

$$\frac{I}{5r} = \frac{14 \times 10^3}{5 \times 0.13} = 21.5 \times 10^3 \text{ gauss}$$

The magnetic pressure $P_m = \frac{B^2}{8\pi} = 1.84 \times 10^7$ dynes $/\text{Cm}^2$

Although during the implosion stage of the dynamic pinch the energy is roughly equally distributed into directed and thermal energy (see sec. 8.2.1.), all of this is however converted to thermal energy at maximum compression. At this stage the temperatures can be estimated from the Bennett relation by assuming the electron and ion temperatures to be equal. This is not strictly true because the ions which are shock heated are at a slightly higher temperature. Randomization, however, takes place very rapidly by ion-electron collisions making the ion and electron temperatures equal. Thus the Bennett relation for the argon plasma, is written as

$$P_m = (\Sigma n_i + n_e) \; KT$$

The electron density $n_e = 2.9 \times 10^{18} \text{ Cm}^{-3}$ (see Fig. 6.28).

If the kinetic pressure of the plasma is assumed to balance the magnetic pressure, we get

$$T \sim 22.5 \times 10^3 \ ^oK$$

From a time integrated spectrum of the argon plasma, it was observed that A_{II} lines were predominant with a much smaller intensity for any A_{III} lines. This strongly suggests that argon atoms are singly ionized with $n_e \simeq n_i$. This is also confirmed by the calculations of Wheeler[10] on the ionic composition of an argon plasma. These calculations show the electron and ion densities to be almost equal for the pressure and temperature values of the plasma given above.

Making use of the entropy-enthalpy charts for an argon plasma of Bosnjakovic et. al.[11], the enthalpy for argon plasma of 22.5×10^3 ^oK and pressure of 18.6×10^6 dynes/Cm^2 ($\sim$ 19 atmospheres) is

$$i = 6 \times 10^5 \text{ K Cal}/_{\text{K Mol.}}$$

Since 1 Cal = 4.2 Joules and the total mass of the argon gas in the tube = 0.475×10^{-3} gms, the total thermal energy stored in the hot plasma in the pinch column is

$$H = 30 \text{ Joules.}$$

Thus it is obvious that the directed kinetic energy is roughly one half of the total heat energy in the pinch at maximum compression. The rest of the energy being the thermal energy evolved in the capture of plasma during the compression process.

8.4 Discussion on the evaluation of the discharge.

Although various simplifying models accurately predict characteristic features of the discharge it is extremely complicated to evaluate the distributions of electron densities and temperatures and their time dependence. Such a calculation was carried out by Hain et. al. [8] on the basis of magneto-hydro dynamic equations (two fluid model), coupled to an equation for the external electric circuit. The fully ionized plasma of hydrogen or hydrogen like atoms was considered. The electrical conductivity was assumed constant. It was assumed that during the compression process all the neutral gas moved with the ions due to charge exchange processes, so that the velocities of the atoms and the ions were identical. Radiation losses, heat transfer to the walls, ionization and atomic excitation were not considered.

Even with these idealizations and simplifications, the problem still involved a complex system of partial differential equations which could be solved only by numerical integration with the aid of large electronic computers. The numerical solutions with a given set of initial conditions provided information on the temperature, density and flow velocity as a function of radius, as well as on the distribution of the current density and the strengths of the magnetic and electric fields.

An improved version of the program described in Ref. (8) was available for general users at Culham

Laboratory Berks (U.K.). This one-dimensional MHD code has the facility of introducing a few percent of impurity atoms which include carbon, oxygen, nitrogen, silicon and neon. Since the present experimental work was performed with argon plasma, the code could not be used as it was designed for hydrogen-like atoms only. It was thought that a hydrogenlike atom with atomic weight 40 would provide an approximation to argon as regards the pinch dynamics. Also the use of neon as a few percent impurity would give some idea of the temperatures involved by giving information about ionization and excitation of neon atoms. Unfortunately the program could not operate for these conditions and resulted in the overflow of computer storage for the use of A = 40. The advantage of this one-dimensional MHD code over the one discussed in Ref. (8) is that the assumption of fully ionized plasma is no longer required.

Apart from the use of Z-pinch as a source for plasma spectroscopy, any application in connection with fusion would employ hydrogen like atoms. The above program and also recent developments in two- and three-dimensional MHD codes (12) are the most valuable assets to predict the plasma parameters for any initial boundary conditions. This would make it possible to design experiments so that the specified field configurations are set up.

8.5 Conclusions.

The simple discussion of the mechanisms of the pinch presented in this chapter is quite useful to get an insight into the dynamics of the discharge. With the experimental knowledge of total current at the time of

pinch and the radius of the plasma column at maximum compression coupled with some energy balance relations provide an estimate of electron temperatures.

Most of the experimental features such as the time to pinch, the rate of collapse of the shell, the thickness of the shell, the axial luminosity prior to the approach of the current sheath at the axis and the pressure dependence of the peak electron density are reasonably well explained by the simple models. The shock wave model being the more comprehensive incorporates the Snowplough model as its special case.

The finer details of the pinch such as electron density and temperature distributions, ion temperatures etc cannot be obtained by such simplified considerations. These of course have to be obtained by very complex computation mentioned in the last section. These in turn deal with only the simple case of hydrogen like atoms. For more complicated situations, one has therefore to rely on the experimental results such as those presented in the last two chapters.

References.

1. Rosenbluth, M.N., Los Alamos Report L.A 1850, (1954).
2. Anderson, O.A., Physics Rev. 110, 6, 1375 (1958).
3. Nation, J.A., Ph.D. Thesis, University of London, (1960).
4. Leontovich, M.A., Osovets, S.M. J. Nuclear Energy 4, P. 209, (1957).
5. Lundquist, S. Ark. Fys, 5, 297, (1952).

6. Osovets, S.M., 'Plasma Physics and the problem of controlled Thermonuclear reactions'. 3, 193, Pergamon Press, (1959).
7. Allen, J.E., Proc. Phys. Soc. B. 70, 24, (1957).
8. Hain, K., Hain, G, Roberts, K.V., Roberts, S.J. and Köppendörfer. Zeitschrift fur Natur forschung, vol. 15a, pp. 1039-1050 (1960).
9. Dangor, A.E. and Chowdhury, S.S., J. Quant. Spectrosc. Radiat. Transfer. 9, 705 (1969).
10. Wheeler, C.B., Proc. VI th Int. Conf. Ion. Pher. in Gases (Paris) vol. I. P. 247, (1963).
11. Bosnjakovic F. 'Technical Thermodynamics', p. 483, Holt, Rinehart and Winston, Inc. New York, (1965).
12. Roberts, K.V. and Potter, D.E. 'Methods in Computational Physics', vol. 9, Academic Press (to be published) edited by B. Alder, S. Fernbach and M. M. Rotenberg.
13. Chisnell, R.F., J. Pluid Mech. 2, 286, (1957).
14. Courant, R. and Friedrichs, K.O. 'Supersonic Flow and Shock waves', New York, Interscience, (1948).

Chapter 9.

Concluding Remarks.

9.1 Summary of the work presented in this thesis.

The work presented in this thesis has been aimed at contributing to the development and successful application of the new field of holographic interferometry to plasma diagnostics. Since it was only in 1966 that the possibility of such an application was envisaged by Ostrovskaya, et. al. (Ref. 1, Chapter 6), the technique was still in its infancy when the present work was started. The growth in the parent field of holography itself was very rapid and the work was being incoherently reported in the literature. To sort out the loose ends for the present application one had to deal with multi-dimensional problems, some of which are listed below along with the steps taken to solve them.

(i) It was essential to grasp the inner details of the working of a hologram. The difficulty in this for a non-especialist in Applied Optics may sometimes be underestimated. An attempt was thus made to give a thorough exposition of the basic principles and practicle details of holography and holographic interferometry and is presented in Chapters 3 and 4.

(ii) The qualities of a hologram and the characteristics of the reconstructed image are strongly dependent on the type of experimental set up adopted to form the hologram. It had to be decided as to which experimental setup to finally use in our application.

(iii) The decision required in (ii) above depended on

the considerations of the coherence of the radiation from the ruby laser.

(iv) Finally, such extraneous factors as the availability of the proper photographic materials for holography also largely determined the choice of the setup. It also placed a requirement of a minimum energy in the output laser radiation. Fortunately, the availability of high resolution fast photographic plates (Chapter 4) made possible the use of the available ruby laser having small output energy.

Realizing that the main limitation of conventional interferometry as applied to plasma diagnostics was its requirement of expensive good quality optics, it was decided to concentrate on the development of a holographic system which will ease the above requirement. This was happily done using the scatter-plate interferometer described in Chapter 4. The advantage of this system was that a) reasonably good quality holograms could be obtained with a simple ruby laser whose spatial coherence is easily improved by the use of an aperture in the laser cavity. It was not necessary to improve the temporal coherence because the reference and object beams travelled almost equal distances in the system so that their difference was well within the coherence length. Due to this reason it was always possible to obtain a hologram with this system. b) All the optical components were mounted on the same optical bench and hence the system had a very good vibrational stability,

an important requirement for holography as discussed in Section (3.9.4).

The application of holographic interferometry to plasma diagnostics is useful in two senses. Firstly the operation of obtaining an interferogram is very much simplified because there are no longer any stringent requirements on the quality of the optical components and the plasma containing vessel. Secondly, any asymmetry in the plasma can be easily reconstructed in three dimensions.

The first aspect is thoroughly exploited in the present work to the best of advantage. Side-on measurements were performed on a Z-pinch device. This is a specially difficult configuration for conventional interferometry and its use served to emphasize relative usefulness of holographic interferometry.

Regarding the second aspect the holographic interferometry is able to provide the required information and the problem is now reduced to obtaining a solution of a few simultaneous equations. This is briefly discussed in chapter six. Since no worth-while information was expected in situations involving asymmetric distributions in the Z-pinch plasma, any further effort in this direction was not justified.

The usefulness of holographic interferometry is best demonstrated by examining the results obtained with the Z-pinch discharge. Radial distributions of the electron densities at or near the time of pinch were calculated from the corresponding fringe distributions using Abel Inversion technique (Section 6.7). These

results agree very well with those obtained by an independent method of CW laser interferometry (Chapter 7). Measurements in the former case could be made to an accuracy of quarter of a fringe by obtaining a microphotodensitometer trace of these fringes. The accuracy with the latter method was also to at least a quarter fringe shift as the fringes were cosine square terms. The perfect reproducibility of the discharge made the results of CW laser interferometry reliable.

These results along with the measurement of discharge current at the time of pinch (Chapter 5), allowed an estimation of the plasma temperature. Assuming 100% trapping of the atoms by the collapsing current sheet, the ion densities at the pinch could also be roughly estimated knowing the pinch radius from the above measurements. These results show the electron and ion densities to be equal for our operating conditions of the discharge.

A brief mention must also be made of a spatial sampling technique using a fly's eye lens which is used to obtain a 'hologram' of an object with white light. This was reported by Pole[1] as a means of reconstructing a real image of the object from the photographic record obtained by spatial sampling. The possibility of using this technique to obtain holograms of the plasma from the plasma light itself was explored by the present author. Workable fly's eye lens was made by depositing optically good quality transparent glass beads on a glass plate with the optical cement. Each bead acted

as a lenslet forming an image of the object at its focal plane. It was, however, realized that the technique is not useful for self-luminous objects like plasmas as the image in this case at the focal plane of each sampling lenslet is an integrated view of the whole plasma column. Unlike non-luminous objects it is not thus possible to reconstruct the correct shape of the plasma column. Some calculations of the resonance absorption of the ruby laser light in nitrogen plasma with N_{II} line at 6942.9Å, performed with a view of measuring temperatures, are presented in Appendix I. The absorption is found to be a function of both the temperature and electron density. Except for electron densities larger than 5×10^{18} Cm^{-3}, there are two values of temperature for the same absorption. This when coupled with the necessity of performing the simultaneous measurements of electron densities adds to the difficulty of estimating temperatures by this method. This is discussed in Appendix I. Suggestions are made in the next section for the future work dealing with problems when holography can be applied with benefit.

9.2 Suggestion for the Future Work.

One can obtain live framing camera interferograms of the plasma using scatter-plate system. This is discussed in Section (3.4.1) which explains how a framing camera can be used to record the whole plasma 'event' as the framing or streak photographs of the interferograms. The same laser must be used for obtaining the original hologram of the system and for observing the

live fringe pattern (3.4.1). The difficulty of using normal Q-switch ruby laser has been that it does not provide a pulse of uniform intensity over the whole life time of the plasma which lasts for about 5 to 10 μsecs. This problem can be solved by using the θ-pinch pumped laser (section 2.3) which can provide a pulse with a width of ≈10μ secs. The quantum efficiency of the image converter camera phototube is usually small in the red wavelength range. The use of this laser, giving large power output, can overcome the above limitation. The other difficulty in the above experiment is that if the hologram is not replaced exactly in its original position, spurious background fringes may be produced in the reconstructed interferogram. The hologram can, however, be visually positioned by using a CW gas laser till the background fringe pattern disappears. Due to the short exposure time of each frame, the gas laser does not provide enough photons for the phototube to be sufficiently sensitive to expose the film. This problem can be resolved if both a CW laser and a pulsed laser of the proper pulse width can be made to operate at the same wavelength. The initial adjustments can then be made with the CW laser while the actual experiment can be done with the pulsed laser.

Recently a pulsed Z-pinch argon laser has been made to operate [2] at 4765Å with a pulse width of 0.2 μ secs. The CW argon laser also gives radiation at this wavelength. The above pulse width is shorter than desired for the above application. Also, there is a

problem of the jitter of the output pulse. The future work can, however, be directed to improve the pulse characteristics by trying to find out the optimum operating conditions of the Z-pinch discharge.

The pulse width of 0.2 μsecs of the above argon laser is useful for doing time resolved holography of the plasma. Although it does not give sufficient time resolution for measurements on our fast Z-pinch discharge (Chapter 5), it is reasonably good for most other laboratory plasmas. For instance the use of holography for performing time resolved temperature measurements by resonance absorption has been mentioned earlier. The feasibility of using the above pulsed argon laser suggests the resonance absorption at 4765Å in argon plasma as an attractive diagnostic technique.

References.

1) R.V. Pole, '3-D Imagery and Holograms of Objects Illuminated in White Light', Applied Physics Letts, 20, 10, (1967).

2) R, Illingworth, Physics Department, University of Strathclyde, Glasgow, Private Communications.

Acknowledgements

It is a pleasure to acknowledge my gratitude to all the members of the Plasma Physics Group, Imperial College where this work was carried out.

In particular, I am very grateful to Dr.R.Latham for his supervision throughout the period of my work. I also thank him for his great help and encouragement from time to time.

To Dr.A.Folkierski, I am very grateful for his help and encouragement especially in the early period of the research. I offer him my thanks for reading part of the manuscript.

I am very grateful to Mr. A.E.Dangor and Mr. C.B.Wheeler for their taking much interest in my work and offering valuable criticism and suggestions throughout the work. I also thank them for reading part of my manuscript.

My thanks are also due to Dr. T.A.Hall for reading a substantial part of the manuscript.

I am very grateful to Mr. A.H.Chapman, Mr. P.Daly and Mr. B.Boreham for constructing most of my apparatus and to Mr. L.Nyman for his help in making the electronics. I am also thankful to Mr. O. Millbank for doing all the glassblowing for me.

To Miss. P.C.W.Grubb and Miss. R.J.Rivett - Carnac are due my thanks for typing the manuscript.

It is a pleasure to recall the joint persuit of concepts, in an attempt to actualize them in the laboratory, with my colleagues Mr. S.J.Fielding and Dr. S.S.Chowdhury and also the assigning of values to facts in the discussions with Mr. A.H.Nelson.

Finally, I would like to thank the Government of Pakistan for the award of the Merit Scholarship which enabled this work to be possible.

Appendix I

Calculation of resonance absorption of ruby laser radiation in nitrogen plasma with N_{II} emission line at 6942.9 Å.

Wheeler et. al.[1] had performed some calculations on the resonance absorption of argon laser radiation in A_{II} emission line at 4880 Å for the measurement of plasma temperature. Following Wheeler's suggestion the absorption of ruby laser light in N_{II} line at 6942.9 Å in nitrogen plasma was calculated. Apart from being the impurity in other laboratory plasmas, nitrogen in itself is utilized in many studies of electric discharges. The above mentioned calculations were performed in view of the feasibility of the method as a possible diagnostic tool for temperature measurements.

If the ruby laser beam of initial intensity I_o traverses the plasma of length ℓ, then the transmission of the beam is given by

$$\Gamma(\nu) = \frac{I_t}{I_o} = \ell^{-k(\nu)\ell} \qquad - (A.1)$$

where I_t is the transmitted intensity and $k(\nu)$ is the absorption coefficeint through the plasma in the region of line radiation of frequency ν_o. The beam is assumed to pass along the axis of symmetry so that $k(\nu)$ is independent of position along the axis. The absorption coefficient can be calculated from the transfer equation of the laser beam through the plasma which is

$$\frac{dI}{dx} = \frac{h\nu}{\Delta\Omega}\left[n(2)\frac{\Delta\Omega}{4\pi} B(2,1)\, I(\nu,x)\,\Psi(\nu) - \frac{n(1)\Delta\Omega}{4\pi} B(1,2)\right.$$

$$\left. I(\nu,x)\,\theta(\nu)\right] \qquad - (A.2)$$

where $\Delta\Omega$ is the solid angle of the laser beam as it passes through the plasma. $\Psi(\nu)$ and $\theta(\nu)$ are normalized profiles for induced emission and absorption respectively. B's are Einstein's intensity coefficients n(1) and n(2) are the number densities of particles in absor-

bing and emitting states of line transition.

If the intensity of the beam at a distance x from the boundary is I, then from Eq. (A.1), we have

$$\frac{dI}{dx} = - k(\nu)\, I_o\, e^{-k(\nu)x}$$

$$= - I\, k(\nu)$$

This when combined with Eq. (A.2) gives,

$$k(\nu) = \frac{h\nu}{4\pi} \left\{ n(1)\, B(1,2)\, \Theta(\nu) - n(2)\, B(2,1)\, \Psi(\nu) \right\} \qquad - (A.3)$$

In the above $B_{mn} = B_{nm}$ for non-degenerate energy levels. - (A.4)

If the laser frequency ν_L lies within the interval $\nu_o \pm W_\nu$ where W_ν is the frequency half-half width of the plasma line profile, and also when LTE prevails, the following profiles are equal, i.e.

$$\Theta(\nu) = \Psi(\nu) = \Phi(\nu) \qquad - (A.5)$$

where $\Phi(\nu)$ is the normalized profile for spontaneous emission. The above assumes that the power in the laser pulse is not too large to upset the population density of the atom levels.

Also if the plasma is in local thermodynamic equilibrium (L.T.E.), then the distributions of the atomic states will follow Boltzmann's law which for non-degenerate energy levels is

$$n(2) = n(1)\, e^{\frac{-h\nu_o}{kT}} \qquad - (A.6)$$

where ν_o is the frequency of the resonant line.

Substituting the above three equations in the Equation (A.3), we obtain

$$k(\nu) = \frac{h\nu_o}{4\pi}\, n(1)B(1,2)\left\{1 - e^{-h\nu_o/kT}\right\}\phi(\nu) \qquad -(A.7)$$

In the above, n(1) can be related to the total number density of the emitting species by Boltzmann statistics(2)

$$n(1) = \frac{Ng(1)}{Z(T)}\, e^{-\frac{E_1}{kT}} \qquad -(A.8)$$

where E_1 is the excitation energy of the lower state and g(1) is its statistical weight and Z(T) is the partition function.

The spontaneous emission line profile $\phi(\nu)$ is dispersive in shape when the electron density is sufficiently high for Stark broadening to dominate over the Doppler broadening. It is

$$\phi(\nu) = \frac{1}{\pi W}\,\frac{1}{1 + \left(\frac{\nu - \nu_o}{W}\right)^2} \qquad -(A.9)$$

The frequency half-half width W can be written as(2)

$$W = N_e\, f(T) \qquad -(A.10)$$

where N_e is the electron number density and f(T) is a weak function of temperature.

One can thus write the Eq. (A.7) as

$$k(\nu) = \frac{h\nu_o}{4\pi}\, B(1,2)(1 - e^{-\frac{h\nu_o}{kT}})\,\frac{1}{1 + (\frac{\nu - \nu_o}{W})^2}\,\frac{g(1)}{Z(T)\,\pi\, f(T)}$$

$$\times\, \frac{N}{N_e}\, e^{-\frac{E_1}{kT}} \qquad -(A.11)$$

where $\frac{N}{N_e}$ can be determined from the equation of charge neutrality and the equation governing the successive stages of ionization

$$N = N_+ = \gamma(N_e, T)\, N_e$$

$$\text{or } \frac{N}{N_e} = \gamma(N_e, T) \qquad -(A.12)$$

γ can be calculated from Saha Eq.(2) if L.T.E. prevails for all levels of all species of ions in the plasma. It is equal to unity for low degrees of ionization and rapidly decreases for increasing ionization. Thus $k(\nu)$ is almost independent of particle densities at low degree of ionization.

Utilizing Eqns. (A.11) and (A.12), the absorption coefficient can be written as

$$k(\nu) = A(T)\ e^{-\frac{E_1}{kT}}$$

where A(T) is a weakly varying function of temperature. Thus the transmission coefficient in Eq. (A.1) is given by

$$\begin{aligned} r(\nu) &= \exp\left[-k(\nu)\,\ell\right] \\ &= \exp\left[-A(T)\,\ell\,\exp\left(-\frac{E_1}{kT}\right)\right] \end{aligned} \qquad - (A.13)$$

Thus it is doubly exponential in temperature.

The N_{II} line at 6942.9 Å belongs to the multiplet no: (53) and corresponds to the transition $3d\,^3p_o - 4p\,^3p$. The excitation energy of the lower state $E_1 = 23.3$ ev.

To calculate $k(\nu)$ from Eq. (A.11) it is written as

$$k(\nu) = C\,\gamma\,F(T)\,e^{-\frac{E_1}{kT}}$$

where $C = \frac{h\nu_o}{4\pi}\ g(1)\ B(1,2)$

$$F(T) = \frac{N_e}{Z(T)W(T)}\ \left(1 - e^{-\frac{h\nu_o}{kT}}\right)\ \frac{1}{1 + \left(\frac{\nu - \nu_o}{W}\right)^2}$$

The multiplicity of the lower level = 2.

Thus $g(1) = 5$

The Einstein's coefficient $B(1,2) = \frac{e^2 \pi}{\nu h m} f_{12}$

The oscillator strength f_{12} for N_{II} line (6942.9 Å) is [3]

$$f_{12} \ (N_{II}) = 0.0457$$

which gives

$$B_{12} \ (N_{II}) = 5.34 \times 10^9$$

The laser frequency can be assumed to be a delta function in comparison with the N_{II} line width especially at electron densities larger than 10^{17} cm^{-3}. Also it can be considered to be at the centre of the plasma line profile.

The partition functions were obtained from Reference (4) and the line width of N_{II} line 6942.9 Å from Griem[2]. $\gamma \ (= \frac{N_{II}}{N_e})$ as a function of temperature was also obtained from Reference (4) at various electron density values.

The absorption coefficient $k(\nu_o)$ obtained as a function of temperature is shown in Fig. (A.1) for different values of electron densities. The percentage transmission was calculated as a function of temperature as shown in Fig. (A.2).

Discussion

As can be seen in Fig. (A.2), there is sufficient absorption of the laser light at density as low as $N_e = 10^{17}$ cm^{-3} for it to be measured both by conventional and holographic technique. Unlike the case of resonance absorption in argon at A_{II} at 4880 Å,[1] the percentage transmission is not independent of electron densities. This necessitates the simultaneous measurements of electron density for the determination of temperatures by this method. This could be done by holographic interferometry in side-on configuration using part of the same laser beam being sent axially for absorption measurements. In this

case the refractive index of the plasma will be determined by Selmeier's formula given in Eq. (5.10).

In the above discussion, the laser frequency was assumed to be at the centre of the plasma emission line. In practice, there is a frequency shift of the plasma line by an amount depending on the electron density. For instance, at $N_e = 10^{17}$ cm^{-3}, there is a shift toward the red by 0.53 Å. The laser line is then at the wings of the plasma line profile and $k(\nu)$ must be modified accordingly. Also, since, in practice, the laser line is not a delta function as assumed earlier, the effect of its line shape becomes important if it falls near the edge of the plasma line profile. This can, however, be avoided if the laser frequency can be shifted to be always at the plasma line centre. This is possible by simply controlling the temperature of the ruby to change the output laser wavelength according to the relation[5]

$$\lambda(T) = 6943.25 + 0.068\ (T - 20)$$

where λ is in angstroms and T in degrees centigrade.

If the Z-pinch is used in end-on configuration, as discussed in Section (5.3.1), there is a strong refraction of the beam due to large refractive index gradients. This was checked by the non-resonant radiation at 6328 Å from a He - Ne laser. The laser beam was sent axially through the discharge tube. It was strongly deflected out of the collecting photodetector placed at a distance from the plasma tube. This is seen in Fig. (A.3) where the dc signal falls to zero near both the first and second pinches. Since there is no absorption at this wavelength the loss of light is entirely due to refraction of the beam. Due to this limitation the resonance absorption experiment could not be performed. The technique can, however, be used in situations like stabilized pinch where the refractive index gradients are less severe.

References

(1) Wheeler, C.B. and Troughton, J. 'Measurement of Plasma Temperature by Absorption of Resonant laser Radiation' (1969). Internal Report Imperial College (London).

(2) Griem, H. Plasma Spectroscopy, McGraw-Hill, (1964).

(3) Wiese, Smith and Glennon, 'Atomic Transition Probabilities", NSRDS - NBS 4 Vol 1.

(4) Drawin, H.W. and Febenbok, P. 'Data for Plasmas in Local Thermodynamic Equilibrium', Gauthier-Villars, Paris.

(5) Lengyl, B.A. 'Introduction to Laser Physics'. P.101. John Wiley and Sons, Inc. (London) 1966.

Fig (A.1)

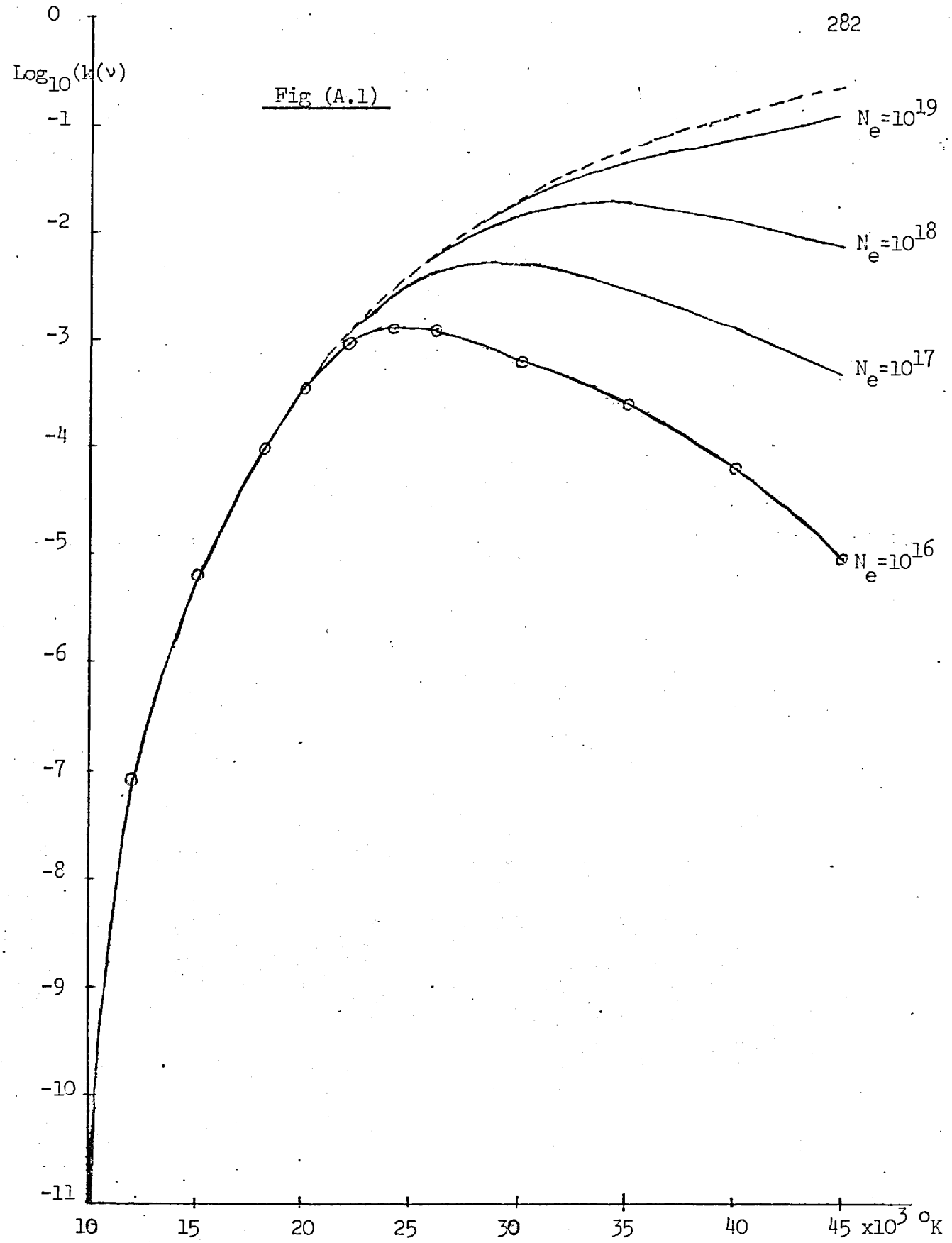
0
$\text{Log}_{10}(k(\nu)$
-1
-2
-3
-4
-5
-6
-7
-8
-9
-10
-11
$N_e=10^{19}$
$N_e=10^{18}$
$N_e=10^{17}$
$N_e=10^{16}$
10
15
20
25
30
35
40
45 x10^3 ^oK

Fig (A:2) Percentage Transmission of Ruby Laser light through the plasma of length ℓ = 29.4 Cms.

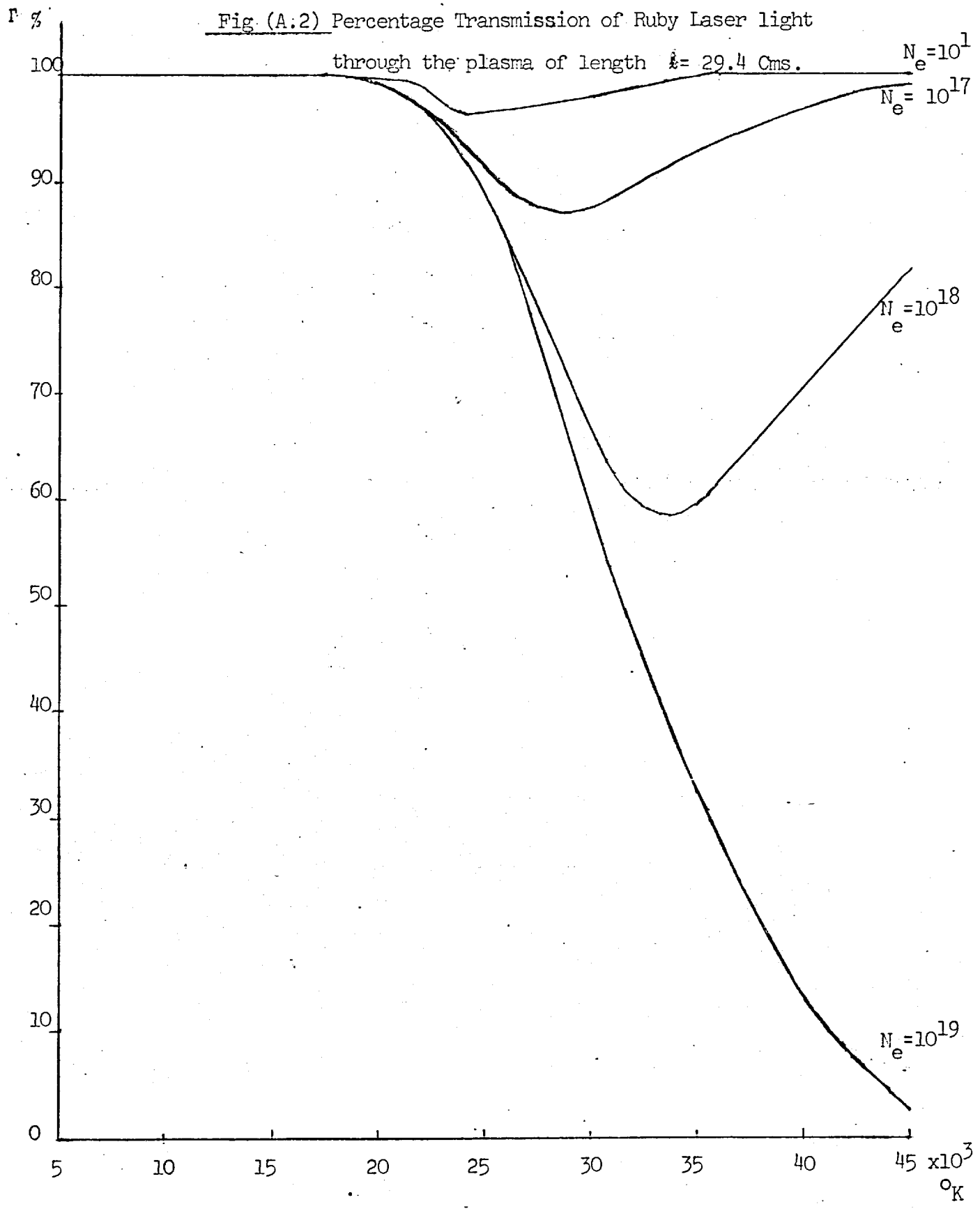

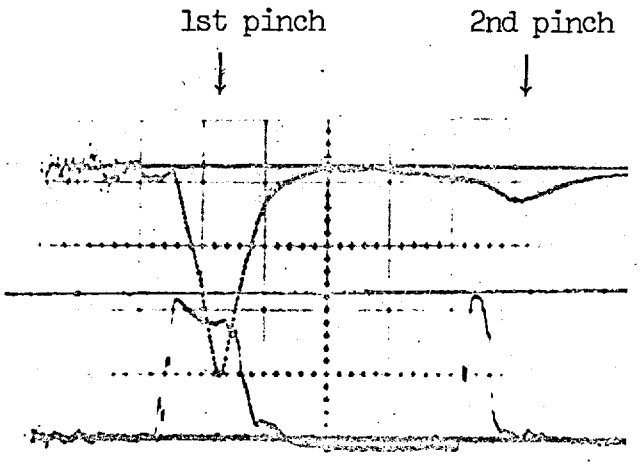
1st pinch
2nd pinch
Plasma Light
(Continuum)
Zero of dc level
He - Ne dc signal
2 μsecs/Cm

Fig (A,3)

Appendix II

Program for the Abel Inversion of experimentally obtained fringe distributions using Bockasten's Polynomial Coefficients[1]

```
      DIMENSIONA(20,20),F(20,10),HEIGHT(20),R(10),RN(20,10),DENSIT(20),
     CPATH(20)
      READ(5,200)((A(J,K),J=1,20),K=1,20)
  200 FORMAT(5(7F10.6/),F10.6)
      DO38K=1,20
      WRITE(6,550)(A(J,K),J=1,20)
  550 FORMAT(7(4X,F9.6)/7(4X,F9.6)/6(4X,F9.6))
   38 CONTINUE
      DO74 N=1,10
      READ(5,300)(F(J,N),J=1,20)
  300 FORMAT(3(5F6.3/),5F6.3)
      WRITE(6,748)(F(J,N),J=1,20)
  748 FORMAT(13(2X,F5.2)/7(2X,F5.2)///)
   74 CONTINUE
      READ(5,121)(R(N),N=1,10)
  121 FORMAT(9(F7.3/),F7.3)
      LIM=5
      N=0
   24 N=N+1
   54 RAD=R(N)
      HINT=RAD/20.
      WRITE(6,100)RAD
  100 FORMAT(17H ASSUMED RADIUS=,F7.3,4H CMS)
      DO22J=1,20
      HEIGHT(J)=(FLOAT(J-1)*HINT)
      RN(J,N)=1.78*1.0E17*F(J,N)
   22 CONTINUE
      J=21
   16 J=J-1
      DENSIT(J)=0.0
      DO89K=1,20
      DENSIT(J)=DENSIT(J)+RN(K,N)*A(J,K)/RAD
   89 CONTINUE
      WRITE(6,551)J,HEIGHT(J),DENSIT(J)
  551 FORMAT(10X,I3,10X,F10.6,10X,1PE20.7)
      IF(J.GT.1)GOTO16
      IF(N.GE.LIM)GOTO36
      GOTO24
   36 STOP
      END
```

Explanations:

A(20,20) ≡ Polynomial Coefficients obtained from reference(1)

F(20,10) ≡ No: of fringes for each of the fringe distributions

(max: number = 10), as those shown in Fig(6.17).
R(N) ≡ Radius for each fringe distribution.

References

(1) Bockasten, Kjell. J.Opt. Soc. Am. 51, 943(1961)